



Swansea University
Prifysgol Abertawe



Swansea University E-Theses

Behaviour of bolted connections with high strength and stainless steel.

Taufik, Syahril

How to cite:

Taufik, Syahril (2008) *Behaviour of bolted connections with high strength and stainless steel..* thesis, Swansea University.

<http://cronfa.swan.ac.uk/Record/cronfa43058>

Use policy:

This item is brought to you by Swansea University. Any person downloading material is agreeing to abide by the terms of the repository licence: copies of full text items may be used or reproduced in any format or medium, without prior permission for personal research or study, educational or non-commercial purposes only. The copyright for any work remains with the original author unless otherwise specified. The full-text must not be sold in any format or medium without the formal permission of the copyright holder. Permission for multiple reproductions should be obtained from the original author.

Authors are personally responsible for adhering to copyright and publisher restrictions when uploading content to the repository.

Please link to the metadata record in the Swansea University repository, Cronfa (link given in the citation reference above.)

<http://www.swansea.ac.uk/library/researchsupport/ris-support/>



**Prifysgol Abertawe
Swansea University**

**Behaviour of Bolted Connections with High Strength
and Stainless Steel**

Syahril Taufik

Thesis submitted to the Swansea University
in candidature for the degree of Doctor of Philosophy

August 2008

School of Engineering
Swansea University
Singleton Park, Swansea, SA2 8PP, UK



ProQuest Number: 10821450

All rights reserved

INFORMATION TO ALL USERS

The quality of this reproduction is dependent upon the quality of the copy submitted.

In the unlikely event that the author did not send a complete manuscript and there are missing pages, these will be noted. Also, if material had to be removed, a note will indicate the deletion.



ProQuest 10821450

Published by ProQuest LLC (2018). Copyright of the Dissertation is held by the Author.

All rights reserved.

This work is protected against unauthorized copying under Title 17, United States Code
Microform Edition © ProQuest LLC.

ProQuest LLC.
789 East Eisenhower Parkway
P.O. Box 1346
Ann Arbor, MI 48106 – 1346

Specimen Layout for Declaration/Statements page to be included in Higher Degree Thesis

DECLARATION

This work has not previously been accepted in substance for any degree and is not being concurrently submitted in candidature for any degree

Signed (candidate)

Date 20th AUGUST 2008

STATEMENT 1

This thesis is the result of my own investigations, except where otherwise stated. Other sources are acknowledged by footnotes giving explicit references. A bibliography is appended.

Signed (candidate)

Date 20th AUGUST 2008

STATEMENT 2

I hereby give consent for my thesis, if accepted, to be available for photocopying and for inter-library loan, and for the title and summary to be made available to outside organizations.

Signed (candidate)

Date 20th AUGUST 2008

Acknowledgement

I would like to thank all these who have supported and provided me with helpful advice throughout the course of this thesis. I would particularly like to thank Dr R.Y. Xiao for his constructive guidance, supervision, knowledge and suggestions throughout the course of the research. I extend my thanks to my family and friends who have provided me continuous encouragement from the start of this research. Sponsorship from The Professional and Skill Development Staff Project (TPSDP) of Lambung Mangkurat University, Indonesia is gratefully appreciated.

Content List

| | |
|------------------------|-----|
| Abstract | i |
| Acknowledgement | ii |
| Content List | iii |
| List of Figures | vii |
| List of Tables | xvi |
| Notations | xix |

Chapter 1 Introduction

| | |
|------------------------------------|---|
| 1.1. General | 1 |
| 1.1 Background | 2 |
| 1.2 Objectives and Methods | 3 |
| 1.3 Brief Description Each Chapter | 4 |

Chapter 2 Literature Review

| | |
|---|----|
| 2.1 Introduction | 6 |
| 2.2 General Introduction on High Strength Steel | 6 |
| 2.3 General Introduction on Stainless Steel | 10 |
| 2.4 Strain Softening | 10 |
| 2.5 Shear Bolted Connections | 17 |
| 2.6 Partially Restrained Connections | 19 |
| 2.7 Finite Element Modelling | 23 |
| 2.8 Need for Further Research | 34 |

Chapter 3 *Introduction of Finite Element Modelling*

| | | |
|--------|---|----|
| 3.1 | Introduction | 35 |
| 3.2 | The Constitutive Modelling | 37 |
| 3.2.1 | The theory of finite element | 38 |
| 3.2.2 | Non linear behaviour of steel | 46 |
| 3.2.3 | Modelling the plasticity behaviour of steel | 46 |
| 3.2.4 | Yield criterion | 47 |
| 3.2.5 | Hardening rule | 48 |
| 3.2.6 | Implementation | 53 |
| 3.2.7 | Multi-linear isotropic hardening (MISO) | 55 |
| 3.3 | Finite Element Modelling and Working with ANSYS | 56 |
| 3.3.1 | Types of Analyses on Structures | 57 |
| 3.3.2 | Typical Modelling Difficulties | 58 |
| 3.3.3 | ANSYS Commands Involved in the Analyses | 59 |
| 3.3.4 | Element Overview | 61 |
| 3.3.5 | Material Properties | 69 |
| 3.3.6 | Model Geometry | 70 |
| 3.3.7 | Substeps | 71 |
| 3.3.8 | Meshing | 71 |
| 3.3.9 | Solution Commands (SOLU) | 72 |
| 3.3.10 | Postprocessor Commands | 74 |
| 3.4 | Finite Element Model | 75 |
| 3.5.1. | SLB model | 76 |
| 3.5.2. | DWA model | 78 |
| 3.5.3. | TSA model | 80 |
| 3.5.4. | TSAW model | 81 |
| 3.5.5. | FEP and EPTB model | 83 |
| 3.5.6. | SCC model | 85 |
| 3.5 | Summary | 88 |

Chapter 4 *Validation of Finite Element Modelling Procedure*

| | | |
|--------|---|-----|
| 4.1 | Introduction | 90 |
| 4.2 | Validation of Finite Element Model | 91 |
| 4.2.1. | Double web angle (DWA) connections | 92 |
| 4.2.2. | Top and seat angle (TSA) connections | 95 |
| 4.2.3. | Top and seat angle with double web angle (TSAW) connections | 97 |
| 4.2.4. | Flush end plate (FEP) connections | 102 |
| 4.2.5. | End plate tubular beam (EPTB) connections | 105 |
| 4.2.6. | Semi continuous composite (SCC) connections | 108 |
| 4.2.7. | Shear bolted (SLB) connections | 109 |
| 4.3 | Comparison between FEA and Test Result | 111 |
| 4.3.1. | PR connections | 111 |
| 4.3.2. | SLB connections | 112 |
| 4.4 | Conclusion from Validation Study | 113 |

Chapter 5 *FE Model with High Strength and Stainless Steel*

| | | |
|-------|--------------------------|-----|
| 5.1 | Introduction | 114 |
| 5.2 | Angle Bolted Connections | 114 |
| 5.2.1 | DWA connections | 118 |
| 5.2.2 | TSA connections | 123 |
| 5.2.3 | TSAW connections | 133 |
| 5.3 | Endplate Connections | 140 |
| 5.3.1 | FEP connections | 140 |
| 5.3.2 | EPTB connections | 147 |
| 5.3.3 | SCC connections | 153 |
| 5.4 | Shear Bolted Connections | 163 |
| 5.5 | Summary and Conclusion | 177 |

Chapter 6 *Parametric Study*

| | | |
|-------|--|-----|
| 6.1 | Introduction | 179 |
| 6.2 | The Parametric Study | 179 |
| 6.2.1 | Effect of different steel grades of the angle and endplate | 179 |
| 6.2.2 | Effect of different thicknesses of the angle and endplate | 185 |
| 6.2.3 | Effect of different sizes of the beam | 191 |
| 6.2.4 | Effect of the stiffened column | 196 |
| 6.2.5 | Effect of different steel grades of the spliced plate | 199 |
| 6.2.6 | Effect of different thicknesses of the spliced plate | 202 |
| 6.2.7 | Effect of different edge distances of the bolt | 204 |
| 6.3 | Discussion from Parametric Study | 207 |
| 6.4 | Static Frame Analysis | 209 |
| 6.3.1 | Non-sway static analysis | 209 |
| 6.3.2 | Sway static analysis | 213 |
| 6.5 | Summary and Conclusion | 217 |

Chapter 7 *The Design Equations*

| | | |
|-----|---|-----|
| 7.1 | Introduction | 219 |
| 7.2 | Analytical model for moment-rotation | 220 |
| 7.3 | Ductility analysis | 231 |
| 7.4 | Proposed equation for resistance design | 233 |
| 7.5 | Summary and Conclusion | 236 |

Chapter 8 *Conclusions and Recommendations*

| | | |
|-----|-----------------|-----|
| 8.1 | Introduction | 238 |
| 8.2 | Conclusions | 239 |
| 8.3 | Recommendations | 242 |

| | |
|---------------------|-----|
| References | 244 |
| Appendix A | 255 |
| Appendix B | 260 |
| Appendix C | 267 |
| Appendix D | 271 |
| Appendix E | 276 |
| Appendix F | 280 |
| Appendix G | 283 |
| Publications | 285 |

List of Figures

Chapter 2 Literature Review

| | | |
|------------|---|----|
| Figure 2.1 | Typical stress-strain curve of HSS | 8 |
| Figure 2.2 | Typical stress-strain curve of stainless steel | 10 |
| Figure 2.3 | The engineering stress-strain curve up to fracture strain | 13 |
| Figure 2.4 | Partially Restrained Connections | 21 |

Chapter 3 Introduction to Finite Element Modelling

| | | |
|-------------|--|----|
| Figure 3.1 | Eight-node hexahedral element | 38 |
| Figure 3.2 | The hexahedral element in the ξ, η, ζ space | 41 |
| Figure 3.3 | The spar element in the global coordinate system | 43 |
| Figure 3.4 | The yield loci of Tresca and von Mises | 48 |
| Figure 3.5 | Perfect plasticity and linear hardening | 49 |
| Figure 3.6 | The hardening rule in isotropic hardening behaviour | 50 |
| Figure 3.7 | Uniaxial behaviour for MISO and σ_k determination | 56 |
| Figure 3.8 | LINK8 Spar element geometry | 61 |
| Figure 3.9 | SOLID45 Structural solid geometry | 62 |
| Figure 3.10 | SOLID65 RC solid geometry | 63 |
| Figure 3.11 | SOLID185 Structural solid geometry | 64 |
| Figure 3.12 | SHELL143 Plastic small strain shell geometry | 64 |
| Figure 3.13 | CONTA178 Node-to-node contact geometry | 65 |
| Figure 3.14 | TARGE170 Target segment geometry | 66 |
| Figure 3.15 | CONTA173 Surface-to-surface contact geometry | 67 |
| Figure 3.16 | COMBIN39 Non linear spring geometry | 67 |
| Figure 3.17 | PRETS179 Pretension geometry | 68 |
| Figure 3.18 | BEAM23 2D-Plastic Beam geometry | 69 |
| Figure 3.19 | Finite element model of the shear bolted connection | 77 |

| | | |
|-------------|---|----|
| Figure 3.20 | Finite element model of bolt | 79 |
| Figure 3.21 | Contact element modelling of the DWA connection | 79 |
| Figure 3.22 | Contact element on the TSA connection | 81 |
| Figure 3.23 | Modelling of contact element of the web angle | 82 |
| Figure 3.24 | FE modelling of the TSAW connection | 83 |
| Figure 3.25 | FE modelling configuration of the TSAW connection | 85 |
| Figure 3.26 | Simplified model of the FEP connection | 86 |
| Figure 3.27 | FE modelling configuration of the SCC connection | 87 |
| Figure 3.28 | FE model of the SCC connection | 87 |

Chapter 4 Validation of Finite Element Modelling Procedure

| | | |
|-------------|--|-----|
| Figure 4.1 | Measurement of rotational angle change | 92 |
| Figure 4.2 | Measurement of rotational endplate change | 92 |
| Figure 4.3 | DWA1 connection geometry | 93 |
| Figure 4.4 | DWA2 connection geometry | 93 |
| Figure 4.5 | M- θ curve of DWA1a from experimental and FE models | 94 |
| Figure 4.6 | M- θ curve of DWA2a from experimental and FE models | 94 |
| Figure 4.7 | Maximum stress of web angles with hexagon hole | 95 |
| Figure 4.8 | Maximum stress of web angles with circular hole | 95 |
| Figure 4.9 | TSA connection geometry | 96 |
| Figure 4.10 | M- θ curve of TSA1a from experimental and FE models | 97 |
| Figure 4.11 | M- θ curve of TSA2a from experimental and FE models | 97 |
| Figure 4.12 | TSAW1 and TSAW2 connection geometry | 98 |
| Figure 4.13 | TSAW3 and TSAW4 connection geometry | 99 |
| Figure 4.14 | Validation of FE modelling against test result (TSAW-1a) | 99 |
| Figure 4.15 | Validation of FE modelling against test result (TSAW-2a) | 100 |
| Figure 4.16 | Validation of FE modelling against test result (TSAW-3a) | 100 |
| Figure 4.17 | Validation of FE modelling against test result (TSAW-4a) | 101 |
| Figure 4.18 | Deformed shape of the TSAW connection | 101 |

| | | |
|-------------|---|-----|
| Figure 4.19 | FE modelling configuration of FEP-1 connection | 103 |
| Figure 4.20 | FE modelling configuration of the FEP-2 connection | 103 |
| Figure 4.21 | FE modelling configuration of the FEP-3 connection | 104 |
| Figure 4.22 | Validation of FE modelling against test result – FEP-1a | 104 |
| Figure 4.23 | Validation of FE modelling against test result – FEP-2a | 105 |
| Figure 4.24 | Validation of FE modelling against test result – FEP-3a | 106 |
| Figure 4.25 | FE modelling configuration of EPTB-1 connection | 106 |
| Figure 4.26 | FE modelling configuration of EPTB-2 connection | 107 |
| Figure 4.27 | Validation of FE modelling against test result - EPTB | 107 |
| Figure 4.28 | FE modelling configuration of SCC connection | 108 |
| Figure 4.29 | Validation of FE modelling against test result - SCC | 108 |
| Figure 4.30 | FE modelling configuration of the SLB connection | 110 |
| Figure 4.31 | Load-displacement relationship of the SLB connection | 111 |

Chapter 5 FE Model with High Strength and Stainless Steel

| | | |
|-------------|--|-----|
| Figure 5.1 | Enhanced strength region of a cold formed angle | 116 |
| Figure 5.2 | Multi-linear stress-strain curve for FE | 117 |
| Figure 5.3 | Moment-rotation relationship of the DWA-1 model | 119 |
| Figure 5.4 | Moment-rotation relationship of the DWA-2 model | 120 |
| Figure 5.5 | Moment-rotation relationship of the DWA-3 model | 120 |
| Figure 5.6 | Moment-rotation relationship of the DWA-4 model | 121 |
| Figure 5.7 | Deformed shape of the DWA-2 connection | 121 |
| Figure 5.8 | Stress contour of S550 web angle | 122 |
| Figure 5.9 | Stress contour of S275 column flange | 122 |
| Figure 5.10 | Deformed shape of the TSA connection | 123 |
| Figure 5.11 | Moment-rotation relationship of the TSA1 model; S690 angle | 124 |
| Figure 5.12 | Moment-rotation relationship of the TSA2 model; S690 angle | 124 |
| Figure 5.13 | Moment-rotation relationship of the TSA1 model; S550 and S690 angle | 125 |

| | | |
|-------------|---|-----|
| Figure 5.14 | Failure modes of the connection | 126 |
| Figure 5.15 | Effective length l_{eff} of an angle flange cleat | 127 |
| Figure 5.16 | Moment-rotation relationship of TSA1 – $t_{sa} = 8.0\text{mm}$ | 129 |
| Figure 5.17 | Moment-rotation relationship of TSA1 – $t_{sa} = 11.0\text{mm}$ | 129 |
| Figure 5.18 | Stress contours of the TSA connections; (a) thick angle (b) column flange | 130 |
| Figure 5.19 | Stress contours of S690 angles with corner enhancement; (a) r_m (b) $r_m + 2t_a$ | 130 |
| Figure 5.20 | Comparison of plastic deformation in the top angles (S690) | 131 |
| Figure 5.21 | Comparison of plastic deformation in the top angles (S550) | 131 |
| Figure 5.22 | M- θ curve with yielding sequence of the components (thin angle) | 132 |
| Figure 5.23 | M- θ curve with yielding sequence of the components (thick angle) | 132 |
| Figure 5.24 | M- θ relationship of TSAW-1; S690, S460 and S275 angle cleats | 136 |
| Figure 5.25 | M- θ relationship of TSAW-2; S690, S460 and S275 angle cleats | 136 |
| Figure 5.26 | M- θ relationship of TSAW-3 with various angle cleat thickness and grade | 137 |
| Figure 5.27 | M- θ relationship of TSAW-3; various web angle | 137 |
| Figure 5.28 | M- θ relationship of TSAW-2; S690 and S460 angle cleats | 138 |
| Figure 5.29 | Comparison of TSAW M- θ relationship | 138 |
| Figure 5.30 | Stress contours of the S460 top angle | 139 |
| Figure 5.31 | Stress contours of the S275 web angle | 139 |
| Figure 5.32 | Stress contours of the S275 web angle | 140 |
| Figure 5.33 | Moment-rotation relationship of the FEP-1 model | 141 |
| Figure 5.34 | Moment-rotation relationship of the FEP-1 model; M20 bolts | 142 |
| Figure 5.35 | Moment-rotation relationship of the FEP-2 model; M20 bolts | 142 |
| Figure 5.36 | Moment-rotation relationship of the FEP-3 model; M27 and M24 bolts | 143 |
| Figure 5.37 | Effective length l_{eff} of equivalent T stub | 143 |
| Figure 5.38 | Stress contour of the FEP model with S275 column | 144 |
| Figure 5.39 | Stress contour of the FEP model with S355 column | 145 |
| Figure 5.40 | Stress contour of the S355 column flange and S690 end plate | 146 |

| | | |
|-------------|---|-----|
| Figure 5.41 | Plastic deformation of the S690 end plate | 146 |
| Figure 5.42 | M- θ relationship of the EPHSa connection; S550 endplate | 148 |
| Figure 5.43 | M- θ relationship of the EPHSa connection; S690 endplate | 149 |
| Figure 5.44 | M- θ relationship of the EPHSb connection; S550 endplate | 149 |
| Figure 5.45 | M- θ relationship of the EPHSb connection; S690 endplate | 150 |
| Figure 5.46 | 3D finite element of the end plate model with deformed shape | 150 |
| Figure 5.47 | Stress contour of the S690 endplate connection | 151 |
| Figure 5.48 | Stress contour of the S690 thin endplate with deformed shape | 151 |
| Figure 5.49 | Stress contour of the endplate with RHS beam: S355-15mm and S690-15mm | 152 |
| Figure 5.50 | Stress contour of the endplate with SHS beam: S550-15mm and S690-12mm | 152 |
| Figure 5.51 | M- θ relationship of the un-stiffened SCC connection: S690 end plate | 154 |
| Figure 5.52 | M- θ relationship of the stiffened SCC connection; S690 endplate | 155 |
| Figure 5.53 | 3D finite element of the SCC model with deformed shape | 156 |
| Figure 5.54 | Stress contour of the bare steel joint with S690 endplate | 157 |
| Figure 5.55 | Equivalent Von Mises stress distribution in of the SCC1b – without stiffener | 158 |
| Figure 5.56 | Equivalent Von Mises stress distribution in of the SCC2b – web stiffener | 158 |
| Figure 5.57 | Stress contour of the connection with S690 thinner endplate | 159 |
| Figure 5.58 | Stress contour of the connection with S690 thicker endplate | 159 |
| Figure 5.59 | Stress contours of the S690 end plate and S355 column | 160 |
| Figure 5.60 | Plastic strain of the S690 end plate and S355 column | 161 |
| Figure 5.61 | M- θ curve with yielding sequence of the components in FEA study | 162 |
| Figure 5.62 | M- θ curve with yielding sequence of the components in FEA study | 162 |
| Figure 5.63 | Load-displacement relationship of the S690 SLB connection | 164 |
| Figure 5.64 | Load-displacement relationship of the SS205 SLB connection | 165 |

| | | |
|-------------|--|-----|
| Figure 5.65 | Load-displacement relationship of the S1350 SLB connection | 165 |
| Figure 5.66 | Deformed shape of the connection with $e_1/d_0=1.0$ under bearing failure | 166 |
| Figure 5.67 | Deformed shape of the connection with $e_1/d_0=1.0$ under net-section failure | 166 |
| Figure 5.68 | Stress contour of the S690 plate with $e_1/d_0=2.0$ at the ultimate stress | 167 |
| Figure 5.69 | Stress contour of the S690 plate with $e_1/d_0=2.0$ at the rupture condition | 167 |
| Figure 5.70 | Stress contour of the S690 plate with at the net section and bearing rupture | 168 |
| Figure 5.71 | Stress contour of the S690 plate with $e_1/d_0=1.2$ at the ultimate stress | 168 |
| Figure 5.72 | Stress contour of the S690 plate with $e_1/d_0=1.2$ at the rupture condition | 169 |
| Figure 5.73 | Stress contour of the SS2205 plate with $e_1/d_0=1.0$ at the ultimate stress | 169 |
| Figure 5.74 | Stress contour of the S2205 plate with $e_1/d_0=1.0$ at the rupture condition | 170 |
| Figure 5.75 | Stress contour of the SS2205 plate with $e_1/d_0=1.5$ at the ultimate stress | 170 |
| Figure 5.76 | Stress contour of the S2205 plate with $e_1/d_0=1.5$ at the rupture condition | 171 |
| Figure 5.77 | Stress contour of the S1350 plate with $e_1/d_0=1.0$ at the ultimate stress | 171 |
| Figure 5.78 | Stress contour of the S1350 plate with $e_1/d_0=1.0$ at the rupture condition | 172 |
| Figure 5.79 | Complete stress-deformation curves of the S690 SLB connection | 172 |
| Figure 5.80 | Complete stress-deformation curves of the SS2205 SLB connection | 173 |
| Figure 5.81 | Complete stress-deformation curves of the S1350 SLB connection | 173 |

Chapter 6 Parametric Study

| | | |
|-------------|--|-----|
| Figure 6.1 | Chart showing ultimate moment for each case study (1) | 180 |
| Figure 6.2 | Chart showing ultimate moment for each case study (2) | 181 |
| Figure 6.3 | Chart showing ultimate moment for each case study (3) | 182 |
| Figure 6.4 | Chart showing ultimate moment for each case study (4) | 183 |
| Figure 6.5 | Chart showing ultimate moment for each case study (5) | 184 |
| Figure 6.6 | Chart showing ultimate moment for each case study (6) | 185 |
| Figure 6.7 | Chart showing ultimate moment for each case study (7) | 186 |
| Figure 6.8 | Chart showing ultimate moment for each case study (8) | 187 |
| Figure 6.9 | Chart showing ultimate moment for each case study (9) | 188 |
| Figure 6.10 | Chart showing ultimate moment for each case study (10) | 189 |
| Figure 6.11 | Chart showing ultimate moment for each case study (11) | 190 |
| Figure 6.12 | Chart showing ultimate moment for each case study (12) | 191 |
| Figure 6.13 | Chart showing ultimate moment for each case study (13) | 192 |
| Figure 6.14 | Chart showing ultimate moment for each case study (14) | 193 |
| Figure 6.15 | Chart showing ultimate moment for each case study (15) | 194 |
| Figure 6.16 | Chart showing ultimate moment for each case study (16) | 195 |
| Figure 6.17 | Chart showing ultimate moment for each case study (17) | 196 |
| Figure 6.18 | Chart showing ultimate moment for each case study (18) | 197 |
| Figure 6.19 | Chart showing ultimate moment for each case study (19) | 198 |
| Figure 6.20 | Chart showing ultimate moment for each case study (20) | 199 |
| Figure 6.21 | Chart showing ultimate moment for each case study (21) | 200 |
| Figure 6.22 | Chart showing ultimate moment for each case study (22) | 201 |
| Figure 6.23 | Chart showing ultimate moment for each case study (23) | 202 |
| Figure 6.24 | Chart showing ultimate moment for each case study (24) | 203 |
| Figure 6.25 | Chart showing ultimate moment for each case study (25) | 204 |
| Figure 6.26 | Chart showing ultimate moment for each case study (26) | 205 |
| Figure 6.27 | Chart showing ultimate moment for each case study (27) | 206 |
| Figure 6.28 | Single storey frame model | 209 |
| Figure 6.29 | Non-sway frame model | 210 |

| | | |
|-------------|---|-----|
| Figure 6.30 | Maximum vertical deflection of the main beams for non-sway frame | 212 |
| Figure 6.31 | Bending moment distribution of the non-sway model for: (a) fully pinned base and beam-to-column joint (b) fully fixed base and beam-to-column joint | 212 |
| Figure 6.32 | Sway frame model | 213 |
| Figure 6.33 | Horizontal deflection at the top of the column for the sway frame (1) | 215 |
| Figure 6.34 | Horizontal deflection at the top of the column for the sway frame (2) | 216 |
| Figure 6.35 | Bending moment distribution of the sway model for: (a) fully pinned base and beam-to-column joint (b) fully fixed base and beam-to-column joint | 216 |

Chapter 7 Design Equations

| | | |
|------------|--|-----|
| Figure 7.1 | Three-Parameter Power Model | 221 |
| Figure 7.2 | Comparison of FEM results with proposed equation; DWA2d | 229 |
| Figure 7.3 | Comparison of FEM results with proposed equation; TSA4c | 229 |
| Figure 7.4 | Comparison of FEM results with proposed equation; EPHS3b | 230 |
| Figure 7.5 | Comparison of FEM results with proposed equation; FEP2a | 230 |

List of Tables

Chapter 4 Validation of Finite Element Modelling Procedure

| | | |
|------------|------------------------------------|-----|
| Table 4.1 | DWA connection parameter | 93 |
| Table 4.2 | TSA connection parameter | 96 |
| Table 4.3 | TSAW connection parameter | 98 |
| Table 4.4 | FEP connection geometry | 102 |
| Table 4.5 | Material properties for FE model | 102 |
| Table 4.6 | Material properties for FE model | 106 |
| Table 4.7 | EPTB connection parameter | 106 |
| Table 4.8 | SCC connection parameter | 108 |
| Table 4.9 | SLB connection parameter | 110 |
| Table 4.10 | Comparison FEA against test result | 112 |
| Table 4.11 | Comparison FEA against test result | 112 |

Chapter 5 FE Model with High Strength and Stainless Steel

| | | |
|------------|--|-----|
| Table 5.1 | Summary of material properties | 117 |
| Table 5.2 | Moment capacity with corner strength enhancement | 119 |
| Table 5.3 | Moment capacity and failure mode | 128 |
| Table 5.4 | TSAW configuration parameter for FEA | 133 |
| Table 5.5 | Material properties for TSAW model | 134 |
| Table 5.6 | Moment capacity with corner strength enhancement | 136 |
| Table 5.7 | FEP configuration parameter for FEA | 141 |
| Table 5.8 | Ultimate moment and failure mode of FEP model | 144 |
| Table 5.9 | Material properties for FE model | 147 |
| Table 5.10 | Moment capacity and failure mode | 148 |
| Table 5.11 | SCC connection performance for FE model | 155 |

| | | |
|------------|--|-----|
| Table 5.12 | Ultimate load and failure mode of the SS690 SLB model | 175 |
| Table 5.13 | Ultimate load and failure mode of the SS2205 SLB model | 175 |
| Table 5.14 | Ultimate load and failure mode of the S1350 SLB model | 176 |

Chapter 6 Parametric Study

| | | |
|------------|--|-----|
| Table 6.1 | Initial stiffness and ultimate moment of 9.5 and 12.5mm angles | 180 |
| Table 6.2 | Initial stiffness and ultimate moment of 9.5 and 12.5mm angles | 181 |
| Table 6.3 | Initial stiffness and ultimate moment of 8.0 and 9.5mm angles | 182 |
| Table 6.4 | Initial stiffness and ultimate moment of 12.0 and 15.0mm plates | 183 |
| Table 6.5 | Initial stiffness and ultimate moment of 10, 12 and 15mm plates | 184 |
| Table 6.6 | Initial stiffness and ultimate moment of 10.0 and 20.0mm plates | 185 |
| Table 6.7 | Initial stiffness and ultimate moment of S460 and S690mm angles | 186 |
| Table 6.8 | Initial stiffness and ultimate moment of S460 and S550mm angles | 187 |
| Table 6.9 | Initial stiffness and ultimate moment of S460 and S690mm angles | 188 |
| Table 6.10 | Initial stiffness and ultimate moment of S550 and S690mm plates | 189 |
| Table 6.11 | Initial stiffness and ultimate moment of S550 and S690mm plates | 190 |
| Table 6.12 | Initial stiffness and ultimate moment of S460 and S690mm plates | 191 |
| Table 6.13 | Initial stiffness and ultimate moment of S460 and S690mm plates | 192 |
| Table 6.14 | Initial stiffness and ultimate moment of S460 and S550mm angles | 193 |
| Table 6.15 | Initial stiffness and ultimate moment of S460 and S690mm angles | 194 |
| Table 6.16 | Initial stiffness and ultimate moment of S550 and S690mm plates | 195 |
| Table 6.17 | Initial stiffness and ultimate moment of S550 and S690mm plates | 196 |
| Table 6.18 | Initial stiffness and ultimate moment of S460 and S690mm angles | 197 |
| Table 6.19 | Initial stiffness and ultimate moment of S550 and S690mm plates | 198 |
| Table 6.20 | Initial stiffness and ultimate moment of S550 and S690mm plates | 199 |
| Table 6.21 | Maximum resistance and rupture load for $e_1/d_0=1.2$ and 1.5 | 200 |
| Table 6.22 | Maximum resistance and rupture load for $e_1/d_0=2.0$ and 2.5 | 201 |
| Table 6.23 | Maximum resistance and rupture load for 2205, S690 and S1350 plates | 202 |

| | | |
|------------|---|-----|
| Table 6.24 | Maximum resistance and rupture load for 2205, S690 and S1350 plates | 203 |
| Table 6.25 | Maximum resistance and rupture load with $t_p=8.0$ and 10mm | 204 |
| Table 6.26 | Maximum resistance and rupture load with $t_p=8.0$ and 10mm | 205 |
| Table 6.27 | Maximum resistance and rupture load with $t_p=8.0$ and 10mm | 206 |
| Table 6.28 | Maximum vertical deflection of the main beams for non-sway frame (1) | 211 |
| Table 6.29 | Maximum vertical deflection of the main beams for non-sway frame (2) | 211 |
| Table 6.30 | Horizontal deflection at the top of the column for the sway frame (1) | 214 |
| Table 6.31 | Horizontal deflection at the top of the column for the sway frame (2) | 214 |

Chapter 7 Design Equations

| | | |
|-----------|--|-----|
| Table 7.1 | Parameter values power model obtained through curve fitting (1) | 226 |
| Table 7.2 | Parameter values power model obtained through curve fitting (2) | 227 |
| Table 7.3 | Parameter values power model obtained through curve fitting (3) | 228 |
| Table 7.4 | Joint ductility index of angle bolted connection | 231 |
| Table 7.5 | Joint ductility index of angle bolted connection | 232 |
| Table 7.6 | The comparison results between (modelling and experiment) and the design equations (experimental and modelling results obtained from Chapters 4 and 5) | 234 |
| Table 7.7 | The comparison results between (modelling and experiment) and the design equations (experimental and modelling results obtained from Chapters 4 and 5) | 235 |

Notations

| | |
|-------------------------|---|
| f_y | Yield strength |
| f_u | Ultimate strength |
| ϵ_y | Ultimate strain |
| ϵ_u | Strain at yield stress |
| ϵ_{fr} | Strain at fracture stress |
| σ_{yn} | Nominal value of yield stress |
| σ_{un} | Nominal value of ultimate stress |
| E | The Young's modulus |
| $E_{0.2}$ | Tangent modulus at 0.2% strain |
| $\epsilon_{0.2}$ | Strain at value of 0.2% |
| $\sigma_{0.2}$ | Proof stress at 0.2% strain |
| m | Parameter defined using ϵ_u , σ_u , ϵ_{fr} , and σ_{fr} |
| β | Parameter defined using ϵ_u , σ_u , ϵ_{fr} , and σ_{fr} |
| e_2 | Edge distance from the centre of the bolt hole |
| p_2 | Bolt spacing |
| d_o | Bolt hole diameter |
| M | Bending moment |
| M_u | Ultimate bending moment |
| \mathbf{q} | The nodal displacement vector |
| $\boldsymbol{\sigma}$ | Stress vector. |
| $\boldsymbol{\epsilon}$ | Strain vector. |
| \mathbf{B} | The strain displacement tensor matrix. |
| \mathbf{D} | A symmetric tangent modulus matrix that has (6×6) dimension |
| ν | Poisson's ratio |
| \mathbf{u} | Displacement vector. |
| \mathbf{N} | The matrix of shape functions. |
| (η, ξ, ζ) | The natural coordinate system of any point in the element. |

| | |
|---|---|
| (x,y,z) | The global coordinate system. |
| Γ | The inverse matrix of the Jacobian matrix. |
| J | Jacobian matrix. |
| k^e | Element stiffness matrix. |
| U | Strain Energy. |
| f | Force vector |
| F | Axial force |
| F_e^a | Applied load factor |
| F_e^{nr} | Newton-Raphson restoring forcer |
| σ_{ij} | Stress |
| C_{ijkl} | Forth order elastic stiffness tensor |
| D | Rate of deformation |
| D^e | Rate of deformation in elastic |
| D^p | Rate of deformation in plastic |
| σ_{eff} | Effective stress |
| f | Yield function |
| σ^y | Yield stress |
| $\sigma^{v,M}$ | von Mises' stress |
| S_{il} | Deviatoric part of the stress |
| D^p_{ij} | Rate of plastic flow |
| $\dot{\lambda}$ | Plastic multiplier |
| Σ | Effective stress in kinematic hardening |
| σ^y_o | Initial yield stress |
| κ | Plastic work |
| M | Coefficient matrix that has (6x6) dimension |
| C | Translation multiplier |
| $\{\epsilon^e\}$ | Elastic strain |
| $\{\epsilon^p\}$ | Plastic strain |
| $\{\epsilon^{tr}\}$ | Trial strain |
| $\hat{\epsilon}^{pl}$ ϵ_{eff} | Equivalent plastic strain |

| | |
|--------------------------------|---|
| $\{\sigma\}$ | Stresses. |
| σ_{eff} | Equivalent stress. |
| $\Delta\varepsilon_{eff}$ | Equivalent plastic strain increment. |
| σ_m | Mean or hydrostatic stress |
| $\sigma_x, \sigma_y, \sigma_z$ | Normal stresses on the x, y and z directions. |
| $M-\theta$ | Moment-rotation |
| F | Applied point load |
| d | The beam length |
| δ | Relative displacement of the beam |
| h | The beam depth |
| W | Left end width |
| b | Right end width |
| t_p | Thickness of the plate |
| e_1 | Distance from the right end |
| e_2 | Distance from the bottom end |
| g | Gauge in leg |
| p | Bolt spacing |
| t_{sa} | Top and seat angle thickness |
| t_{wa} | Web angle thickness |
| t_{ep} | End plate thickness |
| R_{ki} | Initial stiffness |
| θ_{Mu} | Rotation at ultimate moment |
| K_i | Initial stiffness |
| P_u | Ultimate load |
| Δ_C | Elongation capacity |
| $P\Delta_C$ | Load resistance at fracture of the joint |
| r_i | Corner radius |
| t | Nominal core thickness |
| f_{ya} | Average yield strength enhancement |
| f_{yb} | Nominal yield strength |
| A_g | Gross-sectional area |

| | |
|---------------|--|
| k | Numerical coefficient |
| n | Number of 90° bends in the cross section |
| $F_{t,Rd}$ | Design tension resistance |
| l_{eff} | Effective length |
| t_f | Flange thickness |
| $B_{t,Rd}$ | Design tension resistance of a single bolt-plate |
| γ_{M0} | Partial safety factor for steel |
| m | Distance from the bolt centre to the inner side of flange |
| n | Distance from the bolt centre to the edge of flange |
| h_l | Distance from the farthest bolt-row to the centre of resistance of the compression zone |
| h_i | Distance from any bolt-row to the centre of resistance of the compression zone |
| k_1 | Parameter; the smallest of $(2.5 ; 2.8 e_2/d_0 - 1.7 ; 1.4 e_2/d_0 - 1.7)$ |
| α_b | Parameter; the smallest of $(1.0 ; e_1/3d_0 ; p_1/3d_0 - 1/4 ; f_{ub}/f_u)$ |
| f_{ub} | Specified ultimate strength of the bolt |
| d | Nominal bolt diameter |
| t_p | Thickness of plate |
| γ_{M2} | Partial factor for net section resistance for steels, $\gamma_{M2} = \gamma_{M0} = 1.25$ |
| A_{net} | Net area of the plate |
| f_u | Specified ultimate strength |
| γ_{M2} | Partial factor for net section resistance for steels, $\gamma_{M2} = \gamma_{M0} = 1.25$ |
| F | Point load |
| H | Column height |
| L | Beam length |
| Δ_C | Horizontal deflection at top of the columns |
| Δ_{ms} | Deflection at mid-span of the main beams |
| z | Lever arm of the connection |
| k_c | Secant stiffness of the connection |
| n | Rigidity parameter |

| | |
|-------------------------------|--|
| R_{ki} | Initial connection stiffness |
| θ_0 | Reference plastic rotation defined by: $\theta_0 = M_u / R_{ki}$ |
| q | Rigidity parameter with influence of steel grades |
| r | Correlation coefficient |
| η | Joint ductility index |
| $\eta_{j, \max \text{ load}}$ | Joint ductility index at maximum load |
| $\theta_{Mj, \max}$ | Rotation capacity of the joint |
| $\theta_{Mj, R}$ | Rotation value corresponding to the joint plastic resistance |
| $B_{t, Rd}$ | Design tension resistance of a single bolt-plate |
| γ_{M0} | Partial safety factor for steel |
| m | Distance from the bolt centre to the inner side of flange |
| n | Distance from the bolt centre to the edge of flange |
| h_l | Distance from the farthest bolt-row to the centre of resistance |
| h_i | Distance from any bolt-row to the centre of resistance |
| k_l | Parameter; the smallest of $(2.5 ; 2.8 e_2/d_0 - 1.7 ; 1.4 e_2/d_0 - 1.7)$ |
| α_b | Parameter; the smallest of $(1.0 ; e_1/2d_0 ; p_1/3d_0 - 1/4 ; f_{ub}/f_u)$ |
| t_p | Thickness of plate |
| γ_{M2} | Partial factor for net section resistance for steels, $\gamma_{M2} = \gamma_{M2} = 1.15$ |
| A_{net} | Net area of the plate |
| γ_{M2} | Partial factor for net section resistance for steels, $\gamma_{M2} = \gamma_{M2} = 1.20$ |
| α_l | Edge distance factor $(e_1/1.5d_0)^{0.5}$ |

Chapter 1

Introduction

1.1 General

The use of bolted connections, due to the importance in construction, is crucial both economically and structurally. Saving in connection costs as well as the improved construction quality has an impact on building design in overall. Because of the repetitive nature of connections, even minor material or labour savings in one connection are compounded and expanded throughout the entire building. It is important, then, for a design engineer to understand the behaviour of the connection, not only from the point of view of the connection as a structural element, but also from the point of view of the connection as a part of the complete structural system.

During the last decade more advanced manufacturing processes and improved properties of high strength steel (HSS) and stainless steel have made them more attractive in an economic and environmental perspective. An obstacle that reduces the advantages of using high strength steel in structures is that the design rules for compression are not suited to utilize the higher resistance of the high strength steel. The use of stainless steel for structural applications provides some advantages compared with mild carbon steel, so stainless steel is often the least expensive material option because of its anti-corrosion

and better fire resistance properties. There is currently a great deal of interest in the use of high strength and stainless steel in structural engineering applications. Behaviour of bolted connection with high strength and stainless steel will be investigated by using the application of finite element modelling.

1.2 Background

Steel construction, with various structural components connected together have several types of detailing: bolted, welded, riveted and adhesive ones. Among them, the bolted connections exhibit a lot of advantages, such as easy assemblage, re-assemblage, repairing and replacement of damaged structural components, thus making these connections attractive, in particular for the construction of heavy structures. A lot of examples of such joints could be named (e.g. the shear connection, the beam-to-column connection, the column bases, and the column-to-column connection). These joints distribute the internal forces between the connected members in an effective way.

Depending on the action of the external loading acting on a joint, bolted connections can be classified into two categories. The joints is said to be in tension when the forces in the axial direction of the bolts. The joint is said to be in shear when the forces on the connection acting perpendicular to the axis of the bolt. The splice lap connection is formed by a bottom plate or more bolted to a splice plate. One of the primary purposes of the joint is to transfer in-plane loads from one plat to another through shear across the bolt shank. The most important aspect of splice lap connection behaviour is the load-displacement ($P-\Delta$) relationship. The connection failure is distinguished between net cross-section and bearing failure.

In steel framed structures, beam-to-column connections such as partially restrained (PR) connections have been used widely in order to transmit some of the moments between the connected elements and permit some relative rotation depending on their stiffness. More interest has been directed recently towards behaviour of steel frames with PR connections. The most important aspect of connection behaviour is the moment-

rotation ($M-\theta$) relationship. The stiffer connection gives the higher $M-\theta$ curve representing the behaviour of the connection. The primary distortion of a steel beam-to-column connection is its rotational deformation θ_r , caused by in-plane bending moment.

There are some types of PR connections such as angle web angle (SWA), double web angle (DWA), top and seat-angle (TSA), top and seat-angle with double web angle (TSAW), and also a flush end plate connection (FEP). The applications of PR connections have become increasingly popular in civil engineering structure in recent years. This is due to their advantages over the rigid or pinned joints in terms of strength, stiffness, construction procedure, and overall economy. Several aspects of PR connections have been carried out by many researchers. The effect of PR connections on the behaviour of steel frames and their potential economical benefits is well recognised [1].

To achieve a safe and economic design, it is necessary to investigate the structural bolted connection both with numerical modelling and experimental testing. High strength and stainless steel provides designers with the possibility of creating much thinner and weight efficient structure than it would be possible if using steels with lower strength. The use of stainless steel for civil engineering structural application provides possibilities for a more efficient balance between whole-life cost and in-service mechanical response of structural components, connections and the overall system [2]. To achieve a safe and economic design it is necessary to investigate the structural connection with finite element modelling and validated against experimental testing with some development of non linear continuum modelling using high strength and stainless steel.

1.3 Research aim

The aims of this research are:

1. To assess the numerical modelling of the shear bolted and partially restrained connection and to examine validity with experimental results.
2. To investigate bearing capacity, moment strength, ductility and rotational capacity of connections and structures with high strength steel using finite element modelling.

3. To investigate load bearing, moment strength, ductility and rotational capacity of connections and structures with stainless steel using finite element modelling.
4. To determine the strain softening effect of high strength and stainless steel material on overall connection behaviour using developed finite element model.
5. To determine the effect of connection behaviour with high strength and stainless steel material on the structural frame performance.

1.4 Brief Description Each Chapter

This thesis studies experimentally and analytically the behaviour of shear bolted connection and partially restrained (PR) connection with high strength and stainless steel. Research emphasizes on the load bearing resistance, ultimate moment and rotational capacity. Study has aimed to provide a better understanding of the overall behaviour of the connections with applied steel material properties.

Investigations were carried out in two different methods, finite element analysis and analytical studies. Analytical studies were also conducted in two separate methods. The derivations of the ultimate load bearing and displacement capacity of the shear connections and the ultimate moment and rotational capacity of the PR connections were calculated by using the principle of non linear structural analysis. Simplified models were also used to compare with 3D continuum finite element model results and also to study the parameters which can significantly influence on the overall behaviour of the bolted connections.

The layout of the thesis is outlined as follows. An extensive literature review related to the bolted connection and high strength and stainless steel is presented in Chapter 2 in which the achievements of other researchers are discussed and the discrepancies are also identified. Chapter 3 comprises an introduction to the finite element analysis method to emphasis continuum modelling which is discussed and presented for the 3D finite element methodology by using the software ANSYS in order to develop the models according to the specimens used in the experiments. Chapter 4, presents a validation of finite element modelling result against experimental result. Chapter 5 presents the developed finite element model using non linear material of high strength and stainless

steel to highlight the behaviour of bolted connections. Chapter 6 presents the results of a parametric study of the finite element analysis work. Chapter 7 presents the derivation of design formulas for the ultimate capacity of the bolted connection with high strength and stainless steel. Finally, conclusions based on the discussion made in the previous chapters is drawn in Chapter 8, and some suggestions for further work regarding existing findings are also made.

Chapter 2

Literature Review

2.1 Introduction

In recent years the idea of using bolted connection i.e. partially restrained angle connection in building structures has become more practical and economical. Splice lap bolted connection makes a simple shear lap joint more affordable to set up with a plate bolted to the other one. Partially restrained connections resist moment and also allow rotation, therefore distributing the moments and stresses more evenly throughout the element.

The use of high strength and stainless steel for has increased in the last few years. This is because, in addition to some national codes of practice, Eurocode 3 (EC3) also allows the use of these steel grades. There are no special conditions or restrictions for bolted connections for high strength steel in Annex D, and reference is made to clause 6 of EC 3 [5]. According to the EC3 part 1.4 [6], section 5.2 and Section 9 and Annex A of EN 1993-1-3 are applicable to stainless steels.

2.2 General Introduction on High Strength Steel

According to the EC3, mechanical properties of carbon steel: Steel grade S275 with minimum yield strength of 275 MPa, whilst grade S355 with yield strength of 355 MPa. For steel grade S460 with nominal stress of 460 MPa, steel grade S550 with nominal

yield stress of 550 MPa and grade S690 with nominal yield stress of 690 MPa are considered as HSS.

Sivakumaran K.S. et al. [7] investigated the slenderness limit and ductility of high strength steel section. The material ductility were measured to be $\epsilon_u/\epsilon_y = 105$ (300Q) and $\epsilon_u/\epsilon_y = 17$ (700Q). The results have shown that the available compression flange strain ductility is considerably lower than the corresponding material strain ductility. The ductility associated with the 480W and 700Q steel were considerably lower (almost half) than that observed in 300W and 350W steel. The ductility corresponding to a point at which the stress falls below the specified yield strength (D values) for 300W and 350W is more than 3 times the corresponding D, and ductility at the onset of local buckling (D_1) values, whereas the D values for 480W and 700Q are less than 2 times. Therefore, the Class 1 b/t limit defined in the current code may not be directly applicable to 480W and 700Q steel grades. The ductility and the strain hardening strength associated with the 350W steel, are quite similar to that of the 300W steel. On the other hand, the 700Q steel reveals very little compression flange strain ductility and strain hardening. The current study results are expected to increase the efficiency of steel design, particularly for plastic and ductile seismic designs.

The research from Green et al. [8] discussed the inelastic behaviour of welded, I-shaped flexural members fabricated from an high performance steel (HPS), HSLA-80, having a nominal yield stress of 550 MPa and an ultimate strength between 610–690 MPa and compares the results to similar flexural members fabricated from conventional S275 steel. The effects of material properties: yield stress, strain-hardening modulus, yield stress-to-ultimate strength ratio, and strain at ultimate stress; cross-section geometry: flange slenderness, web slenderness, and lateral slenderness; and loading condition: monotonic moment gradient, monotonic uniform moment, and cyclic moment gradient are described from the results of experimental testing and analytical modeling.

In recent years higher strength steels, which do not satisfy the material requirements of these design standards, have become available. It is necessary that the stability and ductility problems associated with these higher strength steels be adequately allowed for in design [9]. Thin high strength steels with 550 MPa yield stress have been

used to investigate the design against the distortional mode of buckling which can occur in compression or flexure. Distortional buckling is a mode of failure where a section changes its cross sectional shape under compressive stress. It may occur in thin sections in compression or bending at stresses significantly below the yield stress, especially for high strength steels. Therefore, the use of thin high strength steel sections warrants consideration of distortional buckling.

The use of HSS made of S690 plate for experimental testing results was extensively emphasized to investigate the ductility problem [10]. The result of tensile test shows the value of yield strength $f_y = 875$ MPa, ultimate strength $f_u = 915$ MPa, ultimate strain $\epsilon_u = 14\%$ and $f_u/f_y = 1.046$ as shown in Figure 2.1. The effect of net cross-section failure on resistance and local ductility was studied using experimental plate specimens with various sizes of circular holes subject to tensile load. The HSS specimens were compared with specimens made of mild steel S235. The f_u/f_y ratio for such steel might be 1.5. Due to a large ratio, the net cross-section might reach a stress far above the yield stress f_y , and due to strain hardening, the gross cross-section of a member in tension can also yield and therefore be exposed to excessive plastic deformations. The load displacement curves of S235 specimens differed in shape as well.

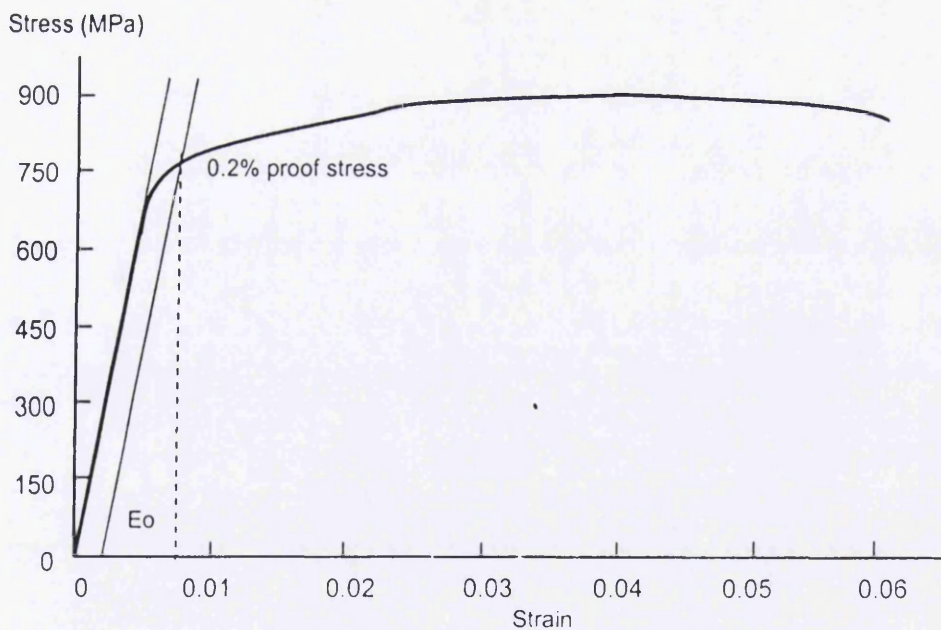


Fig. 2.1 Typical stress-strain curve of HSS

The selection of the material to maintain ductility is very important. Especially, high strength steels (HSS) are less ductile than the usual mild structural steels. Ductility was normally defined as the ability of a material to deform plastically before fracturing [11]. It is usually evaluated by measuring the elongation from a tension test, or the radius or the bend angle from a bending test. Different design standards stipulate minimum ductility requirements for certain analysis methods. Eurocode 3 prEn 1993-1-12 [12], recommends ductility value requirements for high strength steel application of plastic analysis method: (i) $f_u/f_y \geq 1.05$ (ii) $\epsilon_{fr} \geq 10\%$ (iii) $\epsilon_u/\epsilon_y \geq 15$.

Zhao [13] has investigated the section capacity of very high strength (VHS) circular tubes under compression. Full-section tensile tests were performed to determine the Young's modulus of elasticity, tensile yield stress and ultimate tensile strength. The modulus of elasticity was found around 200,000 MPa, the tensile yield stress (0.2% proof stress) was around 1360 MPa which is about 0.7% higher than the nominal value (σ_{yn}) of 1350 MPa and the ultimate tensile strength was around 1519 MPa which is about 1.3% higher than the nominal value (σ_{un}) of 1500 MPa. The average ratio of the ultimate strength to yield stress is 1.117. The stress-strain curve of VHS is shown in Figure 2.2.

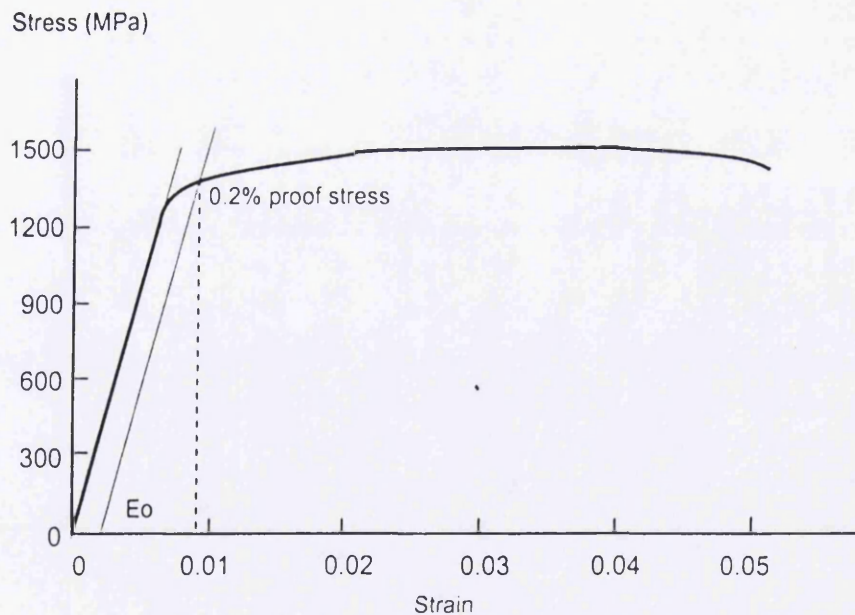


Fig. 2.2. Typical stress-strain curve of VHS

2.3 General Introduction on Stainless Steel

For structural engineers, stainless steel offers strength, ductility and fire resistance that is unparalleled compared with common construction steel. The mechanical behaviour of stainless steel differs from carbon steel in that the stress-strain curve departs from linearity at a much lower stress than that for carbon steel. The material has a greater capacity for work hardening and the elastic modulus of stainless steel reduces with increasing stress, unlike that of carbon steel [14].

Mechanical properties of stainless steel: Austenitic stainless steel grade 1.4031 (304) with minimum 0.2% proof strength or yield strength of 210 MPa, whilst Grade 1.4401 (316) with yield strength of 220 MPa. For duplex stainless steel grade 1.4362 (2304) with minimum 0.2% proof strength or yield strength of 400 MPa, 1.4462 (2205) with yield strength of 460 MPa. Typical stress-strain curve of stainless steel is shown in Figure 2.3.

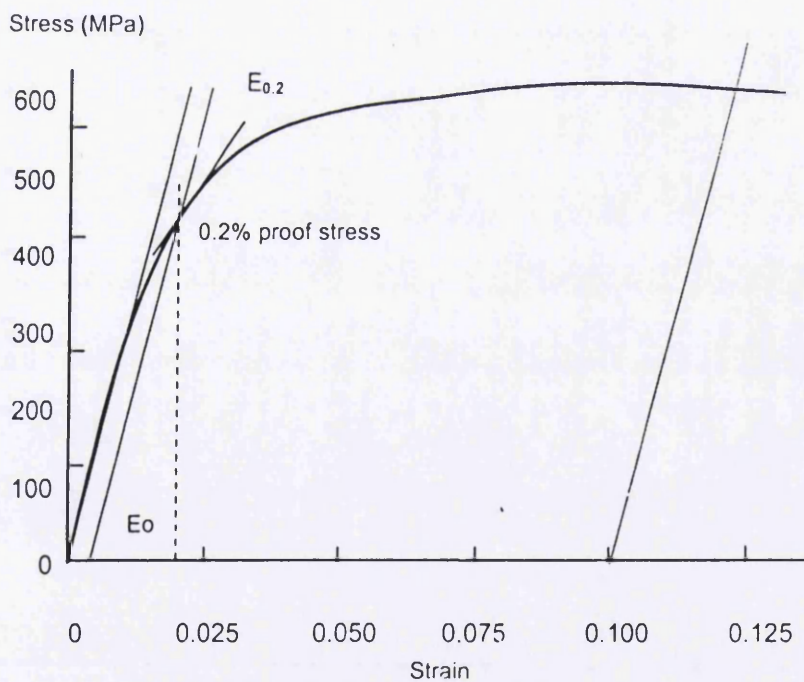


Fig. 2.3. Typical stress-strain curve of stainless steel

Structural stainless steel joints may utilize welding, bolting or other mechanical fasteners. Basic design philosophy is no different from that for carbon steel joints, and the high ductility that stainless steel offers (particularly the austenitic grades) should be beneficial. There are however a number of general design aspects that require consideration, in particular to minimize the risk of corrosion; problems may be experienced where fissures exist, where there is dissimilar metal contact inducing galvanic corrosion (e.g. joints comprising both stainless steel and carbon steel components) and in the heat-affected zone resulting from welding. The common grades of stainless steel are readily weldable: the austenitic grades especially, can be welded with ease, and since there is no change in metallurgical structure with temperature, the weld material and surrounding zone should remain good strength and ductile. As with ordinary carbon steel, stainless steel grades with a low carbon (equivalent) content are desirable for welding (such as EN 1.4306 (AISI 304L) and EN 1.4404 (AISI 316L)), though these grades generally possess slightly lower strengths. The structural behaviour of stainless steel joints is similar to that of carbon steel joints, and this is reflected in design guidance. Design rules are provided in each of the three design standards under consideration, with slight variations from their corresponding carbon steel recommendations. The European guidance for stainless steel joints adopts the rules of Eurocode 3 Part 1.8 [15], subject to some minor modifications given in Part 1.4.

The paper from Rasmussen et al. [16] described the development of numerical models for analysing stainless steel plates in compression. Material tests on coupons cut in the longitudinal, transverse and diagonal directions are included as are the results of tests on stainless steel plates. Detailed comparisons are made between the experimental and numerical ultimate loads, load–displacement curves and load–strain curves. It is shown that excellent agreement with tests can be achieved by using the compressive stress–strain curve pertaining to the longitudinal direction. The effect of anisotropy is investigated using elastic–perfectly-plastic material models, where the anisotropic material model is based on Hill's theory. The models indicate that the effect of anisotropy is small and that it may not be required to account for anisotropy in the modelling of stainless steel plates in compression.

The expression for the stress–strain curves for stainless steel alloys is useful for the design and numerical modelling of stainless steel members and elements which reach stresses beyond the 0.2% proof stress in their ultimate limit state [17]. In this stress range, current stress–strain curves based on the Ramberg–Osgood expression become seriously inaccurate principally because they are extrapolations of curve fits to stresses lower than the 0.2% proof stress. The extrapolation becomes particularly inaccurate for alloys with pronounced strain hardening. The paper also develops expressions for determining the ultimate tensile strength (σ_u) and strain (ε_u) for given values of the Ramberg–Osgood parameters ($E_0, \sigma_{0.2}, n$). The expressions are compared with a wide range of experimental data and shown to be reasonably accurate for all structural classes of stainless steel alloys. Based on the expressions for σ_u and ε_u , it is possible to construct the entire stress–strain curve from the Ramberg–Osgood parameters ($E_0, \sigma_{0.2}, n$). For $\sigma < \sigma_{0.2}$ the Ramberg-Osgood equation is used:

$$\varepsilon = \frac{\sigma}{E_0} + \varepsilon_{p0.2} \left(\frac{\sigma}{\sigma_{0.2}} \right)^n \quad (2.1)$$

For $\sigma > \sigma_{0.2}$ a equation in the new reference system according to [17] is used:

$$\bar{\varepsilon}_{up} = \varepsilon_u - \varepsilon_{0.2} - (\sigma_u - \sigma_{0.2}) / E_{0.2} \quad (2.2)$$

where:

$$E_{0.2} = \frac{E_0}{1 + 0.002n/e} \quad (2.3)$$

2.4 Strain Softening

In the realistic analysis of steel structures, an important criterion that needs to be considered is the implication of strain softening behaviour at an element level. Even though the stress–strain relationship of the steel used may not show a softening nature,

particular elements may do so. For example, local softening is often exhibited as a consequence of the local buckling of stiffeners, the lateral-torsional buckling of beams caused by inadequately provided torsional restraints, the excessive deformation of truss elements caused by inadequately provided side restraints, and by steel connections with certain types of bolted connection. This local constitutive instability is evidenced by a decreasing either bending moment with increasing flexural rotation relationship or axial load with increasing deformation relationship.

Strain-softening models have received a great deal of attention for describing the fracture of steel, fracture of concrete, and other materials where microstructure has a strong influence on macroscopic properties. In general, a macroscopic description of damage (e.g., excessive deformation fracture) is reflected in a constitutive model that exhibits a decrease of stress with increasing strain beyond some critical strain in correlation with tensile strength as shown in Figure 2.4. Ultimate stress is defined as σ_u (MPa) corresponding with ultimate strain ϵ_u , and fracture stress is defined as σ_f (MPa) corresponding with fracture strain ϵ_f , whilst yield stress is defined as 0.2% proof stress $\sigma_{0.2}$ (MPa).

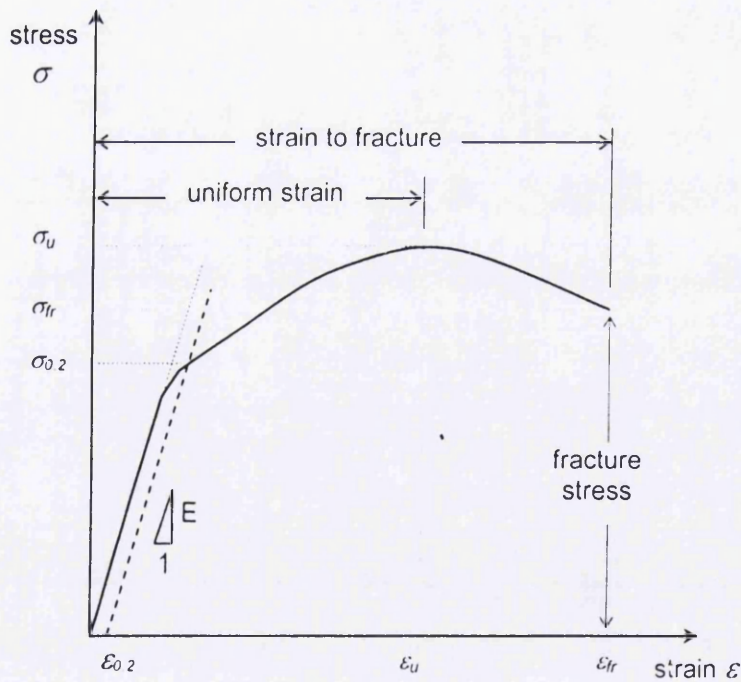


Figure 2.4 The engineering stress-strain curve up to fracture strain

Zhou et al. [18] studied the strain softening constitutive equation for metal material under tensile action. A three-parameter nonlinear constitutive model has been established to describe the strain rate dependent stress–strain curve of the tungsten heavy alloy. The parameters in this model are the modulus E , the strain exponent m and the compliance factor β . All three parameters are strain rate dependent. Strain rate dependent is defined as low rate i.e. $\dot{\varepsilon} = 100\text{s}^{-1}$, therefore the determined parameters in the constitutive equation is written as:

$$\frac{\varepsilon}{\sigma} = \beta(100)\varepsilon^m + \frac{1}{E} \quad (2.4)$$

where:

ε = strain (%)

σ = stress (MPa)

m and β are defined using ε_u , σ_u , ε_r , and σ_r

Tangaramvong et al. [19] presented a method for carrying out, in a single step, an elastoplastic analysis to obtain simultaneously both the ultimate load and corresponding deformation of a strain softening structure. The effect of combined bending moment and axial force is also accounted for in the piecewise linearized softening yield condition. However, a monotonic loading process is assumed within a small displacement framework. A mathematical programming approach has been proposed to tackle this problem. In particular, the formulation leads to an instance of the challenging class of a so-called ‘mathematical program with equilibrium constraints’ (MPEC). Various nonlinear programming based algorithms are proposed to solve the MPEC. Numerical examples are provided to illustrate the described analysis and also to highlight the effects of constitutive local softening instability and of axial forces on the overall structural behaviour of the frames.

Mistakidis et al. [20] presented two methods for the solution of steel structures taking into account softening phenomena. This behaviour results from the coupling of local buckling and lateral-torsional buckling phenomena and leads to a nonconvex function of the potential energy of the structure. The problem is formulated on the rigorous mathematical background of hemivariational inequalities. Both methods reduce

the nonconvex minimization problem to a number of convex minimization subproblems which are treated numerically with the methods used for the solution of the classical plasticity problems. In this sense, both approaches proposed here can be understood as extensions of the classical plasticity theory which is familiar to structural engineers.

Local buckling of beam and/or connection elements is a source of softening in the moment-rotation behaviour in certain connections. This effect can significantly reduce the maximum load-carrying capacity of steel structures. In this study, an elastic-plastic plane frame analysis which includes the effect of nonlinear connection behaviour is presented to predict the ultimate load-carrying capacity of steel frames [21]. The structural model comprises members which are assumed to behave elastically with nonlinear connection moment-rotation behaviour. The main objective of this study is to investigate the effect of connections which exhibit strain-softening behaviour on the ultimate strength and stability of flexible frames. Numerical studies of frames made using the developed computer program are presented. Observations regarding the effects of flexible connections on the strength and deflection of steel framed structures are discussed. The proposed analyses procedure using flexible joints modeled by the Richard function were found to be simple and accurate which compared to elastic-perfectly plastic models.

Tangaramvong et al. [22] presented an extended classical limit analysis approach for steel structures to account for local strain softening behaviour. As is well known, the bound theorems underpinning the collapse load estimation of ductile structures require an assumption of perfect plasticity. They are invalid for the class of structures, such as those being considered here, that exhibit local softening. A method has been proposed, based on the same conditions governing the path-independent state problem, for capturing the maximum load multiplier characterizing the one parameter proportionally applied loading regime. The problem is cast as a special instance of the notoriously difficult to solve class of problems known as a mathematical program with equilibrium constraints (MPEC). Various solution approaches, all based on solving the MPEC as a standard nonlinear programming problem, are briefly presented. One of them, namely the penalty scheme, is used to solve the three numerical examples provided to highlight application of the proposed limit analysis approach.

An experimental investigation and a constitutive modeling of the mechanical response of an interstitial free steel over a wide range of strain rates are presented in reference [23]. Tensile tests at relatively high strain rates, were performed at an initial room temperature, using the so-called one bar technique developed on the basis of the Hopkinson bar method. At a high strain rate, a distinct upper yield limit was observed, and the subsequent flow stress increases remarkably. Furthermore, the ductility was reduced significantly in comparison to the case of low strain rate tension. In order to express such a complicated material response of steel, a new constitutive relationship was developed to model this taking into account effects of a change in the mobile dislocation density and strain softening. An attempt was made to reproduce the tensile response including a diffuse neck formation at high strain rates, using the proposed constitutive model and finite element method. The results indicated that a change in the mobile dislocation density had substantial effects on apparent work hardening behaviour at high strain rates, although the change in the mobile dislocation density was transcribed at macroscopic scale in the model. Finally, characteristics of true stress - true strain curves at various strain rates was discussed, and their correlation with the plastic instability behaviour.

Chausov et al. [24] proposed laws of deformation processes and fracture of plastic steel from the point of view of dynamic overloading. Fragments of stress-strain diagrams of steel ST20 with a dynamic overloading have been presented including on site softening. It has been established, that dynamic overloading carried out on any section of deformations, starting with elastic, greatly change the processes of steel deformation. An essential part in decreasing the strength of plastic deformation influence the damage growth in material during a dynamic overloading. Also it was shown, that for the tested steel the most dangerous case was the dynamic overloading carried out on yield drop and ultimate strength. The range of disorder of specific work of steel fracture, in the view of the influence of dynamic overloading of one intensity at different stages of deformation, achieves 30%. On the basis of new experimental data two approaches for modeling of the processes of deformation and fracture of plastic steel in the view of the influence of dynamic overloading are offered and approved.

2.5 Shear Bolted Connection

There has been much research conducted in the past several years on the analysis of bolted shear lap joints, but only a few studies on connections with high strength are available. Kim and Yura [25] presented the experimental results from tested one- and two-bolt connections made of S460. The testing data have been compared the bearing resistances to AISC specifications and the Eurocode 3 standard. It was shown that steels with an ultimate-to-yield ratio equal to or greater than 1.13 do not influence the strength at a displacement of 6.35 mm. Tested connections with the same geometry have been conducted [26,27], but with steels of S700 and S1100. They also studied the block shear on welded I-sections in HSS and tested tension connections with splice plates [21]. Experimental research on single bolt connections for high strength steel S690 has been conducted with proposed recommendation of edge distance equal to bolt diameter [28].

The paper from Rogers et al. [29] provided a summary of results detailing the behaviour of bolted connections tested in shear, which were composed of 0.42 mm G550, 0.60 mm G550, and 0.60 mm G300 sheet steels. Recommendations concerning the adequacy of current design standards with respect to the design of thin sheet steel bolted connections are made, along with the calibration of applicable limit states resistance equations for the three observed modes of failure: end pull-out, bearing, and net section fracture.

The effect of net cross-section failure on resistance and local ductility of the splice lap connection has been investigated [30]. The effect on end and edge distances in bolted connections influenced on resistance and local ductility such as lower limit for design resistance of net cross section, design ultimate resistance of the net cross-section. And design resistance of the gross cross section. Formula $N_{t,Rd}$ gives upper not lower limit. Net section failure starts at lower end distance. End distance less than 1.5 times diameter results no reduction for bearing value. Minimal distance from prEN 1993-1-12 (12) were reasonable. Net cross-section failure was one of the basic failures in structural elements subjected to tensile stresses. A defect in the structural element, for instance, a hole made by drilling or pinching, may obstruct the stress flow and may therefore cause a

stress concentration. Due to the disturbance in stress flow, the material may start to yield at a load smaller than required to yield the gross area. The area of the structural element subjected to yielding depends on the size of the reduced cross-section and on the material's strain hardening. If the material has no or limited ability of strain hardening, then the concentration of stresses may cause cracks in the material, resulting in brittle failure of the net cross-section. On the other hand, the ability of the material to harden results in the yielding of the area in the vicinity of the obstacle and the consequence is the elimination of the stress concentration and ductile failure at a limited load. The selection of the material to maintain ductility is also important. Especially, high strength steels (HSS) are less ductile than the usual mild structural steels.

Puthli et al. [31] tested two bolted connections in S460. They reported about the conservatism of Eurocode 3 bearing resistance and proposed the reduction of minimal distances. All the connections have also been provided with different bolt spacing to observe the influence of bolt spacing and edge distance. In all tests, the dimensions are such as to include failure of the plate net cross section or bolt shear failure, since bearing resistance is to be investigated. The test results have confirmed that the minimum bolt spacing and edge distance specified in Eurocode 3 can also be used for steel grade S460. The experimental failure loads were compared with those determined from Eurocode 3 and the results interpreted. Before a comprehensive design proposal can be formulated, additional tests on bolted connections in single shear may be required. The variation in the steel grade S460 in consideration of ductility requirements is also not included in the present work. However, the tests indicated that the reduction of the design bearing resistance prescribed in Eurocode 3 for edge distances less than 1.5 times the bolt hole diameter or 3.0 times the bolt spacing may not be necessary for the parameters in the tests. EC3 requires a reduction of the design bearing resistance of bolted connections loaded in shear when the edge distance $e_2 < 1.5d_0$ or bolt spacing $p_2 < 3.0d_0$. For $e_2 = 1.2d_0$ or $p_2 = 2.4d_0$, the design bearing resistance has to be reduced to 2/3. For values lower than $e_2 = 1.2d_0$ or $p_2 = 2.4d_0$, no calculations are possible. For steel grade S460, EC3 also requires the same reduction rules as above for this higher steel grade. The evaluation of the test series on bolted connections on high-strength fine-grained steel grade S460 showed that this limitation was not necessary. The tests indicated that the reduction in

bearing resistance for smaller e_2 or p_2 did not need to be so large. For the investigated tests reported for steel grade S460, it was observed that a reduction of the design bearing resistance was not required for edge distance $e_2 \geq 1.2d_0$ or bolt spacing $p_2 \geq 2.4d_0$. In addition, the minimum edge distance and minimum bolt spacing may be reduced to at least $e_2 = 1.0d_0$ and $p_2 = 2.0d_0$, respectively. However, a reduction of the design bearing resistance of 3/4 is then necessary for these minimum distances on the basis of the present tests. Intermediate values may be interpolated.

2.6 Partially Restrained Connection

There have been much research conducted in the past several years on the analysis of partially restrained connections in building design. The research included the analysis of several types of partially restrained connections to determine their moment rotation behaviour, and the development of design procedures for partially restrained frames using these connections with hot rolled structural steel members. The research that has been done in this area is quite extensive so only research pertaining to the type of connections and the types of partially restrained frames used in this work will be discussed here. The most important part of any partially restrained connection analysis is to obtain an accurate and easy way to determine the moment rotation curve. To develop these curves many different mathematical models have been developed such as linear, bilinear, multi-linear, polynomial, cubic B-spline, power, and exponential [32]. In many cases the power model has been chosen for its ease of use and its accurate representation of the moment rotation curve [33]. The power model is expressed in the following form for partially restrained connections:

$$m = \frac{\theta}{(1 + \theta^n)^{1/n}} \quad (2.5)$$

where $m = M/M_u$ or the connection moment M , divided by the ultimate connection moment M_u , $\theta = \theta_r/\theta_0$, or the relative rotation between beam and column θ_r , divided by the relative plastic rotation, $\theta_0 = M_u/R_{ki}$ which is the ultimate connection moment divided

by the initial connection stiffness R_{ki} , and n is the power that changes the shape of the curve. The larger the value of n , the steeper the transition of the moment rotation curve from the yield point to ultimate. Some of the effects that are neglected in this model are those due to torsion, lateral bending, shear, and strain. These effects tend to be minimal in normal connections and these omissions can be justified. Generalized connection parameters and equations have been developed for framing angle and plate connections, such as double web angle (DWA), top and seat angle (TSA), top and seat angle with double web angle (TSAW) connections and flush endplate (FEP), to aid in the analysis. These connections are illustrated in Figure 2.4. The top and seat angles make up the moment couple in the connection while the top and seat angles with double web angles resist moment and shear. In the design of the members with partially restrained connections, the first step is to design the member as if fully restrained at its ends. Using that member, the partially restrained connection can be modelled and the frame analyzed with the selected members. This design is then altered based on the moments calculated using a second order frame analysis. Several iterations may be needed to produce the most efficient design. The ideal result in any partially restrained frame is to balance the end and mid span moments. Doing such will produce the most efficient frame design. The top and seat angle with double web angle connection is used exclusively in the non-composite, hot rolled member construction designs. This is done because this connection proves to be stiffer, thus reducing lateral deflections. Azizinamini [34] performed an extensive and detailed experimental study for top and seat angle connection with double web angles.

For composite connections, it was suitable to use flush endplate connections to achieve a stiffer connection. In general, flush endplate connections are welded to the beam end along both the flanges and web in the fabricator's shop, and bolted to the column in the field. Davison et al. [35] carried out a series of static cruciform experiments on a variety of different joint typologies including flush endplate joints. Xiao et al. [36] conducted a series of experiments on composite connections. The goal of the test series was to compare the behaviour of different joints in terms of rotational stiffness, ductility and moment resistance capacity. Flush endplate joints displayed large differences in behaviour depending on whether the endplate was connected to the column

web or the un-stiffened column flange. Specimens with and without beam flange welds were tested, and similar performances observed. It was noted that the use of a lighter column section reduced the initial rotational stiffness while increasing the ductility of the joint.

Due to the increase of rectangular hollow sections in mainstream structures coupled with the economics of prefabrication that produce the application of tubular connections. Bolted endplate connection using tubular beam (EPTB) consists of a plate welded to hollow section beam and bolted to the other plate welded to the column. Hollow section beam splice connections have been investigated by Wheller et al. [37], which can be developed into an EPTB connections by the other beam replaced into column as shown in Figure 2.4.d. Willibald et al. [38] carried out experimental on bolted connections for RHS tension members.

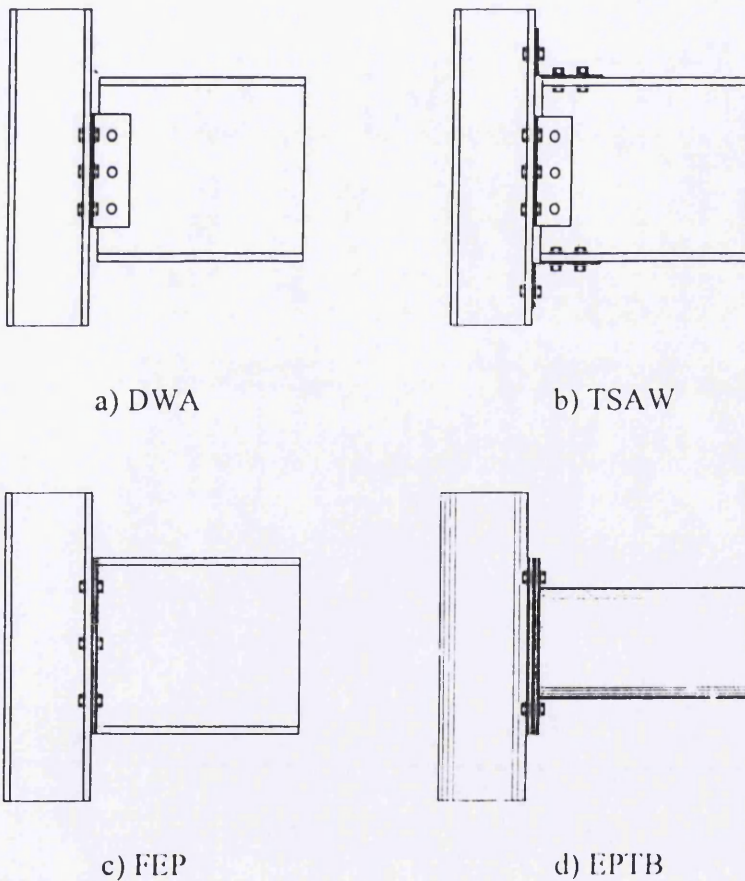


Figure 2.4 a) - d) Partially Restrained Connections

An experimental investigation of the seismic behaviour of flush endplate joints was presented in [39]. Beam-to-column sub-assembly specimens are tested under monotonic and cyclic loading conditions. The model can be used to predict the mode of failure well, but to over-predict stiffness and under-predict moment capacity. Design resistance of un-stiffened column web subject to transverse compression in beam to-column joints has been proposed [40]. Flush endplate and extended endplate have been investigated of resisting concentrated compressive force by the smaller of crushing and buckling resistances. Investigated experimental behaviour of endplate beam-to-column joint under bending and axial force has been conducted [41].

Experimental behaviour of high strength endplate connection has been conducted by Girao Coelho et.al [42]. The use of high strength steel in construction is to minimise the cross-section dimensions with high yield ratio and limited deformation capacity when compared with mild steel grade. Experimental investigation was undertaken of moment connection with endplate made up of high strength steel S690. The major contribution of this study are (i) the characterisation of the non-linear behaviour (ii) the validation of current Eurocode 3 specifications and (iii) the ductility analysis of high strength steel moment connections. The test result show that the tested connections satisfy the current design provisions for stiffness and resistance and achieve reasonable rotation demands.

Kukreti et al. [43] provided an analytical relationship between moment and rotation for flush moment endplate connections. The authors considered a range of connection geometry compatible to the metal building industry. Hasan et al. [44] presented insight into the stiffness and strength requirements of moment endplate connections to be considered as FR connections. By analyzing frames composed of connections with known moment-rotation characteristics, the authors concluded that connections with an initial stiffness $K_1 > 10^6$ kip-in/rad should be considered as FR connections. A similar classification system for rigid and semi-rigid connections was proposed by Goto and Miyashita [45] for general connections.

Foley et al. [46] considered the typical moment-rotation characteristics of moment endplate connections. The analysis and design of steel frames composed of semi-rigid connections was considered by Coric and Markovic [47], Elghazouli [48], Yu et al. [49],

Rodrigues et al. [50], and Fu et al. [51]. Leon [52] discussed PR composite frame design and analysis. Brown et al. [53] presented a method to determine easily the stiffness of semi-continuous connection when one or two bolt-rows are in tension. This provides a basis for determining the sway of an un-braced frame, or estimating the serviceability of a braced one. The proposed method showed good agreement with tests on the standard connections and on similar forms of joint.

2.7 Finite Element Modelling

The literature is filled with papers that use the finite element method to predict the behaviour of different types of steel connections under static loading. In fact, there are several that consider only moment endplate connections. However, the limitations of these works are readily apparent and can be listed as general limitations present in most of the current research on this topic. First, the angle-cleat and endplate behaviour, and not bolt forces, is the prime concern. The angle and endplate strength for most PR connection configurations has been well defined in the literature. However, most bolt force prediction schemes have been shown to be impractical for design applications.

Almost all the papers use truss elements to represent the entire bolt and the results are extremely limited. Second, all of the papers on this topic only consider small endplate configurations (i.e., flush or four-bolt extended). The main reason for this is that these smaller connections provide more flexibility than larger ones. This is needed for efficient PR connection design applications. Finally, the theme of most papers is the adequacy of the finite element method in determining the connection's behaviour. Very few applications are made.

Research by Krishnamurthy and Graddy [54] was one of the earliest papers on the appropriateness of the finite element method for studying moment endplate connections. The paper has many features that can be criticized, but given the computer resources of the time, the limitations in the analysis are expected. The authors attempted to correlate the results from an elastic, three-dimensional, finite element analysis to those from an

elastic, two-dimensional, finite element analysis. The main reason for this correlation was that at the time, computer resources that were needed to consider the problem three-dimensionally were not economically feasible. Thirteen commonly used four-bolt unstiffened moment endplate connections were modelled using two-dimensional three-noded constant strain elements and eight-node brick elements, respectively. The connections were examined under pretension alone and pretension plus some fraction of the expected service load. Plate separation between the endplate and the support, which is modelled as a rigid column flange, and vertical plate bending stresses are compared between the two models using correlation factors. The intent was that these factors could be used to extrapolate results for other connection configurations without the expense of a three-dimensional model. The solutions for the connections were obtained by trial and error in order to represent the contact problem between the endplate and the rigid flange. Since contact algorithms were not available at the time, the user had to turn off spring elements upon each iteration if contact was not made at some location on the endplate. The authors admitted that the mesh refinement of their model was very limited. This was important since three-node constant-strain elements provide highly inaccurate results for a coarse mesh. The correlation factors they developed might be arbitrary if the model was yielding improper results. In conclusion, the idea of correlating a two-dimensional model to a three-dimensional model was no longer necessary, as three-dimensional models were easily constructed.

Bursi and Jaspart [55] summarized part one of a two-part investigation of finite element modelling of bolted connections. It presents a validation for the purpose of the study, which was to show that finite element programs can be used to accurately predict the behaviour of moment endplate connections. Tee stub connections are first modelled to determine the accuracy and/or calibration required when using finite elements to model connection behaviour. Using the LAGAMINE software package, the models are constructed using both hexahedron (more commonly called brick) and contact elements. The contact elements utilize what is called a penalty technique. Here, a value is chosen as a penalty parameter and is similar to placing a spring between two bodies. Contact is simulated only for displacements within this given penalty value. Friction caused by the sliding and sticking between bodies is modelled with an isotropic Coulomb friction law.

Nonlinear finite element analysis that considers large displacements, large rotations, and large deformations was used. Loads were applied using displacement as the controlling parameter. For the bolts, the additional flexibility provided by the nut and threaded region of the bolt were taken into account by using an effective length of the bolt. Due to the symmetry of the tee stub connection, only a quarter of the connection was modelled. Preloading forces in the bolts were taken into account by using applied initial stresses. The material properties were modelled using piece-wise linear constitutive laws for the material from experimentally tested connections. For several of these experimentally tested connections, a finite element analysis was performed. The finite element results compared quite nicely to experimental results. There was a slight difference in deflection values at the onset of yielding, which was primarily due to the presence of residual stresses in the actual tee stubs which was neglected in the finite element models of these members.

Research by Bursi and Jaspart [56] was the second part of the two-part investigation by the authors. This paper uses the finite element method and the ABAQUS finite element code to analyze four-bolt un-stiffened extended moment endplate connections under static loading. The purpose of the study was to examine the stiffness and strength behaviour of these connections. The finite element results are compared to those from an experimental study. Endplate rotation and bolt forces are both considered. The authors' intent is to show the feasibility of using the finite element method via commercial codes to determine moment-rotation characteristics of semi-rigid connections. Although dynamic characteristics of these connections are not considered, the authors do consider thin endplates mainly for their ability to behave in a ductile manner when plate yielding occurs.

The finite element model considered by the authors was quite complex. The bolt and bolt head were modelled using beam elements. Both preloaded and non-preloaded bolts were considered, but only bolts in the tension region are included. The endplate and beam elements were eight-node brick elements that allow plasticity. Contact elements were used to describe the interaction between the endplate and the rigid column flange. Around the bolt holes, nodes were constrained in the direction perpendicular to the face of the endplate.

This assumption was very limiting, as tests and other finite element studies were shown that endplates tend to pull away from the column flange even at the bolt locations. Other than friction forces taken by the contact elements, there were no lateral constraints mentioned in the paper. However, results were obtained even for the zero friction case, which should result in divergence due to a singular stiffness matrix. Thus it was assumed that some other boundary condition was provided, but not discussed. By comparison with experimental results, the results indicates that the model predicted the endplate moment-rotation characteristics quite accurately. However, the bolt forces were not recorded experimentally and no comparison is made. The bolt axial force versus beam flange force seemed reasonable in the plots provided.

Bursi and Jaspart [56] presented basically the same results as the paper discussed in this section and is not considered separately. Bursi and Leonelli [57] presented some additional results that were not discussed in Bursi and Jaspart [55]. Twenty-node brick elements were used to model the beam and plate material. Contact elements were used to represent the endplate/column-flange interaction problem. Once again, beam elements were used to model the bolts, but here the bolts are pre-tensioned to a snug tight condition. The column flange was considered rigid. Endplate rotation and bolt loads were examined using the finite element model. Fairly good correlation with experimental results is obtained. A direct application of Richard and Abbott [58] were used to describe the analytical results obtained from the finite element model. Using the finite element method was to obtain the elastic stiffness, the inelastic stiffness, the plastic failure moment, and the ultimate applied moment for the connection. Where all the parameters were obtained from the results of a finite element analysis.

Research by Sherbourne and Bahaari [59] was the first part of a two-part study that aimed to describe the moment-rotation characteristics of moment endplate connection using results obtained from the finite element method. A three-dimensional finite element model of unstiffened endplate connection was developed using ANSYS finite element code. The bolt shank was modelled using link elements and initial bolt strains are applied to model a snug tight condition. The bolt head and nut were made continuous with the endplate and column flange, respectively. Contact elements were used to describe the endplate to column-flange interaction problem. Material non-

linearities were included in the analysis. Moment rotation curves produced by finite element model were very similar to those of a previous experimental study. The column side of the connection was also considered, and the role played by the column flange strength in providing additional rotation were discussed. The most intriguing part of this study was to consider the effect of geometric parameters of the endplate configuration on the moment-rotation curve developed using the finite element method. The effects of column flange stiffening, endplate thickness, bolt size, and bolt gauge were all shown graphically.

Gebbeken et al. [60] investigated different finite element modelling techniques to investigate the important criteria for describing moment endplate connection behaviour. Also, the authors discussed the results of a parametric study to determine which elements of the connection provide significant amounts of connection flexibility. The four-bolt unstiffened extended endplate connection was considered. First, a two-dimensional model was used. The material stress/strain relationship is represented as a bilinear function. Friction between the column flange and the endplate was neglected. The results from this analysis were poor since strength predictions are very un-conservative when compared to experimental results. The three-dimensional model used by the authors provided some limited success in predicting the moment-rotation characteristics of the connection. The description of the finite element model was vague, yet it is mentioned that brick elements were used. Also, the figures in the paper made it appear that a tee stub and not an actual endplate was considered. In some cases the results were accurate, but in others the strength is off by 50% or more, possibly suggesting inadequate modelling assumptions. Rothert et al. [61] presented similar results and findings based on the same research.

There were several other papers that consider topics dealing with finite element modelling of moment endplate connections, or finite element modelling of steel connections for seismic design. Bahaari and Sherbourne [62] used the ANSYS finite element program to develop a two-dimensional finite element model of four-bolt unstiffened extended moment endplate connections. Sherbourne and Bahaari [63] discussed the results from a three-dimensional finite element model of the same connection constructed using ANSYS. In particular, sources of rotation were tracked for the column flange, the bolts, and the endplate. It was shown that the column flange

provided little rotation when it was stiffened. Choi and Chung [64] investigated the most efficient techniques of modelling four-bolt unstiffened extended endplates using the finite element method. Bose et al. [65] used the finite element method to analyze flush endplate configurations. Troup et al. [66] applied ANSYS to model four-bolt extended unstiffened endplates with shell elements. Leon and Swanson [67] discussed the effectiveness of bolted connections in moment-resisting frames. Fanning et al. [68] studied a non-linear finite element analysis of semi-rigid bolted endplate connections.

Sherbourne and Bahaari [63] presented an analytical method based on finite element modeling to study the moment-rotation relationship for a steel bolted connection. The shell element approach has been used to model the beam, column and endplate. The finite element code ANSYS was used for the equivalent 3-D analysis. The contributions of various connection components, like bolts, endplate and column flanges on the flexibility of the connection was identified. Parametric studies related to various geometric parameters of bolted endplate connections subjected to plane bending were carried out by Gebbeken et. al. [60]. These studies aimed at determining the influence of these parameters on the flexibility of the connection. The main emphasis has been given to the consideration of material non-linearity, contact between deformable members and to the accurate finite element modelling.

Bursi and Jaspart [69] presented an analytical method based on finite element modelling to study the moment-rotation relationship for a steel bolted connection. The finite element code ANSYS was used for equivalent 2D analysis. Based on the deformation and stress contours of the 2D model the contribution of the beam web to the behaviour is discussed from which two types of endplate deformations can be identified. Sherbourne and Bahaari [70] studied the stiffness and strength of a T-stub to the unstiffened column flange bolted connection in a 3D framework using finite element methodology. The finite element code ANSYS was used for the study. Two elementary T-stub connections were proposed as benchmarks in the validation process of finite element software packages for bolted connections and a rational approach that leads to an accurate simulation of these connections by means of a 3-D model.

Bursi and Jaspart [55] provided an overview of the current developments for estimating the moment-rotation characteristics of bolted moment resisting connections and tried to establish a legitimate methodology for the finite element analysis of extended endplate connections. Three-dimensional finite element models were provided for preloaded and non-preloaded bolted T-stubs, which were proposed as benchmarks. A solid model and an assemblage of three-dimensional beam finite elements were proposed to model the bolt behaviour. A 3-D nonlinear finite element model suitable for analysis of isolated extended endplate connections was proposed and validated. Troup et al. [66] presented a numerical model, based on the finite element method, to predict the moment and rotation characteristics of connections. The finite element analysis of a simple T-stub connection and an extended endplate connection was carried out using ANSYS. The numerical model was calibrated against experimental results from full-scale testing of bolted endplate connections. On the basis of the results obtained it was suggested that solid elements were suitable for simple connection problems but shell elements are best suited for more complicated structures like beam to column connections.

Yang et al. [71] developed a 3D finite element model using ABAQUS to study the response of double angle connections subjected to axial and shear loads. For this study steel angles with three different thickness were analysed. The angles were considered welded to the beam web and bolted to the column flange. Thus a number of experimental as well as analytical studies have been carried out which investigate the behaviour of steel connection. Both 2D and 3D finite element models have been employed to investigate the behaviour of these connections. However a major portion of these studies considered static loading. Information regarding the behaviour of steel connections subjected to dynamic loads is based on experimental data where the steel connections are subjected to cyclic loads that simulate seismic loads. Thus limited information is available regarding the behaviour of steel connections subjected to high rate dynamic loading such as blasts. Hence the proposed research aims at providing a better understanding of the behaviour of steel connections subjected to high rate dynamic loads and also to address some issues regarding the finite element modeling of steel connections.

Fanning et al. [68] presented an ANSYS finite element model for flush endplate joints. The model uses a series of solid elements employing material properties determined from the actual specimens. Material non-linearities, contact surfaces and large deflection analysis were included in a non-linear solution. The model proved capable of predicting the moment capacity of a flush endplate joint to within 5% of that measured in an increasing displacement amplitude cyclic test. While the computational requirements for the model are significant, compared with the Eurocode 3 model, a significant improvement in the initial stiffness prediction is seen.

Danesh et al. [72] investigated the study focused on the moment-rotation behaviour of bolted top and seat angles with double web angle connections, especially the initial stiffness of this type of connection under the combination of shear force and moment. Several 3D parametric finite element models were presented for this purpose, with the geometrical and mechanical properties of connections are as parameters. In the models, all the connection components such as beam, column, angles and bolts are modelled using eight-node brick elements. The effects of all component interactions, such as slippage of bolts and frictional forces, were modelled using a surface contact algorithm, and to evaluate the connection behaviour more precisely, bolt pre-tensioning is applied on the bolts shanks as the first load case. To evaluate the effect of shear force on the behaviour of such connections, several models were analysed under different magnitudes of shear force, and the results of the analyses showed that the shear force has a reducing effect on the initial stiffness of bolted angle connections. Therefore, an equation was proposed to determine the reduction factor of a connection's initial stiffness in terms of the connection's initial stiffness and yield moment in the case of no shear force, and any expected shear force that might be applied.

Citipitioglu et al. [73] studied an approach for refined parametric three-dimensional (3D) analysis of partially-restrained (PR) bolted steel beam-column connections. The models included the effects of slip by utilizing a general contact scheme. The effect of several geometrical and material parameters on the overall moment-rotation response of two connection configurations subject to static loading was studied. Models with parameters drawn from a previous experimental study of top and bottom seat angle connections are generated in order to compare the analyses with test

results, with good prediction shown by the 3D refined models. The proposed 3D modelling approach was a general one and can be applied for accurate modelling of a wide range of other types of PR connections. A clear effect of slip and friction, between the connection components was shown with connections having thicker (stiffer) seat angles. This study demonstrates the effects of clamping through the bolts and contact between the components on the overall non-linear moment–rotation response. Equivalent moment–rotation responses of pull-test simulations are compared to FE model responses of full connections without web angles. The moment–rotation from the pull test was shown to be equivalent to that of the full FE model for small rotations. As the rotation increases a softer response is shown by the pull tests.

An analytical procedure was proposed to establish the nonlinear moment-rotation (M- θ) characteristics for the bolted endplate connections in flexibly jointed steel frames [74]. The connection characteristics were assumed to depend on the component behaviour of the tension zone, the compression zone, and the shear zone. The column flange and endplate with each bolt row in the tension zone are considered as a series of T-stub assembly with the effective length recommended by the Eurocode 3. Based on the beam and yield-line theory, the elastoplastic force-deformation relationship for each T-stub assembly was derived. With the consideration of the deformation of column web in compression and shear zone, the connection rotation ϕ under bending moment M was evaluated accordingly. The proposed analytical model was compared with some experimental results of extended and flush endplate connections, and the feasibility and validation of the proposed model are demonstrated.

The behaviour of angle bolted connections with high strength steel has been well predicted in [75]. The finite element code ANSYS was used for the equivalent 3-D analysis. A finite element model with three dimensional shell and solid elements was established to investigate the structural performance of bolted connections between carbon steel and high strength steel angle cleats. The result showed that the effect of angle thickness gave slightly change of the initial stiffness whilst the thicker one will pronounce on the slippage of TSAW connection.

A finite element modelling of beam-column bolted connection with simplified approach was proposed [76]. The finite element code ANSYS was used for the equivalent 3-D analysis. The authors admitted that how simplified finite element modelling of DWA and TSA connection with shell elements might predict structural performance with reduced number of elements and degree of freedoms. The connection capacity of a high strength thicker angle of TSA connection was slightly more than that of DWA connection except for the connection with higher beam depth and very high strength angles. The higher angles gave significant proportion of maximum stress distribution, when the beam and column were kept with lower stress.

Reference [77] presented a three dimensional finite element modelling of flush endplate (FEP) with high strength steel using ANSYS. Non-linear 3D continuum 8-node isoparametric solid elements were used for all parts of the connection to investigate the structural performance of FEP connection between mild carbon steel and HSS. The effect of plate thickness and higher strength endplate gave significant increase on the moment capacity of the connection. The high strength endplate gave significant proportion of maximum stress distribution whereas the beam and column are kept with mild steel grade.

A three dimensional finite element methodology to predict the behaviour of bolted endplate connection with hollow section beam has been studied [78]. Using the ANSYS software package, the models were constructed using both octahedron isoparametric (more commonly called brick) and contact elements. The analysis result of moment-rotation relationship and behaviour characteristic of the connection with mild carbon steel and high strength steel were compared and discussed. It was found that bolt configuration, endplate properties and beam geometry were important parameter for accurate prediction of endplate bolted connection behaviour with high strength steel endplate.

Reference [79] presented a three dimensional finite element modeling of endplate semi continuous composite connection with high strength steel using ANSYS. Non-linear 3D continuum elements of concrete, steel and shear connectors were used to model the connection. The proposed models were compared using a simplified approach using

spring stiffness analysis. From these models it will be possible to establish suitable design methods utilising the strength and stiffness of semi-continuous composite connections with high strength steel.

An approach for three dimensional (3D) finite element analysis was established by rigorous application of ANSYS to investigate behaviour of partially restrained (PR) connection with cold-formed high strength steel section [80]. A refined model approach was proposed to predict connection behaviour within angle cleat and bolt. The analysis results of the moment-rotation relationship and behaviour characteristic of the connection with different steel grade were compared and discussed. It was found that contact element and strength enhancement of the corner regions employed in the model were very important parameters for accurate prediction of PR connection behaviour with high strength steel. The moment capacity prediction of TSA connections based on EC3 shown to be reasonable compared with FE modelling. The high strength angles gave significant proportion of maximum stress distribution close to their ultimate stresses, whereas the beam and column are kept with mild carbon steel. Taking into account strength enhancement of corner region gave slightly increasing in ultimate moment capacity.

Development of moment-rotation model equations for flush endplate connection was studied by Abolmali et al [81]. The authors used the development of Ramberg-Osgood and Three-Parameter Power Model prediction equations for the moment-rotation ($M-\theta$) behaviour of FEP connection with one of bolts below tension and compression flanges. A finite element model (FEM) using ANSYS of the connection region along with the connected beam and column has been developed for load deformation analyses, which included material, geometric, and contact non-linearity. The models were developed by varying the flush endplate's geometric variables within their practical ranges. Regression equations were developed for the prediction model, which predicted the $M-\theta$ relationship closely, with more accurate model being the Three-Parameter Power model.

Faella et al. [82] considered the theory and design of steel semi-rigid connections and contains a chapter specifically on moment endplate connections. Design procedures presented for extended endplates based on yield line theory were very complex and are

modified to correlate with test results. Yield line patterns for the limit states of endplate bending only considered the part of the plate above the tension flange. This was abnormal since sufficient experimental testing exists to show that most of the endplate yielding takes place inside the beam flange.

2.8 Needs for Further Research

The need for bigger capacity and performance of bolted connections using stainless and high strength steel is presented in Chapter 1, where it is shown that current code requirements and design recommendations are leaning away from allowing connection yielding as a structure's primary source of inelastic behaviour. However, as shown in this literature survey, very little research on bolted connections configuration with high strength and stainless steel for both experimental and finite element modeling has been conducted. What is available on bolted connections usually only presents the results of experimental testing with mild carbon steel. Papers dealing with finite element modeling of bolted connections deal almost exclusively with simple detailing e.g. the four-bolt flush-endplate connection and the shear joint. This is primarily due to its common use, relatively well-understood behaviour, and modeling simplicity. It is evident in the research discussed in this chapter that the finite element method has evolved significantly over the years. Crude models of bolted connections have become very refined and required correlation factors have become more clear, since one can effectively model all the components of the connection more accurately. However, as discussed in the previous sections of this chapter, limitations or assumptions established in previous studies should be addressed, and the research of this thesis aims to provide the more accurate and detailed models of PR and shear connections. Using this proposed model (Chapter 3), the FE model are validated against previous related experimental result Chapter 4), the finite element development using HSS and SS is used to investigate the behaviour of the connections, a parametric study of the effects of high strength and stainless steel material on connection response is presented (Chapter 6), and a design procedure for bolted connections with HSS and SS is developed (Chapter 7).

Chapter 3

Introduction of Finite Element Modelling

3.1 Introduction

Computer modelling is required to provide a comprehensive understanding of the process behaviour and rapid evaluation amongst design alternatives and optimization. Finite element modelling also provides a reduction in the cost of physical testing. In structural steel connection analyses, one of the most critical analytical steps is the modelling process. The modelling of any structure begins with an accurate representation of its members and components hence allowing for a realistic, economic and safe design. The most difficult part of structural analyses is to develop an accurate model that will correctly represent the total structural system. In many cases it is impossible to represent any building structure exactly with a model without making some general assumptions. For instance, structural materials are assumed to deform according to basic mechanics of materials. This assumption is reasonable for modelling purposes whilst bearing in mind possible 'real world' issues, such as changing weather conditions, standards of construction and the actual consistency of the material. In developing a model there are different levels of precision that can be achieved, reflecting in large part of the structure, time allocated for design, cost of engineering and the uniqueness of the geometry or loads.

Designs developed in this project research have focussed on structures of ordinary geometry and loading. The only uniqueness is in the presence of bolted connections. This means that many of the modelling methods used on typical steel connections will not

work. Because most companies use computers in the analyses of steel structures, there are many software packages designed to analyze structures. Some programs can not represent detailed connection behaviour due to limitation on the element types available. So for this reason a general purpose finite element package, ANSYS 10.0, is used to analyze the steel bolted connections and frames [83].

Finite Element Analyses (FEA) enables evaluation of a detailed and complex structure, in a computer, during the planning of the structure. The demonstration in the computer of the adequate strength of the structure and the possibility of improving the design during planning will generally justify the cost of this analytical work. FEA has also been known to increase the rating of structures that were significantly overdesigned and built many decades ago.

In the absence of FEA (or other numerical analyses), development of structures will be based on hand calculations only. For complex structures, the simplifying assumptions required to make any calculations possible can lead to a conservative and heavy design. Further, there will likely be considerable insecurity in evaluating whether or not the structure will be adequate for all design loads. Significant changes in designs involve risk. Designs will require prototypes to be built and field tested. The field tests may involve expensive strain gauging to evaluate strength and deformation. By using FEA, the weight of a design can be minimized, and there can be a reduction in the number of prototypes built. Field testing will be used to establish loading on structures, which can be used to do future design improvements via Finite Element Analyses.

FEA is a computer-based numerical technique for calculating the strength and behaviour of engineering structures. It can be used to calculate deflection, stress, vibration, buckling behaviour and many other phenomena. It can be used to analyze either small or large-scale deflection under loading or applied displacement. It can analyze elastic deformation, or "permanently bent out of shape" plastic deformation. The computer is required because of the large number of calculations needed to analyze a large structure. The power and low cost of modern computers has made FEA available to many disciplines and problems.

In the finite element method, a structure is divided into many small simple blocks or elements. The behaviour of an individual element can be described with a relatively simple set of equations. Just as the set of elements would be joined together to build the whole structure, the equations describing the behaviours of the individual elements are joined into an extremely large set of equations that describe the behaviour of the whole structure. The computer can solve this large set of simultaneous equations. From the solution, the computer extracts the behaviour of the individual elements. From this, it can get the stress and deflection of all the parts of the structure. The stresses will be compared to allowed values of stress for the materials to be used, to see if the structure is strong enough.

3.2 The Constitutive Modelling

Finite element model may be categorised as being 2D or 3D. Choice of model dimensionality and related element types will often determine which method of model generation will be most practical for particular problem. ANSYS has different type of models viz, 2-D solid models, 3-D shell models and 3-D solid models.

a) 2-D solid models

These type of models are used for thin planar structures (plane stress), infinitely long structures having a constant cross section (plain strain), or symmetric ax solid structures. Although many 2-D analyses models are relatively easy to create by direct generation methods, they are usually easier to create with solid modelling.

b) 3-D shell models

3-D shell models are used for thin structures in 3-D space. Although some 3-D shell analyses models are relatively easy to create by direct generation methods, they are usually easier to create with solid modelling.

c) 3-D solid models

These models are used for thick structures in 3-D space that have neither a constant cross section nor an axis of symmetry. Creating a 3-D solid analyses model by direct

generation methods usually requires considerable effort. Solid modelling always makes the job easier.

3.2.1 The theory of finite element

The best representation for structural steel modelling in the finite element analyses is the three-dimensional model. Three-dimensional models can show the appropriate and realistic dimensions of steel structures. ANSYS software is a sufficient tool to handle the complexity of the three-dimensional structural steel connection model. Therefore, the concept of a three-dimensional hexahedral element will be presented. That element is similar to the steel element that was used in this investigation. The hexahedral element (or a brick element) is a typical eight nodes 3D solid finite element (Figure 3.2) with three translational degrees of freedom (DOF) per node^[84] along the x, y and z axis. A consistent scheme must be followed in node numbering for connectivity definition. The nodal displacement vector can be presented as follows:

$$\mathbf{q} = [q_1, q_2, q_3, \dots, q_{24}]^T \quad (3.1)$$

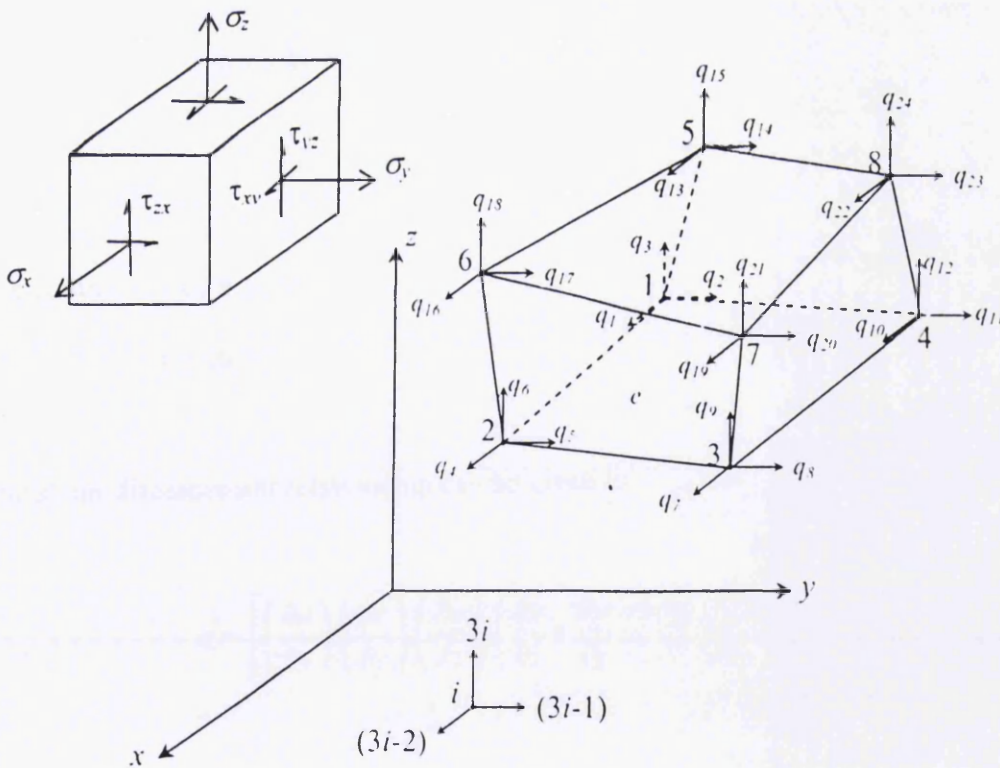


Figure 3.1 Eight-node hexahedral element

The stress and strain tensors can be expressed as follows:

$$\boldsymbol{\sigma} = [\sigma_x, \sigma_y, \sigma_z, \tau_{yz}, \tau_{xz}, \tau_{xy}]^T \quad (3.2)$$

$$\boldsymbol{\varepsilon} = [\varepsilon_x, \varepsilon_y, \varepsilon_z, \gamma_{yz}, \gamma_{xz}, \gamma_{xy}]^T \quad (3.3)$$

The total potential energy has two parameters: the stress $\boldsymbol{\sigma}$ and the strain $\boldsymbol{\varepsilon}$. The $\boldsymbol{\sigma}$ can be expressed in the stress-strain relationship and can be given as follows:

$$\boldsymbol{\sigma} = \mathbf{D}\boldsymbol{\varepsilon} \quad (3.4)$$

Where \mathbf{D} is the tangent modulus, which is a symmetric matrix for the isotropic material model that has a dimension of (6×6). In the case of linear elasticity this tensor is given by:

$$\mathbf{D} = \frac{E}{(1+\nu)(1-2\nu)} \begin{bmatrix} 1-\nu & \nu & \nu & 0 & 0 & 0 \\ \nu & 1-\nu & \nu & 0 & 0 & 0 \\ \nu & \nu & 1-\nu & 0 & 0 & 0 \\ 0 & 0 & 0 & 0.5-\nu & 0 & 0 \\ 0 & 0 & 0 & 0 & 0.5-\nu & 0 \\ 0 & 0 & 0 & 0 & 0 & 0.5-\nu \end{bmatrix} \quad (3.5)$$

The strain $\boldsymbol{\varepsilon}$ can be expressed as:

$$\boldsymbol{\varepsilon} = \mathbf{B}\mathbf{q} \quad (3.6)$$

The strain-displacement relationship can be given as:

$$\boldsymbol{\varepsilon} = \left[\left(\frac{\partial u}{\partial x} \right), \left(\frac{\partial v}{\partial y} \right), \left(\frac{\partial w}{\partial z} \right), \left(\frac{\partial v}{\partial z} + \frac{\partial w}{\partial y} \right), \left(\frac{\partial u}{\partial z} + \frac{\partial w}{\partial x} \right), \left(\frac{\partial u}{\partial y} + \frac{\partial v}{\partial x} \right) \right]^T \quad (3.7)$$

The shape function can be used to define displacement inside the element at any point expressed in its nodal values^[85]:

$$u = N_1 q_1 + N_2 q_4 + \dots + N_8 q_{22} \quad (3.8)$$

$$v = N_1 q_2 + N_2 q_5 + \dots + N_8 q_{23} \quad (3.9)$$

$$w = N_1 q_3 + N_2 q_6 + \dots + N_8 q_{24} \quad (3.10)$$

The displacement can be expressed in terms of unknown nodal values as:

$$\mathbf{u} = \mathbf{Nq}$$

Where \mathbf{N} is the matrix of shape functions relating to the continuous field of displacement, and is expressed in the following equation:

$$\mathbf{N} = \begin{bmatrix} N_1 & 0 & 0 & N_2 & 0 & 0 & \dots & N_8 & 0 & 0 \\ 0 & N_1 & 0 & 0 & N_2 & 0 & \dots & 0 & N_8 & 0 \\ 0 & 0 & N_1 & 0 & 0 & N_2 & \dots & 0 & 0 & N_8 \end{bmatrix} \quad (3.11)$$

Where N_i has been given for an 8 nodes hexahedral as follows:

$$N_i = \frac{1}{8} (1 + \xi_i \xi)(1 + \eta_i \eta)(1 + \zeta_i \zeta) \quad (3.12)$$

Where i is the node number from 1 to 8. η , ξ and ζ are the natural or local coordinate system of any point in the element^[86]. Using a numbering system (Figure 3.2) the shape function can be obtained, for example, to calculate the shape function for node 1 in the hexahedral element, the corresponding coordinates for the natural coordinate system ξ_i , η_i and ζ_i on node number 1 are 1 (-1, -1, -1), therefore the shape function for node 1 will be as follows:

$$N_1 = \frac{1}{8} (1 + (-1)\xi)(1 + (-1)\eta)(1 + (-1)\zeta) \quad (3.13)$$

$$N_i = \frac{1}{8} (1 - \xi)(1 - \eta)(1 - \zeta) \quad (3.14)$$

Following the steps in equations (3.13) and (3.14) the shape function of all nodes can be calculated.

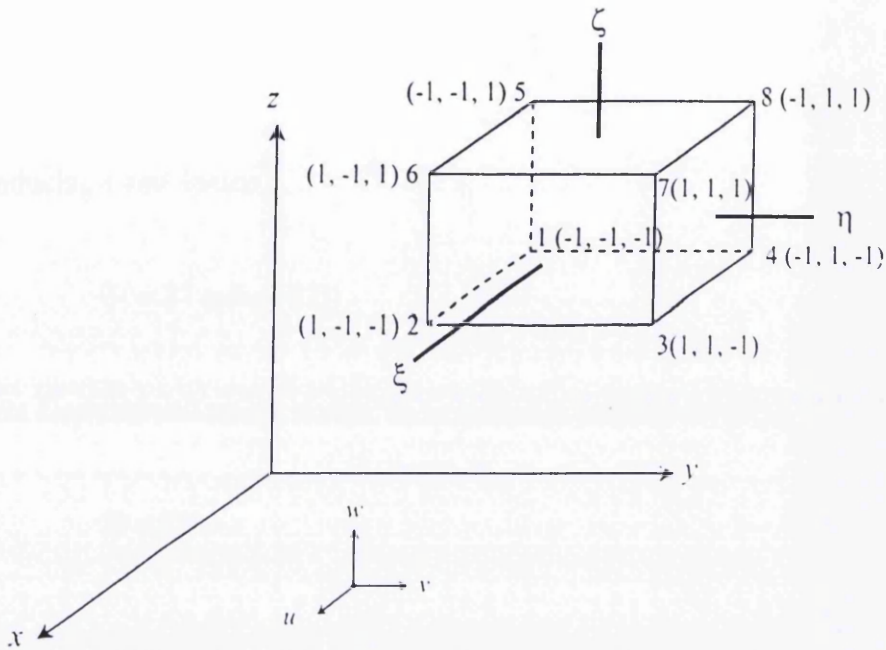


Figure 3.2: The hexahedral element in the ξ, η, ζ space.

The coordinate of a point within the element in terms of nodal coordinates by using the same aforementioned shape functions^[83] can be expressed as follows:

$$x = N_1x_1 + N_2x_2 + \dots + N_8x_8 \quad (3.15)$$

$$y = N_1y_1 + N_2y_2 + \dots + N_8y_8 \quad (3.16)$$

$$z = N_1z_1 + N_2z_2 + \dots + N_8z_8 \quad (3.17)$$

The shape function obtained from equation (3.13) and (3.14) can be substituted in equations (3.15), (3.16) and (3.17) and the derivative taken. Thus the Jacobian matrix (3×3) for the hexahedral element can be obtained.

$$\mathbf{J} = \begin{bmatrix} \frac{\partial x}{\partial \xi} & \frac{\partial y}{\partial \xi} & \frac{\partial z}{\partial \xi} \\ \frac{\partial x}{\partial \eta} & \frac{\partial y}{\partial \eta} & \frac{\partial z}{\partial \eta} \\ \frac{\partial x}{\partial \zeta} & \frac{\partial y}{\partial \zeta} & \frac{\partial z}{\partial \zeta} \end{bmatrix} \quad (3.18)$$

By introducing a new tensor,

$$\mathbf{\Gamma} = \mathbf{J}^{-1} \text{ (after [87])} \quad (3.19)$$

The strain displacement tensor matrix, \mathbf{B} , is given by the following expression:

$$\mathbf{B} = \mathbf{\Gamma N} \quad (3.20)$$

The dimension of the strain displacement tensor matrix depends on the number of nodes, the degree of freedom of each node as well as the components in the stress and the strain tensors. In this particular case it has a dimension of (24x6).

The strain energy yields to the discrete form of strain energy equation which is the element stiffness matrix for the hexahedral element, which can be assembled as follows:

$$\mathbf{k}^e = \int_{-1}^1 \int_{-1}^1 \int_{-1}^1 \mathbf{B}^T \mathbf{D B} |\det \mathbf{J}| d\xi d\eta d\zeta \quad (3.21)$$

Where $\det \mathbf{J}$ is the determinant of the Jacobian matrix. It is a measure of the distortion of the element when mapping from the basis to the real space. Yielding to the assembly of strain energy as:

$$U_e = \frac{1}{2} \mathbf{k}^e \mathbf{q}^e \quad (3.22)$$

The potential term associated with the body force is expressed as:

$$\int_V \mathbf{u}^T \mathbf{f} dV \Rightarrow \mathbf{q}^T \int_{-1}^1 \int_{-1}^1 \int_{-1}^1 \mathbf{N}^T \mathbf{f} \det \mathbf{J} d\xi d\eta d\zeta \quad (3.23)$$

The potential term associated with the external traction force is expressed as:

$$\int_S \mathbf{u}^T \mathbf{T} dS \Rightarrow \mathbf{q}^T \int_S \mathbf{N}^T \mathbf{T} dS \quad (3.24)$$

In this section, the finite element formulation of spar element is presented. The theory of the linear and nonlinear behaviour of the spar element was discussed in detail in previous section. The spar element is not capable of bearing bending loads and a uniform stress over the entire element is assumed. All finite element formulations of this element are generated in its coordinate system and then, they are converted to the global coordinate system. Figure 3.3 is the spar element in the global coordinate system. Using (Figure 3.3) the shape function for the spar element is expressed as follows:

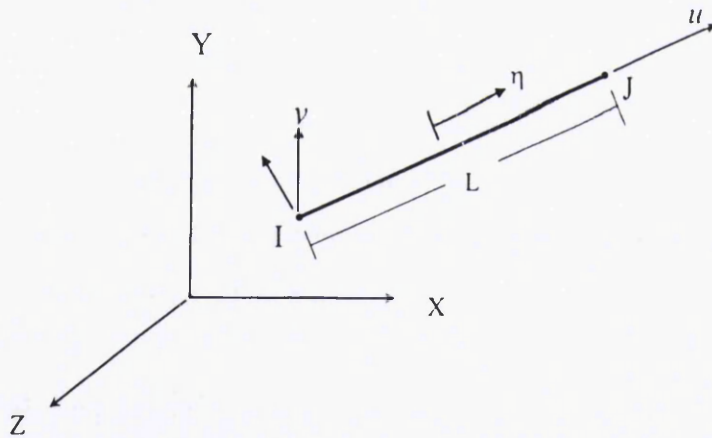


Figure 3.3: The spar element in the global coordinate system.

$$u = \frac{1}{2}(u_i(1-\eta) + u_j(1+\eta)) \quad (3.25)$$

$$v = \frac{1}{2}(v_i(1-\eta) + v_j(1+\eta)) \quad (3.26)$$

$$w = \frac{1}{2}(w_i(1-\eta) + w_j(1+\eta)) \quad (3.27)$$

The stiffness matrix of this spar (steel reinforcement) element is described in the following equation:

$$[k^e] = \frac{A\hat{E}}{L} \begin{bmatrix} 1 & 0 & 0 & -1 & 0 & 0 \\ 0 & 0 & 0 & 0 & 0 & 0 \\ 0 & 0 & 0 & 0 & 0 & 0 \\ -1 & 0 & 0 & 1 & 0 & 0 \\ 0 & 0 & 0 & 0 & 0 & 0 \\ 0 & 0 & 0 & 0 & 0 & 0 \end{bmatrix} \quad (3.28)$$

The stress stiffness matrix for the spar (steel reinforcement) element can be calculated as follows:

$$[S^e] = \frac{F}{L} \begin{bmatrix} 0 & 0 & 0 & 0 & 0 & 0 \\ 0 & 1 & 0 & 0 & -1 & 0 \\ 0 & 0 & 1 & 0 & 0 & -1 \\ 0 & 0 & 0 & 0 & 0 & 0 \\ 0 & -1 & 0 & 0 & 1 & 0 \\ 0 & 0 & -1 & 0 & 0 & 1 \end{bmatrix} \quad (3.29)$$

Where, F is the axial force and it is equal to $AE\varepsilon^m$, for the first iteration and for the next iteration it is computed in the previous stress pass of the element^[83]. The element load vector can be calculated as follows:

$$\{F_e\} = \{F_e^a\} - \{F_e^{nr}\} \quad (3.30)$$

where,

$\{F_e^a\}$ is the applied load vector = $AE\varepsilon_n^T [-1 \ 0 \ 0 \ 1 \ 0 \ 0]^T$

$\{F_e^{nr}\}$ is the Newton-Raphson restoring force.

3.2.2 Nonlinear Behaviour of Steel

The nonlinear behaviour of steel bolted connections is due to material nonlinearities or geometric nonlinearities. The finite element simulation of bolted connections is generally complicated because the problem is three-dimensional (3D) in nature. In addition, combined nonlinear phenomena like material and geometrical nonlinearities, friction, slippage, contact, bolt-plate interaction and fracture have to be reproduced [55].

Geometric nonlinearities are associated only with certain special structure elements and systems in which the effect of displacement on internal forces must be considered in the analyses (e.g. unrestrained beams, and thin plates). With material nonlinearities there are two factors, which cause the nonlinear behaviour of steel structure: time-independent and time-dependent factors. Time-independent factors, which usually occur simultaneously under the propagation of loads, are: cracking of steel and the plastic behaviour of the steel. Other time-independent factors that cause nonlinear behaviour of bolted connection are: nonlinear stress-strain relations for steel, contact between steel plate and bolt, bond slip between angle and beam flange and splice plate fracture due to excessive deformation. Fracture, plastic behaviour and nonlinear stress-strain relations in steel are the only effects that will be included in this investigation.

The steel element that is used in this investigation is capable of nonlinear behaviour. It can present plasticity and fracture as well as distortion. In this section the plasticity behaviour of high strength and stainless steel material as well as strain softening effect of bolted connection behaviour will be presented.

3.2.3 Modelling the plasticity behaviour of steel

In this Section, a brief introduction to plasticity theory will be given. The theory is described in the literature, and suggested reading are Ottosen and Rinstinmaa [89], Lemaitre and Chaboche [90], and Stein, de Borst and Hughes [91].

- **Elasticity Theory**

In elasticity, the stress is found from

$$\sigma_{ij} = \frac{\partial W}{\partial \varepsilon_{ij}} \quad (3.31)$$

where it is assumed that the strain energy W is independent of the loading history. For small elastic strains, the stress state can be evaluated from the hypo-elastic relation

$$\dot{\sigma}_{ij} = C_{ijkl} \dot{\varepsilon}_{kl} \quad (3.32)$$

where C is the elastic stiffness tensor. However, the elastic strains are small in present applications and thus the hypo-elastic formulation is well motivated. Whether the fourth order tensor C_{ijkl} in Equation (40) is a constant tensor or not will not be treated in this work, but it can play an important role when evaluating spring-back.

- **Fundamentals of plasticity**

When the stress reaches the yield stress σ_y , the material starts to flow plastically, and an irreversible deformation occurs. The strain rate is then a sum of an elastic and a plastic part

$$\dot{\varepsilon}_{ij} = \dot{\varepsilon}_{ij}^e + \dot{\varepsilon}_{ij}^p \quad (3.33)$$

where $\dot{\varepsilon}_{ij}^e$ can be evaluated from the hypo-elastic relation given in Equation (3.33). For large deformations, the rate of deformation is divided in the same way

$$D = D^e + D^p \quad (3.34)$$

The modelling the plastic behaviour in the finite element analyses will be presented. The characterization of the rate-independent plasticity in general is presented as having irreversible strain when the material reaches a certain level of stress. The plastic strains are assumed to develop instantaneously, that is, independent of time^[57]. The mathematical relationship of the elasto-plastic behaviour of materials in terms of finite element form will be discussed. Rate-independent plasticity has three components: the yield criterion, the flow rule and the hardening rule.

3.2.4 Yield Criterion

The yield criterion defines the stress value where yielding is initiated. In multi component stresses, the yield criterion is denoted as a function of each of the stress components. Therefore, it can be illuminated in the form of equivalent stress as follows:

$$\sigma_{eff} = f(\{\sigma\}) \quad (3.35)$$

If the equivalent stress σ_{eff} is equal to the material yield parameter σ_y (equation 3.39 below) then plastic strain will be developed in the material. However, if it is less than the material yield parameter σ_y , then the material will be in the elastic state and stresses will be developed in accordance with the elastic behaviour of the stress-strain relationships.

$$f(\{\sigma\}) = \sigma_y \quad (3.36)$$

The material flows plastically if the yield criterion is fulfilled. The yield function f is commonly expressed as

$$f(\sigma, \sigma^y) = \bar{\sigma} - \sigma^y \leq 0 \quad (3.37)$$

for perfect plasticity, where $\bar{\sigma}$ is the equivalent stress and σ_y is the yield stress. The stress can never be greater than S_{ij} the yield stress. Modifications of f also include hardening (or softening) will be given in this section.

The simplest yield criteria are the isotropic ones, and the most well known yield criteria is the von Mises criteria, where von Mises yield criterion yields

$$f(\sigma) = \bar{\sigma}^{VM} - \sigma^y \leq 0 \quad \text{where} \quad \bar{\sigma}^{VM} = \sqrt{\frac{3}{2} S_{ij} S_{ij}} \quad (3.38)$$

where S_{ij} is the deviatoric part of the stress, i.e. $S_{ij} = \sigma_{ij} - \frac{\sigma_{kk}}{3} \delta_{ij}$.

Figure 3.4 shows the yield loci of von Mises. In a) it can be seen that both criteria constitute a cylinder in space, with center axis $\sigma_1 = \sigma_2 = \sigma_3$. In b) plane stress is assumed. The von Mises effective stress is independent of hydrostatic pressure.

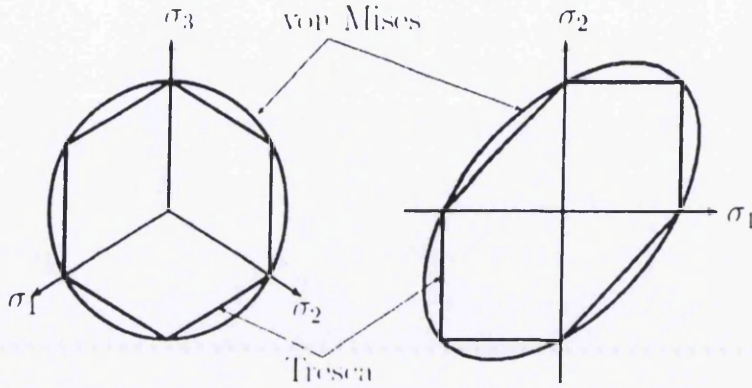


Figure 3.4: The yield loci of Tresca and von Mises

The rate of plastic flow is given by

$$D''_{ij} = \dot{\lambda} \frac{\partial g}{\partial \sigma_{ij}}, \dot{\lambda} \geq 0 \quad (3.39)$$

where g is the plastic potential. If an associated flow law is assumed $g = f$, otherwise not.

$\dot{\lambda}$ is the plastic multiplier, which equals zero at elastic loading and is greater than zero at plastic loading. If the load path follows the yield function $f = \dot{\lambda} = 0$. The conditions on f and $\dot{\lambda}$ give the Karush-Kuhn-Tucker (KKT) conditions,

$$\begin{aligned} f &\leq 0 \\ \dot{\lambda} &\geq 0 \\ \dot{\lambda} f &= 0 \end{aligned} \quad (3.40)$$

3.2.5 Hardening Rule

In case of perfect plasticity, the yield function is unchanged during plastic deformation. However, this is not the case for most materials. Either, the yield locus can be moved (kinematic hardening) or it can grow (isotropic hardening). In case of isotropic hardening,

the yield stress is a function of history variables \mathbf{A} , i.e. $\sigma^y = \sigma^y(\mathbf{A})$. The history variables can be internal variables.

For kinematic hardening, the effective stress is a function of the overstress Σ which is defined by

$$\Sigma = \sigma - b \quad (3.41)$$

where b is called the backstress and is a measure of how much the yield locus has been moved.

Thus, the yield function can be written

$$f(\Sigma, \sigma^y) = \bar{\sigma}(\sigma - b) - \sigma_y(A) \quad (3.42)$$

Also the shape of the yield locus can be changed, which is referred to as distortional or anisotropic hardening, c.f. Ottosen and Ristinmaa [89].

In order to approximate the yield stress σ_y as a function of ε^p several proposals have been found. Below a review of some models will be given. Figure 3.5 shows a perfect plasticity stress-strain relation which is the simplest model, i.e. no hardening at all. Next to it comes linear hardening, with hardening modulus H .

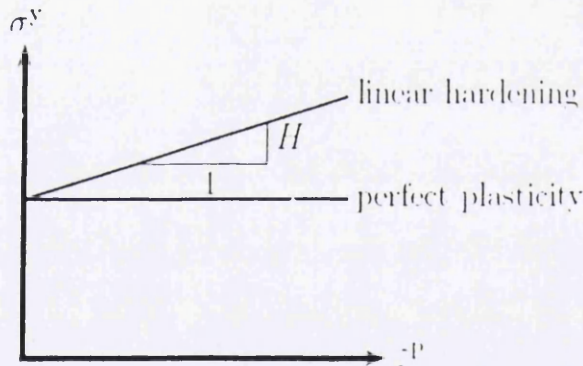


Figure 3.5: Perfect plasticity and linear hardening.

Another simple approximation is the power law where

$$\sigma^y = \sigma_o^y + K\varepsilon^n \quad (3.43)$$

where n and K are material parameters and σ_o^y is the initial yield stress.

The Ludwik curve has some similarities to the power law

$$\sigma^y = \sigma_o^y \left(\frac{E\varepsilon}{\sigma_o^y} \right)^n \quad (3.44)$$

where n and K are material parameters and σ_o^y is the initial yield stress.

Other examples are the Ramberg-Osgood curve, which is described by

$$\varepsilon^p = \frac{\sigma}{E} \left[1 + \alpha \left(\frac{\sigma}{\sigma_o^y} \right)^{n-1} \right] ; n < 1 \quad (3.45)$$

which here is expressed in terms of plastic strain as a function of stress.

The hardening rule expresses the yield surface change along with the yielding progress where the stress states of the second yielding can be initiated. There are two hardening rules that can be applied to the plasticity behaviour of the materials: isotropic hardening and kinematic hardening. Figure 3.6 shows the isotropic hardening behaviour of materials where the yield surface in the stress space stays in the centre of its initial centreline and as the plastic strain develops it expands in size and remains in its initial centreline.

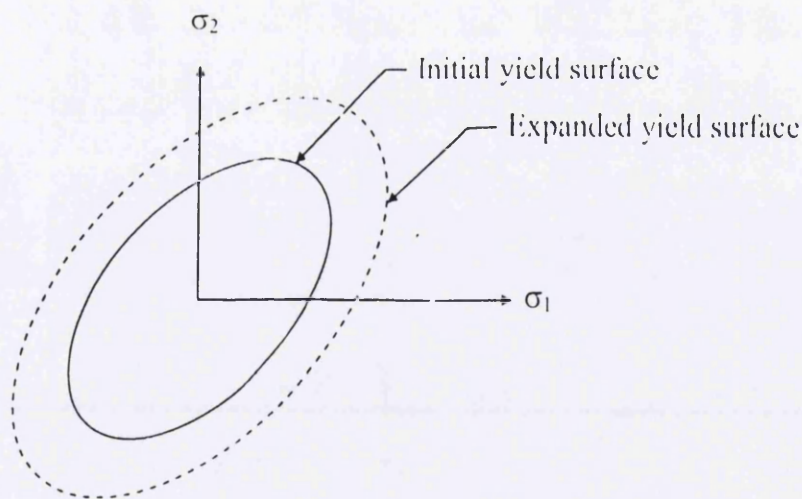


Figure 3.6: The hardening rule in isotropic hardening behaviour (after [85]).

The plastic straining would occur even when computing the equivalent stress by using elastic properties that exceed the material yield. In order to satisfy the yield criterion in equation (3.40), the plastic strains decrease the stress state. Therefore, from the aforementioned theory, the increment of the plastic strain can be easily obtained. As it has been stated in the early part of this section, the hardening rule is the change of the yield criterion with either isotropic hardening or kinematic hardening. After adding the hardening dependencies into the equation (3.50), it will yield the following form:

$$f(\{\sigma\}, \kappa, \{\lambda\}) = 0 \quad (3.46)$$

Where κ and $\{\lambda\}$ are the stress state variables. Where $\{\lambda\}$ is the shift of the yield surface and κ is the sum of the plastic work done over the history of loading. The stress state variables are history dependent and are defined as follows:

$$\kappa = \int \{\sigma\}^T [M] \{d\epsilon^p\} \quad (3.47)$$

$$\{\lambda\} = \int C \{d\epsilon^p\} \quad (3.48)$$

The differentiation of equation (3.83) and (3.84) yield to the following expressions:

$$d\kappa = \{\sigma\}^T [M] \{d\epsilon^p\} \quad (3.49)$$

$$\{d\lambda\} = C \{d\epsilon^p\} \quad (3.50)$$

The differentiation of equation (3.48) yields to the following consistency condition expression:

$$df = \left\{ \frac{\partial f}{\partial \sigma} \right\}^T [M] \{d\sigma\} + \frac{\partial f}{\partial \kappa} d\kappa + \left\{ \frac{\partial f}{\partial \lambda} \right\}^T [M] \{d\lambda\} \quad (3.51)$$

Where,

$$[M] = \begin{bmatrix} 1 & 0 & 0 & 0 & 0 & 0 \\ 0 & 1 & 0 & 0 & 0 & 0 \\ 0 & 0 & 1 & 0 & 0 & 0 \\ 0 & 0 & 0 & 2 & 0 & 0 \\ 0 & 0 & 0 & 0 & 2 & 0 \\ 0 & 0 & 0 & 0 & 0 & 2 \end{bmatrix} \quad (3.52)$$

Substituting equation (3.49) and (3.50) into equation (3.51), the following expression can be obtained:

$$\left\{ \frac{\partial f}{\partial \sigma} \right\}^T [M] \{d\sigma\} + \frac{\partial f}{\partial \kappa} \{\sigma\}^T [M] \{d\varepsilon^p\} + \left\{ \frac{\partial f}{\partial \sigma} \right\}^T [M] C \{d\varepsilon^p\} = 0 \quad (3.52)$$

The increment of stress can be calculated by using the stress-strain relations as follows:

$$\{d\sigma\} = [D] \{d\varepsilon^e\} \quad (3.53)$$

With,

$$\{d\varepsilon^e\} = \{d\varepsilon\} - \{d\varepsilon^p\} \quad (3.54)$$

To compute the plastic multiplier α in terms of hardening variables, equation (3.54) can be substituted into equation (3.52) as well as (3.54) and consolidating equations (3.52), (3.53) and (3.54) together, yields to the following equation:

$$\alpha = \frac{\left\{ \frac{\partial f}{\partial \sigma} \right\}^T [M][D]\{d\varepsilon\}}{-\frac{\partial f}{\partial \kappa} \{\sigma\}^T [M] \left\{ \frac{\partial Q}{\partial \sigma} \right\} - C \left\{ \frac{\partial f}{\partial \sigma} \right\}^T [M] \left\{ \frac{\partial Q}{\partial \sigma} \right\} + \left\{ \frac{\partial f}{\partial \sigma} \right\}^T [M][D] \left\{ \frac{\partial Q}{\partial \sigma} \right\}} \quad (3.55)$$

3.2.6 Implementation

To implement the consistency condition in equation (3.51), an Euler backward method is adopted to ensure that the updated stress, strain and internal variables are on the yield surface. The implementation steps are as follows:

1- For a substep n , the material yield parameter σ_y is calculated by using equation (3.53).

2- The trial stresses $\{\epsilon^{tr}\}$ can be computed as follows (thermal and other effects are ignored):

$$\{\epsilon_n^{tr}\} = \{\epsilon_n\} - \{\epsilon_{n-1}^p\} \quad (3.56)$$

where

$\{\epsilon_n\}$ is the strain in the current substep n

$\{\epsilon_{n-1}^p\}$ plastic strain from the previous substep.

After computing the trial strain, the trial stress can be calculated as follows:

$$\{\sigma^{tr}\} = [D] \{\epsilon^{tr}\} \quad (3.57)$$

3- By using equation (3.52) the equivalent stress σ_{eff} at the trial stress level is computed. A comparison between the equivalent stress σ_{eff} and the material yield parameter σ_y is performed concluding that no plastic strain increment is computed if the equivalent stress σ_{eff} is less than the material yield parameter σ_y indicating that material is still in the elastic behaviour. On the other hand, if the equivalent stress σ_{eff} exceeds the material yield parameter σ_y , therefore, the plastic multiplier α is evaluated by using a local Newton-Raphson iteration procedure^[92]. The Euler backward integration

method for this step procedure is the radial return algorithm^[93] for the von Mises yield criterion.

- 4- The plastic strain $\{\Delta\epsilon^p\}$ is computed by using equation (3.54).
- 5- The current plastic strain $\{\epsilon_n^p\}$ is updated, then the elastic strain $\{\epsilon^e\}$ and the stresses vector $\{\sigma\}$ are computed as follows respectively:

$$\{\epsilon_n^p\} = \{\epsilon_{n-1}^p\} + \{\Delta\epsilon^p\} \quad (3.58)$$

$$\{\epsilon^{el}\} = \{\epsilon^{tr}\} - \{\Delta\epsilon^p\} \quad (3.59)$$

$$\{\sigma\} = [\mathbf{D}] \{\epsilon^e\} \quad (3.60)$$

- 6- By using equations (3.59) and (3.60) the incremented plastic work $\Delta\kappa$ and the yield surface centre $\{\Delta\lambda\}$ are computed and their current values are updated by using the following expressions respectively:

$$\kappa_n = \kappa_{n-1} + \Delta\kappa \quad (3.61)$$

$$\{\lambda_n\} = \{\lambda_{n-1}\} + \{\Delta\lambda\} \quad (3.62)$$

- 7- The equivalent plastic strain ϵ_{eff} and the equivalent stress parameter $\bar{\sigma}_e^{pl}$ are computed. In addition, The equivalent plastic strain increment $\Delta\epsilon_{eff}$ can be evaluated by using the following expression:

$$\Delta\epsilon_{eff} = \left(\frac{2}{3} \{\Delta\epsilon^p\}^T [\mathbf{M}] \{\Delta\epsilon^p\} \right)^{\frac{1}{2}} \quad (3.63)$$

3.2.7 Multilinear Isotropic Hardening (MISO)

This plastic material option uses von Mises yield criterion, flow rule and isotropic hardening. Figure 3.7 is the stress-strain behaviour of a multilinear isotropic material in general. The equivalent stress for this option is in the following format:

$$\sigma_{eff} = \left[\frac{3}{2} \{S\}^T [M] \{S\} \right]^{\frac{1}{2}} \quad (3.64)$$

where $\{S\}$ is the deviatoric stress and can be calculated as follows:

$$\{S\} = \{\sigma\} - \sigma_m [1 \ 1 \ 1 \ 0 \ 0 \ 0]^T \quad (3.65)$$

where, σ_m is the mean stress and can be calculated as follows:

$$\sigma_m = \frac{1}{3} (\sigma_x + \sigma_y + \sigma_z) \quad (3.66)$$

The yield criterion for the MISO plastic option can be expressed in the following form:

$$f = \left[\frac{3}{2} \{S\}^T [M] \{S\} \right]^{\frac{1}{2}} - \sigma_k = 0 \quad (3.73)$$

σ_k is the current yield stress and is a function of the amount of plastic work in the isotropic (work) hardening^[82] it can be determined from the uniaxial stress-strain behaviour curve (Figure 3.7). Material using the MISO plastic option is assumed to yield when the equivalent stress is equal to the current stress.

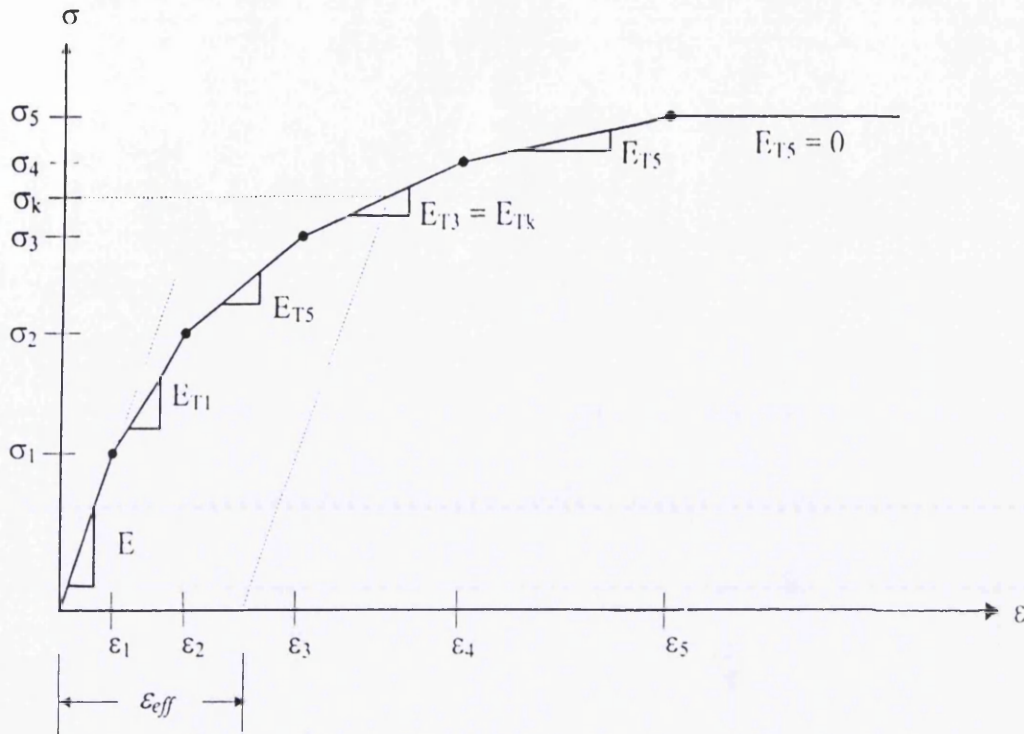


Figure 3.7: Uniaxial behaviour for MISO and σ_k determination (after [83]).

3.3 Finite Element Modelling and Working with ANSYS

In general, a finite element solution may be broken into the following three stages. This is a general guideline that can be used for setting up any finite element analyses.

1. Preprocessing: defining the problem; the major steps in preprocessing are given below:

- Define keypoints/lines/areas/volumes
- Define element type and material/geometric properties
- Mesh lines/areas/volumes as required
- The amount of detail required will depend on the dimensionality of the analyses (i.e. 1D, 2D, axi-symmetric, 3D).

2. Solution: assigning loads, constraints and solving; here we specify the loads (point or pressure), constraints (translational and rotational) and finally solve the resulting set of equations.
3. Postprocessing: further processing and viewing of the results; in this stage one may wish to see:
 - Lists of nodal displacements
 - Element forces and moments
 - Deflection plots
 - Stress contour diagrams

3.3.1 Types of Analyses on Structures

Structures can be analyzed for small deflection and elastic material properties (linear analyses), small deflection and plastic material properties (material nonlinearity), large deflection and elastic material properties (geometric nonlinearity), and for simultaneous large deflection and plastic material properties.

By plastic material properties, one means that the structure is deformed beyond yield of the material, and the structure will not return to its initial shape when the applied loads are removed. The amount of permanent deformation may be slight and inconsequential, or substantial and disastrous. In some structures, "shakedown" producing residual stress due to local permanent deformation, may in some circumstances reduce fatigue problems in zones that will remain in compressive stress as a consequence. Local yielding means that some zones will usually be in compressive stress during conventional use of the pressure vessel, and may be less prone to fatigue crack development.

By large deflection, one means that the shape of the structure has changed enough that the relationship between applied load and deflection is no longer a simple straight-line relationship. This means that doubling the loading will not double the deflection. The material properties can still be elastic.

In addition to analyzing structures for their stress and deflection, other typical analyses are an evaluation of the natural frequency of vibration, and calculation of buckling loads. Steady state, transient, and random vibration behaviour can be analyzed, too.

Loads on structures can be represented by using the force of gravity on the mass of the structure, by applying distributed pressure over surfaces of the structure, or by applying forces directly to positions in the structure. Centrifugal load can be entered by indicating the axis for the motion, and the rate of rotation. Displacements of the structure can be specified at positions in the structure. This can include boundary conditions that imply symmetric structures where only a portion of the structure is modeled. Other boundary conditions will indicate where the structure is supported against movement, by the outside world. Temperature distribution that causes thermal expansion and stress can be applied directly to nodes or to elements with appropriate commands. Uniform temperatures and reference temperatures can also be applied to full models.

3.3.2 Typical Modeling Difficulties

A typical user modeling problem is the case of key-points, lines, areas, volumes, nodes, and elements that are identical and occupy the same space. This can lead to erroneous models. Proper use of the merge command can eliminate many instances of these problems. The merge can fail if, for example, two elements share the same space, but were defined via alternative sequences of nodes (e.g. elements in the same place, one numbered by nodes selected clockwise, the other counterclockwise).

Another problem is failure of key-points, or lines, or areas to be shared by higher geometric modeling entities. When this happens, the higher entities are not "fused" or "welded" together as intended. Consequently, the elements will not share nodes along what should have been the common boundary. The analyst must always use caution and double-check everything while developing a model.

The most common of all errors in Finite Element Modeling is the incorrect application of loads and boundary conditions. This must be thought about very carefully. Most models (not all) are prevented from undergoing free body motion in 2-D or 3-D space, by eliminating at least a minimal number of degrees of freedom (2 translations plus 1 rotation in 2-D, and 3 translations plus 3 rotations in 3-D). Rotations can be prevented either by having constraints on translations at enough distinct nodes in space, or by directly constraining a rotational degree of freedom at a node. A common check on results is to see whether the sums of the reaction forces at the constrained nodes equal the sums of the applied forces and gravity loads.

On rare occasions, the Finite Element Analyses model may not be bug-free as a result of imperfect programming of the FEA software, not the user's mistakes. An FEA software package has to keep track of the relationships between key-points, lines, areas and volumes, including the changes that result from Boolean operations. In addition it must keep track of the relationships between those geometric entities and the nodes and elements that result from meshing, even when geometric entities are cleared, and the model is modified. The process for coordinating all the pointers and tables that are generated and changed is not perfect. There are times when the relationships will be erroneous.

3.3.3 ANSYS Commands Involved in the Analyses

In this section, the ANSYS[®] input commands will be demonstrated and where relevant, the command usage will only be briefly discussed. For descriptions on more command usage and reference, see [83].

The ultimate purpose of a finite element analyses is to recreate mathematically the behaviour of an actual engineering system. In other words, the analyses must be an accurate mathematical model of a physical prototype. In the broadest sense, this model comprises all the nodes, elements, material properties, real constants, boundary

conditions, and other features that are used to represent the physical system. To build the model, the ANSYS preprocessor (PREP7) is used to define the element types, element real constants, material properties, and the model geometry.

A static analyses can be either linear or nonlinear. All types of nonlinearities are allowed - large deformations, plasticity, creep, stress stiffening, contact (gap) elements, hyperelastic elements, and so on. Nonlinear structural behaviour arises from a number of causes, which can be grouped into these principal categories:

- Changing status

Many common structural features exhibit nonlinear behaviour that is status-dependent. Status changes might be directly related to load, or they might be determined by some external cause. Situations in which contact occurs are common to many different nonlinear applications. Contact forms a distinctive and important subset to the category of changing-status nonlinearities.

- Geometric nonlinearities

If a structure experiences large deformations, its changing geometric configuration can cause the structure to respond nonlinearly. Geometric nonlinearity is characterized by large displacements and/or rotations.

- Material nonlinearities

Nonlinear stress-strain relationships are a common cause of nonlinear structural behaviour. Many factors can influence a material's stress-strain properties, including load history (as in elastoplastic response), environmental conditions (such as temperature), and the amount of time that a load is applied (as in creep response).

3.3.4 Element Overview

- LINK8

LINK8 is 3-D spar, uniaxial, tension-compression element with three degrees of freedom at each node: translations in the nodal x, y, and z directions. As in a pin-jointed structure, no bending of the element is considered. Plasticity, creep, swelling, stress stiffening, and large deflection capabilities are included. The element is defined by two nodes, the cross-sectional area, an initial strain, and the material properties. The element x-axis is oriented along the length of the element from node I toward node J. The initial strain in the element is given by Δ/L , where Δ is the difference between the element length, L , (as defined by the I and J node locations) and the zero strain length. The geometry and node location of the element are shown in Figure 3.8.

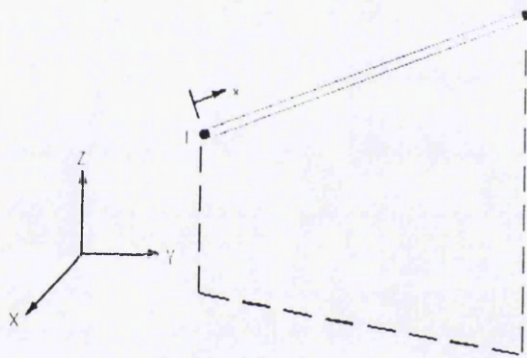


Figure 3.8 – LINK8 spar element geometry ^[83]

- SOLID45

SOLID45 is used for the 3-D modelling of solid structures. The element is defined by eight nodes having three degrees of freedom at each node: translations in the nodal x, y, and z directions. The geometry and node location of the element are shown in Figure 3.9. The element has plasticity, creep, swelling, stress stiffening, large deflection, and large strain capabilities. A reduced integration option with hourglass control is available. The element is defined by eight nodes and the orthotropic

material properties. Orthotropic material directions correspond to the element coordinate directions. The element stress directions are parallel to the element coordinate system. The surface stress outputs are in the surface coordinate systems and are available for any face.

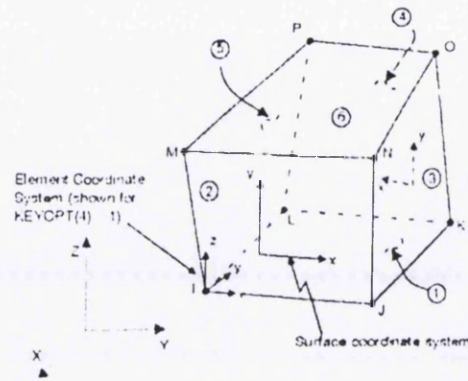


Figure 3.9 – SOLID45 Structural solid geometry; Alphabets I-P and the circled integers represents the nodes and element surfaces respectively ^[83]

- SOLID65

SOLID65 is used for the 3-D modeling of solids with or without reinforcing bars (rebar). The solid is capable of cracking in tension and crushing in compression. In concrete applications, for example, the solid capability of the element may be used to model the concrete while the rebar capability is available for modeling reinforcement behaviour. The element is defined by eight nodes having three degrees of freedom at each node: translations in the nodal x, y, and z directions. The most important aspect of this element is the treatment of nonlinear material properties. The concrete is capable of cracking (in three orthogonal directions), crushing, plastic deformation, and creep. The rebar are capable of tension and compression, but not shear. They are also capable of plastic deformation and creep. The geometry, node locations, and the coordinate system for this element are shown in Figure 3.10.

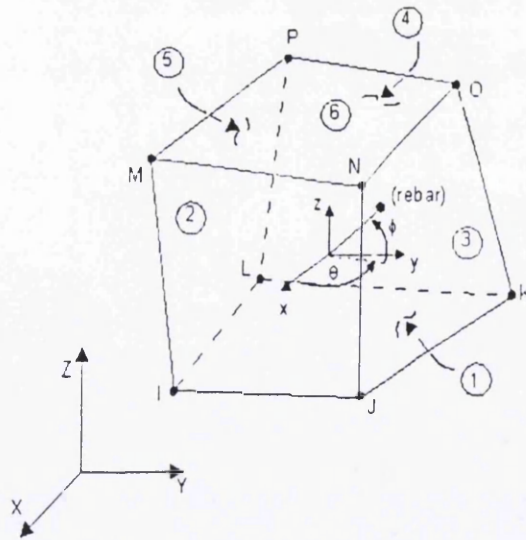


Figure 3.10 – SOLID65 RC solid geometry; Alphabets I-P and the circled integers represents the nodes and element surfaces respectively ^[83]

- SOLID185

SOLID185 is used for 3-D modeling of solid structures. It is defined by eight nodes having three degrees of freedom at each node: translations in the nodal x, y, and z directions. The element has plasticity, hyperelasticity, stress stiffening, creep, large deflection, and large strain capabilities. It also has mixed formulation capability for simulating deformations of nearly incompressible elastoplastic materials, and fully incompressible hyperelastic materials. SOLID185 is available in two forms: structural solid and layered solid. SOLID185 Structural Solid is suitable for modeling general 3-D solid structures. It allows for prism and tetrahedral degenerations when used in irregular regions. Various element technologies such as B-bar, uniformly reduced integration, and enhanced strains are supported. The element is defined by eight nodes and the orthotropic material properties. The default element coordinate system is along global directions. The geometry, node locations, and the coordinate system for this element are shown in Figure 3.11.

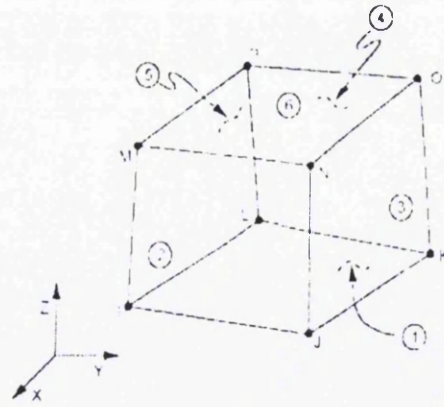


Figure 3.11 – SOLID185 Structural solid geometry; Alphabets I-P and the circled integers represents the nodes and element surfaces respectively [83]

• SHELL143

SHELL143 is well suited to model nonlinear, flat or warped, thin to moderately-thick shell structures. The element has six degrees of freedom at each node: translations in the nodal x, y, and z directions and rotations about the nodal x, y, and z-axes. The deformation shapes are linear in both in-plane directions. The geometry, node locations, and the coordinate system for this element are shown in Figure 3.12. A consistent tangent stiffness matrix (that is, a matrix composed of the main tangent stiffness matrix plus the consistent stress stiffness matrix) option is available for use in large deflection (finite rotation) analyses. The element is defined by four nodes, four thicknesses, and the orthotropic material properties. The element may have variable thickness. The thickness is assumed to vary smoothly over the area of the element, with the thickness input at the corner nodes.

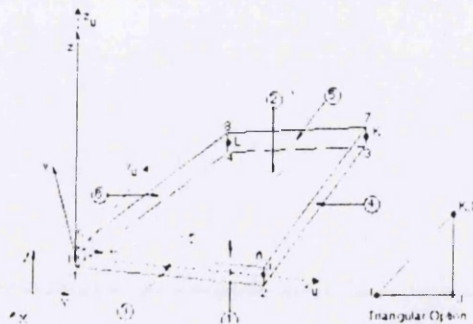


Figure 3.12 – SHELL143 Plastic small strain shell geometry; Alphabets I-L and the circled integers represents the nodes and element surfaces respectively [83]

- CONTA178

CONTA178 represents contact and sliding between any two nodes of any types of elements. The element has two nodes with three degrees of freedom at each node with translations in the X, Y, and Z directions. It can also be used in 2-D and axisymmetric models by constraining the UZ degree of freedom. The element is capable of supporting compression in the contact normal direction and Coulomb friction in the tangential direction. The element may be initially preloaded in the normal direction or it may be given a gap specification. The element is defined by two nodes, an initial gap or interference, an initial element status, and damping coefficients. The geometry, node locations, and the coordinate system for this element are shown in Figure 3.13. The interface is assumed to be perpendicular to the I-J line or to the specified gap direction. The element coordinate system has its origin at node I and the x-axis is directed toward node J or in the user specified gap direction. The interface is parallel to the element y-z plane. The force deflection relationships for the contact element can be separated into the normal and tangential (sliding) directions.

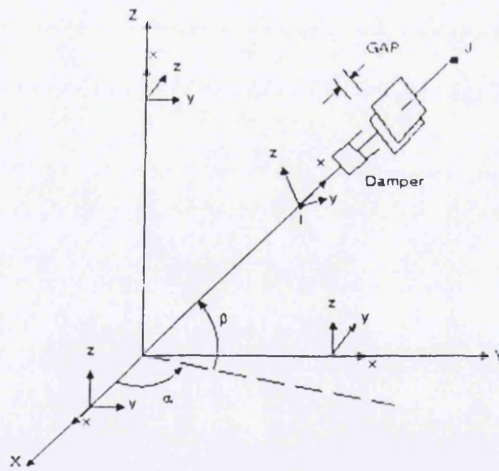


Figure 3.13 – CONTA178 Node-to-node contact geometry ^[83]

- TARGET170

The contact and target surfaces constitute a “Contact Pair”. TARGET170 is used to represent various 3-D target surfaces for the associated contact elements

(CONTA173). The contact elements themselves overlay the solid elements describing the boundary of a deformable body that is potentially in contact with the rigid target surface, defined by TARGE170. Hence, a “target” is simply a geometric entity in space that senses and responds when one or more contact elements move into a target segment element. The target surface is modelled through a set of target segments; typically several target segments comprise one target surface. Each target segment is a single element with a specific shape or segment type. The reaction forces on the entire rigid target surface are obtained by summing all the nodal forces of the associated contact elements. The geometry, node locations, and the coordinate system for this element are shown in Figure 3.14.

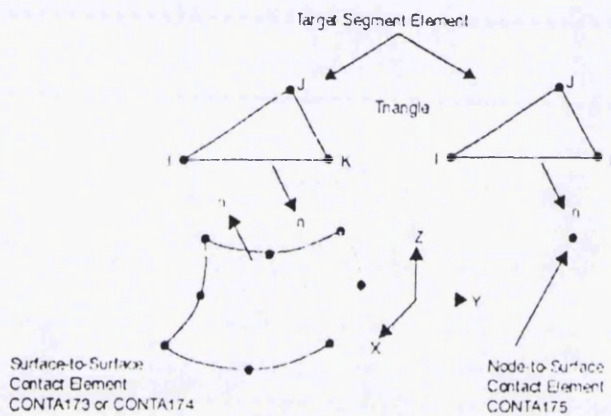


Figure 3.14 – TARGE170 Target segment geometry ^[83]

CONTA173

CONTA173 is defined as 3-D 4-node surface-to-surface contact element that is used to represent contact and sliding between 3-D “target” surfaces (TARGE170) and a deformable surface, defined by this element. This element is located on the surfaces of 3-D solid or shell elements without midside nodes. It has the same geometric characteristics as the solid or shell element face with which it is. Contact occurs when the element surface penetrates one of the target segment elements (TARGE170) on a specified target surface. Coulomb and shear stress friction is allowed. The element is defined by four nodes (the underlying solid or shell element has no midside nodes). The geometry, node locations, and the coordinate system for this element are shown in Figure 3.15.

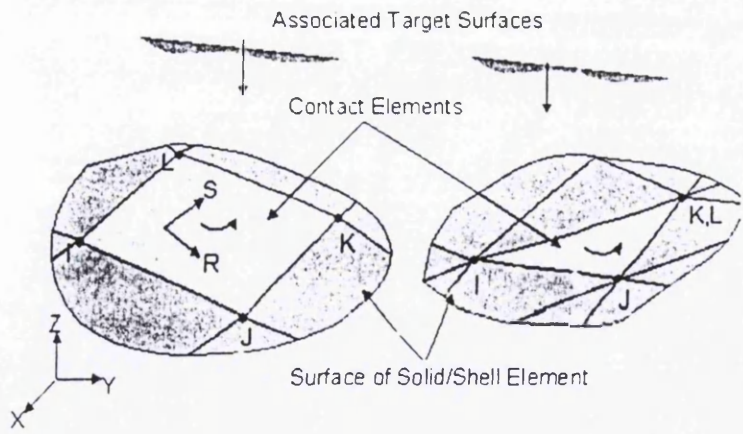


Figure 3.15 – CONTA175 Surface-to-surface contact geometry [83]

COMBIN39

COMBIN39 is a unidirectional element with nonlinear generalized force-deflection capability that can be used in any analyses. The element has longitudinal or torsional capability in 1-D, 2-D, or 3-D applications. The longitudinal option is a uniaxial tension-compression element with up to three degrees of freedom at each node: translations in the nodal x, y, and z directions. The geometry, node locations, and the coordinate system for this element are shown in Figure 3.16. The element has large displacement capability for which there can be two or three degrees of freedom at each node. The element is defined by two (preferably coincident) node points and a generalized force-deflection curve. The points on this curve represent force (or moment) versus relative translation (or rotation) for structural analyses.

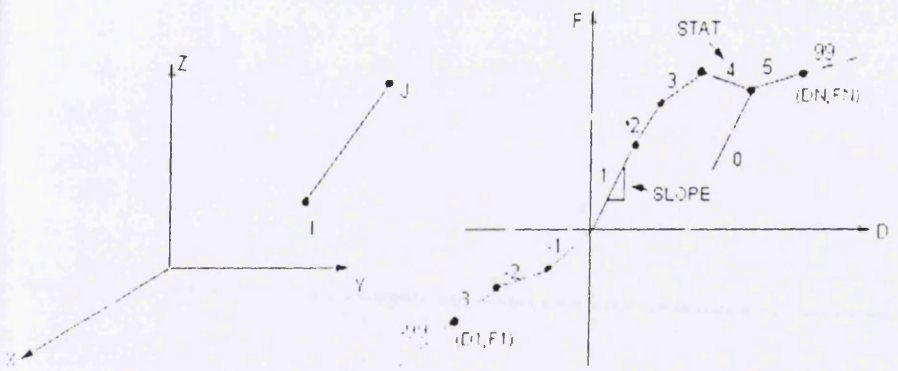


Figure 3.16 – COMBIN39 Non linear spring geometry [83]

- PRETS179

PRETS179 is used to define a 2-D or 3-D pretension section within a meshed structure. The structure can be built from any 2-D or 3-D structural elements (solid, beam, shell, pipe, or link). The PRETS179 element has one translation degree of freedom, UX. (UX represents the defined pretension direction. ANSYS transforms the geometry of the problem so that, internally, the pretension force is applied in the specified pretension load direction, regardless of how the model is defined.). The pretension section is modelled by a set of pretension elements. The pretension element is defined by three nodes I, J, K and the section data NX, NY, NZ which define the pretension load direction relative to surface A. The pretension load direction is constant and is not updated for large displacements. The geometry, node locations, and the coordinate system for this element are shown in Figure 3.17.

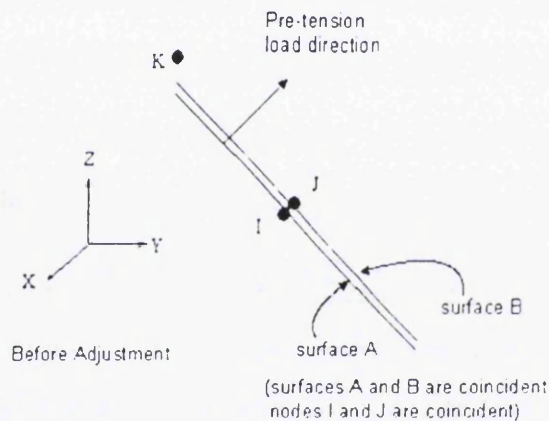


Figure 3.17 – PRETS179 Pretension geometry ^[83]

- BEAM23

BEAM23 is a uniaxial element with tension-compression and bending capabilities. The element has three degrees of freedom at each node: translations in the nodal x and y direction and rotation about the nodal z-axis. The element has plastic, creep, and swelling capabilities. The geometry, node locations, and the coordinate system for this element are shown in Figure 3.18. The element is defined by two nodes, the cross-sectional area, moment of inertia, the height for rectangular beams, the outer

diameter, and the wall thickness, for thin walled pipes, the outer diameter for solid circular bars, and the isotropic material properties.

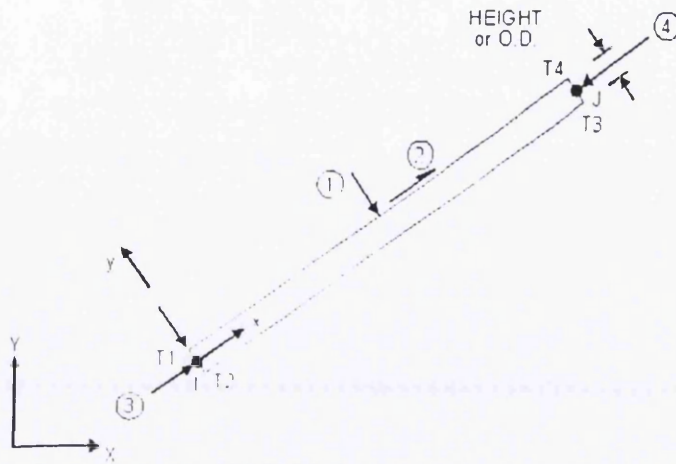


Figure 3.18 – BEAM23 2D-Plastic Beam geometry ^[83]

3.3.5 Material Properties

Most element types require material properties. Depending on the application, material properties can be linear or nonlinear. As with element types and real constants, each set of material properties has a material reference number. The table of material reference numbers versus material property sets is called the material table. Within one analyses, you may have multiple material property sets (to correspond with multiple materials used in the model).

- Linear Material Properties

Linear material properties can be constant, and isotropic or orthotropic using specify the appropriate property label; for example EX, EY, EZ for Young's modulus, and so forth. For isotropic material such as steel, it is needed to define only the X-direction property; the other directions default to the X-direction value. Young's modulus (EX)

and Poisson's ratio (NUXY) for material are 2.0E5 and 0.3 respectively. Shear modulus (GXY) defaults to $EX/2(1+NUXY)$, and emissivity (EMIS) defaults to 1.0.

- **Nonlinear Material Properties**

Nonlinear material properties are usually tabular data, such as plasticity data (stress-strain curves for different hardening laws), creep data, etc. The models of non linear material are further categorized so that material property sets or material models can be chosen that are included under that category (for example, under von Mises plasticity are: bilinear, multilinear, and nonlinear). When performing a structural analyses, several inelastic material models (listed in the tree structure: structural, nonlinear, inelastic) require to input values for elastic material properties (elastic modulus and/or Poisson's ratio) in addition to the inelastic constants that are specific to the model. In these instances, the elastic material properties must be entered before the inelastic constants entered.

3.3.6 Model Geometry

Once material properties have defined, the next step in an analyses is generating a finite element model - nodes and elements - that adequately describes the model geometry. There are two methods to create the finite element model: solid modelling and direct generation. With solid modelling, the geometric shape of the model is described, then the ANSYS program can be instructed to automatically mesh the geometry with nodes and elements. The size and shape in the elements can be controlled that the program creates. With direct generation, the location of each node and the connectivity of each element are defined. Several convenience operations, such as copying patterns of existing nodes and elements, symmetry reflection, etc. are available.

With solid modelling, the geometric boundaries of the model are described, controls establish over the size and desired shape of the elements, and then instruct the ANSYS program to generate all the nodes and elements automatically. By contrast, with the direct generation method, the location of every node and the size, shape, and

connectivity of every element is determined prior to defining these entities in the ANSYS model. Solid modelling is usually more powerful and versatile than direct generation, and is commonly the preferred method for generating the model.

In spite of the many advantages of solid modelling, circumstances might be occasionally encountered where direct generation will be more useful. It can be easy to switch back and forth between direct generation and solid modelling, using the different techniques as appropriate to define different parts of the model. On the plus side, solid modelling is generally more appropriate for large or complex models, especially 3-D models of solid volumes with a relatively small number of data items. However, solid modelling can sometimes require large amounts of CPU time.

3.3.7 Substeps

When using multiple substeps, it is needed to achieve a balance between accuracy and economy: more substeps (that is, small time step sizes) usually result in better accuracy, but at a cost of increased run times. ANSYS provides automatic time stepping that is designed for this purpose. Automatic time stepping adjusts the time step size as needed, gaining a better balance between accuracy and economy. Automatic time stepping activates the ANSYS program's bisection feature. Bisection provides a means of automatically recovering from a convergence failure. This feature will cut a time step size in half whenever equilibrium iterations fail to converge and automatically restart from the last converged substep. If the halved time step again fails to converge, bisection will again cut the time step size and restart, continuing the process until convergence is achieved or until the specified minimum time step size is reached.

3.3.8 Meshing

In nonlinear structural analyses, better accuracy at less expense will be usually obtained if a fine mesh of these linear elements is used rather than a comparable coarse mesh of quadratic elements. Automatic meshing is a huge improvement over direct generation of nodes and elements, but it can sometimes be computationally time consuming. If the

model contains repetitive features, it might be found that the most efficient approach to model generation would be to model and mesh a pattern region of the model, then generate copies of that meshed region. Before meshing the model, and even before building the model, it is important to think about whether a free mesh or a mapped mesh is appropriate for the analyses.

A free mesh has no restrictions in terms of element shapes, and has no specified pattern applied to it. Compared to a free mesh, a mapped mesh is restricted in terms of the element shape it contains and the pattern of the mesh. A mapped area mesh contains either only quadrilateral or only triangular elements, while a mapped volume mesh contains only hexahedral or tetrahedral elements. In addition, a mapped mesh typically has a regular pattern, with obvious rows of elements. If this type of mesh is considered, the geometry as a series of fairly regular volumes and/or areas must be built that can accept a mapped mesh.

3.3.9 Solution Commands (SOLU)

The SOLUTION commands are used to set general analyses options. In the solution phase of the analyses, the computer takes over and solves the simultaneous set of equations that the finite element method generates. The results of the solution are nodal degree of freedom values, which form the primary solution and derived values, which form the element solution.

The primary objective of a finite element analyses is to examine how a structure or component responds to certain loading conditions. Specifying the proper loading conditions is, therefore, a key step in the analyses. The loads can be applied on the model in a variety of ways in the ANSYS program. With the help of load step options, it can be controlled how the loads are actually used during solution.

Load categories in structural analyses of the models are applied into these conditions:

- A degree of freedom (DOF) constraint fixes a degree of freedom to a known value, i.e. specified displacements and symmetry boundary conditions

- A force is a concentrated load applied at a node in the model i.e. forces and moments.
- A surface load is a distributed load applied over a surface. Examples are pressures in a structural analyses.

In the solution phase of an analyses, the computer takes over and solves the simultaneous set of equations that the finite element method generates. The results of the solution are: nodal degree of freedom values, which form the primary solution and derived values, which form the element solution.

ANSYS employs the "Newton-Raphson" approach to solve nonlinear problems. In this approach, the load is subdivided into a series of load increments. The load increments can be applied over several load steps. Before each solution, the Newton-Raphson method evaluates the out-of-balance load vector, which is the difference between the restoring forces (the loads corresponding to the element stresses) and the applied loads.

The program then performs a linear solution, using the out-of-balance loads, and checks for convergence. If convergence criteria are not satisfied, the out-of-balance load vector is reevaluated, the stiffness matrix is updated, and a new solution is obtained. This iterative procedure continues until the problem converges. A number of convergence-enhancement and recovery features, such as line search, automatic load stepping, and bisection, can be activated to help the problem to converge. If convergence cannot be achieved, then the program attempts to solve with a smaller load increment. In some nonlinear static analyses, if the Newton-Raphson method is used alone, the tangent stiffness matrix may become singular (or non-unique), causing severe convergence difficulties. For such situations, you can activate an alternative iteration scheme, the arc-length method, to help avoid bifurcation points and track unloading. The arc-length method causes the Newton-Raphson equilibrium iterations to converge along an arc, thereby often preventing divergence, even when the slope of the load vs. deflection curve becomes zero or negative. The ANSYS program gives a number of choices when convergence criteria is designated: convergence checking on forces, moments, displacements, or rotations, or on any combination of these items. Additionally, each item can have a different convergence tolerance value. For multiple-degree-of-freedom problems, it also has a choice of convergence norms.

3.3.10 Postprocessor Commands

Postprocessing means reviewing the results of an analyses. It is probably the most important step in the analyses, because it is very important to understand how the applied loads affect your design, how good your finite element mesh is, how high are the stresses in this region and so on. Two postprocessors are available to review your results: POST1, the general postprocessor, and POST26, the time-history postprocessor. POST1 allows you to review the results over the entire model at specific load steps and substeps (or at specific time-points or frequencies).

Use POST1, the general postprocessor, to review analyses results over the entire model, or selected portions of the model, for a specifically defined combination of loads at a single time (or frequency). POST1 has many capabilities, ranging from simple graphics displays and tabular listings to more complex data manipulations such as load case combinations. Once the desired results data stored in the database can be reviewed through graphics displays and tabular command. Graphics displays are perhaps the most effective way to review results such as: contour displays, deformed shape displays, and reaction force displays.

Contour displays show how a result item such as stress varies over the model. Four commands are available for contour displays, as follows: nodal solution, element solution, element table and line element table. The nodal solution command produces contour lines that are continuous across the entire model. Derived solution data, which are typically discontinuous from element to element, are averaged at the nodes so that continuous contour lines can be displayed. The element solution command produce contour lines that are discontinuous across element boundaries. The nodal and element solution command can be used to produce contour line such as von Mises equivalent stresses and strains (EQV).

Deformed shape displays can be used in a structural analyses to see how the structure has deformed under the applied loads. Deformed shape can be superimposed over undeformed shape. If load symbols in POST1 turned on, the resulting display will show the loads on the deformed shape.

POST1 can be used for listing reaction loads and applied loads at constrained nodes in the selected set except for any zero values. Listing reaction loads and applied loads is a good way to check equilibrium. It is always good practice to check a model's equilibrium after solution. That is, the sum of the applied loads in a given direction should equal the sum of the reactions in that direction. The presence of coupling or constraint equations can induce either an actual or apparent loss of equilibrium. Actual loss of load balance can occur for poorly specified couplings or constraint equations (an usually undesirable effect).

POST 26 commands as the time-history postprocessor is used to review analyses results at specific locations in the model as a function of time, frequency, or some other change in the analyses parameters that can be related to time. In this mode, results data were processed in many ways, such as constructed graphics displays, chart representations or tabular listings, or performed math operations on the data sets. A typical time-history task has been to graph force versus deflection in a non-linear structural analyses.

The time-history operations deal with variables, tables of result item versus time. The result item may be the UX, UY or UZ displacement at a node, the force developed at a node, the stress in an element, etc. By default, results data for shell elements are assumed to be at the top surface of the shell or layer. The "Graph Data" button in the variable viewer allows to plot all the selected variables. The variable viewer stores all the time points available on the results file. A portion of this data can be displayed by selecting a range for the X-axis value.

3.4 Finite Element Model

The proper use of finite element model may provide a viable procedure to the basis for justifying a connection configuration for steel frame design use. A finite element approach is the appropriate solution to examine this possibility and the results compared to results from several tests conducted by different authors.

Several connection components are modeled to achieve the following aims:

1. Examine the precision of the mechanical model for both steel and concrete and suitability of their application in the ANSYS programme.
2. Check the applicability of the selections for finite element analyses such as element types, mesh generation, loading and solutions.
3. Investigate the behaviour of some well known connections which are tested by other researchers, so that reliability of the modeling in the present work can be verified.
4. Finally, based on the above work, standardization of FEA techniques with development of the models using application of high strength and stainless steel material properties can be completed.

In lieu of an exhaustive discussion of all validation tests performed, eight representative cases are described to demonstrate the accuracy of finite element modeling. Specimen brief details and results are reported here.

A finite element analyses program ANSYS was used to develop the 3D computer modelling of steel bolted connections. In order to model the prototype connection, the finite element program should include the effects of material and geometric non-linearity, residual stresses, and local buckling. The boundary conditions and element types considered to develop finite element model explained in the following sections.

3.4.1 SLB model

The SLB connection consists of middle-plate, four side-plates and bolt. Figure 3.19 is a FE model of the four-member splice lap bolted connection with double shear boundary condition. The middle-plate (plate A) of the connection with length (L), left end width (W), right end width (b) and thickness (t_p) has the hole diameter (d_o) in which the centre is located at a distance from the right end (e_1) and a distance from the bottom end (e_2). The middle-plate is adjoined to the other two side-plates (plate B) and clamped by two side-plates (plate C) by bolts with diameter (ϕ), where the thickness of the middle-plates

equals t_p and the side-plate equals t_p . In actual engineering applications, there always exists a clearance (k) between the bolt and the hole. Both middle- and side-plates are subjected to a uniform tension, s , which is far from the bolt. The friction between bolts and plates, side-plates and the middle plate, and side-plates were considered.

Plates are considered using solid elements SOLID45. Bolt head, shank and nut are idealized using eight-node isoparametric solid elements, i.e. SOLID185, that has mixed formulation capability for simulating deformations of nearly incompressible elastoplastic materials. The interactions between plates and side plates and also between bolt hole and bolt shank are simulated by 3D surface-to-surface contact pair element i.e. TARGET170 and CONTA173 elements. The bolt head and nut are modelled as hexagons, whilst the shank is modelled as cylinder with solid elements. Interface element is considered to accommodate the effect of friction between the plates. The interface elements connect the surface at the hole of the plate to corresponding surface at the bolt shank. A high contact stiffness was specified to prevent excessive penetration of the contact nodes. It is important to provide a bolt model that satisfies the overall deformation whilst using a small number of elements in its construction.

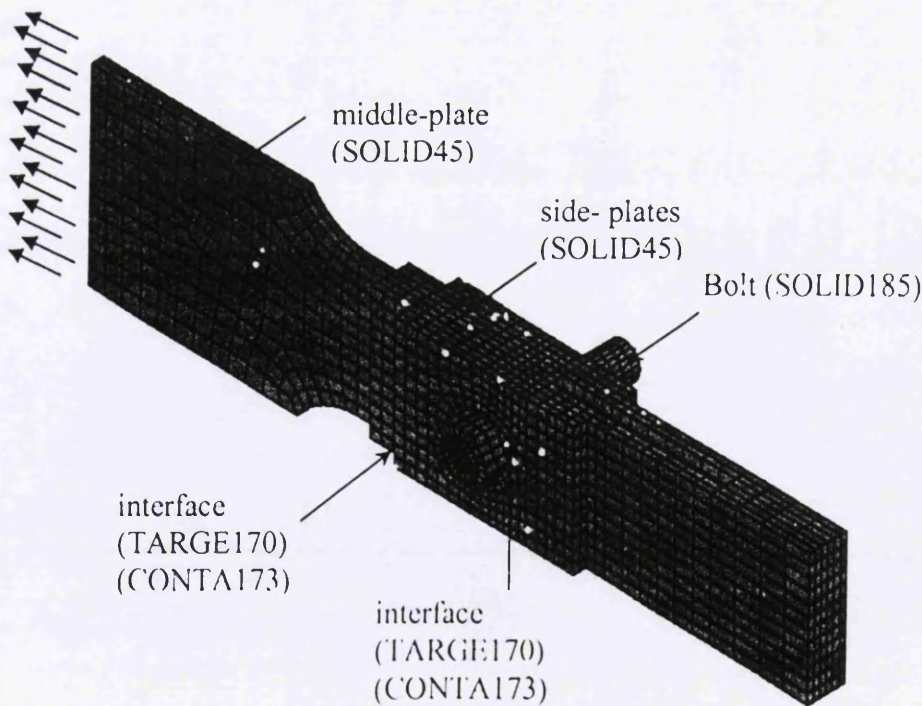


Figure 3.19 Finite element model of the splice lap bolted connection

3.4.2 DWA model

The DWA connection is built with beam web bolted to the column flange with double web angle. Non linear DWA connection model is symmetric about the centre of the beam web and no lateral displacement is assumed, so only one side of the plane of symmetry is modelled. The geometry of the model now represents one half of the full scale connection in the terms of area and moment of inertia, so the capacity of the connection model is only a half that of the actual load capacity. Symmetrical boundary condition is applied along beam web and column web.

The beam and column is modelled by SHELL143. The angle is simplified by SHELL143 element with no fillet. The bolt head and nut are modelled as hexagon solid element, SOLID185. There is no contact between bolt shank with bolt hole, therefore bolt shank is modelled using spar element, LINK8, instead of solid element, connecting the farthest corner nodes of head and nut to each other, as shown in Figure 3.20. The effective area of the bolt is split one twelfth equally among the spar elements. The bolt holes are modelled as circular. Bolt pretension caused by bolt tightening is simulated by applying equivalent initial strains for bolt shank elements. Since the bolt is tightened, the head and/or nut stay in close contact with their connecting angles and flanges, therefore the bolt share their nodes with the plate ones.

Interface element is considered to accommodate the effect of friction and slip. Friction coefficient value of 0.25 is used to capture experimental response and previous FE modelling [73]. The contact element is modelled as shown in Figure 3.21. The model of interface element is designated as an initial gap 0.5mm line of 3D node to node contact element CONTA178. The element is defined by two nodes, two stiffnesses, an initial gap or interference and an initial element status. The interface elements connect the nodes at the back of the angles to corresponding nodes at the column and beam flange and/or web. The normal stiffness value and sticking stiffness value are based upon the maximum expected force divided by the maximum allowable surface displacement. A high contact stiffness was specified to prevent excessive penetration of the contact nodes. Trilinear elastic-plastic approach is used to determine the material properties of mild carbon steel for the FE model.

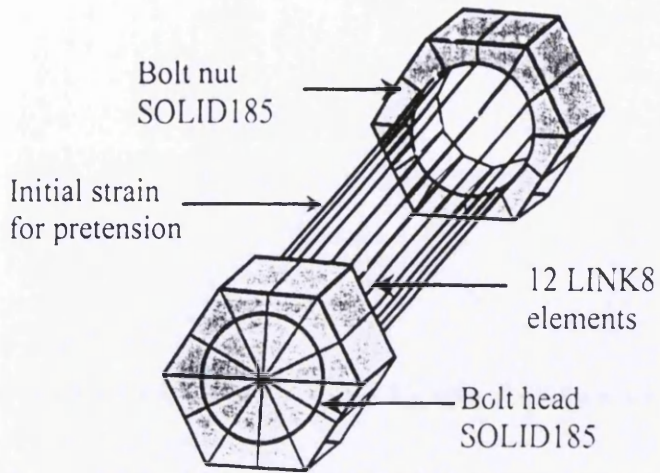


Figure 3.20 Finite element model of bolt

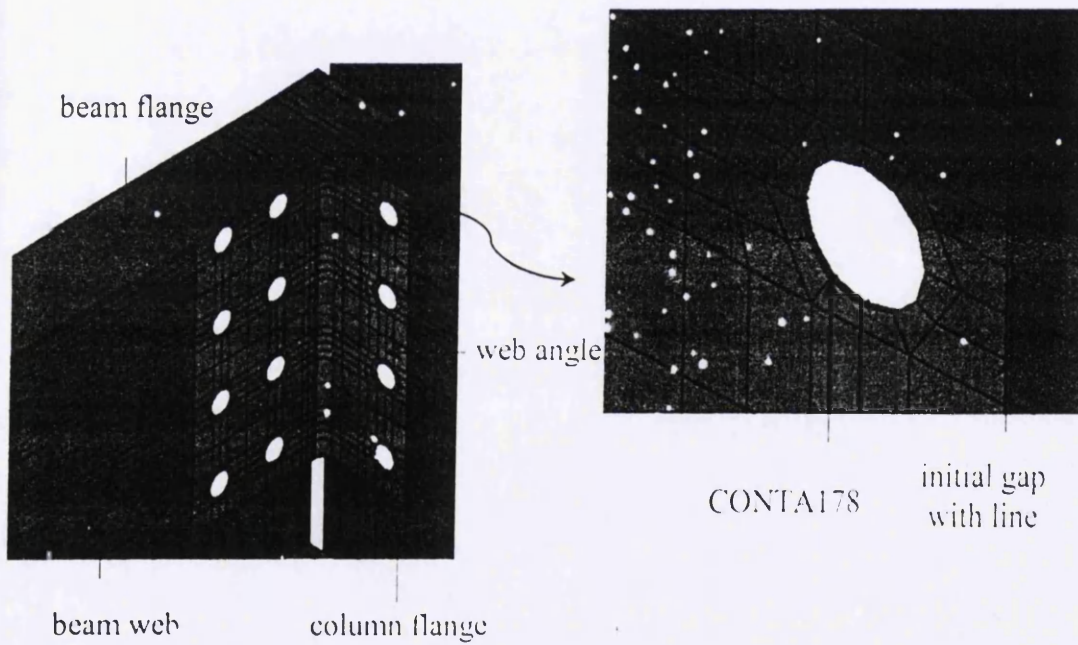


Figure 3.21 Contact element modelling of the DWA connection

3.4.3 TSA model

The TSA connection is built with beam flange and column flange bolted to top and seat angle cleats. Non linear TSA connections model are symmetric about the centre of the beam web and no lateral displacement is assumed, so only one side of the plane of symmetry is modelled. The geometry of the model now represents one half of the full scale connection in the terms of area and moment of inertia, so the capacity of the connection model is only a half of the actual load capacity.

The beam and column are modelled by SHELL143 elements. The angles are simplified by SHELL143 elements with radiused corner. The bolt head and nut are modelled as hexagon solid elements, SOLID185. The bolt shank is modelled using spar elements, LINK8, connecting the farthest corner nodes of head and nut to each other, as shown in Figure 3.20. The effective area of the bolt is split one twelfth equally among the spar elements. The bolt holes are modelled as circular. Bolt pretension caused by bolt tightening is simulated by applying equivalent initial strains for bolt shank elements. Since the bolt is tightened, the head and/or nut stay in close contact with their connecting angles and flanges, therefore the bolt share their nodes with the plate ones.

Interface element is considered to accommodate the effect of friction and slip. Friction coefficient value of 0.25 is used to capture experimental response and previous FE modelling [72]. The contact element is modelled as shown in Figure 3.22. The model of interface element is designated as an initial gap 0.5mm line of 3D node to node contact element using CONTA178. The element is defined by two nodes, two stiffness, an initial gap or interference and an initial element status. The interface elements connect the nodes at the back of the angles to corresponding nodes at the column and beam flange. The normal stiffness value and sticking stiffness value are based upon the maximum expected force divided by the maximum allowable surface displacement. A high contact stiffness was specified to prevent excessive penetration of the contact nodes. Trilinear elastic-plastic approach is used to determine the material properties of mild carbon steel for the FE model.

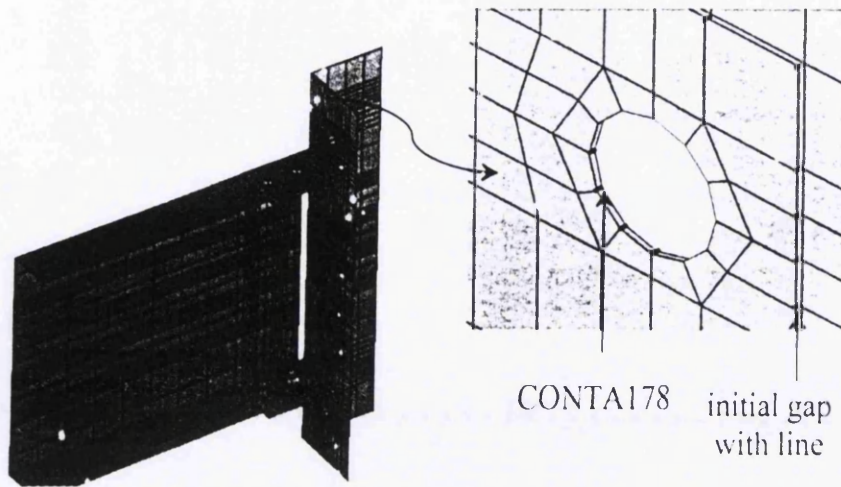


Figure 3.22 Contact element on the TSA connection

3.4.4 TSAW model

The TSAW model is built from TSA with double web angle. The Non linear TSAW connection model is symmetric about the centre of the beam web and double web angles, that no lateral displacement is assumed, so only one side of the plane of symmetry is modelled. The geometry of the model now represents one half of the full scale connection in the terms of area and moment of inertia, so the capacity of the connection model is only a half of the actual load capacity. Plastic shell elements, SHELL143, are used to model beam, column and angles. Bolt head and nut are idealized using eight-node isoparametric solid elements, i.e. SOLID45.

Bolt shank is modelled using six 3D spar element of LINK8 elements. The interactions between angle and column or beam are simulated by CONTA178 elements. Shell element was considered more appropriate for beam, column and angle elements because it can provide a more efficient geometry modelling and analyses. The top and seat angle cleats are modelled as half portion of angle connected beam flange and column flange as shown in Figure 3.22. The double web angles are modelled as single angle

connected beam web and column flange as shown in Figure 3.23. The bolt shank is modelled using spar element connecting the farthest corner nodes of head and nut to each other. The effective area of the bolt is split one twelfth equally among the spar elements. Bolt pretension caused by bolt tightening is simulated by applying equivalent initial strains for bolt shank elements. Since the bolt is tightened, the head and/or nut stay in close contact with their connecting angles and flanges, therefore the bolt share their nodes with the plate ones.

Interface element is considered to accommodate the effect of friction and slip. Friction coefficient value is used to capture experimental response and previous FE modelling. The model of the interface element is modeled as a line of 3D point to point contact elements with coincident nodes. The interface elements connect the nodes at the back of the angles to corresponding nodes at the column flange and beam web. The TSAW model is shown on Figure 3.24.

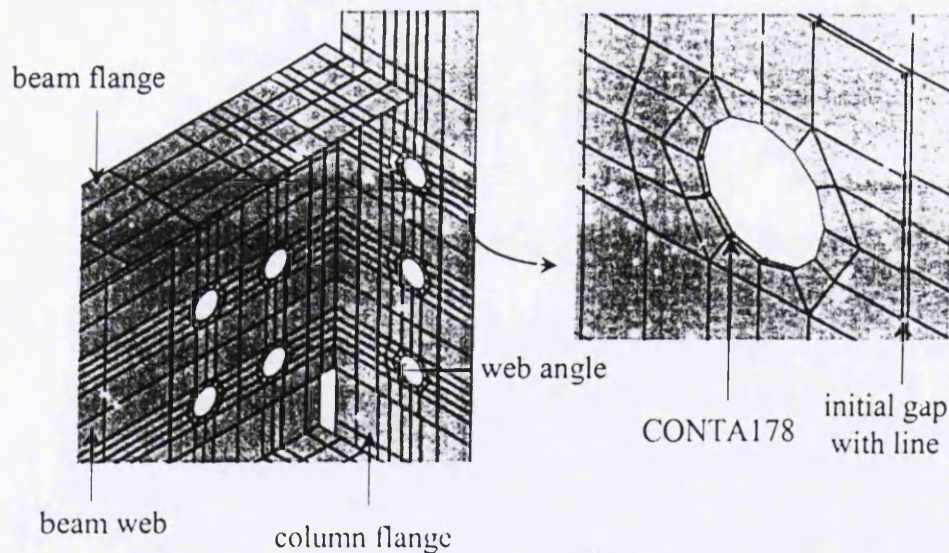


Figure 3.23: Modelling of contact element of web angle

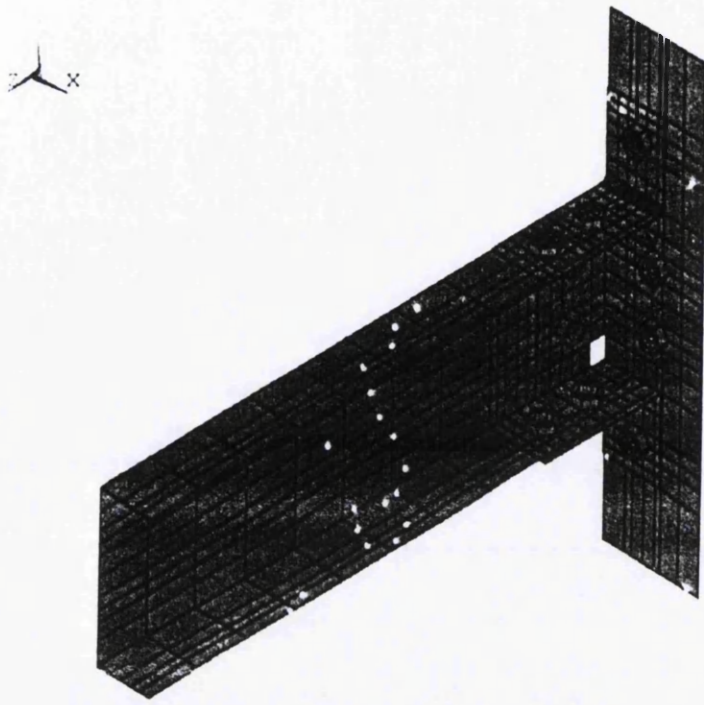


Figure 3.24: Modelling of TSAW connection

3.4.5 FEP and EPTB model

The flush endplate (FEP) connection is built with beam welded to the endplate and bolted through column flange. Non linear flush endplate connection model is symmetric about the centre of the beam web and no lateral displacement is assumed, so only one side of the plane of symmetry is modelled. The geometry of the model now represents one half of the full scale connection in the terms of area and moment of inertia, so the capacity of the connection model is only a half of the actual load capacity. A symmetry boundary condition applied accordingly to reduce the size of the model. Similar model is applied to EPTB connection with I-section beam is replaced with hollow section beam. The end plate is welded to the hollow section beam and bolted to the column flange.

Three dimensional eight-node structural solid elements, SOLID45, are used to model beam, column and plate. Bolt head, shank and nut are idealized using eight-node isoparametric solid elements, i.e. SOLID185 elements. The interactions between plate and column are simulated by 3D node-to-node contact element i.e. CONTA178 elements.

The PRETS179 pretension element is used for model preload in bolts. The material behaviour for all the elements was described by multi-linear stress-strain curves.

The bolt head and nut are modelled as hexagons, whilst the shank is modelled as cylinder with solid elements, SOLID185 elements. Bolt pretension caused by bolt tightening is simulated by applying pretension. Interface element is considered to accommodate the effect of prying forces. The interface elements connect the nodes at the back of the plate to corresponding nodes at the column flange. A high contact stiffness was specified to prevent excessive penetration of the contact nodes. It is important to provide a bolt model that satisfies the overall deformation whilst using a small number of elements in its construction. Figure 3.25 indicates the finite element modelling configuration used.

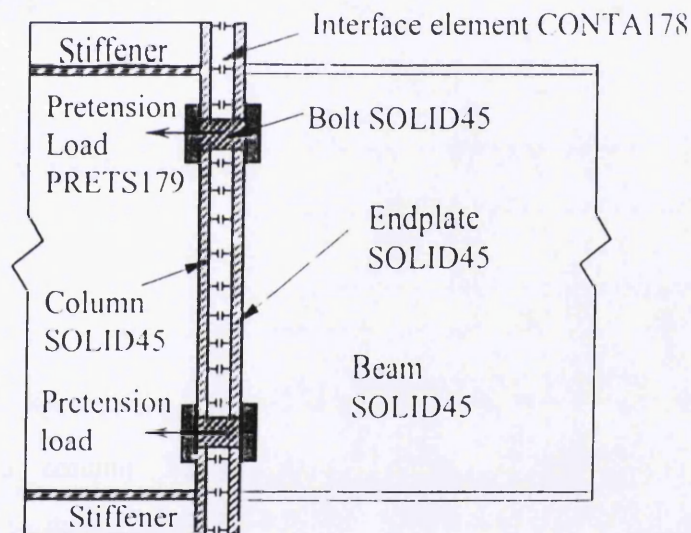


Figure 3.25 FE modelling configuration of FEP connection

In order to minimise the complexity of the model, simplified approach model has been introduced with shell elements. The beam, column and endplate are modelled using SHELL143 elements, whilst the solid bolt shanks are simplified with LINK8 elements. Non linear flush endplate connection model is symmetric about the centre of the beam web and no lateral displacement is assumed, so only one side of the plane of symmetry is modelled. Simplified model of FEP connection is shown on Figure 3.26. By replacing the

solid elements with shell elements the number of degrees of freedom was approximately halved. As a consequence the size of the model was reduced significantly.

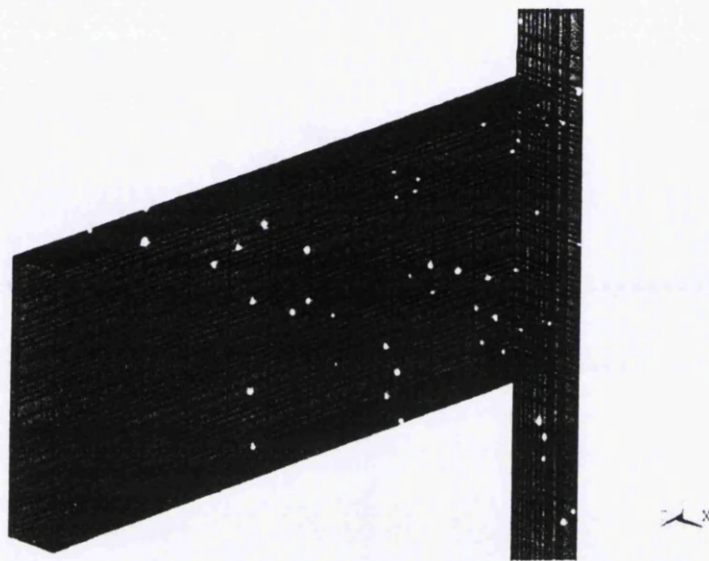


Figure 3.26: Simplified model of FEP connection

3.4.6 SCC model

The following ANSYS element types are used for only one half of an entire SCC connection on internal column. 3D 4-node plastic small strain shell elements, i.e. SHELL143, are used to model beam, column and plate. Bolt head, shank and nut are idealized using 8-node solid elements, i.e. SOLID185 elements. The interactions between plate and column are simulated by 3D node-to-node contact element i.e. CONTA178 elements. The LINK8 elements are used for model spar and preload in bolts. The SOLID65, 3-D reinforced concrete solid element, is used for model concrete slab. The LINK8 elements also are used to model the reinforcement as well as shear studs. The material behaviour for all the elements is described by multi-linear stress-strain curves.

Non linear flush endplate connection model with concrete slab is symmetric about the centre of the column web and no lateral displacement is assumed, so only one side of the plane of symmetry is modeled. A symmetry boundary condition applied accordingly

to reduce the size of the model. The bolt head and nut are modeled as hexagon solid element. The bolt shank is modeled using spar element connecting the farthest corner nodes of head and nut to each other. The effective area of the bolt is split one twelfth equally among the spar elements. The bolt holes are modeled as circular. Bolt pretension caused by bolt tightening is simulated by applying equivalent initial strains for bolt shank elements. Since the bolt is tightened, the head and/or nut stay in close contact with their connecting angles and flanges, therefore the bolt share their nodes with the plate ones.

Interface element is considered to accommodate the effect of contact between end plate and column flange. Friction coefficient value of 0.25 is used to capture experimental response and previous FE modelling. Figure 3.27 indicates a schema of the finite element configuration model used. The model of interface element is designated as an initial gap of 3D node to node contact element. The interface elements connect the nodes at the back of the endplate to corresponding nodes at the column and beam flange and/or web. The normal stiffness value and sticking stiffness value are based upon the maximum expected force divided by the maximum allowable surface displacement.

Bolt pretension caused by bolt tightening is simulated by applying initial strain. Interface element is considered to accommodate the effect of prying forces. The interface elements connect the nodes at the back of the plate to corresponding nodes at the column flange. A high contact stiffness was specified to prevent excessive penetration of the contact nodes. It is important to provide a bolt model that satisfies the overall deformation whilst using a small number of elements in its construction. The SCC model is symmetric about the centre of the column web and no lateral displacement is assumed, so only one side of the plane of symmetry is modelled. The point load is applied to the top of beam web at the beam end. The finite element model is shown in Figure 3.28.

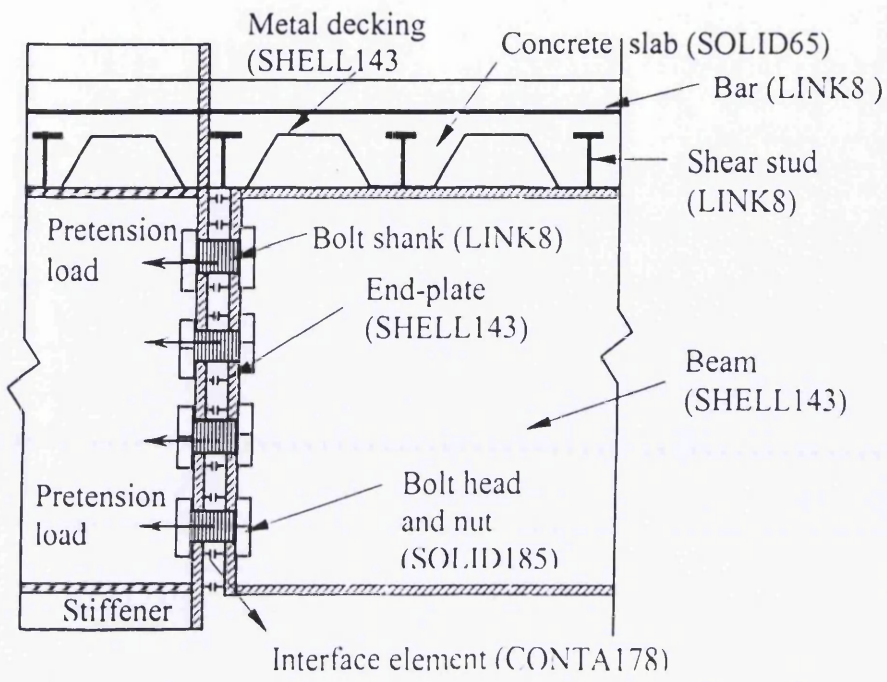


Figure 3.27 FE modelling configuration of the SCC connection

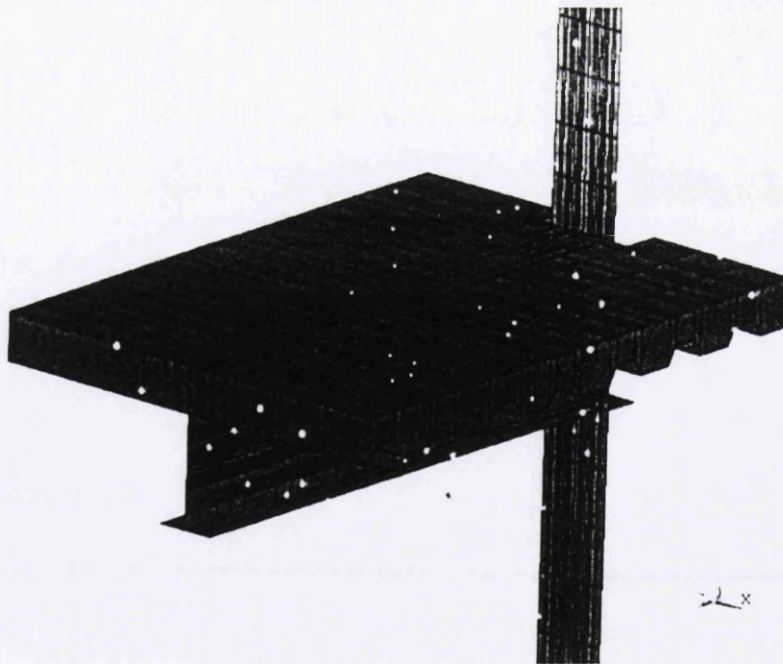


Figure 3.28 FE model of the SCC connection

3.5 Summary

Chapter 3 presented the concept of finite elements and the derivation of all expressions that were required to develop the firm understanding of finite element analyses. In addition, the constitutive model and the failure criteria for steel materials were given. The theoretical explanation of bolted connection modelling, which is employed in the ANSYS program, such as yield criterion, plasticity and hardening rules were presented in detail. From the study carried out, the following conclusions are drawn:

Experimental work demonstrates the actual behaviour of steel structures. On the other hand, experimental work is expensive and time consuming. Therefore, the finite element analyses method is an alternative method to predicting and simulating the actual behaviour of steel structures similar to the experimental work if a correct model and correct material properties of steel are employed. Three-dimensional modelling is the best to simulate steel bolted connection structures. However, it is very complicated to programme. As a result, finite element analyses software such as ANSYS should be employed for this task.

Modelling and analysing non-linear geometry and non-linear materials such as partially restrained structures with the simulation of bolt action and contact behaviour is very difficult in finite element analyses. Therefore, an appropriate element should be selected from the proposed software that can best predict the deformation mode of bolted connection elements and can develop the excessive deformation behaviour in steel. Consequently, the appropriate solid element that can best describe steel bolt is the hexahedral element that has eight nodes with three degrees of freedom along the x, y, z axis. On the other hand, the element that can best simplified describe the behaviour of the bolt shank is the three-dimensional spar element, which has two nodes with three degrees of freedom along the x, y, z axis. If the bolt is defined as solid element and bolt pretension is applied, therefore two elements will be used such as SOLID185 and PRETS179. In the present of simplified model used, spar element LINK8 can be used to model the bolt shank.

The appropriate solid element that can best describe beam, column, angle and plate in the actual behaviour is the hexahedral element that has eight nodes with three

degrees of freedom along the x, y, z axis. In order to minimise the complex of model, simplified approach model has been introduced with shell elements. The beam, column and endplate are modelled using SHELL143 elements. By replacing the solid elements with shell elements the number of degrees of freedom was approximately halved. As a consequence the size of the model was reduced significantly. The non linear partially restrained connection model is symmetric about the centre of the beam web and no lateral displacement is assumed, so only one side of the plane of symmetry is modelled. This FE model with a symmetry boundary condition has reduced the number of elements required by a half.

Chapter 4

Validation of Finite Element Modelling Procedure

4.1 Introduction

Since the introduction of steel materials, many experimental investigations have been conducted to understand the behaviour of steel structures under various conditions. The experimental investigations are time consuming and the materials used in those experiments are quite costly. Finite element analysis is an engineering tool developed to simulate the behaviour of various materials. Therefore, nonlinear finite element analysis can realistically predict the behaviour of steel structures and assess the performance of existing steel beam-column connection structure under various load conditions. However, the accomplishment of this method was also time consuming due to the lack of knowledge and lack of suitable computer software and hardware. In recent years, the evolution of finite element analysis has reached its peak as both computer software and hardware became more reliable. Finite element analysis is the recommended method to

analyse steel connection by using computer software because it is fast and extremely cost effective.

At this time, despite the sophisticated technology of computer software, characterizing the steel bolted connection properties to finite elements is an obstructing and challenging point due to the complexity of the contact element matrix of the connection. Once these obstacles are overcome, design and analysis of bolted connection structures using finite elements and computers will be effortless and produce reliable results. In previous chapters, the finite element modelling of the bolted connection have been investigated and presented. In this chapter a validation of the finite element model will be presented by using other researchers' data and results. Furthermore, a parametrical study on the proposed finite element of bolted connection modelling will be conducted by using different section properties and different connection configurations.

4.2 Validation of Finite Element Model

The external monotonic static point load is applied in increments to obtain a converged solution to a nonlinear analysis. The convergence criteria is based on the force and displacement for tracking the maximum plastic strain step. The deformation measurement is based on the deformation of the angle. The relative displacements at the locations of the beam tension and compression flanges were used to calculate the rotation of a connection. The rotation of connection is defined as relative horizontal displacement over the depth of the beam measured from the centre of top flange to the centre of bottom flange. The most important aspect of PR connection behaviour is the moment-rotation ($M-\theta$) relationship. The stiffer the connection the higher is the $M-\theta$ curve representing the behaviour of the connection. Double web angle connections represents flexible connections due to the geometry displacement of web angles, whilst top and seat angle connections represents flexible connections due to the geometry displacement of the top seat angle. Figure 4.1 presents the measurement of rotational angle change when load is applied. The geometry displacement of end plate is considered as the flexibility of the end plate connections as shown in Figure 4.2.

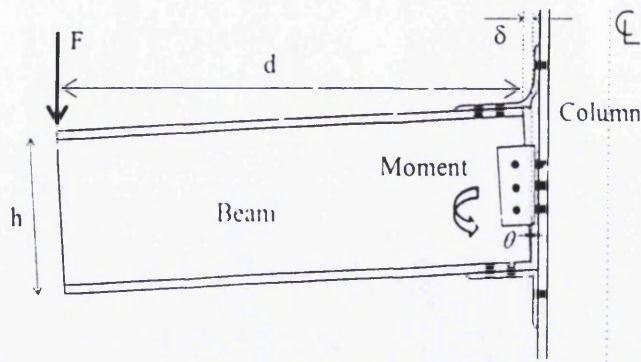


Fig. 4.1 Measurement of rotational angle change

The moment rotation curve of the connection is based on the simple relations: $M = Fd$, $\theta = \arctan(\delta/h)$; where M is the moment, θ is the rotation of the connection, F is twice as much as the applied point load, d is the length of the beam, δ is relative displacement of the beam and h is the depth of the beam measured from the centre of top flange to the centre of bottom flange.

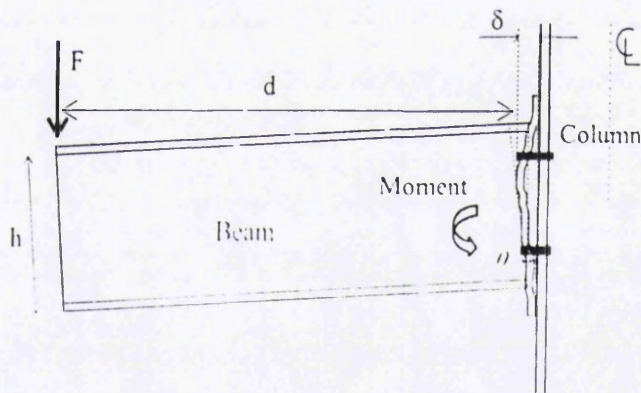


Fig. 4.2 Measurement of rotational endplate change

4.2.1 DWA connection

The results of FE analysis for the DWA connection are presented in comparison with the test results. Comparisons are made with experimental results obtained from reference [93]. The connection geometry is shown in Figures 4.3 and 4.4, and the connection parameter is depicted in Table 4.1. Beam and column for DWA1 and DWA2 are designated as W12x27 and W18x50 respectively. Bolt M19 grade 8.8 is used

gage on column is 63mm. The finite element models were validated against the recorded load-displacement curves from the tests. The analysis result of DWA connections is presented in Figures 4.5 and 4.6 for three and four row bolt configuration. The FE models show an ultimate moment of 22.4 KN.m and 49.6 KN.m, respectively. The $M-\theta$ curve shape of the DWA connections from experimental and theoretical results shows a difference due to a lack of material properties data from experimental testing. It assumed that stress-strain data for FEA with bi-linear elastic perfectly plastic approach.

Table 4.1
DWA connection parameter

| connection | beam | web angle (1) | web angle (2) | g (mm) | p (mm) |
|------------|--------|---------------|---------------|--------|--------|
| DWA1a | W12x27 | L-152x101x9.5 | L-152x101x9.5 | 63.0 | 76.0 |
| DWA2a | W18x50 | L-152x101x9.5 | L-152x101x9.5 | 63.0 | 76.0 |

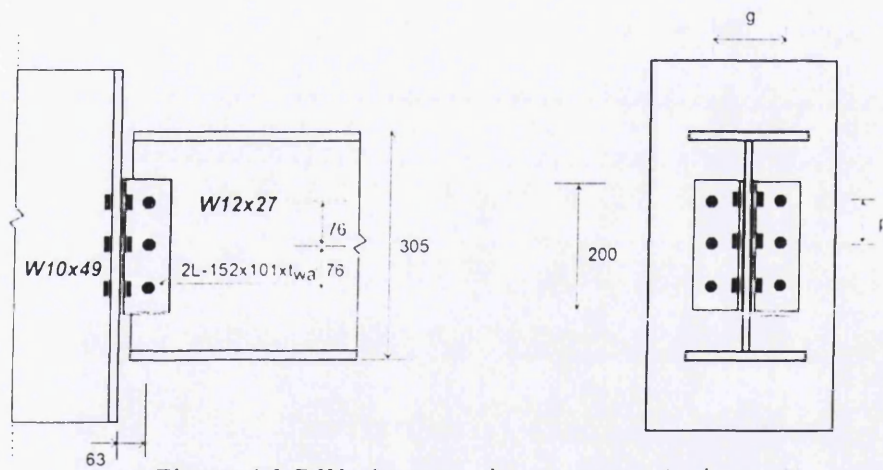


Figure 4.3 DWA1 connection geometry (unit: mm)

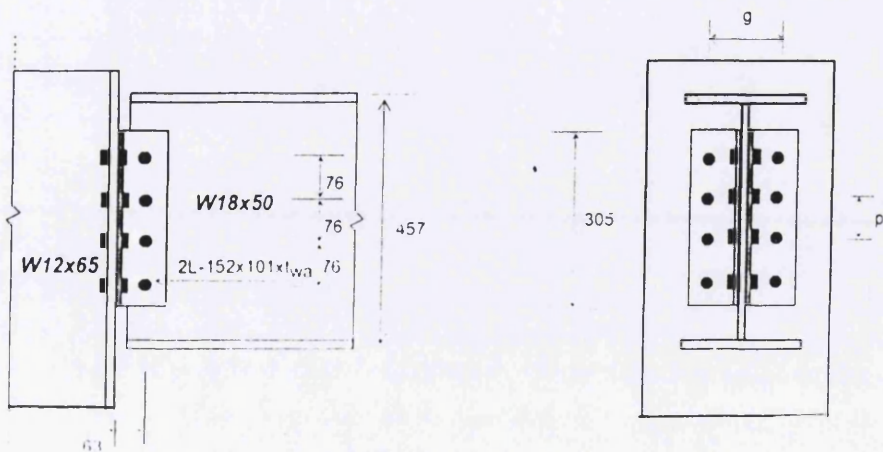


Figure 4.4 DWA2 connection geometry (unit: mm)

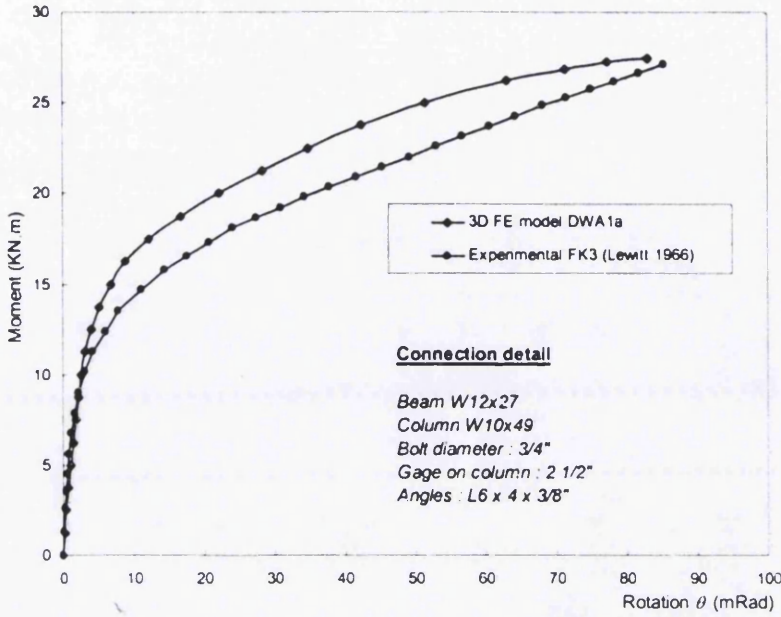


Figure 4.5 M-θ curves of DWA1a from experimental and FE models

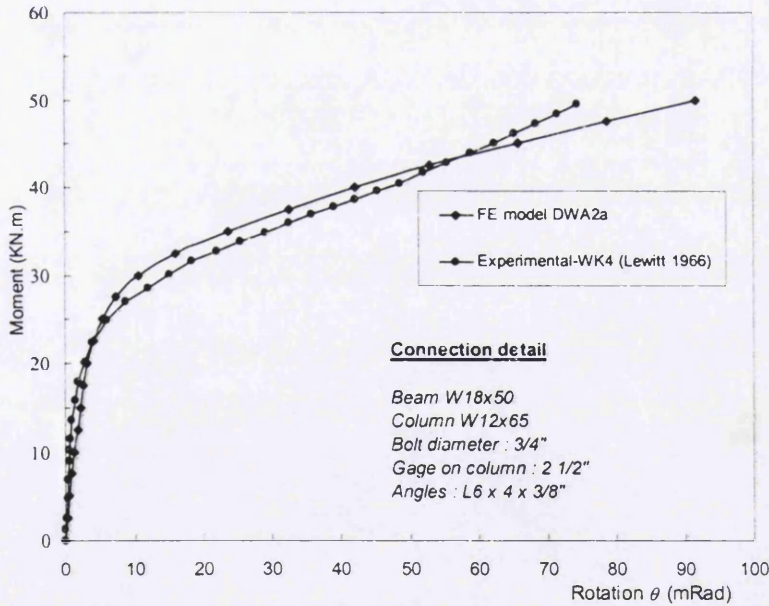


Figure 4.6 M-θ curves of DWA2a from experimental and FE models

The refined model with a circular hole and the shank with twelve spar elements gives a good prediction of connection behaviour. In order to investigate further the difference between the response of the connection with a hexagonal hole and a circular hole

response, the stress contours at the maximum capacity are shown. The maximum stress values are nearly the same at 456 MPa, since the hole area and shank cross section area are kept equal as illustrated in Figures 4.7 – 4.8.

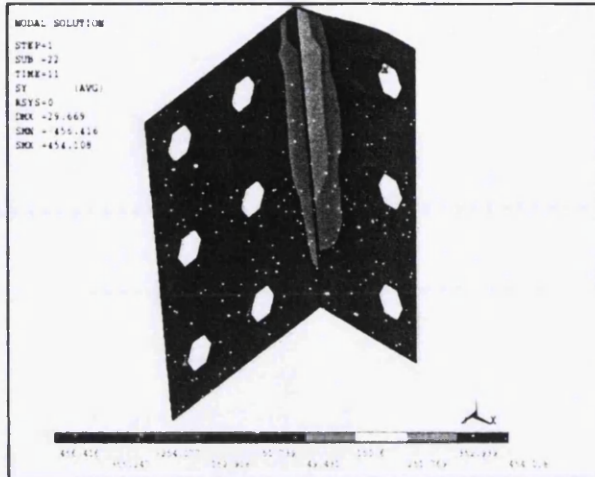


Figure 4.7 Maximum stress of the web angles with hexagonal holes: in MPa

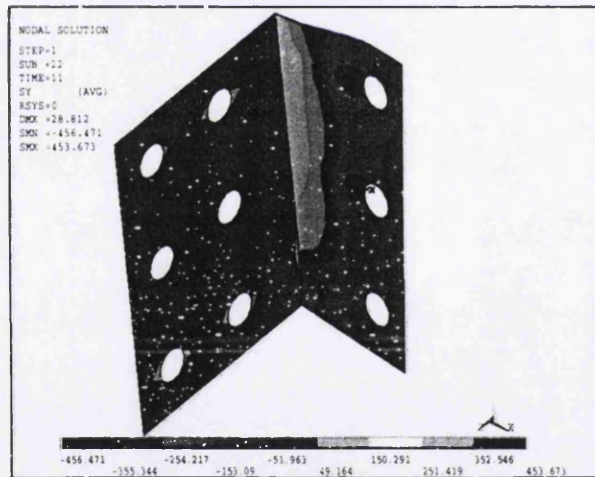


Figure 4.8 Maximum stress of the web angles with circular holes: in MPa

4.2.2 TSA connection

The FE analysis result of the TSA connection are presented in comparison with the test results. Comparisons are made with experimental results obtained from reference [16].

The connection geometry is shown in Figure 4.9, and the connection parameter is depicted in Table 4.2. Beam and column for TSA1 and TSA2 are designated as 457x191x67UB and 305x305x97UC, respectively. Bolt diameter is 20mm whilst bolt gauges on column are 50mm and 63mm, respectively. The finite element models were validated against the recorded load-displacement curves from the tests. The analysis results of TSA connections are presented in Figures 4.10 and 4.11. The FE models show ultimate moment of 115.2 KN.m, 98.3 KN.m, 120.4 KN.m and 114.2 KN.m, respectively.

Table 4.2
TSA connection parameter

| connection | beam | top angle | seat angle | g (mm) | p (mm) |
|------------|--------------|-------------|-------------|--------|--------|
| TSA1o | 457x191x67UB | L-150x90x10 | L-150x90x10 | 50.0 | 140.0 |
| TSA1a | 457x191x67UB | L-150x90x10 | L-150x90x10 | 63.0 | 140.0 |
| TSA2o | 457x191x67UB | L-150x90x12 | L-150x90x12 | 50.0 | 140.0 |
| TSA2a | 457x191x67UB | L-150x90x12 | L-150x90x12 | 63.0 | 140.0 |

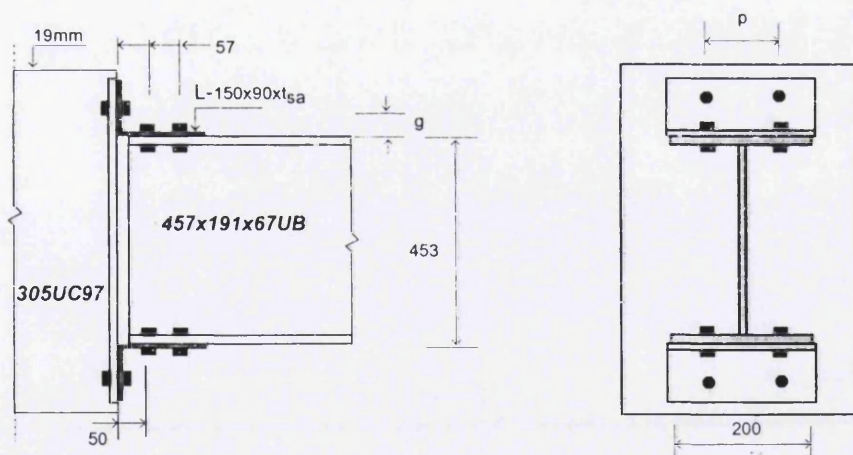


Figure 4.9 TSA connection geometry (unit: mm)

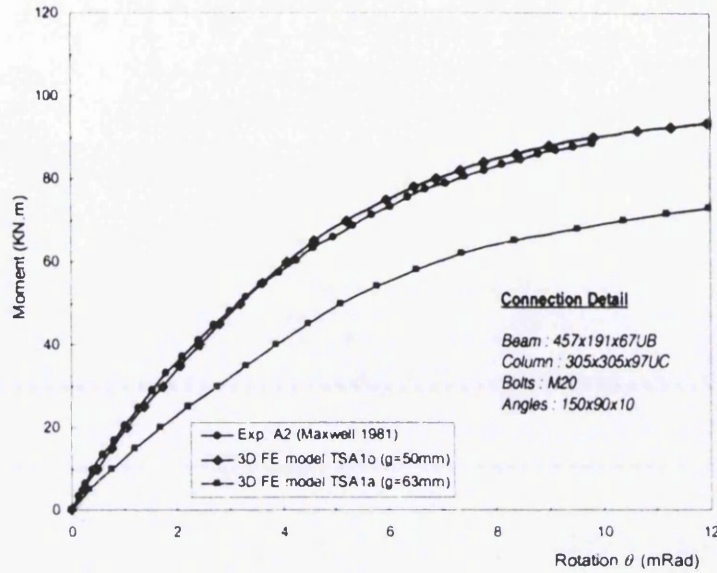


Fig. 4.10 Moment rotation curve of TSA1a from experimental and FE models

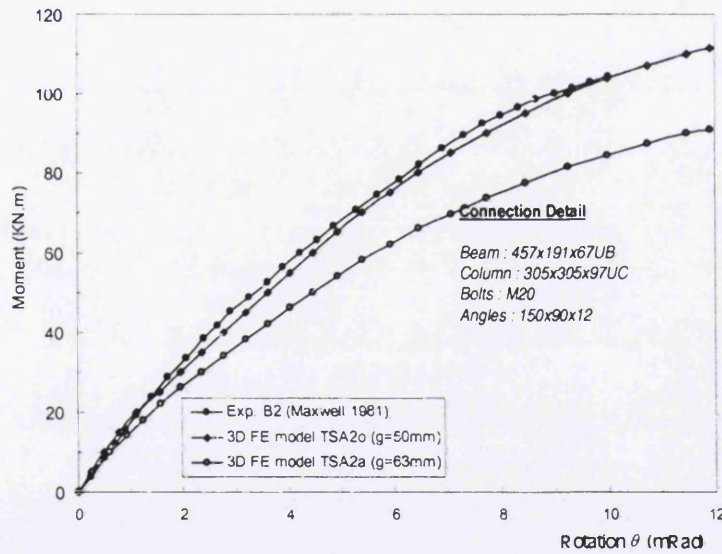


Fig. 4.11 Moment rotation curve of TSA2a from experimental and FE models

4.2.3 TSAW connection

The FE analysis result of the TSAW connection are presented in comparison with the test results. Comparisons are made with experimental results obtained from reference [32] and [72]. The connection geometry is shown in Figures 4.12 and 4.13, and the

connection parameter is detailed in Table 4.3. Beam and column for TSAW1a and TSAW1b are designated as W8x21 and W12x58 respectively, whilst W14x38 and W12x98 are used for TSAW1c. Gauge in leg on column flange (g) and bolt spacing on column flange (p) on top and seat (t & s) angle are 50.0mm and 89.0mm for TSAW1a and TSAW1b, and 63mm and 140mm for TSAW1c respectively. Bolt spacing on web angle is 76mm. The finite element models were validated against the recorded load-displacement curves from the tests. The initial stiffness and moment capacity are predicted well by the proposed model. The analysis result of TSAW connections is presented in Figures 4.14 to 4.17. The FE models show ultimate moment of 42.2 KN.m, 43.1 KN.m, 99.5 KN.m and 179.5 KN.m, respectively. The FE model with its deformed shape of the connection is presented in Figure 4.18.

Table 4.3
TSAW connection parameter

| connection | beam | t&s angle | web angle | g (mm) | p (mm) |
|------------|--------|---------------|---------------|----------|----------|
| TSAW1a | W8x21 | L-152x89x8.0 | 2L-101x89x6.3 | 50.0 | 89.0 |
| TSAW2a | W8x21 | L-152x89x9.5 | 2L-101x89x6.3 | 50.0 | 89.0 |
| TSAW3a | W14x38 | L-152x101x9.5 | 2L-101x89x6.3 | 63.0 | 140.0 |
| TSAW4a | W14x38 | L-152x101x16 | 2L-101x89x6.3 | 63.0 | 140.0 |

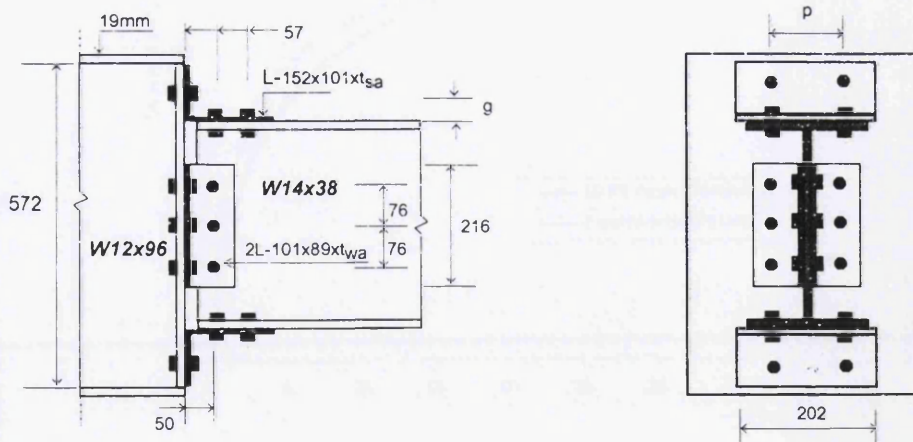


Figure 4.12 TSAW1 and TSAW2 connection geometry (unit: mm)

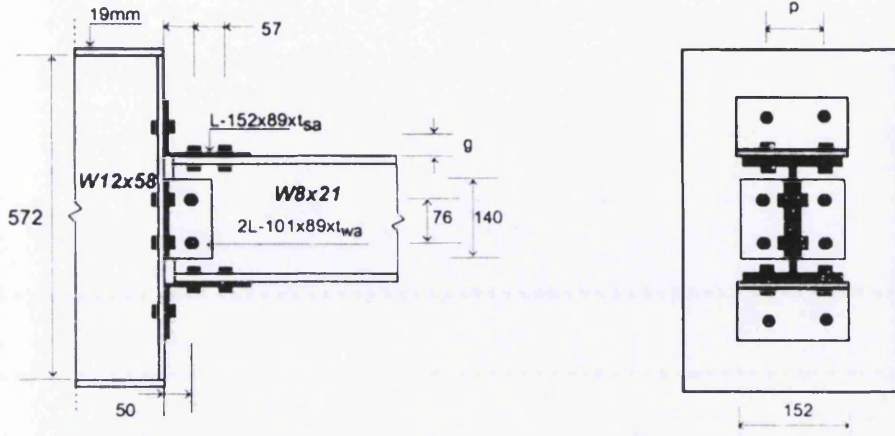


Figure 4.13 TSAW3 and TSAW4 connection geometry (unit: mm)

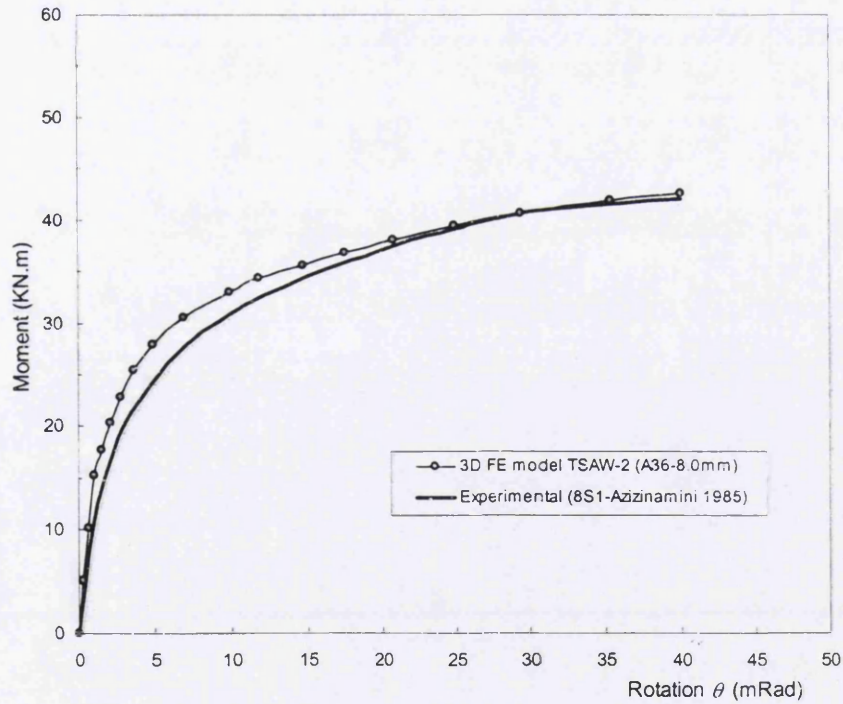


Figure 4.14 Validation of FE modelling against test result (TSAW-1a)

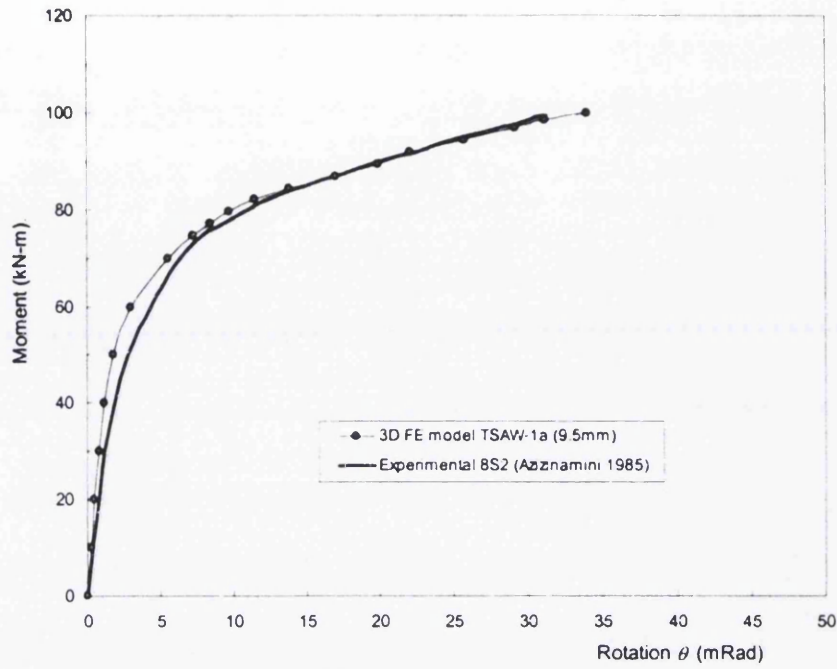


Figure 4.15 Validation of FE modelling against test result (TSAW-2a)

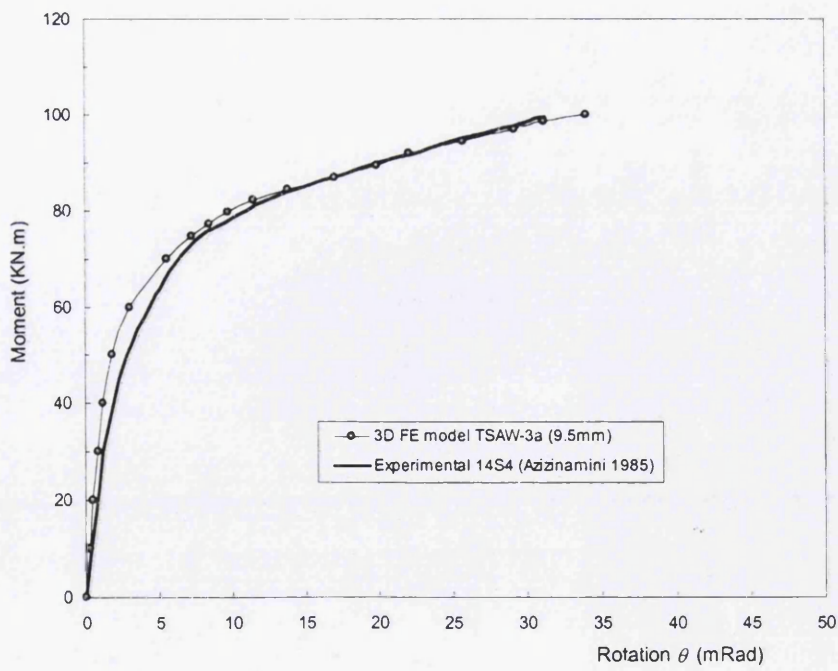


Figure 4.16 Validation of FE modelling against test result (TSAW-3a)

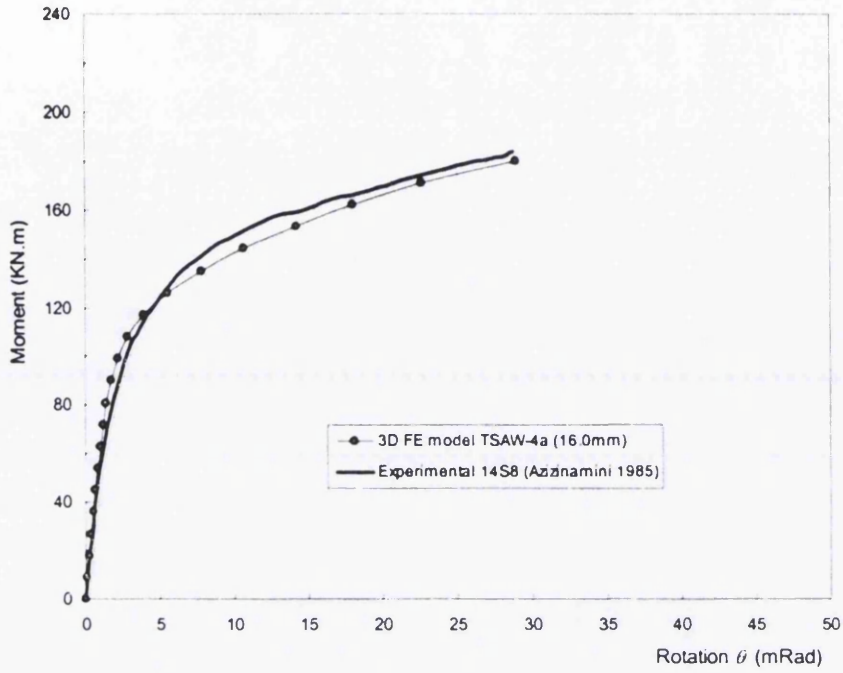


Figure 4.17 Validation of FE modelling against test result (TSAW-4a)

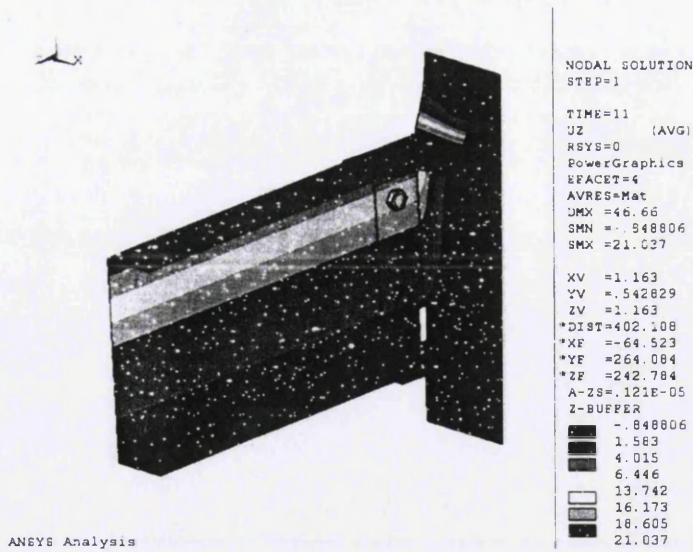


Figure 4.18 Deformed shape of the TSAW connection

4.2.4 FEP connection

The FE analysis results of the FEP connection are presented in comparison with the test results. Comparisons are made with experimental results obtained from reference [39], [40] and [41]. The connection geometry is shown in Figures 4.19 - 4.21, and the connection parameter is detailed in Table 4.4. Beam and column for FEP-1a are designated as IPE240 and HEA240, respectively, whilst 406x178x60UB and 254x254x73UC are used for FEP-2a, and HE320A and HE300M are used for FEP-3. Bolt gauge on column flange (g) and bolt spacing (p) are 50.0mm and 89.0mm for FEP-1, whilst 63mm and 140mm for FEP-2, 150mm and 140mm for FEP-3 respectively.

Table 4.4
FEP connection parameter

| connection | beam | endplate | bolt - grade | g (mm) | p (mm) |
|------------|--------------|-------------------------|--------------|--------|--------|
| FEP-1a | IPE240 | 268x160xt _{cp} | M20 – 10.9 | 98 | 158 |
| FEP-2a | 406x178x60UB | 460x200xt _{cp} | M24 – 8.8 | 90 | 286 |
| FEP-3a | HE320A | 360x300xt _{cp} | M24 – 8.8 | 150 | 160 |

Steel material properties for FE analysis is based on experimental data. All steel materials for connection used are S275, M24 bolts grade 8.8 and M20 bolts grade 10.1, except for FEP-3a using S355 column and beam, and S690 endplate as shown in Table 4.5.

Table 4.5
Material properties for FE model

| specimen | steel grade | σ_y (MPa) | σ_u (MPa) | σ_y / σ_u |
|-----------------|-------------|------------------|------------------|-----------------------|
| column (1-2) | S275 | 340 | 520 | 0.654 |
| beam (1-2) | S275 | 360 | 530 | 0.679 |
| column (3) | S355 | 450 | 580 | 0.776 |
| beam (3) | S355 | 450 | 580 | 0.776 |
| bolt (1) | Grade10.9 | 1010 | 1108 | 0.912 |
| bolt (2) | Grade 8.8 | 810 | 900 | 0.900 |
| bolt (3) | Grade 8.8 | 840 | 940 | 0.894 |
| end plate (1-2) | S275 | 380 | 540 | 0.704 |
| end plate (3) | S690 | 698 | 749 | 0.950 |

The finite element models were validated against the recorded load-displacement curves from the tests. A close correlation between the model and test was observed, with a good comparison of the stiffness and moment-rotation capacity. The analysis result of the FEP connections is presented in Figures 4.22 - 4.24. The FE models show ultimate moment of 87.2 KN.m, 166.5 KN.m, 130.5 KN.m and 210.0 KN.m, respectively. The FE model with its deformed shape of the connection is presented in Figure 4.25.

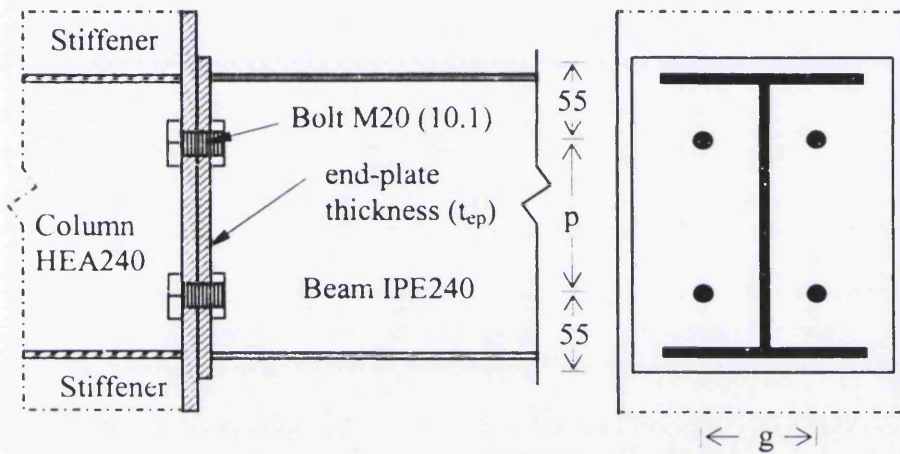


Figure 4.19 FE modelling configuration of the FEP-1 connection

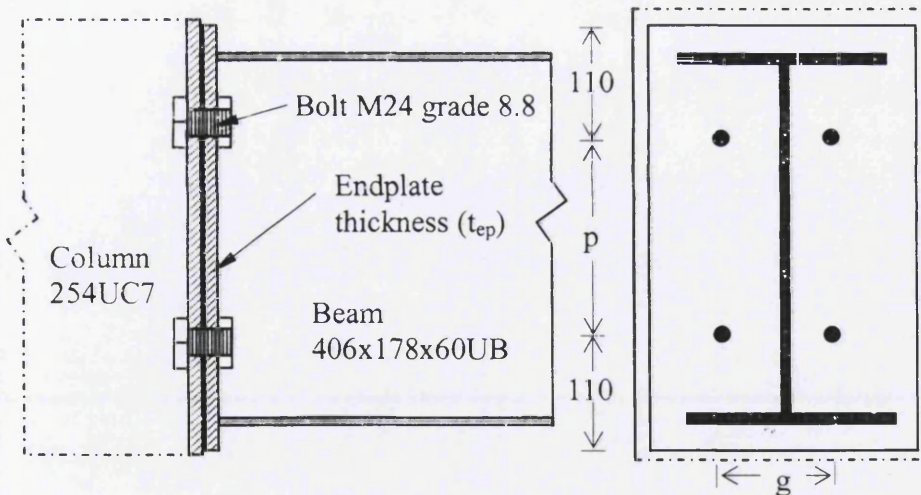


Figure 4.20 FE modelling configuration of the FEP-2 connection (unit: mm)

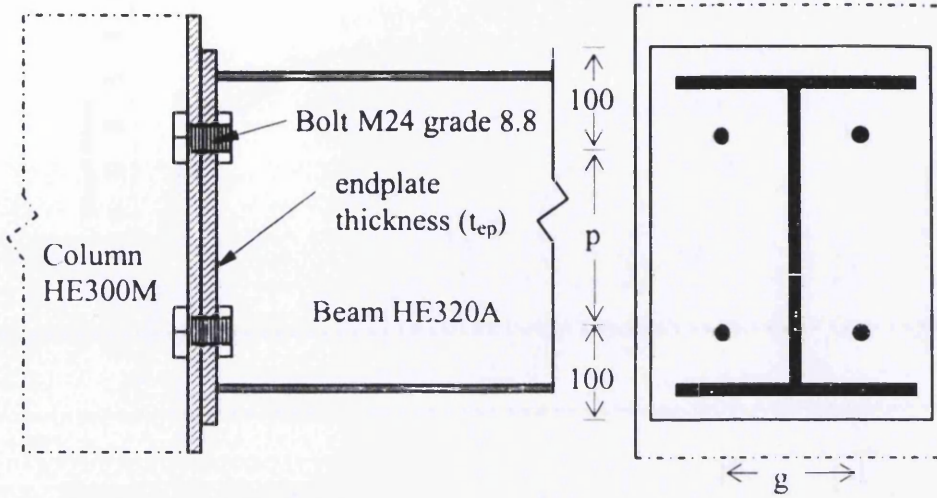


Figure 4.21 FE modelling configuration of the FEP-3 connection (unit: mm)

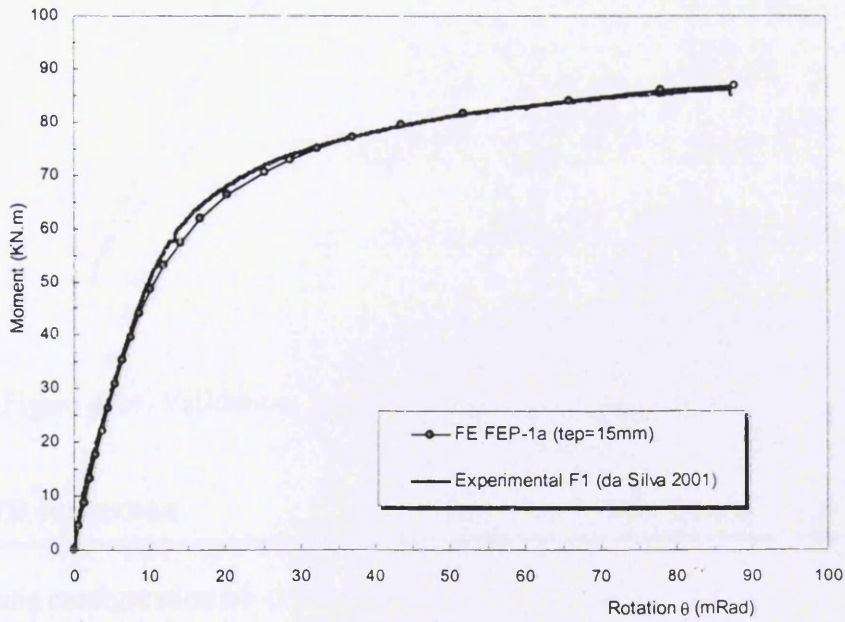


Figure 4.22 Validation of FE modelling against test result – FEP-1a

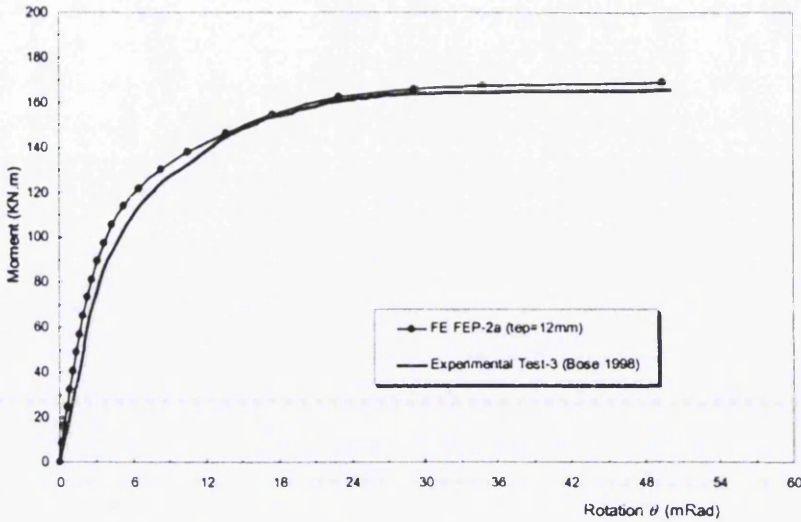


Figure 4.23: Validation of FE modelling against test result – FEP-2a

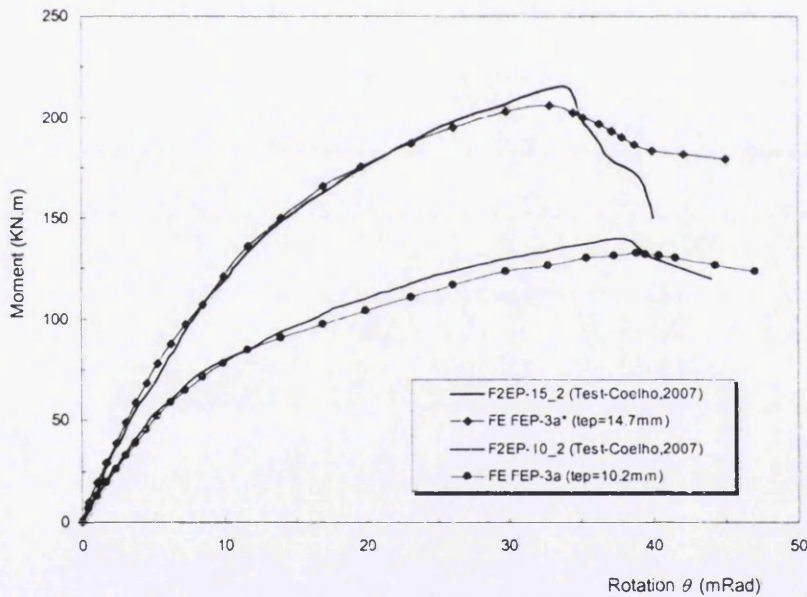


Figure 4.24: Validation of FE modelling against test result – FEP-3a

4.2.5 EPTB connection

FE modelling configuration of an endplate connection with a tubular section as shown in Figures 4.25 and 4.26. Steel material properties for FE analysis of endplate connection with tubular section beam (EPTB) is based on experimental data obtained from reference [36]. All steel materials for connection used are S355 with $\sigma_y = 398$ MPa and $\sigma_u = 430$

MPa for SHS beam, S355 with $\sigma_y = 370$ MPa and $\sigma_u = 466$ MPa for RHS beam and M20 bolts grade 10.9 with $\sigma_y = 940$ MPa and $\sigma_u = 1070$ MPa. All steel material properties for FE model is presented as shown in Table 4.6.

Table 4.6
Material properties for FE model

| Specimen | steel grade | σ_y (MPa) | σ_u (MPa) | σ_y / σ_u |
|-----------|-------------|------------------|------------------|-----------------------|
| column | S355 | 420 | 500 | 0.840 |
| beam RHS | S355 | 370 | 466 | 0.794 |
| beam SHS | S355 | 398 | 430 | 0.926 |
| bolt | Grade 10.9 | 940 | 1070 | 0.879 |
| end plate | S355 | 384 | 499 | 0.770 |

The connection parameter is detailed in Table 4.7. Beam and column for EPHS-1 are designated as 200x100x9RHS and 203x203x46UC, respectively, whilst 150x150x9SHS and 254x254x73UC are used for EPTB-2. Bolt gauge on column flange (g) and bolt spacing (p) are 100.0mm and 260.0mm for EPTB-1, whilst 150.0mm and 210.0mm for EPTB-2 respectively.

Table 4.7
EPTB connection parameter

| connection | beam | endplate | bolt - grade | g (mm) | p (mm) |
|------------|--------------|------------|--------------|----------|----------|
| EPTB-1a | 200x100x9RHS | 330x160x12 | M20 - 10.1 | 100 | 260 |
| EPTB-2a | 150x150x9SHS | 280x210x12 | M20 - 10.1 | 150 | 210 |

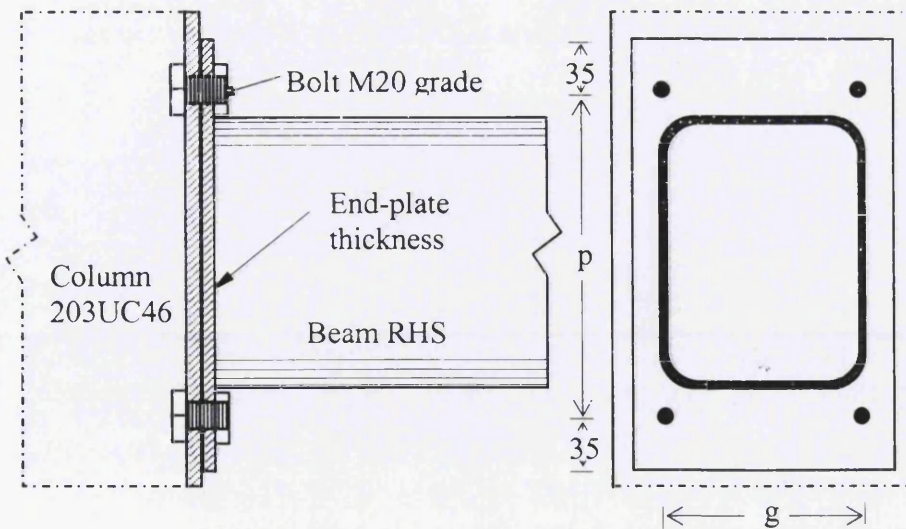


Figure 4.25: FE modelling configuration of the EPTB-1 connection

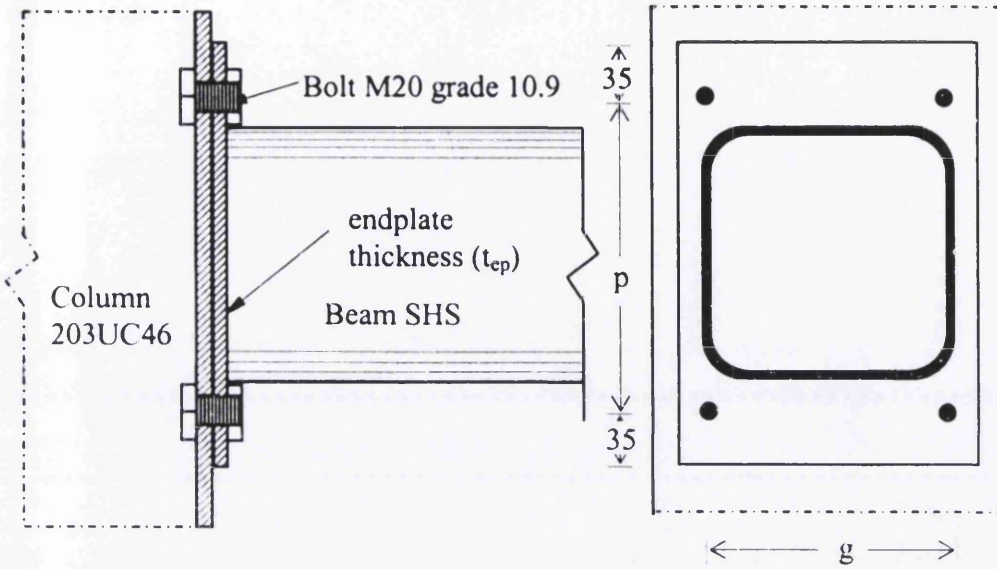


Figure 4.26: FE modelling configuration of the EPTB-2 connection

Figure 4.27 indicates the comparison between the test results and the finite element analysis. The FE models show ultimate moment of 47.0 KN.m, and 56.5 KN.m, respectively.

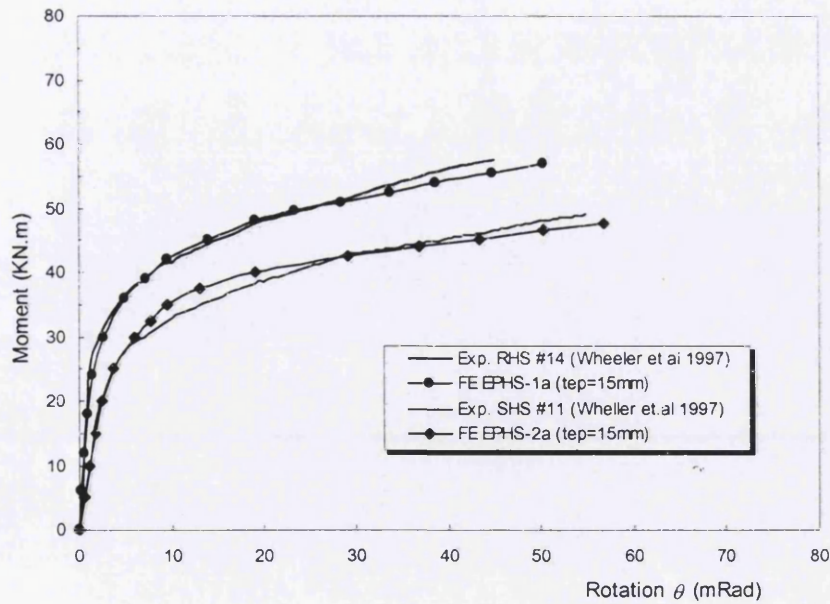


Figure 4.27: Validation of FE modelling against test result (EPTB)

4.2.6 SCC connection

FE modelling configuration of the SCC connection is shown in Figure 4.28. Steel material properties for FE analysis is based on experimental data. All steel materials for connection used are S275 beam with $\sigma_y = 310$ MPa and $\sigma_u = 480$ MPa, S275 column with $\sigma_y = 290$ MPa and $\sigma_u = 460$ MPa, whilst M20 bolts grade 8.8 with $\sigma_y = 750$ MPa and $\sigma_u = 850$ MPa. The elastic modulus of concrete is defined as $3.4E4$ N/mm², whilst the ultimate compressive strength is 34.0 MPa. Reinforcement bar grade S460 is used with $\sigma_y = 500$ MPa and $\sigma_u = 640$ MPa. The connection parameter is tabulated as Table 4.8.

Table 4.8
SCC connection parameter

| connection | beam | endplate | stiffener (mm) | g (mm) | p (mm) |
|------------|--------------|------------|----------------|--------|--------|
| SCC-1a | 305x165x40UB | 305x165x15 | 20.0 | 75 | 55 |
| SCC-2a | 305x165x40UB | 305x165x15 | un-stiffened | 75 | 55 |

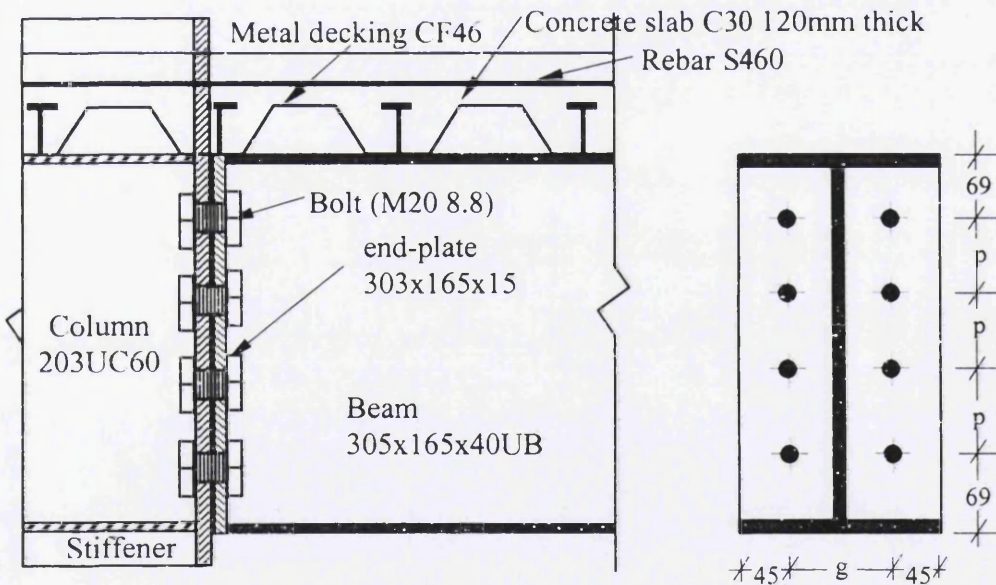


Figure 4.28 FE modelling configuration of the SCC connection

The SCC model is symmetric about the centre of the column web and no lateral displacement is assumed, so only one side of the plane of symmetry is modelled. The point load is applied to the top of beam web at the beam end. It is assumed that no slip

occurred between concrete and metal decking. Comparisons are made with experimental results obtained from reference [36]. The finite element model was validated against the recorded load-displacement curve from the tests. Figure 4.29 indicates the comparison between the test results and the FE analysis. The FE models show ultimate moment of 205.0 KN.m, and 241 KN.m, respectively.

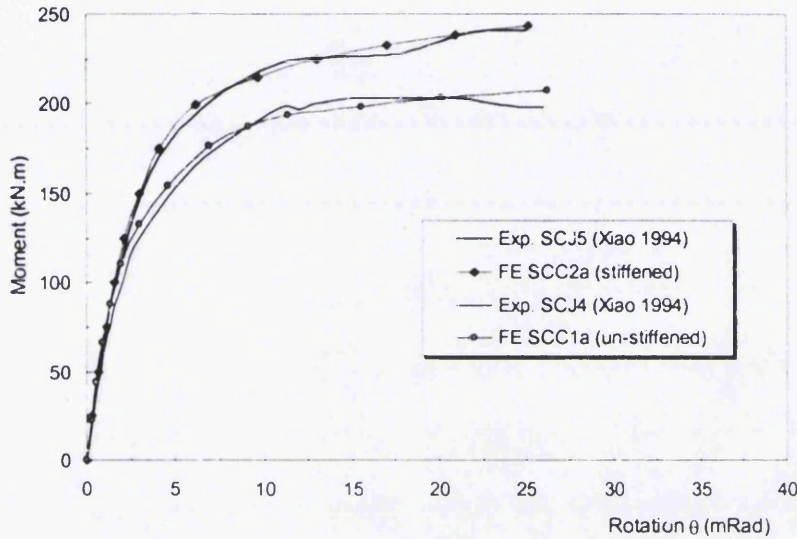


Figure 4.29 Validation of FE modelling against test result (SCC)

4.2.7 Shear connection

The shear connection configuration is shown as Figure 4.30 and connection parameter is depicted in Table 4.9. The middle-plate of the connection with length $L = 374$ mm, left end width $W = 148$ mm, right end width $b = 100$ mm and thickness $t_p = 10$ mm has the hole diameter $d_o = 30$ mm in which the centre is located at a distance from the right end $e_1 = 36$ mm and a distance from the bottom end $e_2 = 45$ mm. The side-plates (plate B) and other side-plates (plate C) are defined with their thickness equal to t_p .

Moreover, one M27 grade 10.9 high-strength bolt with $\sigma_y = 1010$ MPa, $\sigma_u = 1100$ MPa arranged in a line of the bolted connection was investigated. Both bearing and slip-critical types were considered in the simulation. Trilinear elastic-plastic approach is used to determine the material properties of connection member for the FE model. Multilinear elastic-plastic approach is used to determine the material properties of high strength steel

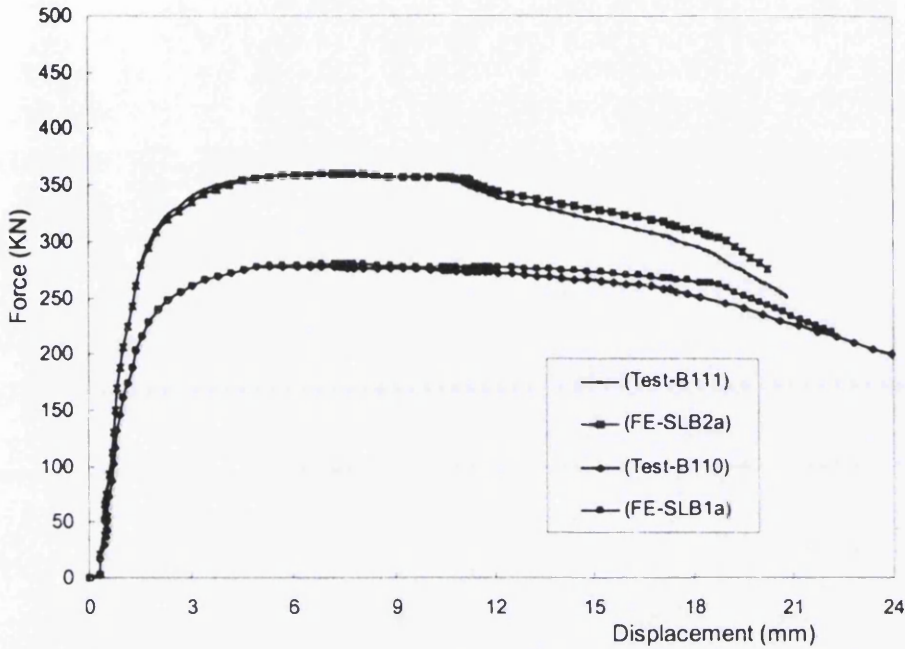


Figure 4.31 Load-displacement relationship of the SLB connection

4.3 Comparison between FEA and Test Result

This section contains the results from the previous analysis. These are the results of FEA against experimental of the PR connection and SLB connection. The comparisons were produced with initial stiffness (R_{ki}), ultimate moment (M_u), and rotation at ultimate moment (θ_{Mu}) for the PR connection. On the other hand, the comparisons were made with initial stiffness (K_i), ultimate load (P_u), elongation capacity (Δ_C) and load resistance at fracture of the joint ($P_{\Delta C}$) for SLB connection.

4.3.1 PR connection

Comparison between the FEA and test results for the PR connection is presented in Table 4.10.

Table 4.10.
Comparison FEA against test result

| Connection destination | FEA | | | Test result | | |
|------------------------|-------------------------|-----------------|-------------------------|-------------------------|-----------------|-------------------------|
| | R_{ki} (KN.m/mRad) | M_u (KN.m) | θ_{Mu} (mRad) | R_{ki} (KN.m/mRad) | M_u (KN.m) | θ_{Mu} (mRad) |
| DWA-1a | 4.28 | 22.4 | 94.3 | 6.37 | 22.3 | 95.2 |
| DWA-2a | 18.95 | 49.6 | 91.2 | 21.97 | 49.8 | 74.0 |
| TSA1o | 23.42 | 115.2 | 68.5 | 24.85 | 116.5 | 67.0 |
| TSA2o | 20.32 | 120.4 | 64.2 | 15.76 | 121.5 | 65.2 |
| TSAW1a | 15.59 | 42.2 | 40.0 | 14.12 | 41.5 | 40.0 |
| TSAW2a | 23.60 | 43.1 | 32.5 | 25.00 | 42.5 | 28.5 |
| TSAW3a | 40.99 | 99.5 | 34.0 | 35.16 | 97.5 | 32.0 |
| TSAW4a | 57.69 | 179.5 | 27.5 | 66.04 | 180.5 | 27.5 |
| FEP-1a | 7.96 | 87.2 | 88.0 | 7.85 | 86.5 | 88.0 |
| FEP-2a | 46.38 | 166.5 | 49.5 | 40.0 | 165.0 | 50.0 |
| FEP-3a | 21.57 | 130.5 | 39.0 | 19.0 | 140.0 | 38.0 |
| FEP-3a* | 14.39 | 210.0 | 32.5 | 14.00 | 218.5 | 34.0 |
| EPTB-1a | 9.50 | 57.0 | 50.0 | 9.00 | 57.5 | 45.0 |
| EPTB-2a | 23.18 | 47.5 | 56.5 | 25.00 | 49.0 | 55.0 |
| SCC-1a | 83.60 | 205.0 | 25.5 | 80.60 | 200.0 | 26.0 |
| SCC-2a | 74.70 | 241.0 | 26.5 | 70.00 | 240.0 | 25.0 |

4.3.2 SLB connection

Comparison between the FEA and test results for the SLB connection is presented in Table 4.11.

Table 4.11.
Comparison FEA against test result

| Connection destination | FEA | | | | Test result | | | |
|------------------------|------------------|---------------|------------------------|-----------------------|------------------|---------------|------------------------|-----------------------|
| | K_i (KN/mm) | P_u (KN) | $P_{\Delta C}$ (KN) | Δ_{Pu} (mm) | K_i (KN/mm) | P_u (KN) | $P_{\Delta C}$ (KN) | Δ_{Pu} (mm) |
| SLB1a | 74.1 | 280.8 | 220.0 | 20.0 | 64.0 | 286.0 | 200.0 | 24.0 |
| SLB2a | 74.8 | 360.3 | 276.0 | 22.0 | 66.9 | 365.0 | 252.0 | 21.0 |

4.4 Conclusions from Validation Study

Chapter 4 has two parts. Part one has presented the validation of the proposed finite element modelling to the laboratory work of partially restrained connections conducted by other investigators. The initial stiffness and ultimate moment of the PR connections from FE model were compared. In addition, to this moment-rotation behaviour of experimental work and analytical modelling was presented. The second part, has presented the validation of bolted shear connection. The initial stiffness and ultimate load of the shear connections from FE model were compared. In addition, the load-displacement behaviour of experimental work and analytical modelling was presented. From the study carried out, the following conclusions could be drawn.

The validation of the proposed finite element modelling to the experimental work, conducted by other investigators, was satisfactory. All modelled PR connections reached the ultimate applied loads which were achieved in the experimental work. The initial stiffness and ultimate moment collected from the experimental work and employed in the analysis were closely matched with the output of the moment-rotation relationship results. All modelled SLB connections reached the ultimate applied loads which were achieved in the experimental work. The initial stiffness and ultimate load collected from the experimental work and employed in the analysis were satisfactorily compared with the output of the load-displacement relationship results.

Chapter 5

FE Model with High Strength and Stainless Steel

5.1 Introduction

This chapter is intended to establish finite element modeling on the bolted connection with high strength and stainless steel material. The objective of this study is to examine the overall behaviour of bolted connections with high strength and stainless steel with an emphasise on the ductility problem behaviour of the angle and plate of the connection.

5.2 Angle Bolted Connection

As the initial stiffness of the angle bolted connection is governed by the geometry of the top seat angle and web angle, the non-linear behaviour is related to material properties (strain hardening). To establish the effects of angle configurations, the angle thickness and strength are selected as two main parameters. Multilinear elastic-plastic approach is used to determine the material properties of high strength steel for the FE model, whilst the yield stress is defined as 0.2% proof stress. By these parameters combination, various moment-rotation curves can be obtained from 3D nonlinear finite element analyses. The thinner angle thickness with higher strength steel is applied to keep

moment capacity and reduce the effect of slip. In order to increase the connection capacity, the higher strength angles are applied with different thickness. Gauge length, bolt spacing and bolt diameter are kept in the same value. Plots of the Von Mises equivalent stress and plastic strain were used to assess the predicted yield line patterns.

Top and seat angle cleats of the TSA and TSAW connections and web angles of DWA connections are modeled as radiused corner angle sections with enhanced strength region. Strength enhancement due to cold-forming at the corners of carbon steel sections was firstly studied by Karren [93]. Based on the examination of a substantial amount of test data, Karren proposed two analytical models to predict the changes caused by cold-forming at the corners. The r_i/t ratio was identified as having a significant effect on the corner strength, a decrease in r_i/t ratio causing an increase in the corner strength. The σ_u/σ_y ratio of the virgin material was also identified as an important parameter. ENV 1993-1-3 (1996) [94] accounts for enhanced strength corners in the design of cold-formed carbon steel sections, by allowing an increase in the average strength of the entire section. The average yield strength f_{ya} is defined by Eq. (5.1). It should be noted that ENV 1993-1-3 (1996) only allows strength enhancements for cross-sections that are fully effective:

$$f_{ya} = f_{yb} + (f_u - f_{yb})knt^2/A_g \quad (5.1)$$

but, $f_{ya} \leq (f_u + f_{yb})/2$

- where,
- f_{yb} = is the nominal yield strength
 - A_g = is the gross cross-sectional area
 - k = is a numerical coefficient that depends on the type of forming as follows:
 - $k=7$ for cold-rolling
 - $k=5$ for other methods of forming
 - n = is the number of 90° bends in the cross-section with an internal radius $r \leq 5t$
(fractions of 90° bends should be counted as fractions of n)
 - t = is the nominal core thickness t_{cor} of the steel material before cold-forming, exclusive of zinc or organic coatings.

Previous research showed that enhanced strength should be included beyond the curved corner of the numerical models to achieve the exact replication of the test results [95]. For carbon steel sections the effect of cold-forming extends beyond the corner to a distance approximately equal to the thickness t_a [93]. A parametric study was carried out to investigate the extent to which corner enhancement continues beyond the curved region. Keeping all other parameters the same, two different cases were studied—enhanced strength only in the curved corner region, enhanced strength region extended to a distance t_a beyond the corner as shown in Figure 5.1. The core thickness on corner region is assumed with no reduction to the material properties of angle shell elements for FE analyses.

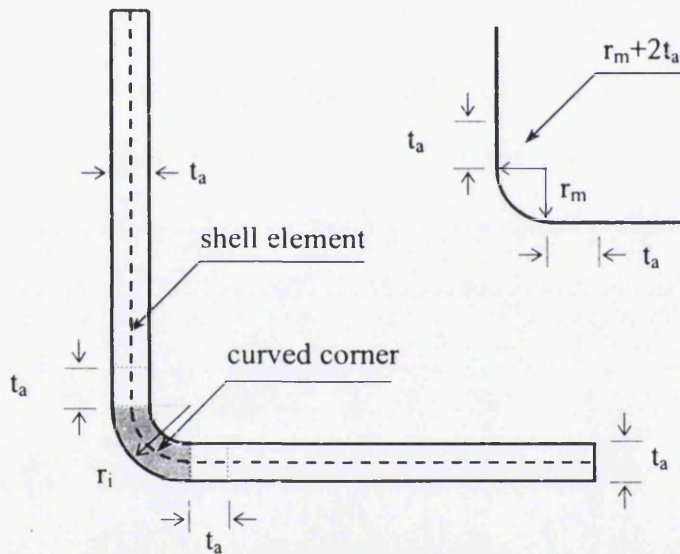


Figure 5.1 Enhanced strength region of a cold formed angle

Mild carbon steel S275 was used for beams and columns with yield stress of 300 MPa and Young's modulus of 2.1E5 MPa. High strength bolt M20 grade 8.8 with yield stress of 840 MPa is applied for all types of connections. High strength steels were used for all angles except for double web angles of DWA connection. Multilinear elastic-plastic approach is used to determine the material properties of high strength steel for the FE model, whilst the yield stress is defined as 0.2% proof stress, as shown in Figure 5.2. Material properties of carbon steel grade S275 and high strength steel grade S460, S550

5.2.1 DWA connection

After following the procedures in section 3.5.2, different thicknesses of higher strength web angles (t_{wa}) are applied. The web angles are determined with different high strength steel grade, whilst the beam and column are kept with mild carbon steel. The effect of angle thickness and strength is more pronounced on the rotational capacity with the thinner angle. Table 5.2 indicates the observed failure moments from the finite element analyses, compared with the EC3 design predictions. The comparisons of the ultimate moment from FEA with corner strength enhancement are made with no corner strength enhancement [M_{ult} FE (ncs)] and corner strength enhancement extended to a distance t_a [M_{ult} FE (r_m+2t_a)]. The moment-rotation curves of the DWA connection from FE model with corner strength enhancement are shown in Figures 5.3 - 5.6. Deformed shape of FE model is shown in Figure 5.7. The curve shape of DWA-1a is different from the other ones due to the angles using cold formed section and mild carbon steel.

The ultimate moment with corner strength enhancement in the region of a distance r_m+2t_a gives no significant influence compared with no corner strength enhancement. The difference between two approaches is only about 1%. The initial stiffness is slightly higher with the thicker angle, whilst the rotational capacity is lower. The result shows that the S460 angles reduced the moment capacity by up to 10%, due to existing of curved corner region angle. The S550 angles increase the capacity by up to 5%, whilst the S690 angles reach the ultimate moment by nearly twice as much as S275 angles, respectively. The moment capacity is much higher by up to 45% for a thinner angle, whilst it is only up to 20% for thicker angle due to the excessive deformation around larger curved corner region.

In order to investigate the behaviour of the connection, the stress contours of angles are compared with those of the column flange. The patterns of stress contours of the column flanges and angles with different steel grade and thickness of angles are very similar in general with differences only in the value and the spread of plasticity. Stress concentration of web angle occurs around top and bottom corner region as shown in Figure 5.8, whilst stress concentration of column flange occurs around the inner side of the top row of bolt holes as shown in Figure 5.9.

Table 5.2

Moment capacity with corner strength enhancement

| Connection destination | bolts in row | t_a (mm) | r_m (mm) | M_{ult} FE _(ncs) (KN.m) | M_{ult} FE _(r_m+2t_a) (KN.m) | Failure mode |
|------------------------|--------------|------------|------------|--------------------------------------|--|----------------|
| DWA1-b | 3 | 9.5 | 7.0 | 25.3 | 25.6 | angle yielding |
| DWA1-c | 3 | 9.5 | 7.0 | 27.4 | 28.1 | angle yielding |
| DWA1-d | 3 | 9.5 | 7.0 | 32.3 | 32.8 | angle yielding |
| DWA2-b | 4 | 11.0 | 6.0 | 59.0 | 60.0 | angle yielding |
| DWA2-c | 4 | 11.0 | 6.0 | 64.6 | 64.8 | angle yielding |
| DWA2-d | 4 | 11.0 | 6.0 | 74.4 | 75.0 | angle yielding |
| DWA3-b | 3 | 11.0 | 6.0 | 34.5 | 35.0 | angle yielding |
| DWA3-c | 3 | 11.0 | 6.0 | 36.9 | 38.1 | angle yielding |
| DWA3-d | 3 | 11.0 | 6.0 | 42.0 | 42.4 | angle yielding |
| DWA4-b | 4 | 12.5 | 5.0 | 73.7 | 75.0 | angle yielding |
| DWA4-c | 4 | 12.5 | 5.0 | 79.1 | 80.0 | angle yielding |
| DWA4-d | 4 | 12.5 | 5.0 | 92.2 | 93.0 | angle yielding |

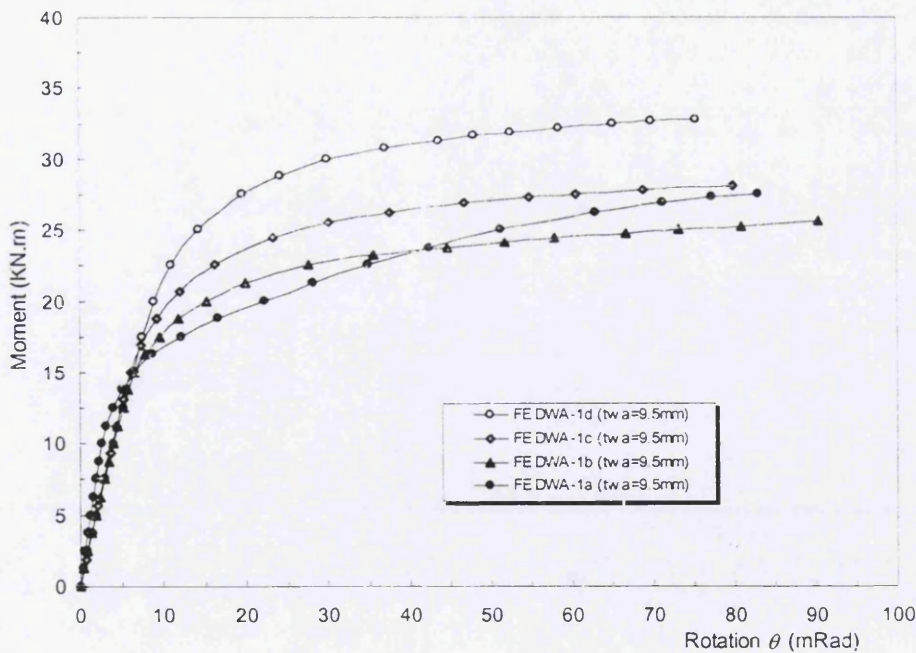


Figure 5.3 Moment-rotation relationship of the DWA-1 model

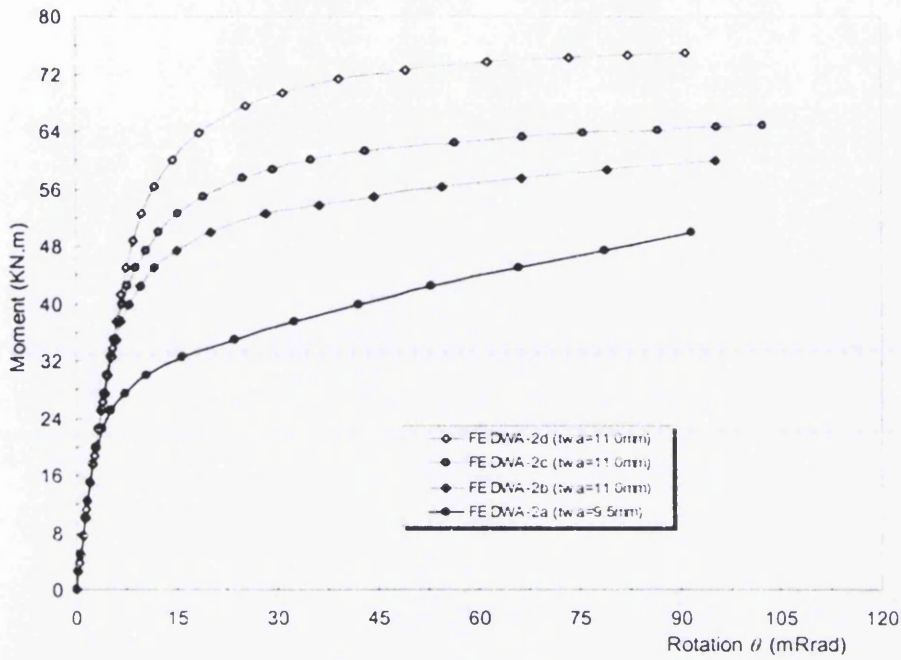


Figure 5.4 Moment-rotation relationship of the DWA-2 model

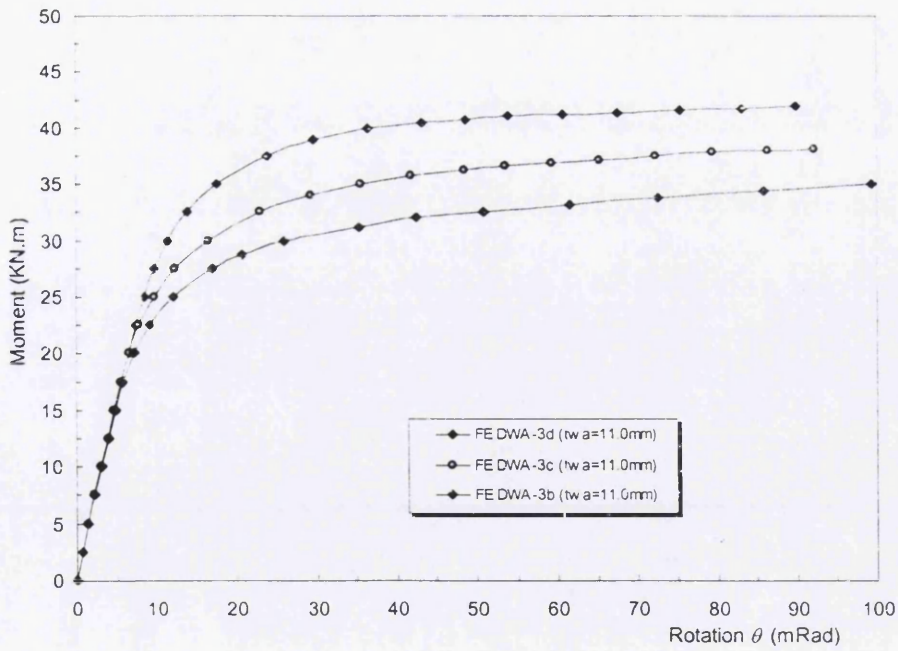


Figure 5.5 Moment-rotation relationship of the DWA-3 model

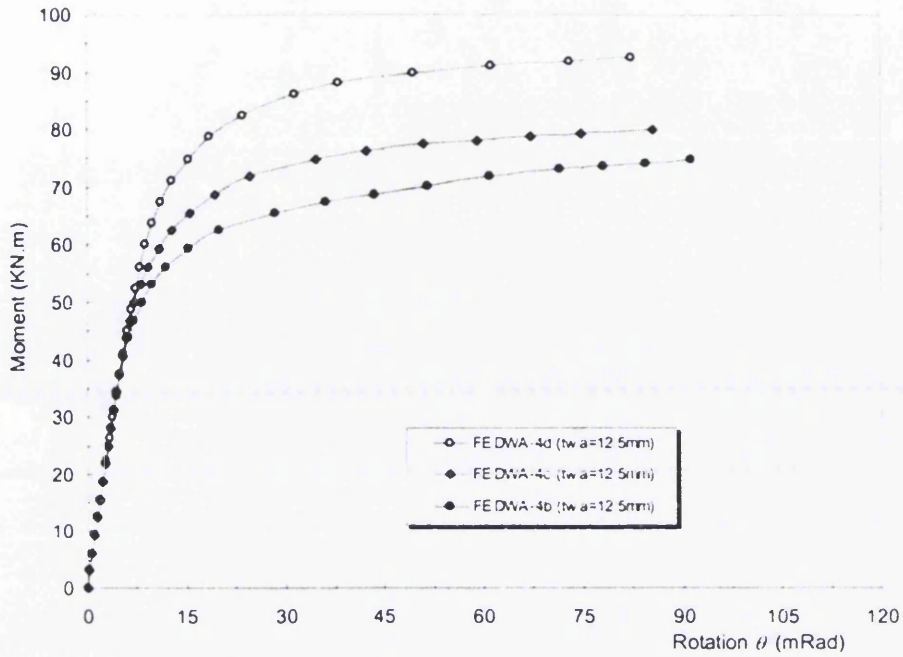


Figure 5.6 Moment-rotation relationship of the DWA-4 model

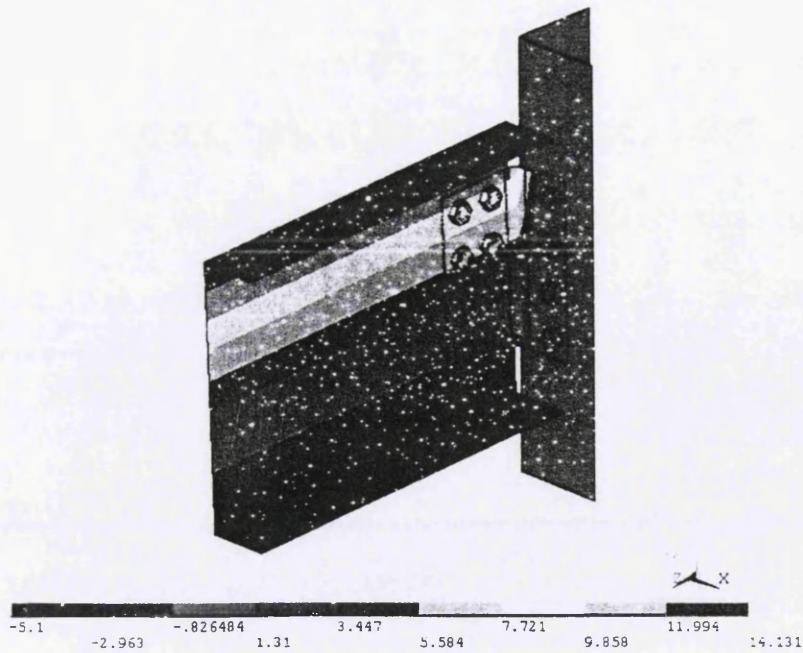


Figure 5.7 Deformed shape of the DWA-2 connection; unit in mm

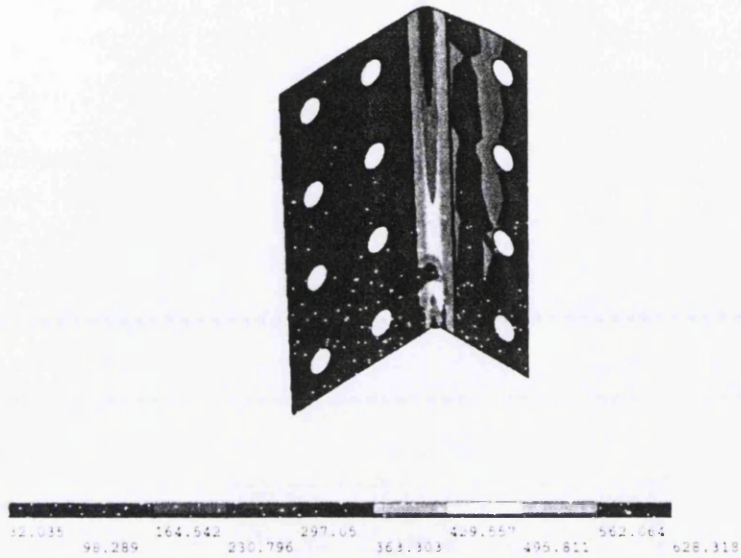


Figure 5.8 Stress contours of the S550 web angle; unit in MPa

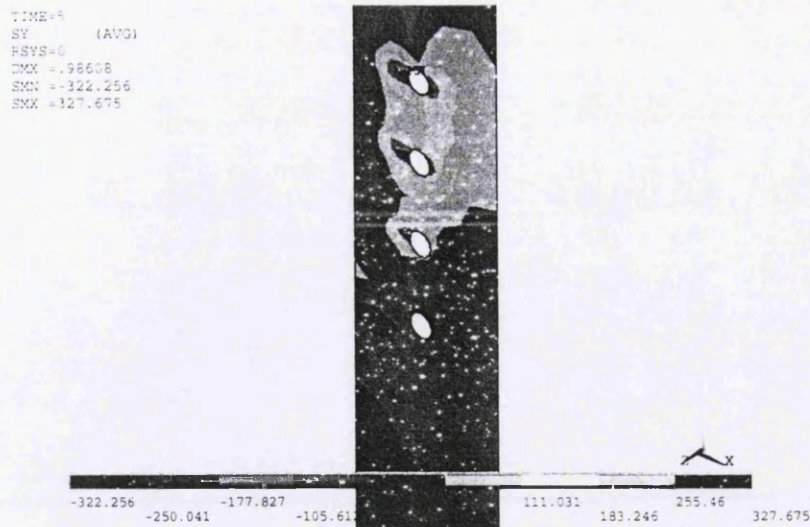


Figure 5.9 Stress contours of the S275 column flange; unit in MPa

5.2.2 TSA connection

After following the procedures in section 3.5.3, different thicknesses of higher strength seat and top angles (t_{sa}) are applied. The angle cleats are determined with different high strength steel grade, whilst the beam and column are kept with mild carbon steel. Effect of angle thickness and strength is more clear on the rotational capacity with the thinner angle. The moment capacity of TSA connection with S690 angle is higher than that of S275 angle by up to 45% for a thinner angle ($t_{sa}=8.0\text{mm}$), whilst it is only up to 20% for a thicker angle ($t_{sa}=12.5\text{mm}$). The moment capacity of S550 TSA is higher than that of S275 angle by up to 25% for thinner angle ($t_{sa}=8.0\text{mm}$), whilst it is only up to 10% for thicker angle ($t_{sa}=12.5\text{mm}$). High strength thicker angles give no much improvement on the connection capacity, because of the slippage. The moment capacity is still reached far below the ultimate moment on the maximum plastic strain limit, whilst earlier slip occurs.

As the initial stiffness of the connection is governed by the geometry of the top seat angle, the non-linear behaviour is related to material properties (strain hardening). The FE model with its deformed shape of the connection is presented in Figure 5.10. The variation in the TSA connections response due to different thickness and strength of the angle cleats is shown in Figures 5.11 – 5.13.

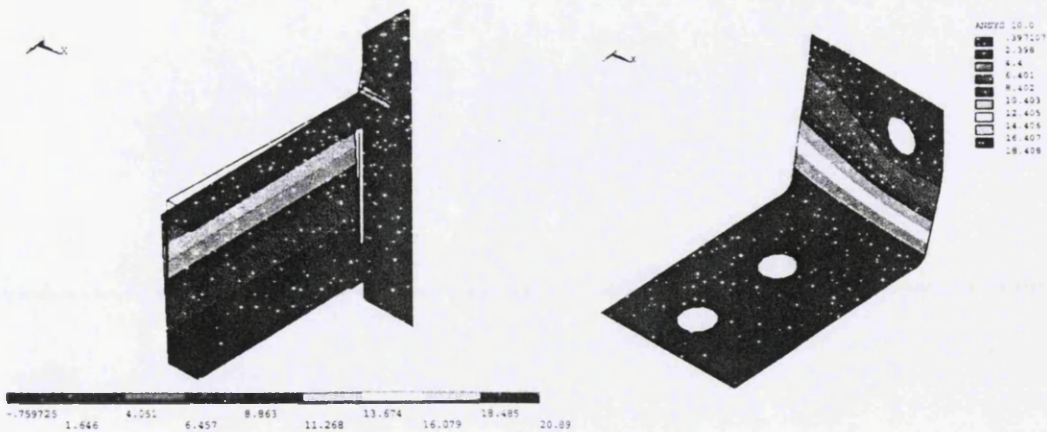


Figure 5.10 Deformed shape of the TSA model at ultimate moment; unit in mm

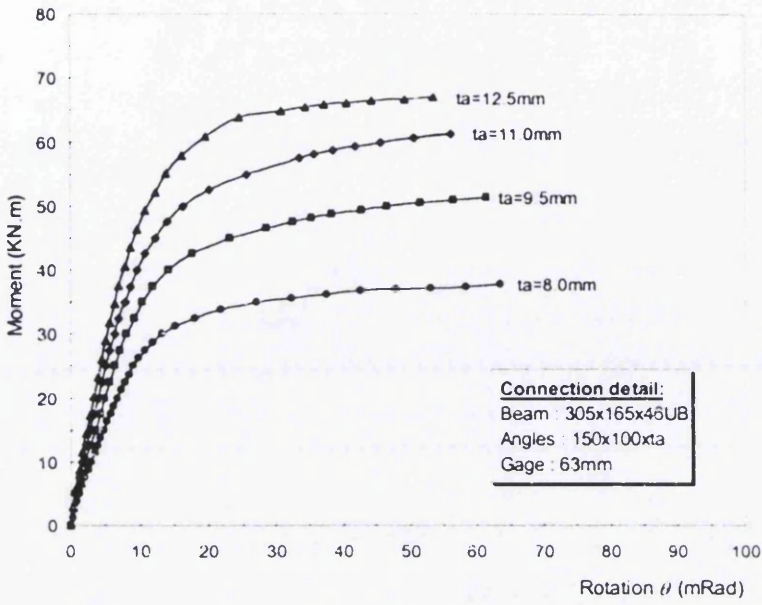


Figure 5.11 Moment-rotation relationship of the TSA1 model; S690 angle

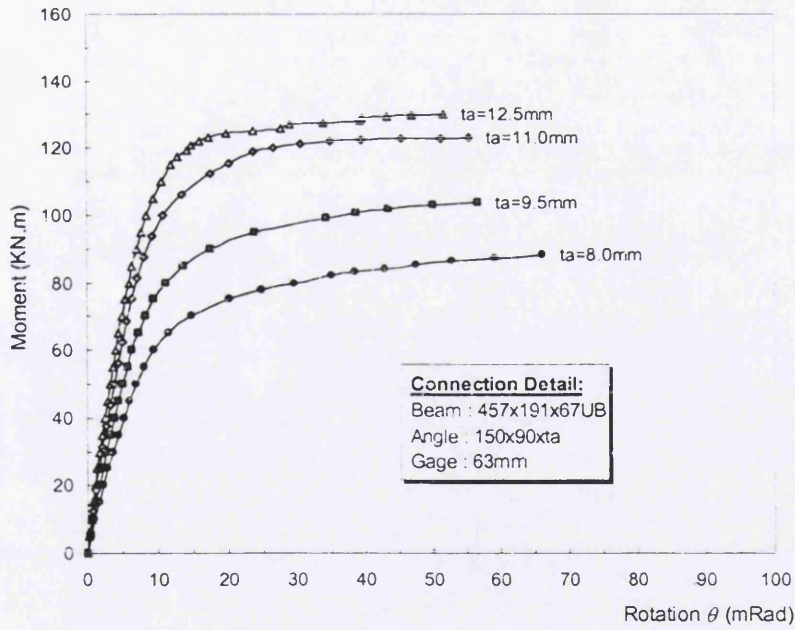


Figure 5.12 Moment-rotation relationship of the TSA2 model; S690 angle

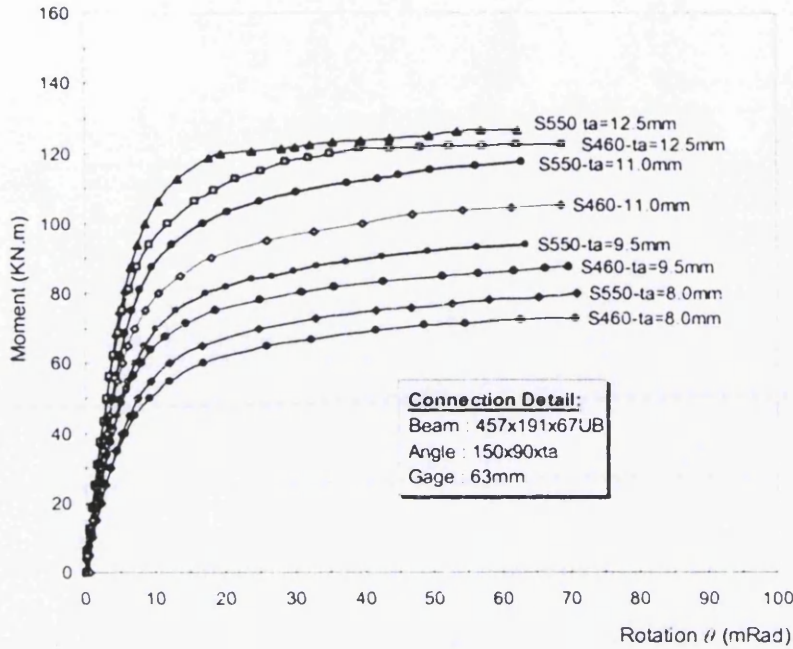


Figure 5.13 Moment-rotation relationship of the TSA2 model; S460 and S550 angles

The mean ultimate moment capacity shows an increase of approximately 1% for strength enhancement on corner region only, and increase of approximately by 2% for strength region extended to a distance t_a beyond the corner. Top and seat angle connections based on FE modelling with un-stiffened column are also analyzed with reference [96] to modern design codes EC3. The design tension resistance of the column flange and of the beam top and seat are given in terms of an equivalent T-stub. The effective length of plate and column flange is based on the yield line patterns around bolt holes. The possible modes of the yielding of the connection are 1) complete flange yielding 2) bolt failure with flange yielding, and 3) bolt failure as shown in Figure 5.14. The smallest value for the three possible modes of the yielding is chosen with three possible modes of the yielding from Equations 5.2 - 5.4 as follows:

$$F_{t,Rd} = \frac{4(0.25\ell_{eff}t_y^2f_y/\gamma_{M0})}{m} \quad (5.2)$$

$$F_{t,Rd} = \frac{2(0.25\ell_{eff}t_y^2f_y/\gamma_{M0}) + n\Sigma B_{t,Rd}}{m+n} \quad (5.3)$$

$$F_{t,Rd} = \Sigma B_{t,Rd} \quad (5.4)$$

where:

$F_{t,Rd}$ is the design tension resistance (N)

l_{eff} is the effective length (mm)

t_f is the flange thickness (mm)

f_y is the yield stress (N/mm²)

$B_{t,Rd}$ is the design tension resistance of a single bolt-plate (N)

γ_{M0} is the partial safety factor for steel

m is the distance from the bolt centre to the inner side of flange (mm)

n is the distance from the bolt centre to the edge of flange (mm)

Determine the design value of the moment resistance of the connection M_{Rd} based on the bolt-rows in the reduced tension zone, from:

$$M_{Rd} = F_{t,Rd} \left(\frac{\sum h_i^2}{h_1} \right) \quad (5.5)$$

where:

$F_{ti,Rd}$ is the design value of the effective resistance of an individual row of bolts (N)

h_1 is the distance from the farthest bolt-row to the centre of resistance of the compression zone (mm)

h_i is the distance from any bolt-row to the centre of resistance of the compression zone (mm)

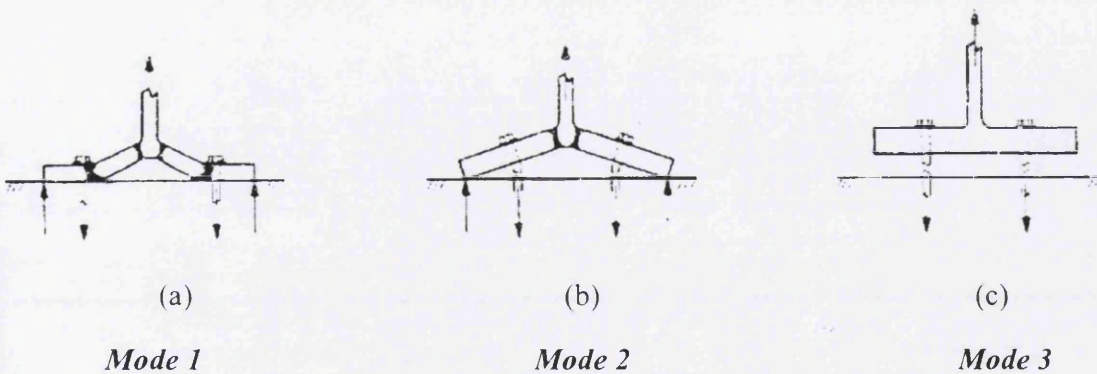


Figure 5.14 Failure modes of the connection.

The resistance and failure mode of a bolted angle flange cleat in bending, together with the associated bolts in tension, should be taken as similar to those of an equivalent T-stub flange. The effective length l_{eff} of the equivalent T-stub flange should be taken as $0.5b_a$ where b_a is the length of the angle cleat as shown in figure 5.15.

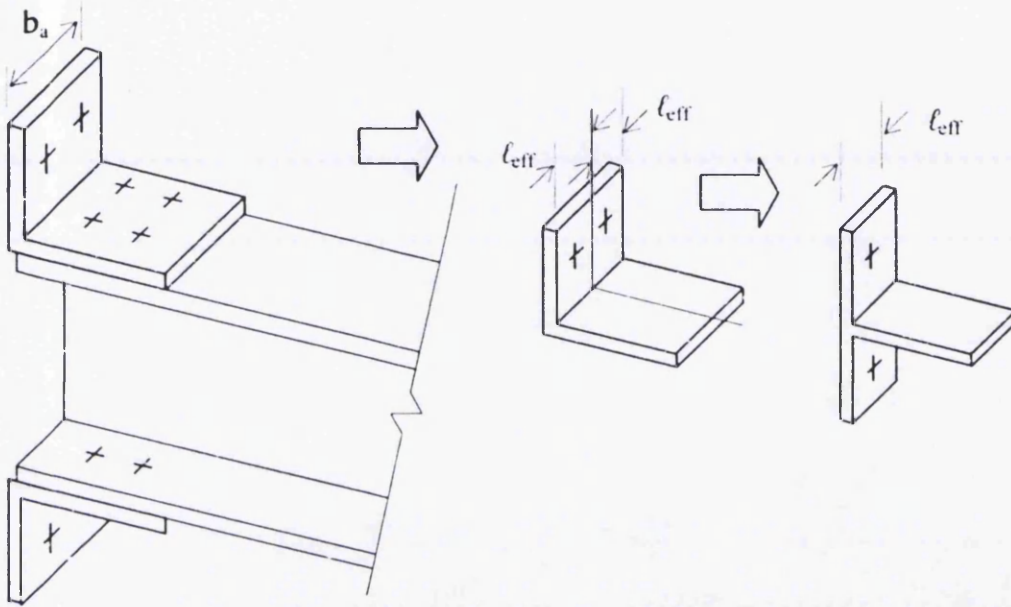


Figure 5.15 Effective length l_{eff} of an angle flange cleat

Moment connection capacity of the FE result and the EC design prediction for high strength TSA connection has been compared. The comparisons of the ultimate moment from FEA with corner strength enhancement are made within corner region only [$M_{ult} FE (r_m)$] and extended to a distance t_a [$M_{ult} FE (r_m+2t_a)$]. Table 5.2 indicates the observed failure moments from the finite element analyses, compared with the design predictions. The moment-rotation curves of the TSA connection from FE model with corner strength enhancement are shown in Figures 5.16-5.17.

From the results on Table 5.3, it can be seen that the designs are somewhat conservative despite the omission of factors of safety. The FE model of the TSA connection with thin angle and low beam depth shows significant results close to EC3 predictions, and also for connections with thicker angle and higher beam depth. Modern

design methods such as EC3 use yield line analyses of the angle cleat to predict the capacity of the tensile region. At the ultimate load, the failure mode type 1) which is complete yielding of the angle occurred for almost all of the TSA connection except for thicker S550 and S690 angle of the TSA2 connection on the column flange. The finite element model was used to confirm the predictions by studying the yielding of the angle and column flange.

Table 5.3
Moment capacity and failure mode

| Connection destination | t_a (mm) | r_m (mm) | M_{ult} FE (r_m) (KN.m) | M_{ult} FE (r_m+2t_a) (KN.m) | M_{ult} EC3 (KN.m) | Failure mode |
|------------------------|------------|------------|-------------------------------|------------------------------------|----------------------|---------------|
| TSA1-4b | 8.0 | 7.0 | 29.51 | 31.62 | 35.94 | top angle (1) |
| TSA1-4c | 8.0 | 7.0 | 34.00 | 34.35 | 39.40 | top angle (1) |
| TSA1-4d | 8.0 | 7.0 | 38.50 | 38.87 | 47.06 | top angle (1) |
| TSA1-3b | 9.5 | 6.0 | 41.10 | 42.75 | 48.37 | top angle (1) |
| TSA1-3c | 9.5 | 6.0 | 45.20 | 45.31 | 53.02 | top angle (1) |
| TSA1-3d | 9.5 | 6.0 | 51.40 | 51.87 | 66.97 | top angle (1) |
| TSA1-2b | 11.0 | 5.0 | 51.32 | 53.25 | 65.69 | top angle (1) |
| TSA1-2c | 11.0 | 5.0 | 56.15 | 57.37 | 72.01 | top angle (1) |
| TSA1-2d | 11.0 | 5.0 | 62.50 | 62.75 | 90.95 | top angle (1) |
| TSA2-4b | 8.0 | 7.0 | 74.00 | 74.50 | 47.78 | top angle (1) |
| TSA2-4c | 8.0 | 7.0 | 80.50 | 81.00 | 52.37 | top angle (1) |
| TSA2-4d | 8.0 | 7.0 | 88.60 | 89.00 | 66.15 | top angle (1) |
| TSA2-3b | 9.5 | 6.0 | 92.10 | 93.75 | 67.99 | top angle (1) |
| TSA2-3c | 9.5 | 6.0 | 96.00 | 98.30 | 74.52 | top angle (1) |
| TSA2-3d | 9.5 | 6.0 | 105.00 | 105.75 | 94.48 | top angle (1) |
| TSA2-2b | 11.0 | 6.0 | 108.00 | 110.25 | 91.99 | top angle (1) |
| TSA2-2c | 11.0 | 6.0 | 118.00 | 118.75 | 100.80 | top angle (1) |
| TSA2-2d | 11.0 | 6.0 | 124.25 | 125.25 | 119.80 | column (1) |
| TSA2-1b | 12.5 | 5.0 | 123.50 | 124.50 | 119.80 | column (1) |
| TSA2-1c | 12.5 | 5.0 | 127.00 | 127.50 | 119.80 | column (1) |
| TSA2-1d | 12.5 | 5.0 | 131.00 | 131.75 | 119.80 | column (1) |

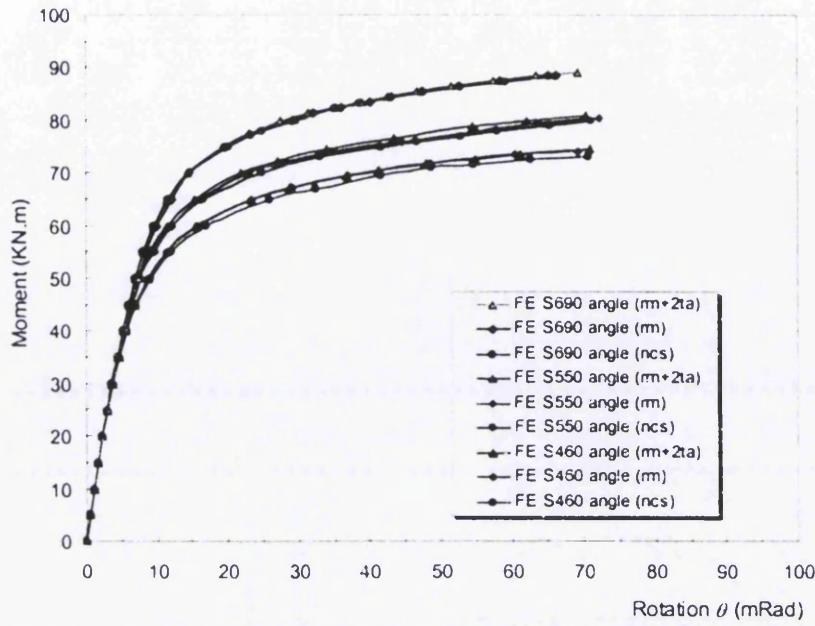


Figure 5.16 Moment-rotation curve of the TSA2 model; $t_{sa} = 8.0\text{mm}$

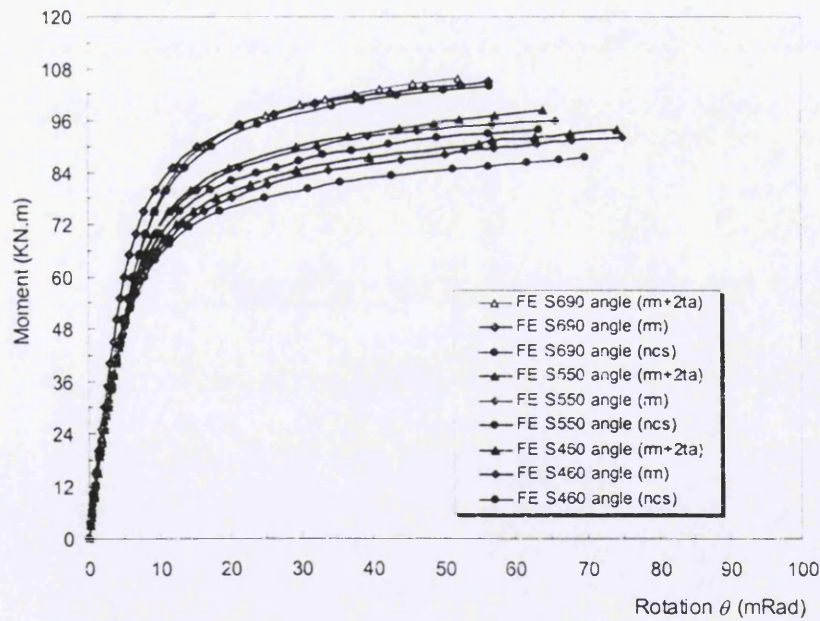


Figure 5.17 Moment-rotation curve of the TSA2 model; $t_{sa} = 11.0\text{mm}$

In order to investigate the behaviour of the connection, the stress contours of angles are compared with those of the column flange. The patterns of stress contours of the column flanges and angles with different steel grade and thickness of angles are very similar in general with differences only in the value and the spread of plasticity. The

S690 top angles and S275 column flange stresses, as was expected, are less than the ultimate stresses. Figure 5.18 illustrates the maximum stresses of the angles are located at a corner region and beside the bolt hole.

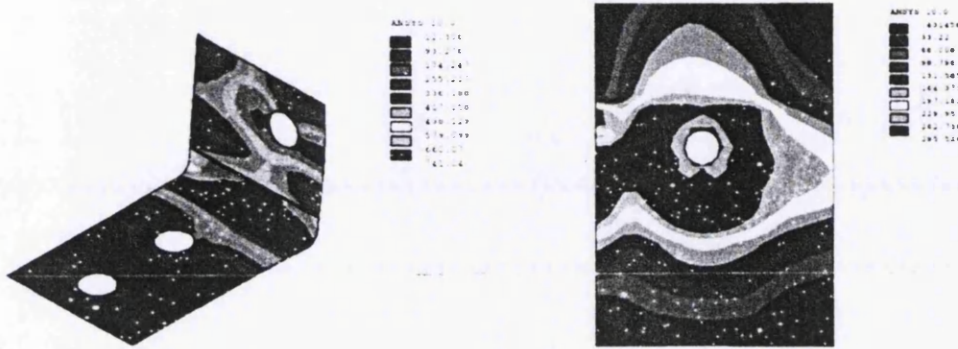


Figure 5.18 Stress contours of the TSA model; (a) thick angle (b) column flange

The stress contours at the ultimate load of top seat angle are compared as shown in Figure 5.19, which illustrates the maximum stress of top angle is located at a corner of angle and below the bolt hole. Application of high strength angle to the connection configuration gives larger area of maximum stress distribution, whereas the beam and column are kept in small area with carbon steel.



Fig. 5.19 Stress contours of the S690 angles with strength enhancement; (a) r_m (b) $r_m + 2t_a$

In order to investigate further the difference between response of top angle with different grade and thickness, the plastic equivalent strain fields are compared in Figures 5.20 and 5.21. The plastic strain values almost reach at the ultimate plastic strain unless

an earlier failure occurs because of stress concentration and ductility problems, whilst the value of maximum equivalent plastic strain is only at around 1.1×10^{-2} radian until slip occurs.

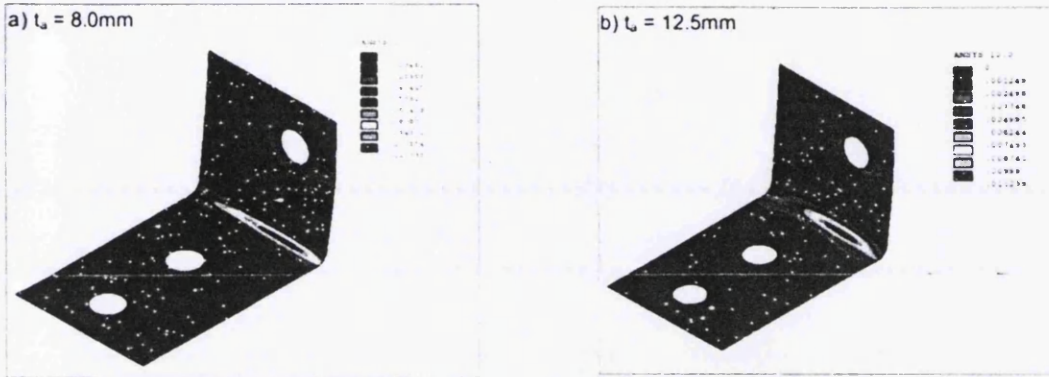


Figure 5.20 Comparison of plastic deformation in the S690 top angles

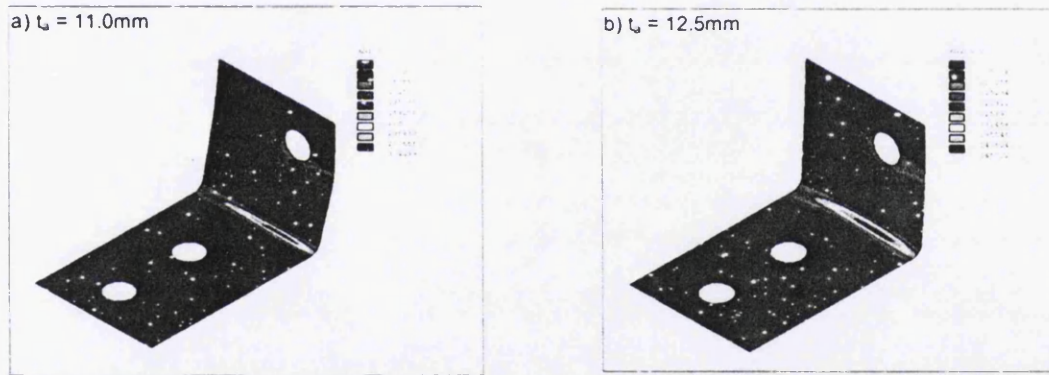


Figure 5.21 Comparison of plastic deformation in S550 the top angles

In Figures 5.22 and 5.23, the moment-rotation curves of the FE results can be observed with the stress identification of the yielding sequence of the several components. It is clearly noticed that application of the thicker angle changes the yielding sequence of top angle (in bending) and column flange (in bending). The response of beam flange (in compression) shows early yield due to thicker angle applied, whilst the maximum stress close to its ultimate stress. The high strength angles give significant proportion of maximum stress distribution, whereas the beam and column are kept with mild carbon steel.

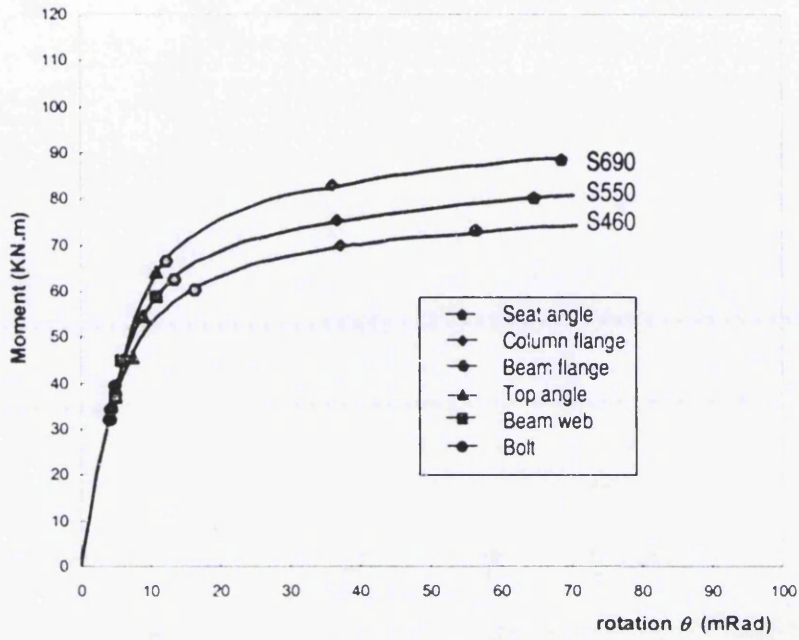


Figure 5.22 M-θ curve with yielding sequence of the components (thin angle)

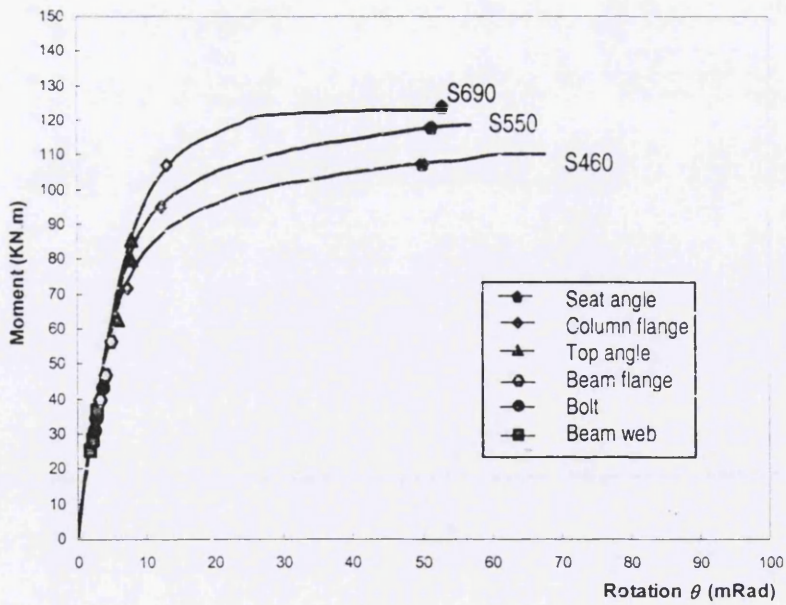


Fig. 5.23 M-θ curve with yielding sequence of the components (thick angle)

5.2.3 TSAW connection

To establish the effects of angle configurations, an angle thickness and strength are selected as two main parameters. By the combination of these parameters, various moment-rotation curves can be obtained from 3D nonlinear finite element analyses. In order to increase the connection capacity, the higher strength angles are applied with different thicknesses. They have six different thicknesses of the top and seat angles (t_{sa} =12.5mm, 9.5mm, 8.5mm, 8.0mm, 6.7mm and 6.5mm), three different thicknesses of the web angles (t_{wa} =6.5mm, 4.0mm, 8.0mm) and two different yield stresses ($\sigma_y = 484$ MPa and $\sigma_y = 711$ MPa). Gauge length, bolt spacing and bolt diameter are kept at the same value. The TSAW configuration parameter for FE analyses is presented in Table 5.4. Material properties for TSAW model are depicted in Table 5.5.

Table 5.4
TSAW configuration parameter for FEA

| connection destination | web angle | t_{wa} (mm) | top & seat angle | t_{sa} (mm) | g (mm) | p (mm) | p_b (mm) |
|------------------------|-----------|---------------|------------------|---------------|--------|--------|------------|
| TSAW-1a | S275 | 6.5 | S275 | 8.0 | 50.0 | 89.0 | 76.0 |
| TSAW-1b | S275 | 6.5 | S460 | 8.0 | 50.0 | 89.0 | 76.0 |
| TSAW-1c | S275 | 6.5 | S690 | 9.5 | 50.0 | 89.0 | 76.0 |
| TSAW-2b | S275 | 6.5 | S460 | 9.5 | 50.0 | 89.0 | 76.0 |
| TSAW-2c | S275 | 6.5 | S690 | 9.5 | 50.0 | 89.0 | 76.0 |
| TSAW-3a | S275 | 6.5 | S275 | 9.5 | 63.0 | 89.0 | 76.0 |
| TSAW-3b | S275 | 6.5 | S460 | 8.5 | 63.0 | 140.0 | 76.0 |
| TSAW-3c | S275 | 6.5 | S690 | 6.7 | 63.0 | 140.0 | 76.0 |
| TSAW-3b* | S275 | 8.0 | S460 | 9.5 | 63.0 | 140.0 | 76.0 |
| TSAW-3c* | S275 | 4.0 | S690 | 9.5 | 63.0 | 140.0 | 76.0 |
| TSAW-3b** | S275 | 8.0 | S460 | 6.5 | 63.0 | 140.0 | 76.0 |
| TSAW-3c** | S275 | 4.0 | S690 | 6.5 | 63.0 | 140.0 | 76.0 |
| TSAW-3a*) | S275 | 6.5 | S275 | 9.5 | 63.0 | 140.0 | 76.0 |
| TSAW-3b*) | S275 | 6.5 | S460 | 8.5 | 63.0 | 140.0 | 76.0 |
| TSAW-3c*) | S275 | 6.5 | S690 | 8.5 | 63.0 | 140.0 | 76.0 |
| TSAW-4a | S275 | 6.5 | S275 | 12.5 | 63.0 | 140.0 | 76.0 |

Table 5.5
Material properties for TSAW model

| Specimen | steel grade | σ_y (MPa) | σ_u (MPa) | σ_y / σ_u | ϵ_y (%) | ϵ_u (%) |
|------------------|-------------|------------------|------------------|-----------------------|------------------|------------------|
| column | S275 | 277 | 510 | 0.543 | 0.134 | 18.5 |
| beam | S275 | 277 | 510 | 0.543 | 0.134 | 18.5 |
| web angle | S275 | 277 | 510 | 0.543 | 0.134 | 18.5 |
| bolt | grade10.1 | 1010 | 1108 | 0.912 | 0.345 | 10.5 |
| angle cleat (i) | S460 | 484 | 584 | 0.829 | 0.480 | 15.5 |
| angle cleat (ii) | S690 | 711 | 805 | 0.883 | 0.552 | 6.5 |

The FE analyses results are presented in comparison with test results. Different thicknesses of higher strength angles are applied. The analyses results of TSAW connections are presented in Table 5.6 and Figures 5.24 – 5.27. The top and seat angles are determined with different yield stresses, whilst the web angle used mild carbon steel. The thickness of web angles (t_{wa}) is kept at 6.4 mm with steel grade of S460. Effect of angle thickness and strength are more important on the rotational capacity compared with a thinner angle. The initial stiffness is slightly higher with the thicker angle, whilst the rotational capacity is lower. Thinner top and seat angles with high strength steel might keep the moment capacity constant, whilst the rotational capacity can be increased significantly. As the thickness of top and seat angles is fixed, the initial stiffness of different steel grades is not changed on the response of connections. The result shows that the S460 angles increase the moment capacity by up to 20% whilst the S690 angles increase those capacities by up to 50%, respectively. The rotational capacity is much higher by up to 40% for thinner angles, whilst it is only up to 20% for thicker angle.

In order to determine the effect of web angle to the connection behaviour, the angles are determined with different yield stresses, whilst the thinner web angle is applied. The analyses result of the connections is presented in Figures 5.28 and 5.29. From Table 5.6, it can be seen that most of the failure modes of angle yielding occurred for all types of connection except for the connection with thicker and high strength angle as well as the S275 thicker web angle because of slippage. The results from the

connection modelling with corner strength enhancement show that the ultimate moment increase is in the range of 3% to 5% compared with no corner strength enhancement. The TSAW-3b* with S275 8.0mm thick web angle and S550 12.5mm thick top and seat angle gives the ultimate moment less than that of the TSAW-3c* with S275 4.0mm thick web angle because of the slippage of the top angle.

Table 5.6

Moment capacity with corner strength enhancement

| Connection destination | t_{wa} (mm) | t_{sa} (mm) | r_m (mm) | M_{ult} FE _(ncs) (KN.m) | M_{ult} FE _(r_m+2t_a) (KN.m) | Failure mode |
|------------------------|------------------|------------------|---------------|---|---|----------------|
| TSAW-1b | 6.5 | 8.0 | 7.0 | 51.0 | 51.5 | angle yielding |
| TSAW-1c | 6.5 | 8.0 | 7.0 | 75.8 | 76.5 | angle yielding |
| TSAW-2b | 6.5 | 9.5 | 6.0 | 51.9 | 52.5 | angle yielding |
| TSAW-2c | 6.5 | 9.5 | 6.0 | 76.7 | 78.5 | angle yielding |
| TSAW-3b | 6.5 | 8.5 | 6.0 | 82.0 | 82.6 | angle yielding |
| TSAW-3c | 6.5 | 6.7 | 7.0 | 84.4 | 85.0 | angle yielding |
| TSAW-3b* | 8.0 | 9.5 | 5.0 | 94.8 | 96.5 | angle slip |
| TSAW-3c* | 4.0 | 9.5 | 5.0 | 109.2 | 110.8 | angle yielding |
| TSAW-3b** | 6.5 | 6.5 | 8.0 | 65.0 | 65.5 | angle yielding |
| TSAW-3c** | 6.5 | 6.5 | 8.0 | 73.9 | 74.5 | angle yielding |
| TSAW-3c*) | 6.5 | 8.5 | 6.0 | 119.5 | 120.0 | angle slip |

It shows that a thinner web angle gives less ultimate moment of connection restraint, although the thicker top and seat angle is applied. The ultimate moment capacity is reached before the maximum plastic strain limit, while the earlier slip occurs. For the improved connection capacity of TSAW connection, it is necessary to consider applying only a higher strength top and seat angle, whilst the web angle is kept as mild carbon steel. When the thicker and higher strength web angles are applied, the connection restraint is only slightly changed because of slippage.

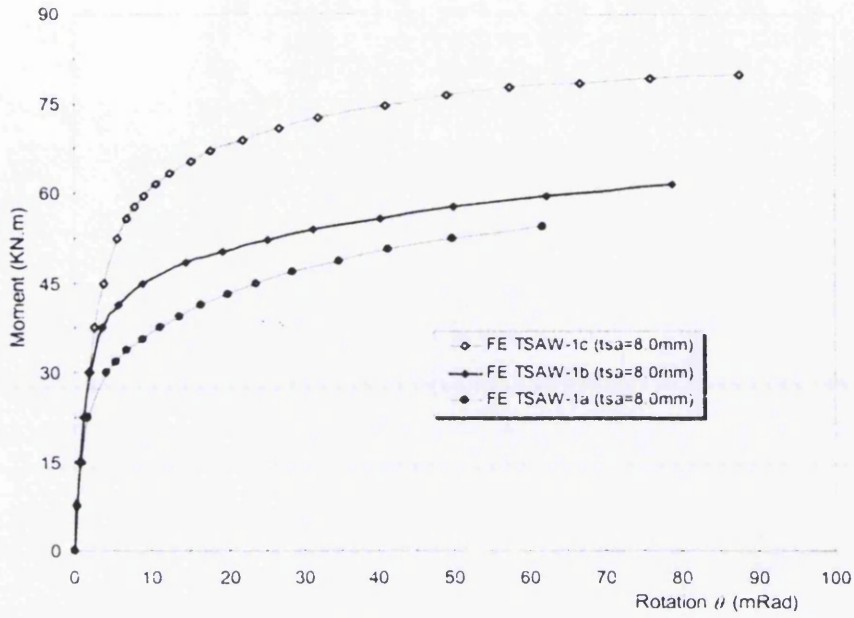


Figure 5.24 M- θ relationship of the TSAW-1 model; S690, S460 and S275 angle cleats

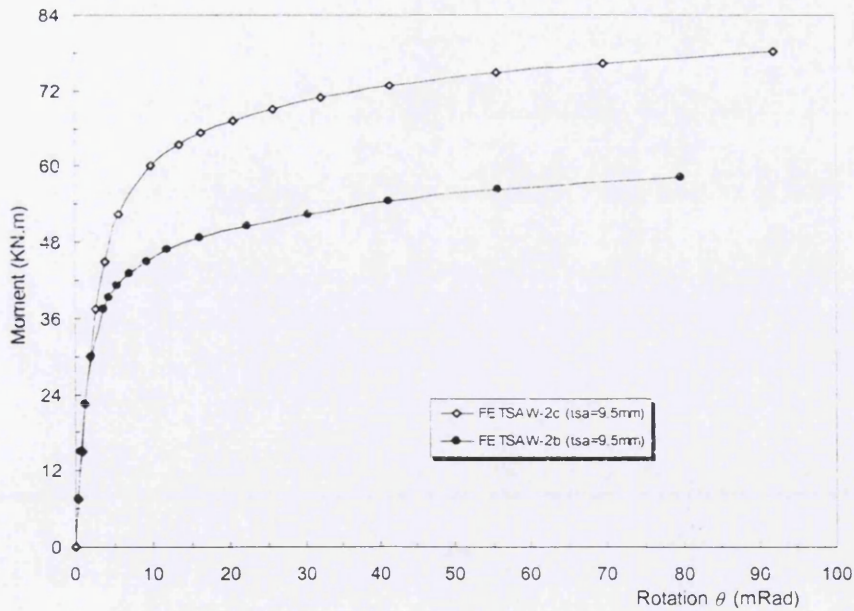


Figure 5.25 M- θ relationship of the TSAW-2 model; S690 and S460 angle cleats

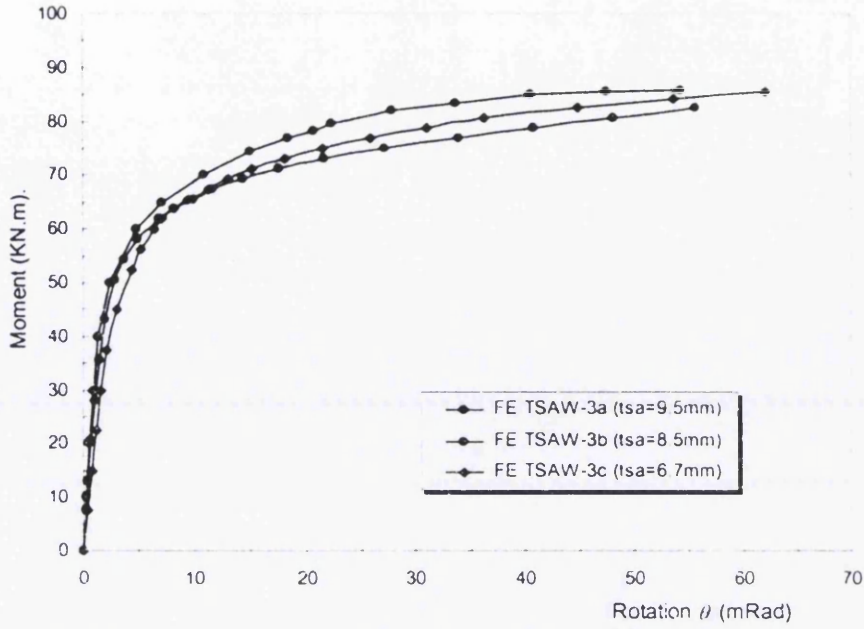


Figure 5.26. $M-\theta$ relationship of the TSAW-3 model with various angle cleats

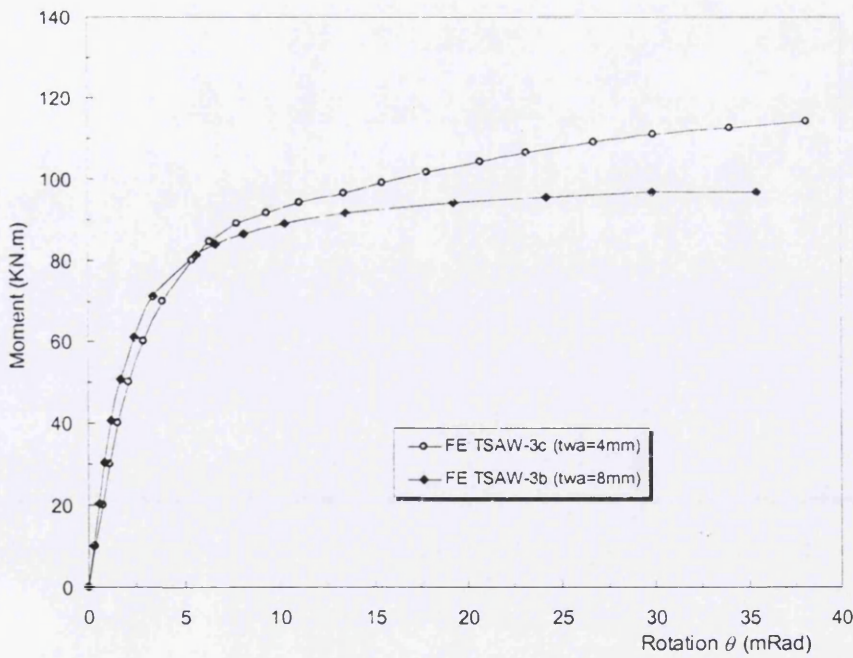


Figure 5.27 $M-\theta$ relationship of the TSAW-3 model; various web angles

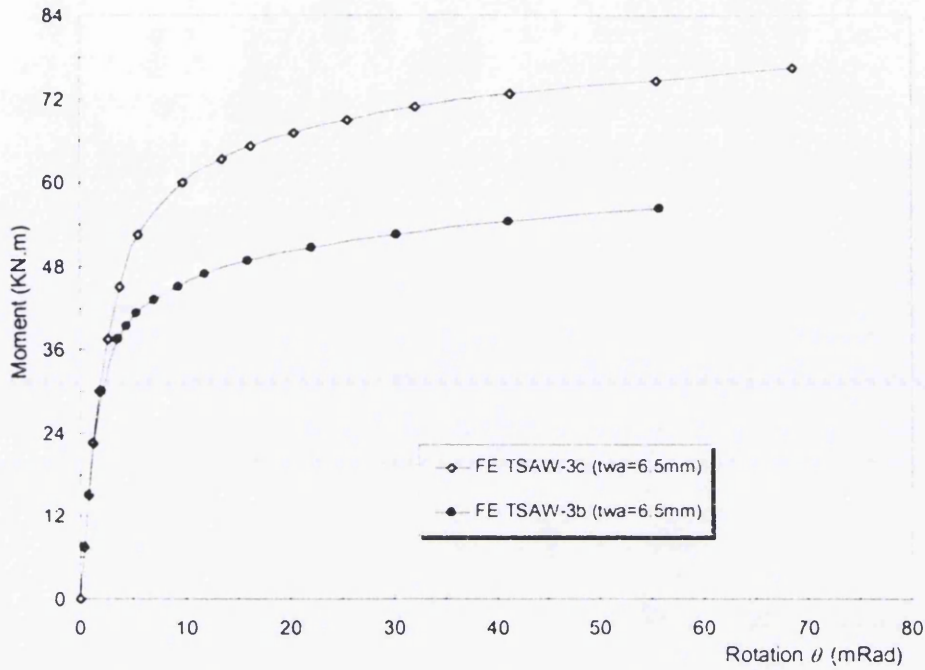


Figure 5.28 $M-\theta$ relationship of the TSAW-3 model; S690 and S460 angle cleats

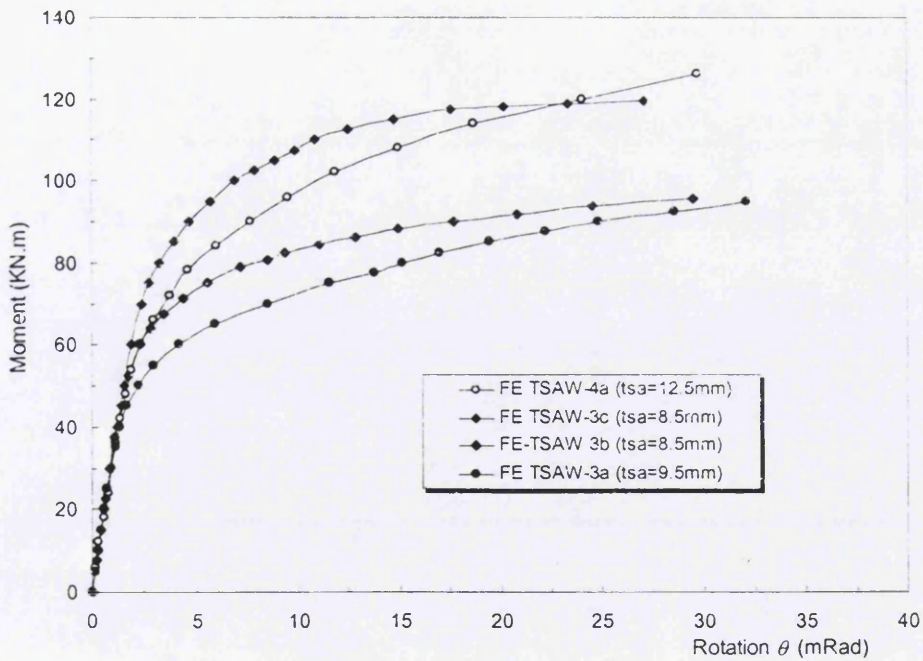


Figure 5.29 Comparison of the TSAW $M-\theta$ relationship

In order to investigate the behaviour of the connection, the stress contours of angles are compared for top angle and web angle. The equivalent stress of the TSAW connection at the ultimate load for the S275 web angle, S275 column and S690 top angle is close to the ultimate stress, as shown in Figures 5.30 – 5.31. The resistance of web angles to connection deformation contributes largely to the connection capacity. The slippage is less pronounced with maintaining the thickness and yield stress of the web angle. The maximum plastic strain of the TSAW model at the ultimate load until slip occurs for both top and web angles is close to the equivalent plastic strain limit. The geometry of the connection is still governed by top angle. The patterns of plastic equivalent strain of S460 and S690 top angles are very similar, in general. Figure 5.32 illustrates the maximum plastic strain of top angle is located at a corner of angle and below the bolt hole.

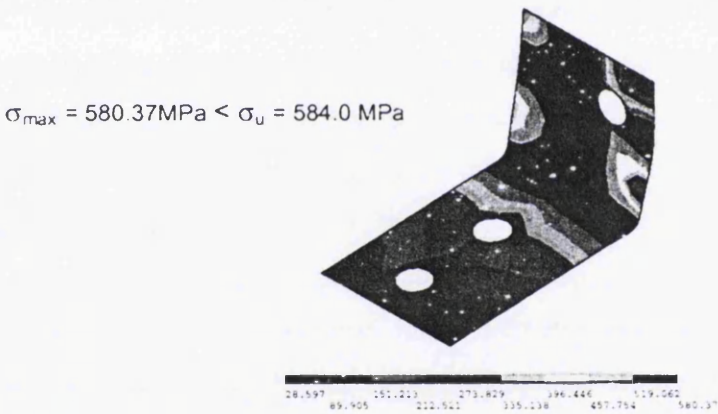


Figure 5.30 Stress contours of S460 top angle at ultimate moment; unit in MPa

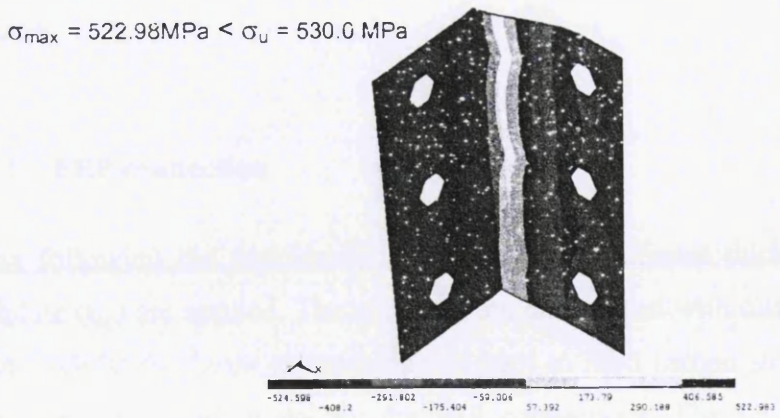


Figure 5.31 Stress contours of the S275 web angle at ultimate moment; unit in MPa

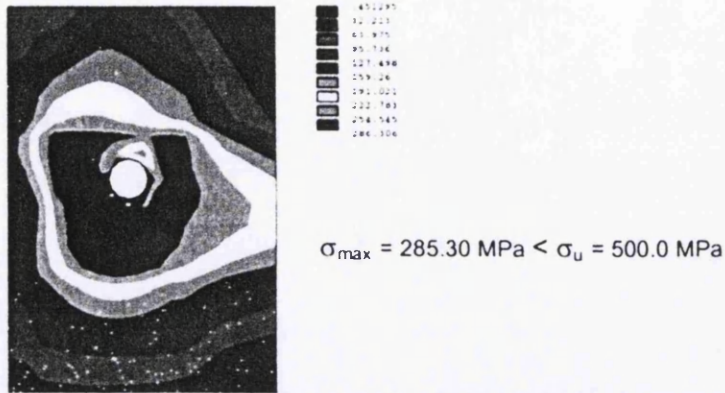


Figure 5.32 Stress contours of the S275 column flange; unit in MPa

5.3 Endplate Connection

As the initial stiffness of the endplate connection is governed by the geometry of the endplate, the non-linear behaviour is related to material properties. To establish the effects of endplate configurations, plate thickness and strength are selected as two main parameters. Multi-linear elastic-plastic approach is used to determine the material properties of high strength steel for the FE model, whilst the yield stress is defined as 0.2% proof stress. By these parameters combination, various moment-rotation curves can be obtained from 3D nonlinear finite elements analyses. In order to increase the connection capacity, the higher strength endplates are applied with different thickness. Bolt gauge, bolt spacing and bolt diameter are kept in the same value. Plots of the Von Mises equivalent stress and plastic strain were used to assess the predicted yield line patterns.

5.3.1 FEP connection

After following the procedures in section 3.5.4, different thickness of higher strength endplate (t_{ep}) are applied. The endplates are determined with different high strength steel grade, whilst the beam and column are kept to mild carbon steel. Table 5.5 shows the configuration of FE model for the FEP connections. The FEA results are shown in Figures 5.33 – 5.36

Table 5.7
FEP configuration parameter for FEA

| connection destination | beam grade | beam size | stiffener (mm) | endplate grade | t_{ep} (mm) | g (mm) | p (mm) |
|------------------------|------------|--------------|----------------|----------------|---------------|--------|--------|
| FEP-1a | S275 | IPE240 | - | S550 | 15.0 | 98.0 | 158.0 |
| FEP-1b | S275 | IPE240 | 10.0 | S550 | 15.0 | 98.0 | 158.0 |
| FEP-1c | S275 | IPE240 | - | S690 | 15.0 | 98.0 | 158.0 |
| FEP-1d | S275 | IPE240 | 10.0 | S690 | 15.0 | 98.0 | 158.0 |
| FEP-1d* | S355 | IPE240 | 10.0 | S690 | 12.0 | 98.0 | 158.0 |
| FEP-1e* | S355 | IPE240 | 10.0 | S550 | 15.0 | 98.0 | 158.0 |
| FEP-1f* | S355 | IPE240 | 10.0 | S690 | 15.0 | 98.0 | 158.0 |
| EP-1g* | S355 | IPE240 | 10.0 | S550 | 18.0 | 98.0 | 158.0 |
| FEP-2a | S355 | 406x178x60UB | - | S550 | 15.0 | 98.0 | 158.0 |
| FEP-2b | S355 | 406x178x60UB | 10.0 | S550 | 15.0 | 98.0 | 158.0 |
| FEP-2c | S355 | 406x178x60UB | - | S690 | 15.0 | 98.0 | 158.0 |
| FEP-2d | S355 | 406x178x60UB | 10.0 | S690 | 15.0 | 98.0 | 158.0 |
| FEP-3a | S355 | HE320A | - | S690 | 10.0 | 150.0 | 160.0 |
| FEP-3b | S355 | HE320A | - | S690 | 15.0 | 150.0 | 160.0 |
| FEP-3a* | S355 | HE320A | - | S690 | 10.0 | 150.0 | 160.0 |
| FEP-3b* | S355 | HE320A | - | S690 | 15.0 | 150.0 | 160.0 |

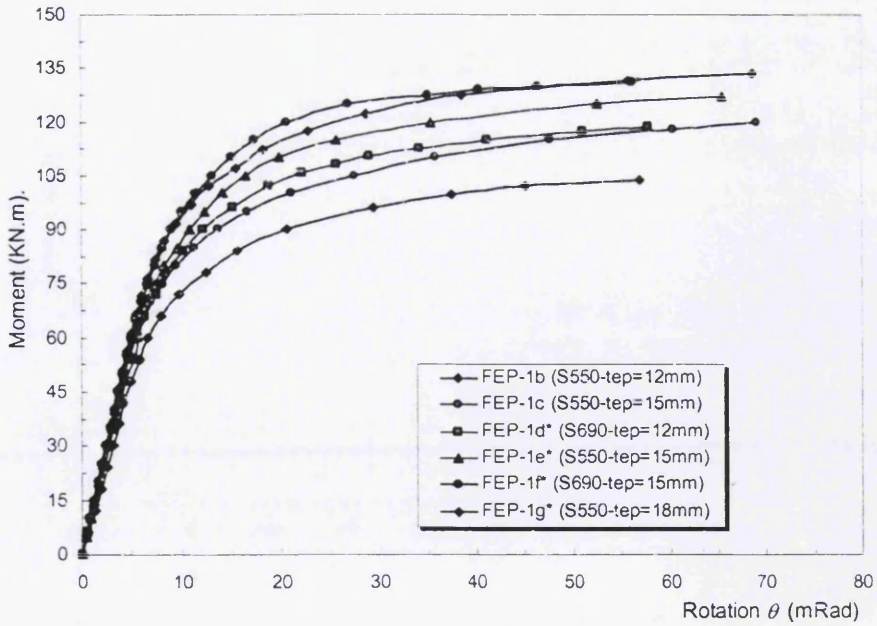


Figure 5.33 Moment-rotation relationship of the FEP-1 model; M22 bolts

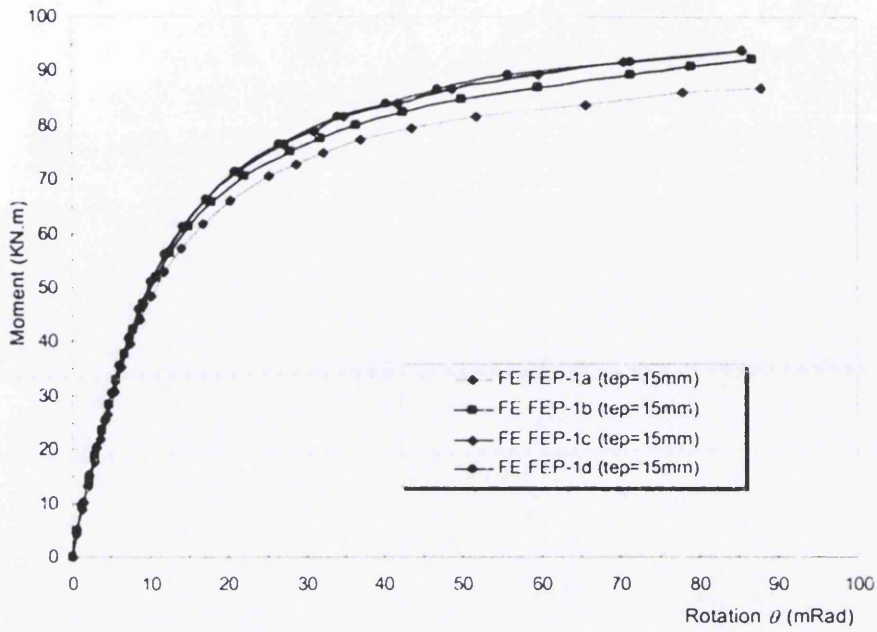


Figure 5.34 Moment-rotation relationship of the FEP-1 model; M20 bolts

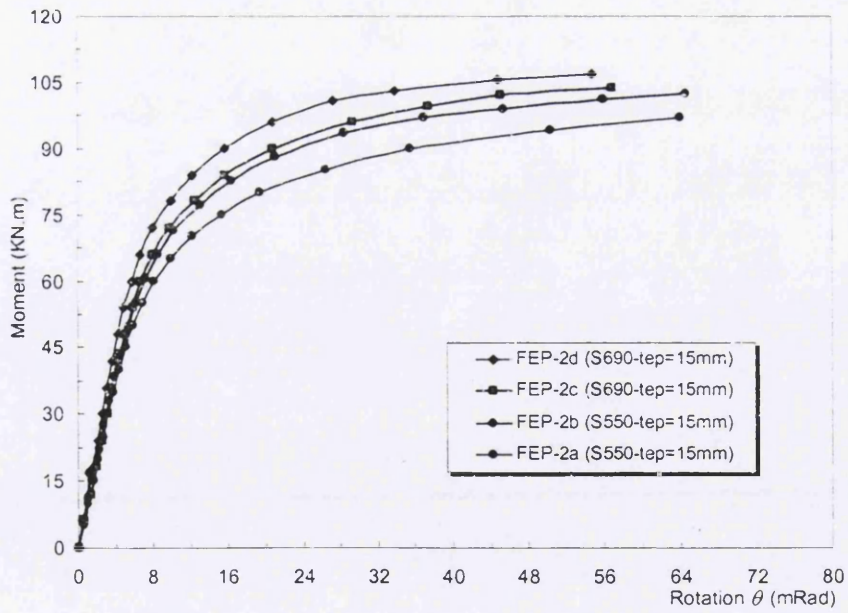


Figure 5.35 Moment-rotation relationship of the FEP-2 model; M20 bolts

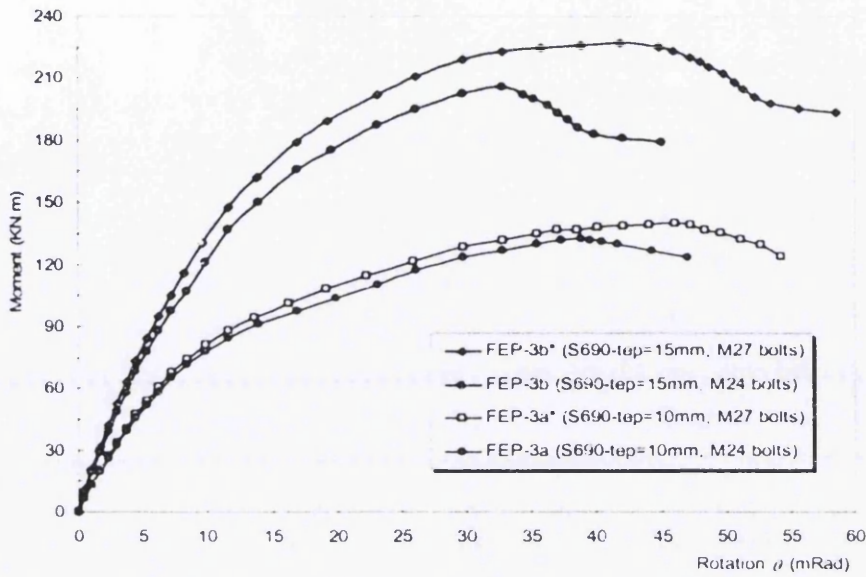


Figure 5.36 Moment-rotation relationship of the FEP-3 model; M24 bolts

The flush end-plate connections based on FE modelling with stiffened and un-stiffened column are also analyzed using design equations to modern design codes EC3 [97]. The design tension resistance of the column flange and of the end plate are given in terms of equivalent T-stub. The effective length ℓ_{eff} of plate and column flange is based on the yield line patterns around bolt holes and should be taken as the height of the end plate d as shown in Figure 5.37. The three possible modes of the yielding of the connection are considered, as shown in Figure 5.14. Moment resistance of the FEP connection is derived from Equations 5.2 – 5.4.

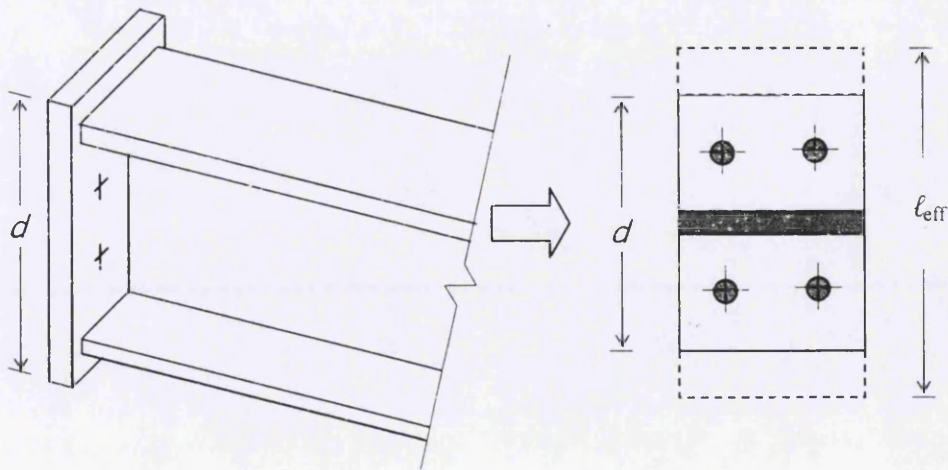


Figure 5.37 Effective length ℓ_{eff} of equivalent T stub

Table 5.8

Ultimate moment and failure mode of FEP model

| connection destination | column (stiffened) | endplate (mm), grade | M _{ult} (FE) (KN.m) | M _{ult} (EC3) (KN.m) | Failure mode |
|------------------------|--------------------|----------------------|------------------------------|-------------------------------|-------------------|
| FEP-1a | S275 (n) | 15.0, S550 | 96.0 | 80.2 | column flange (2) |
| FEP-1b | S275 (s) | 15.0, S550 | 102.3 | 81.7 | column flange (2) |
| FEP-1c | S275 (n) | 15.0, S690 | 103.8 | 80.2 | column flange (2) |
| FEP-1d | S275 (s) | 15.0, S690 | 106.8 | 81.7 | column flange (2) |
| FEP-1d* | S275 (s) | 12.0, S690 | 107.0 | 91.3 | column flange (2) |
| FEP-1e* | S355 (s) | 15.0, S550 | 127.0 | 95.4 | end plate (2) |
| FEP-1f* | S355 (s) | 15.0, S690 | 130.0 | 102.7 | column flange (2) |
| FEP-1g* | S355 (s) | 18.0, S550 | 131.5 | 102.7 | column flange (2) |
| FEP-2a | S355 (n) | 15.0, S550 | 97.0 | 80.2 | end plate (1) |
| FEP-2b | S355 (s) | 15.0, S550 | 100.0 | 95.4 | end plate (2) |
| FEP-2c | S355 (n) | 15.0, S690 | 104.5 | 95.4 | column flange (2) |
| FEP-2d | S355 (s) | 15.0, S690 | 106.8 | 102.7 | column flange (2) |
| FEP-3a | S355 (n) | 10.0, S690 | 132.6 | 104.8 | end plate (1) |
| FEP-3b | S355 (n) | 15.0, S690 | 205.7 | 194.1 | bolt failure (2) |
| FEP-3a* | S355 (n) | 10.0, S690 | 139.7 | 104.8 | end plate (1) |
| FEP-3b* | S355 (n) | 15.0, S690 | 227.7 | 194.1 | column flange (2) |

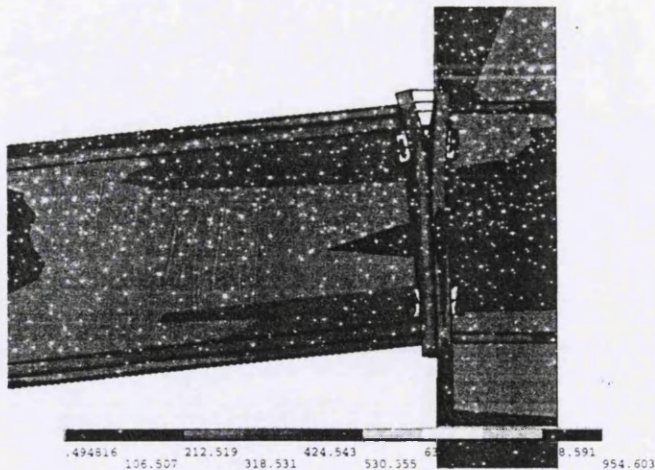


Figure 5.38 Stress contours of the FEP model with S275 column; unit in MPa

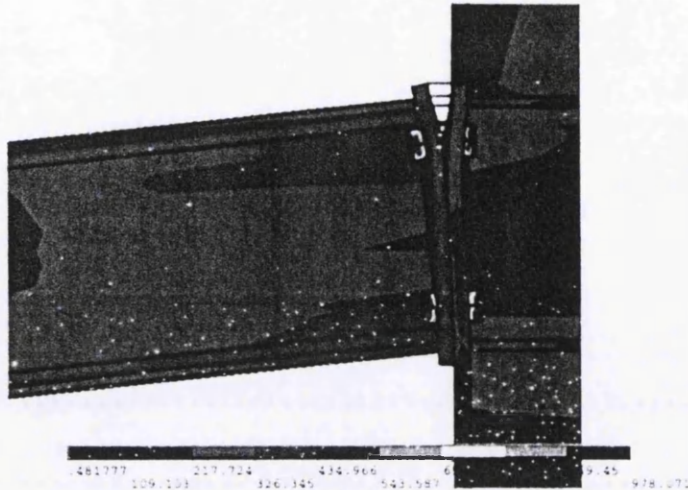


Figure 5.39 Stress contour of the FEP model with S355 column; unit in MPa

From the results in Table 5.8, it can be seen that the designs are somewhat conservative despite the omission of factors of safety. The FE model of the FEP connection with thin end plate and low beam depth shows significant results close to EC3 prediction, and also for connection with thicker angle and higher beam depth. Modern design methods such as EC3 use yield line analyses of the end plate to predict the capacity of the tensile region. At the ultimate load, the failure mode type 1) which is complete yielding of the column flange occurred for almost all of the FEP connection except for thinner S550 and S690 angle of the FEP connection on the end plate. The finite element model was used to confirm the predictions by studying the yielding of the end plate and column flange.

Waving of column web stiffeners is not advisable because their absence causes premature failure in the column flange. This consequently leads to a drastic drop in moment and rotation capacities. The ultimate moment of S690 15.0mm thick end plate without column stiffener reached 96.0 KN.m, and it can be increased by 102.3 KN.m if the column stiffeners exist. However, a connection with column web stiffeners is advisable because their presence increases moment capacity up to 20%.

Plots of von Mises' stress contours of the FEP connection with S275 and S355 column are shown in Figures 5.38 and 5.39, respectively. Plots of von Mises' stress contour of the FEP connection with the 15mm thick S690 end plate and S355 column are

presented in Figure 5.40. Plastic deformation of S690 end plate is shown in Figure 5.41. The maximum stress of endplate and the ultimate stress of column flange closely reach the ultimate stress and also for the column flange stress. The ratio between maximum stress and the ultimate stress of the endplate is 99.0%, whilst the ratio between maximum stress and the ultimate stress of the column flange is 86.0%.

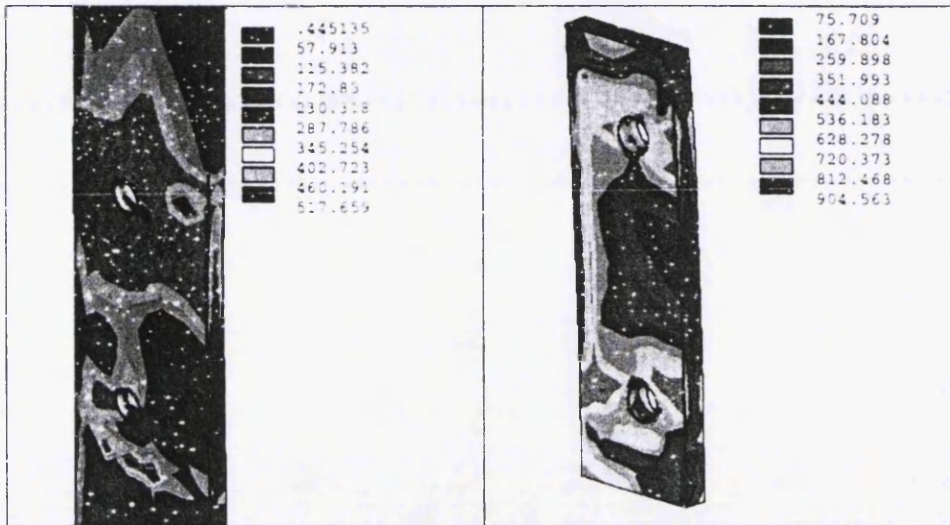


Figure 5.40 Stress contour of the S355 column flange and S690 endplate; unit in MPa

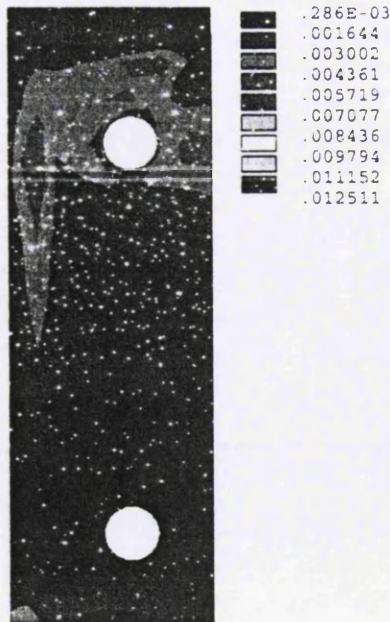


Figure 5.41 Plastic deformation of the S690 endplate

5.3.2 EPTB connection

All steel material properties of the connection for FEA used are S355 and M20 bolts grade 10.9. The higher strength of steel materials are employed to endplate with S550 and S690, as shown in Table 5.9. Multilinear elastic-plastic approach is used to determine the material properties of high strength steel for the FE model, whilst the yield stress is defined as 0.2% proof stress. Strength enhancement of the corner regions of hollow section beam is employed to the material properties of FE model.

Table 5.9
Material properties for FE model

| specimen | steel grade | E (MPa) | σ_y (MPa) | σ_u (MPa) |
|-------------------|-------------|---------|------------------|------------------|
| SHS beam (flat) | S355 | 205,000 | 398.0 | 430.0 |
| RHS beam (flat) | S355 | 205,000 | 370.0 | 446.0 |
| SHS beam (corner) | S355 | 208,000 | 467.0 | 511.0 |
| RHS beam (corner) | S355 | 208,000 | 444.0 | 482.0 |
| bolt | Grade 10.9 | 200,000 | 940.0 | 1070.0 |
| end plate (i) | S550 | 205,000 | 580.0 | 680.0 |
| end plate (ii) | S690 | 202,000 | 700.0 | 780.0 |

Two different high strength endplates are applied for the FE models, whilst the beams are kept to mild carbon steel S355 grade. Two types of endplate connection are investigated such as EPTBa with RHS beam 100x200x9mm and EPTBb with SHS beam 150x150x9mm. Moment rotation curves in Figures 5.42 – 5.46 shows that resistance of higher strength end plate may increase moment capacity by up to 50% for S550 endplate and up to 65% for S690. The maximum stress of the beam shows the value below the yield stress, whilst the maximum stress of the endplate reach close to the yield stress.

In order to investigate the connection behaviour due to the bolt spacing and beam geometry, different thicknesses and high strength endplates are applied to the FE model. Effect of endplate thickness and strength is more important on the moment capacity and rotational capacity with the thinner endplate. The initial stiffness is slightly higher with the thicker endplates, whilst the rotational capacity is lower. The result shows that the EPTBa with S550 plate increases the moment capacity by up to 50 % whilst the S690

endplate reach the ultimate moment by nearly two third as much as S355 endplate, respectively. The moment capacity is much higher by up to 50% for thicker endplate with S690 endplate compared to S355 one, whilst it is only up to 40% for thicker S550 endplate, due to the lower resistance of the plate and bolts as depicted in Table 5.10. The variation in the EPTB connection with RHS and SHS beam response due to the change in the endplate thickness and strength is shown in Figures 5.42 – 5.45.

Table 5.10
Moment capacity and failure mode

| connection destination | bolt spacing (mm) | thickness (mm) - grade | M_{ult-FE} (KN.m) | failure mode |
|------------------------|-------------------|------------------------|---------------------|--------------|
| EPTBa-1b | 100.0 | 15.0 – S550 | 101.56 | deformation |
| EPTBa-5b | 100.0 | 10.0 – S550 | 61.22 | bolt |
| EPTBa-3c | 100.0 | 11.0 – S690 | 80.84 | deformation |
| EPTBa-7c | 100.0 | 9.0 – S690 | 57.34 | deformation |
| EPTBb-2b | 150.0 | 14.0 – S550 | 93.91 | bolt |
| EPTBb-6b | 150.0 | 10.0 – S550 | 55.01 | deformation |
| EPTBb-4c | 150.0 | 11.0 – S690 | 73.25 | deformation |
| EPTBb-8c | 150.0 | 9.0 – S690 | 52.12 | deformation |

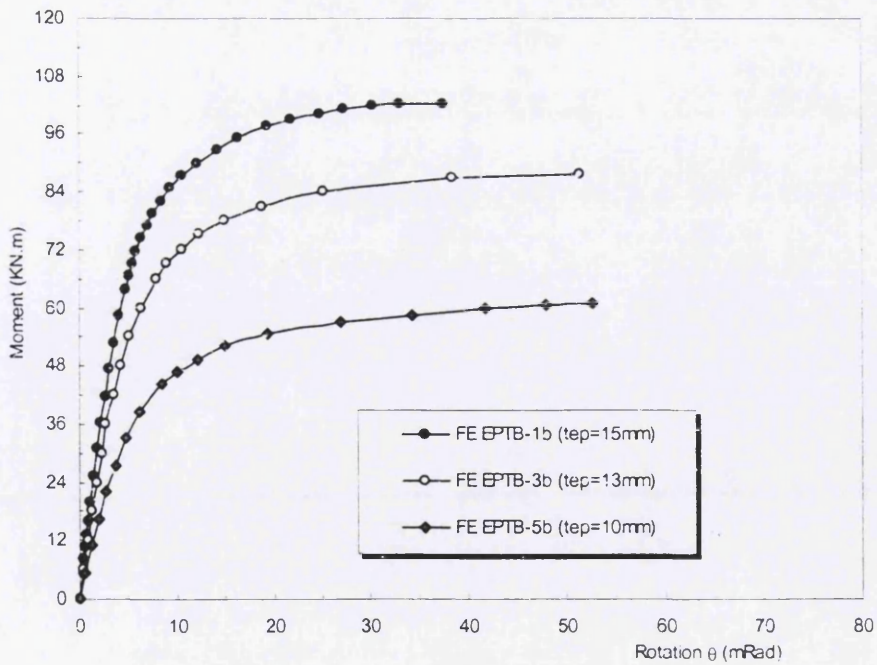


Figure 5.42 M- θ relationship of the EPTBa connection; S550 endplate

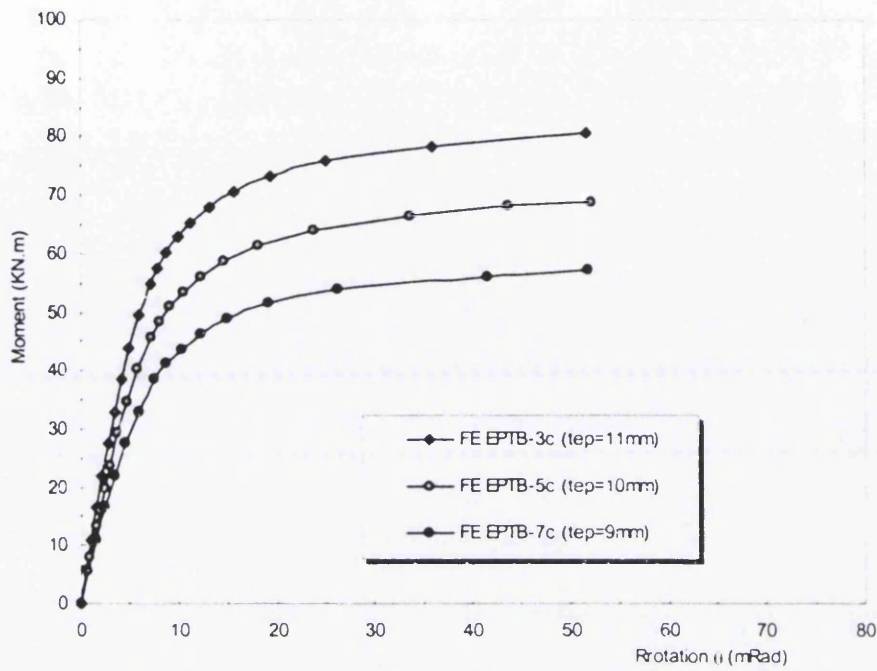


Figure 5.43 M- θ relationship of the EPTBa connection; S690 endplate

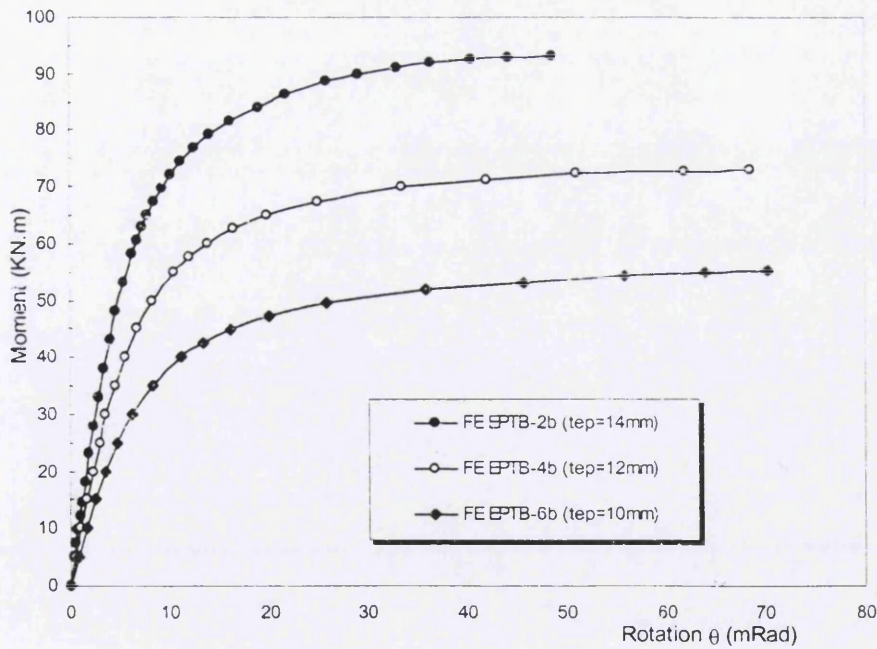


Figure 5.44 M- θ relationship of the EPTBb connection; S550 endplate

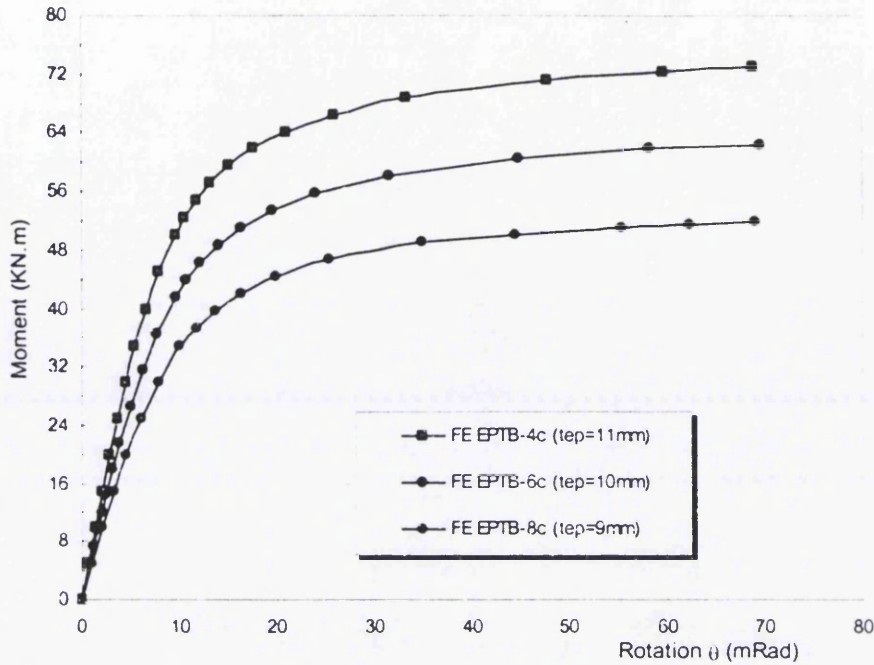


Figure 5.45 M- θ relationship of EPTBb connection; S690 endplate

The fully FE model and its deformed shape of the connection with S550 12.0mm thick endplate is presented in Figure 5.46. The S690 thicker endplate with 15.0mm thick is applied to the connection in order to enhance connection resistance. Significant response from thicker endplate gives a connection capacity which has increased significantly with a reduced response of deformation.

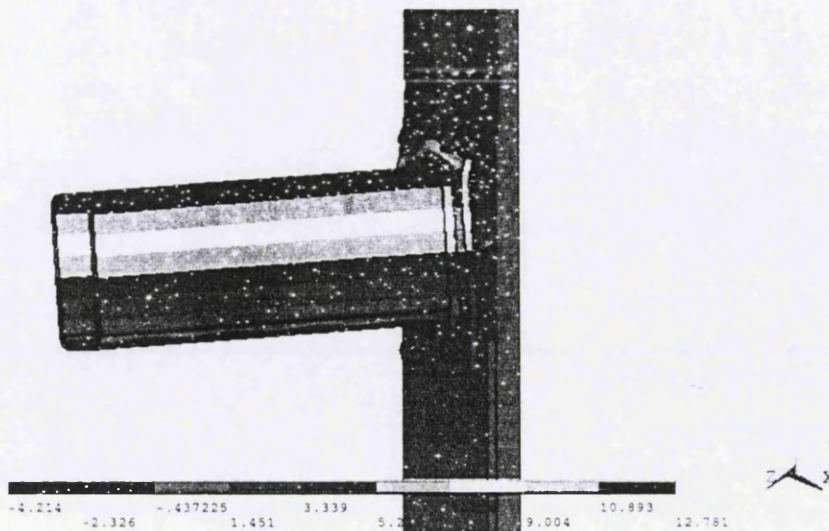


Figure 5.46 3D finite element of the endplate model with deformed shape; unit in mm

A plot of the Von Mises equivalent stress of the EPTB connection with 10mm S690 end plate is presented in Figure 5.47. The maximum stress of the endplate is around 818.5 MPa, whilst the maximum stress of the beam is around 456.0 MPa. It can be seen that the model is successful in predicting maximum stress of all connection members almost reaching their ultimate stresses. The ultimate stress of the thin endplate is developing around the top corner of beam flange as shown in Figure 5.48. This stress distribution occurs due to excessive deformation of the end plate, whilst the yielding around bolt hole has just started. The deformation of the connection is governed by the deformation of the end plate that the maximum deformation in z-direction is around 13.5mm at the top flange of the beam.

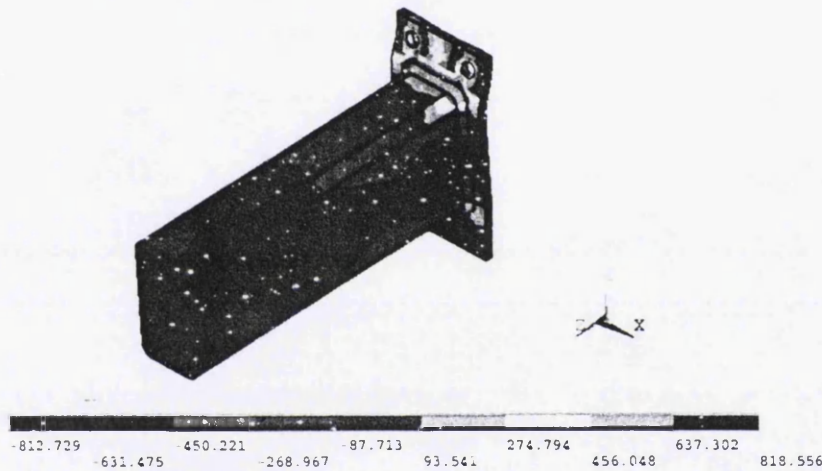


Figure 5.47 Stress contours of the S690 endplate connection; unit in MPa

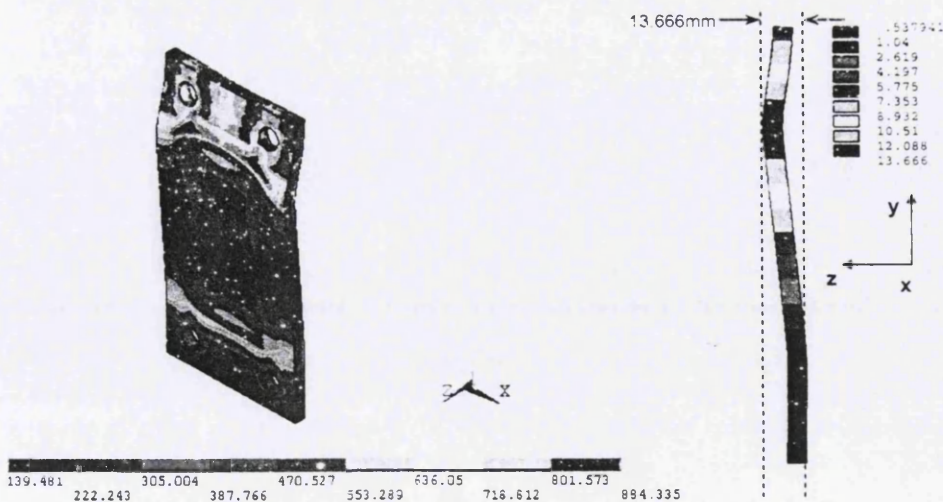


Figure 5.48 Stress contours of the S690 thin endplate with deformed shape

Plots of the von Mises' stress contour of the EPTBa connection with 15mm S355 and S690 endplate is presented in Figure 5.49. The maximum stresses of endplate reaches very close to the ultimate stresses. The yielding in the thin plate is developing around the top corner of the beam, whilst that of thick high strength plate is also centralized around the bolt hole. Application of high strength plate to the connection configuration gives significant proportion of maximum stress distribution.



Figure 5.49 Stress contours of the endplate with RHS beam: S355 and S690-15mm

Plots of the von Mises' stress contour of the EPTBb connection with 15mm S550 and 12mm S690 endplate is presented in Figure 5.50. The maximum stress of S550 endplate reaches very close to the ultimate stress, whilst that of S690 reaches 85% of the ultimate stress due to bolt failure. The yielding in the thicker plate is fully centralized around the bolt hole due to delaying the yield line until after the bolts have begun to yield. This response shows that for the higher thick endplate the yield pattern is not so crucial because failure should occur through the bolts. Lower depth of beam and higher horizontal bolt spacing gives low response to the connection capacity with lower ultimate moment and higher rotational capacity due to excessive deformation.

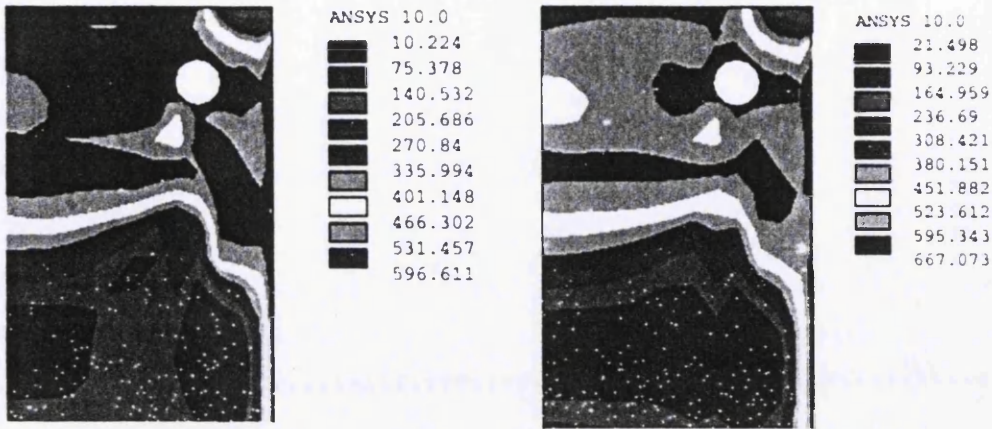


Figure 5.50 Stress contours of the endplate with SHS beam: S550-15mm and S690-12mm

5.3.3 SCC connection

After following the procedures in section 3.5.5, different thicknesses of higher strength endplates (t_{ep}) are applied. The endplates are defined with S690 high strength steel grade, whilst the beam and column are kept to mild carbon steel. Multilinear elastic-plastic approach is used to determine the material properties of high strength steel for the FE model, whilst the yield stress is defined as 0.2% proof stress. The steel properties of S690 end plate having a Young's modulus of 202000 MPa and a Poisson ratio of 0.3 The yield stress of S690 (σ_y) is 780.0 MPa, whilst the ultimate stress (σ_u) is 840.0 MPa.

Two types of semi-continuous composite connection are investigated such as SCC1 for un-stiffened column and SCC2 for stiffened column. There is no former concrete slip considered to take into account. Moment rotation curves in Figure 5.51 shows that resistance of higher strength endplate of the un-stiffened SCC connection increase moment capacity slightly. Moment capacity of S690 20.0 mm thick endplate (233.0 KN.m) increases by only 3% compared to S690 10.0 mm thick endplate. When the endplate thickness is doubled to 20 mm gives no significant resistance due to less response from un-stiffened column. Figure 5.52 shows that resistance of higher strength endplate with stiffened column may increase moment capacity by up to 15%.

In order to investigate the connection behaviour due to the stiffener, different thicknesses and high strength endplates are applied to FE model. The effect of endplate

thickness and strength is more pronounced on the moment capacity and rotational capacity with the thinner one. The initial stiffness is slightly higher for stiffened column connection (73.7 KN.m/mRad). The response from stiffened column may increase moment capacity by up to 20% (288.0 KN.m). Double thicker endplate may increase moment capacity up to 8% with maximum stress reach just below the ultimate stress. The maximum stress of the beam shows the value still below the yield stress, whilst column flange maximum stress reach beyond the yield stress.

The initial stiffness is slightly higher with the thicker endplate, whilst the rotational capacity is lower. The result shows that the 12mm endplate of un-stiffened SCC connection increase the moment capacity by up to 2% whilst 15mm endplate reach the ultimate moment by nearly 4% as much as 10mm endplate, respectively. The moment capacity of stiffened SCC connection is much higher by up to 20% for thinner plate with S690 endplate, whilst it is only up to 15% for thicker S690 plate due to the lower resistance of the column flange and bolts. The variation in the connection with stiffened column flange response due to the change in the endplate thickness and strength is shown in Figure 5.52.

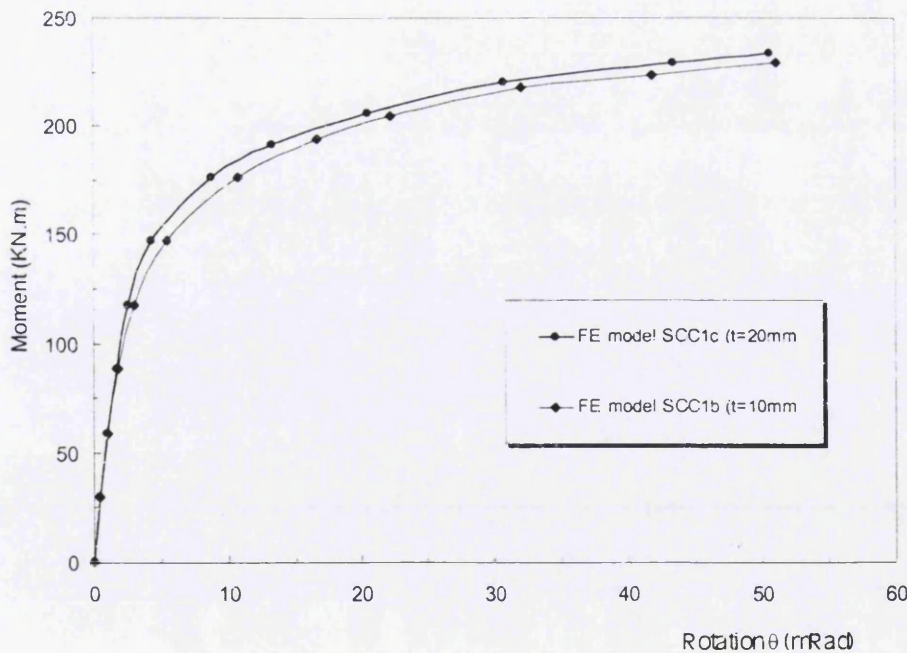


Figure 5.51 M- θ relationship of the un-stiffened SCC connection; S690 endplate

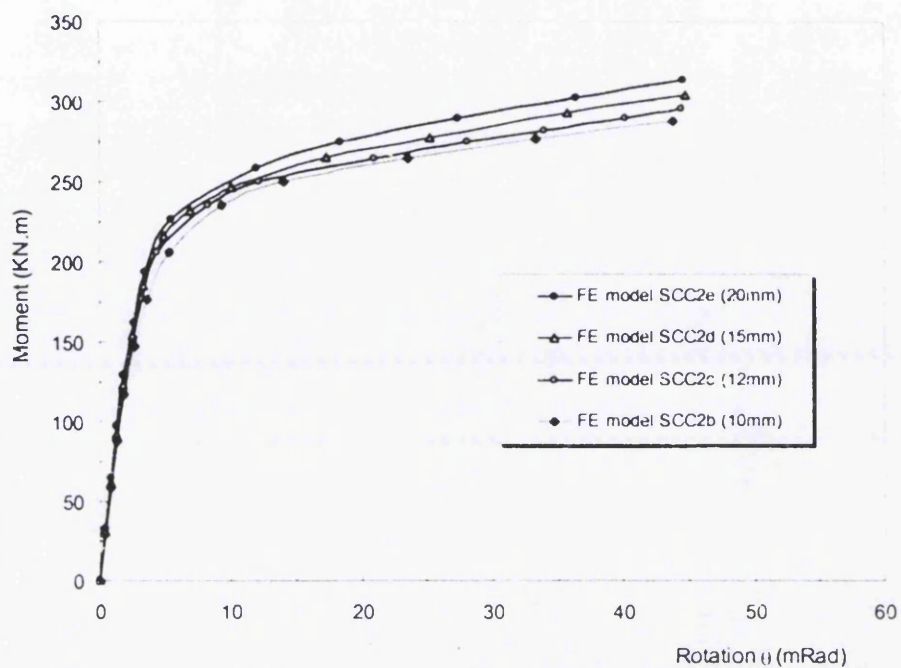


Figure 5.52 M- θ relationship of the stiffened SCC connection; S690 endplate

Table 5.11

SCC connection performance for FE model

| FE model | Initial stiffness (KN.m/mRad) | Moment capacity S275 (KN.m) | Moment capacity S690 (KN.m) |
|-----------|----------------------------------|--------------------------------|--------------------------------|
| SCC1-10mm | 66.33 | 207.2 | 229.2 |
| SCC1-12mm | 68.83 | 213.3 | 230.2 |
| SCC1-15mm | 70.84 | 216.7 | 231.7 |
| SCC1-20mm | 72.80 | 220.2 | 233.4 |
| SCC2-10mm | 73.71 | 243.1 | 288.1 |
| SCC2-12mm | 77.17 | 255.5 | 295.5 |
| SCC2-15mm | 81.05 | 267.1 | 304.1 |
| SCC2-20mm | 84.71 | 278.3 | 313.7 |

The ultimate moment of S690 10.0mm thick endplate without column stiffener reached 229.2 KN.m, and it can be increased to 288.1 KN.m if the column stiffeners exist. The ultimate moment of S690 12.0mm thick endplate without column stiffener reached 230.2 KN.m, and it can be increased to 295.5.1 KN.m if the column stiffeners exist. However, the connection with column web stiffeners is advisable because their presence increases moment capacity up to 25%.

The FE model and its deformed shape of the stiffened connection with 20mm S690 endplate are presented in Figure 5.53. Stiffener 12.0mm thick is applied to the column flange in order to enhance connection resistance. Significant response from composite action and column stiffener increases connection capacity significantly. Also it is observed that, the waiving of column web stiffeners is not advisable because their absence causes premature failure in the column web. This consequently leads to a drastic drop in moment and rotation capacities.

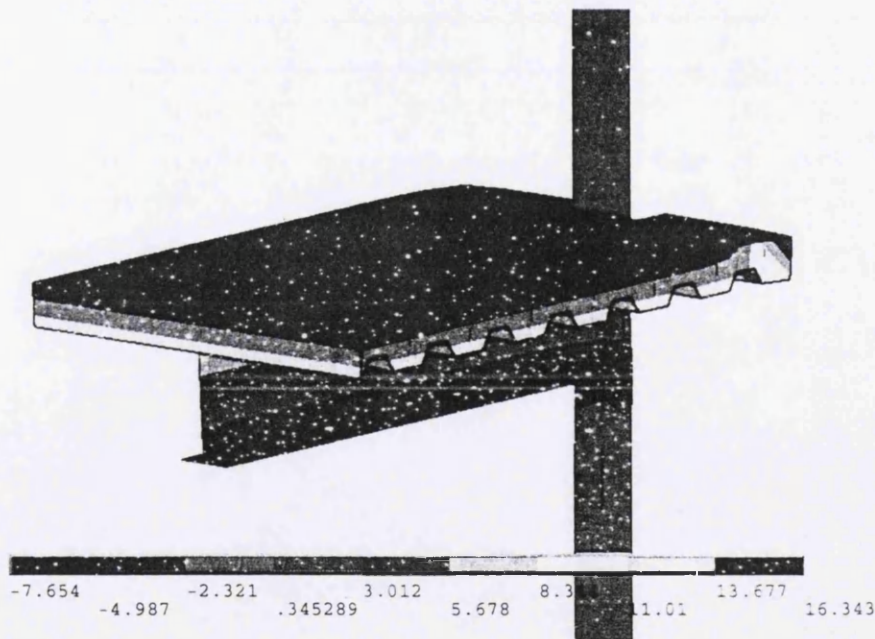


Figure 5.53 Deformed shape of the SCC model; unit in mm

Plots of Von Mises equivalent stress of the SCC connection showing bare steel joint only with S690 20mm thick endplate and S355 column is presented in Figure 5.54.

It can be seen that the model is successful in predicting maximum stress of all connection members below their ultimate stress. The maximum stress of the endplate reaches below the ultimate stress and also for the column flange stress. The response from stiffener and high strength endplate gives a moment connection capacity increase significantly. Figures 5.55 and 5.56 show equivalent Von Mises stress distribution of the SCC connection without and with column web stiffener.

The maximum stress of high strength thick endplate reaches just below the ultimate stress. The maximum stress of the beam shows the value beyond the yield stress, whilst column flange maximum stress reach just below the ultimate stress. It is clearly noticed that application of the thicker endplate changes the yielding sequence of endplate (in bending) and column flange (in bending). The response of beam flange (in compression) shows early yield due to thicker plate applied, whilst the maximum stress is close to its ultimate stress. The high strength endplates give significant proportion of maximum stress distribution, whereas the beam and column are kept with mild carbon steel. Figure 5.57 shows stress contour of the S690 thinner endplate. Figure 5.58 shows stress contour of the S690 thicker endplate.

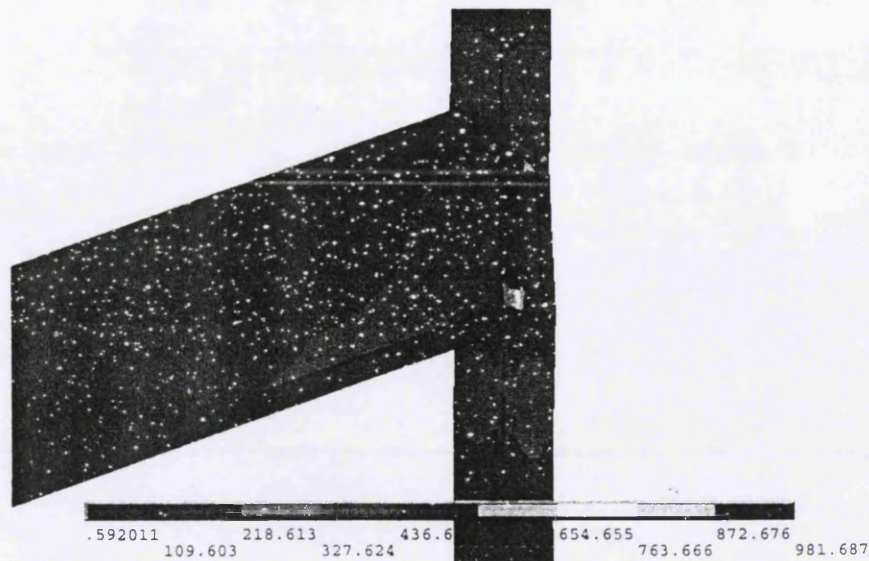


Figure 5.54 Stress contour of the bare steel joint with the S690 endplate; unit in MPa

NODAL SOLUTION
STEP=1
SUB =10
TIME=10
SEQV (AVG)
DMX =49.085
SMN =.450289
SMX =1088

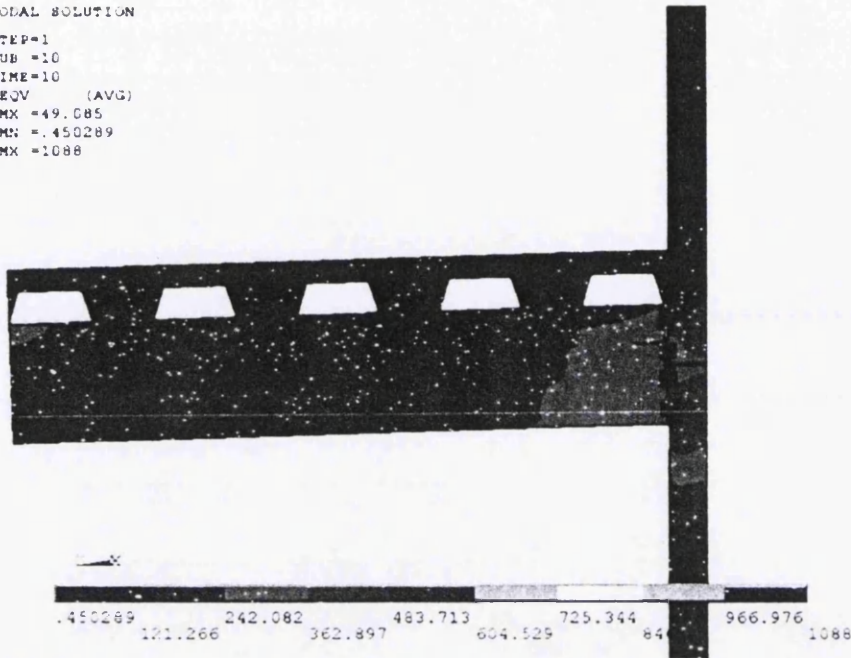


Figure 5.55 Equivalent Von Mises stress distribution in of the SCC1b – without stiffener

NODAL SOLUTION
STEP=1
SUB =12
TIME=10
SEQV (AVG)
DMX =67.901
SMN =.391885
SMX =982.813

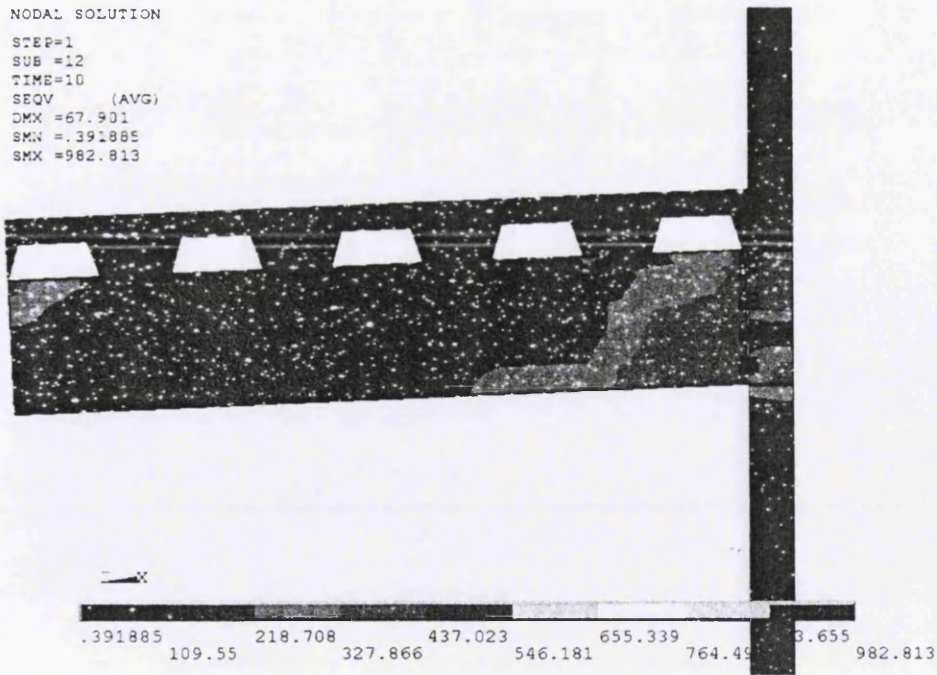


Figure 5.56 Equivalent Von Mises stress distribution in of the SCC2b – web stiffener

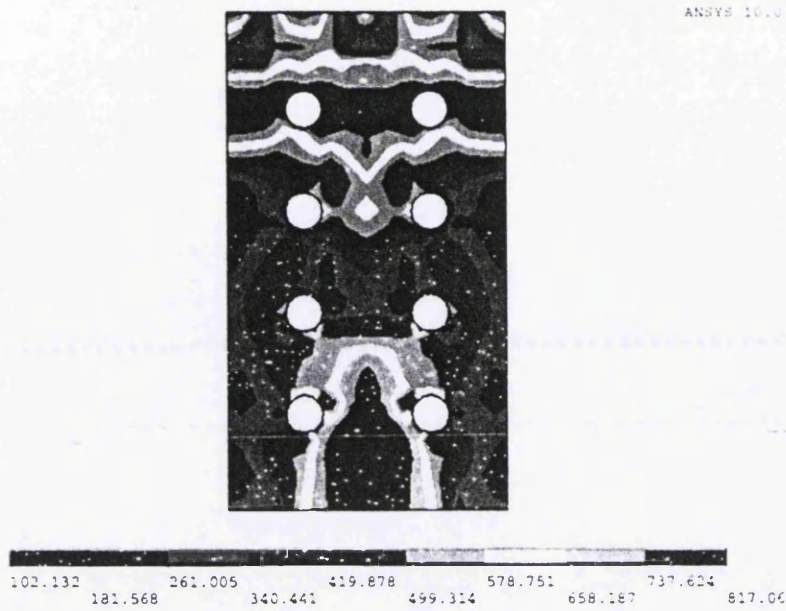


Figure 5.57 Stress contours of the connection with S690 thinner endplate; unit in MPa

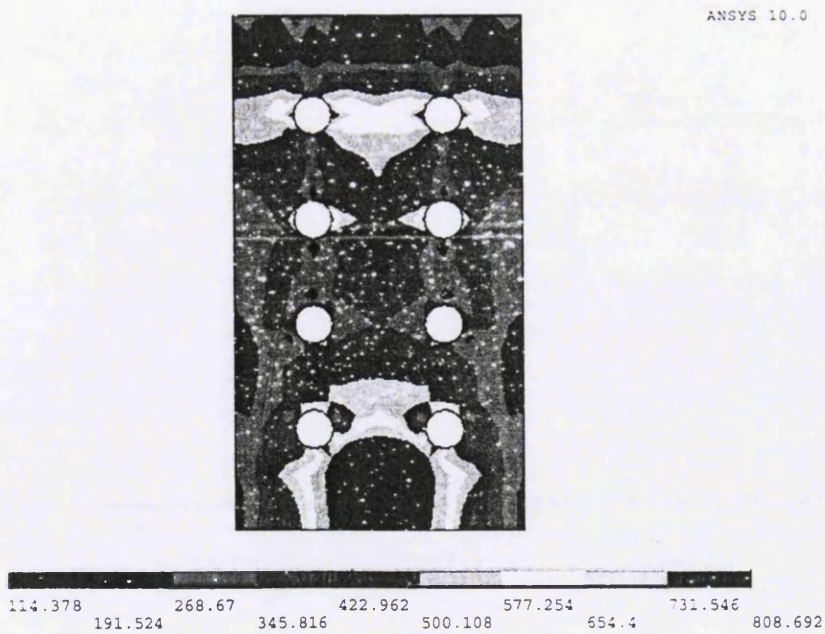


Figure 5.58 Stress contours of the connection with S690 thicker endplate; unit in MPa

In order to investigate the behaviour of the connection, the stress contours of angles are compared with those of the column flange. The patterns of stress contours of column flanges and endplates with different grade and thickness of endplates are very similar in general with differences only in the value and the spread of plasticity. The stresses of S690 endplate and S355 column flange, as was expected, are less than the ultimate stresses. Figure 5.59 shows that the maximum stresses of endplate are located at both sides of the bolt holes. Application of a high strength endplate to the connection configuration gives significant proportion of maximum stress distribution of the endplate and column close to their ultimate stress, whereas the beam and column are kept to carbon steel.

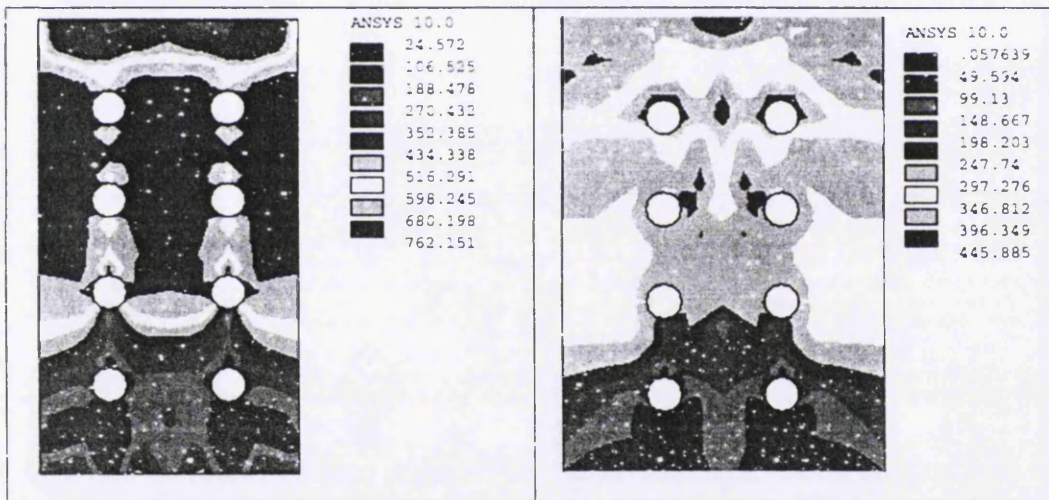


Figure 5.59 Stress contours of the S690 endplate and S355 column; unit in MPa

In order to investigate further the difference between the response of endplates with different grades and thicknesses, the plastic equivalent strain fields are compared in Figure 5.60. The plastic strain contours with two different steel grades are shown. The plastic strain values reach at almost the ultimate plastic strain until an earlier failure occurs because of stress concentration and ductility problem, whilst the value of maximum equivalent plastic strain is only at around 3.5×10^{-2} radian until bolt failure occurs.

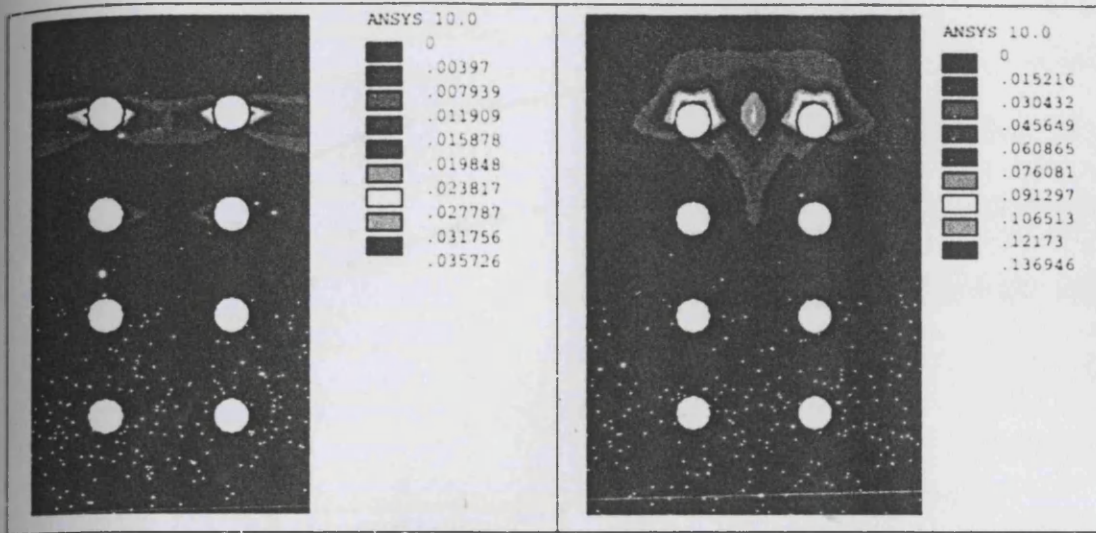


Figure 5.60 Plastic strain of the S690 endplate and S355 column; unit in MPa

In Figures 5.52 and 5.53, the moment-rotation curves of the SCC1b and SCC2b observed with the yielding sequence of several components during the FE study. It is clearly noticed that, in the SCC1b column web yields earlier than endplate, the column flange and other components, whereas this trend is entirely different in case of the SCC2b because of the web stiffener. In this case, yielding of the column web takes place with a higher initial moment capacity of 195 KN.m as compared to SCC1b i.e. 105 KN.m. However in both the cases, yielding of beam bottom flange and bolts are in last order. It is clearly observed that, if the thickness of endplate is less than the thickness of the column flange and higher than the column web, the yielding of the column web is prior to the endplate. As the thickness of endplate increases to be higher than the column flange (i.e. up to 40%) the trend of the yielding sequence is entirely different.

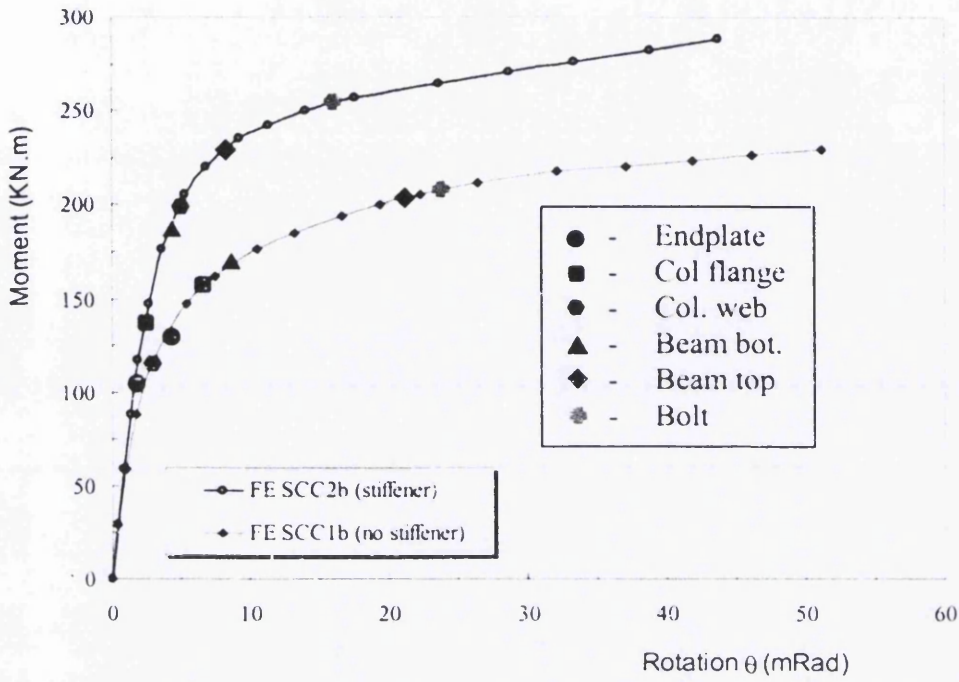


Figure 5.61 M- θ curve with yielding sequence of the components in FEA study.

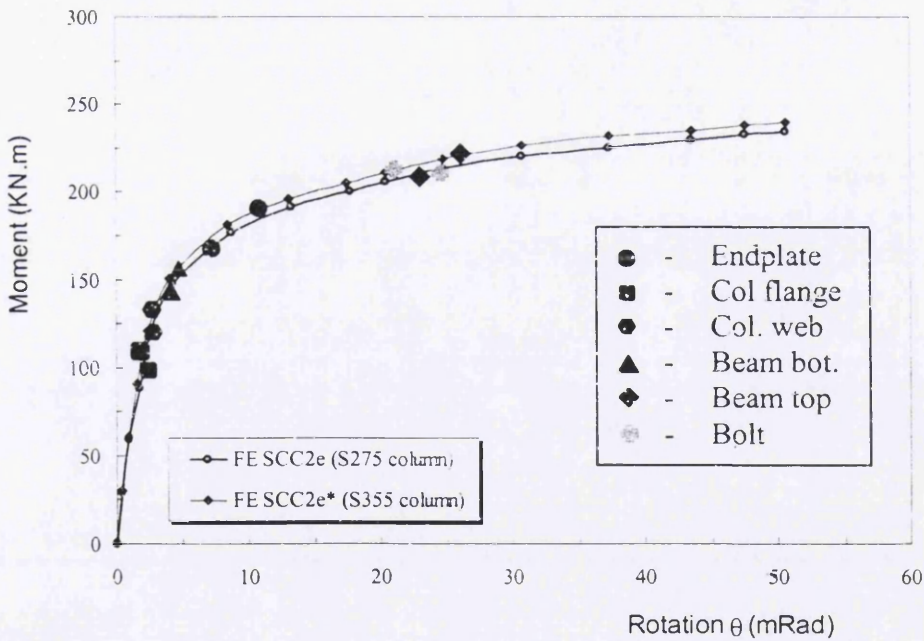


Figure 5.62 M- θ curve with yielding sequence of the components in FEA study.

Increasing the thickness of the endplate from 10 mm to 20 mm increases both the moment capacity and the rotation with almost the same percentage in the range of 20% to 30%. But the trend of the curves in all the cases follows the same patterns with a marginal increase in initial stiffness. In the case of thickness of plate almost twice than the column flange, it is found that, no advantage will be gained to increase the moment capacity of connection for S275 grade steel due to excessive deflection of the column flange and web. However, marginal increase in moment capacity can be achieved by increasing grade of steel to S355 in the column section only.

5.4 Shear Bolted Connection

After following the procedures in section 3.5.5, different thicknesses of higher strength spliced plate (t_p) are applied on the shear connection. The plates are determined with different high strength steel grade such as S690, stainless steel (SS) 2205, and very high strength steel (VHS) S1350. Multilinear elastic-plastic approach with softening region is used to determine the material properties of the plates for the FE model, whilst the yield stress is defined as 0.2% proof stress. The steel properties of S690 plate having a Young's modulus of 202000 MPa and a Poisson's ratio of 0.3. The yield stress of S690 (f_y) is 875.0 MPa, whilst the ultimate strength (f_u) is 915.0 MPa. The steel properties of stainless steel grade 2205 plate having a Young's modulus of 200000 MPa and a Poisson ratio of 0.3. The yield stress of SS 2205 (f_y) is 590.0 MPa, whilst the ultimate strength (f_u) is 740.0 MPa. The steel properties of VHS S1350 plate having a Young's modulus of 200,000 MPa and a Poisson ratio of 0.3. The yield stress of S1350 (f_y) is 1385.0 MPa, whilst the ultimate strength (f_u) is 1510.0 MPa. The steel properties of grade 10.9 bolt having a modulus of elasticity of 200,000 MPa and a Poisson ratio of 0.3. The yield stress of 10.9 bolt (f_y) is 940.0 MPa, whilst the ultimate strength (f_u) is 1070.0 MPa. The steel properties of grade 10.9 bolt having a Young's modulus of 200,000 MPa and a Poisson ratio of 0.3. The yield stress of 12.9 bolt (f_y) is 1150.0 MPa, whilst the ultimate strength (f_u) is 1250.0 MPa.

The load-deformation response of the softening model shows in Figures 5.63 – 5.65, that the failure behaviour of the plate was initiated by deformation according to stress-strain curve patterns until the ultimate stress was reached. Model SLB1a represents the S690 connection with the right end distance from bolt centre (e_1) of 36.0 mm and decreased by 6.0 mm. The ultimate force of SLB-1a is 280.6 KN, whilst it reaches 265.3 KN for SLB-5a with 5.8% lower. The result shows that softening effect on both model resulted in similar pattern with failure load nearly same. Deformation mode under softening effect of the connection model with bearing failure mode showing plate and bolt is presented in Figure 5.66. The right end distance from bolt centre (e_1) is increased from 36.0 mm to 24mm as designated in SLB-3a. The result shows that softening effect on both model resulted in different pattern that the ultimate force is 71.7% higher at the value of 480.4 KN. The deformation mode under softening effect of the connection model with net section failure mode showing plate and bolt is presented in 5.67.

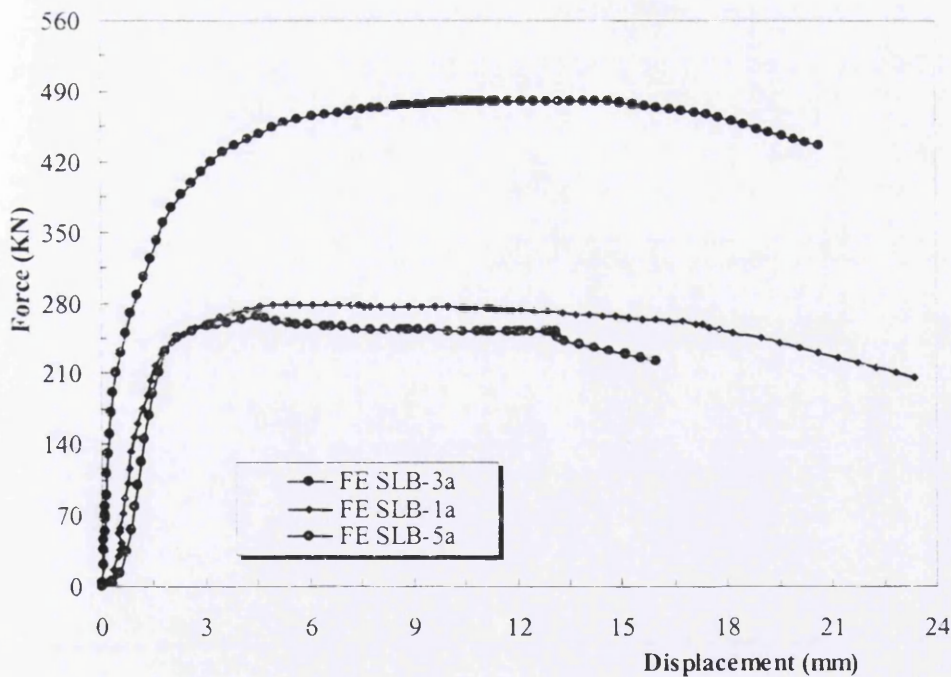


Figure 5.63 Load-displacement relationship of the S690 SLB connection

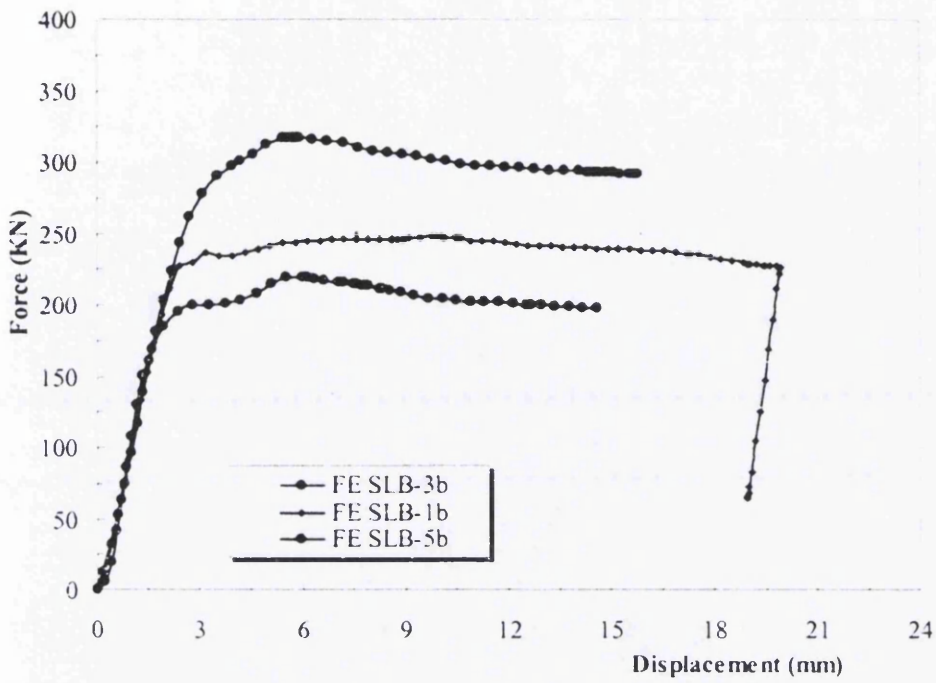


Figure 5.64 Load-displacement relationship of the SS 2205 SLB connection

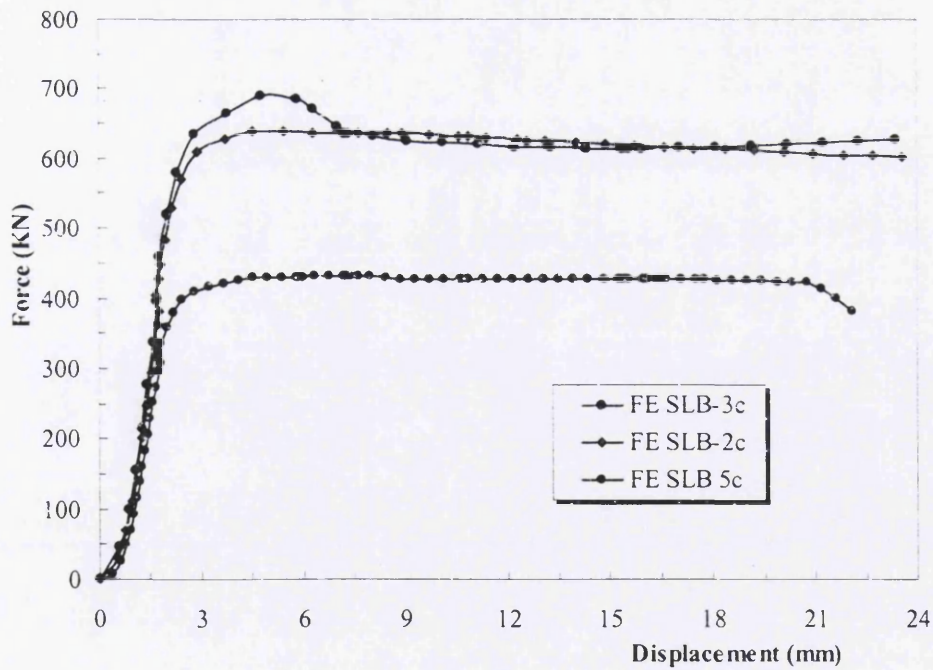


Figure 5.65 Load-displacement relationship of the S1350 SLB connection

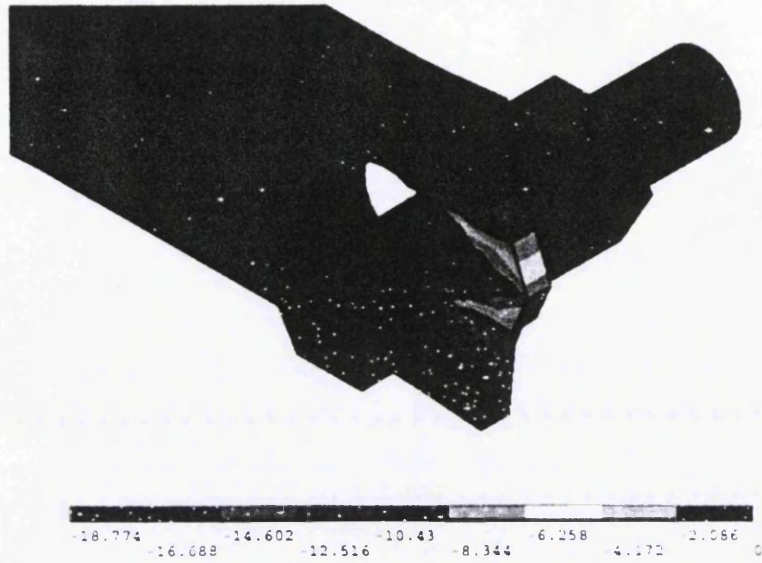


Figure 5.66 Deformed shape of the connection with $e_1/d_0=1.0$ under bearing failure

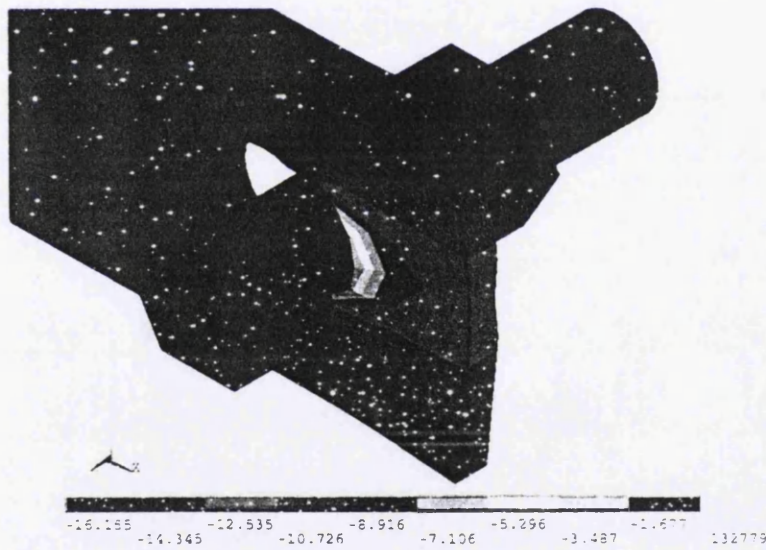


Figure 5.67 Deformed shape of the connection with $e_1/d_0=2.0$ under net-section failure

In order to investigate further the difference between the response of the plate with different grade and end distances, the plots of von Mises' stress contours are compared in Figures 5.68 -5.80. The stress contours at the ultimate load and rupture with three different steel grades are shown. The von Mises stress contours of the S690 SLB connection are shown in Figures 5.68 – 5.75. The plot of von Mises stress contours of the

SS 2205 SLB connection are shown in Figures 5.76 – 5.78. The von Mises stress contours of the S1350 SLB connection are shown in Figures 5.79 – 5.80

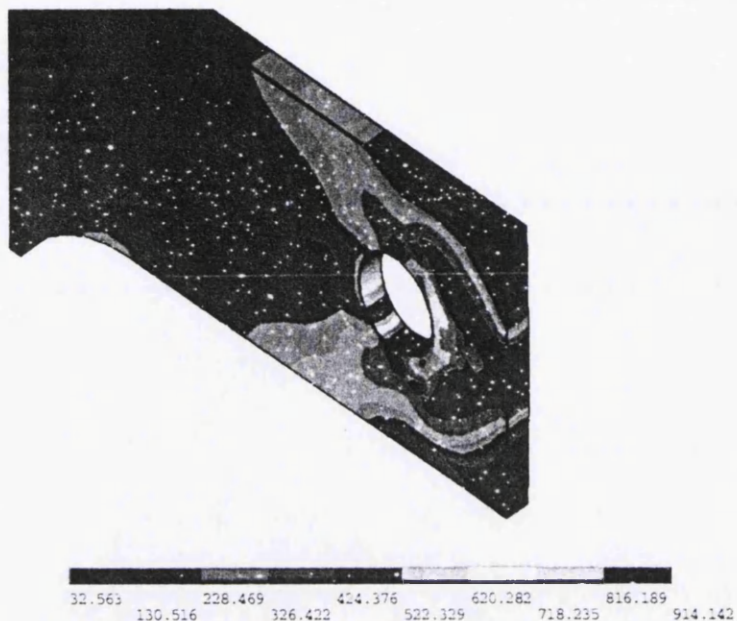


Figure 5.68 Stress contours of the S690 plate with $e_1/d_0=2.0$ at the ultimate stress

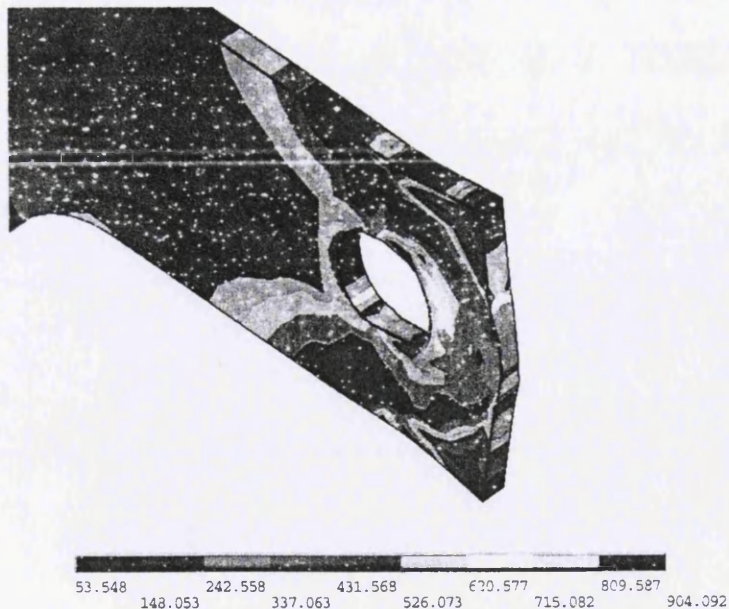


Figure 5.69 Stress contours of the S690 plate with $e_1/d_0=2.0$ the rupture condition

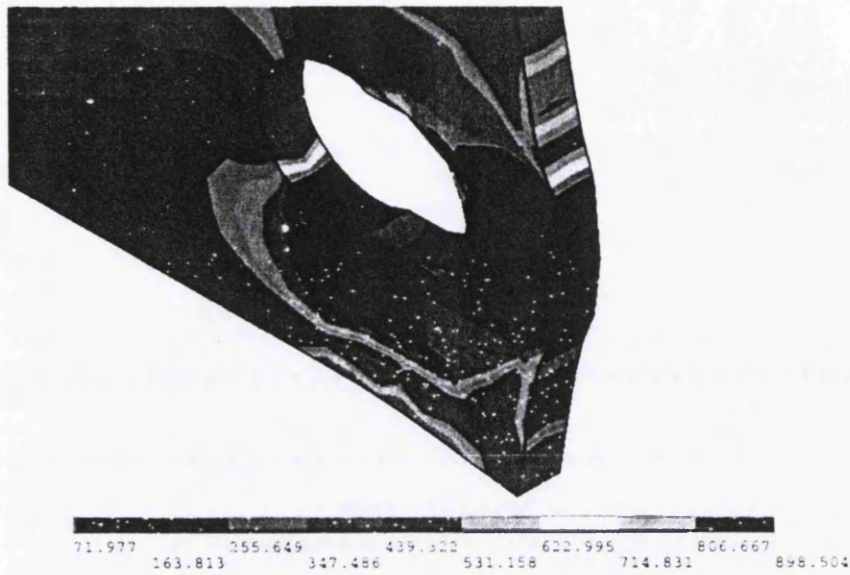


Figure 5.70 Stress contours of the S690 plate with at the net section and bearing rupture

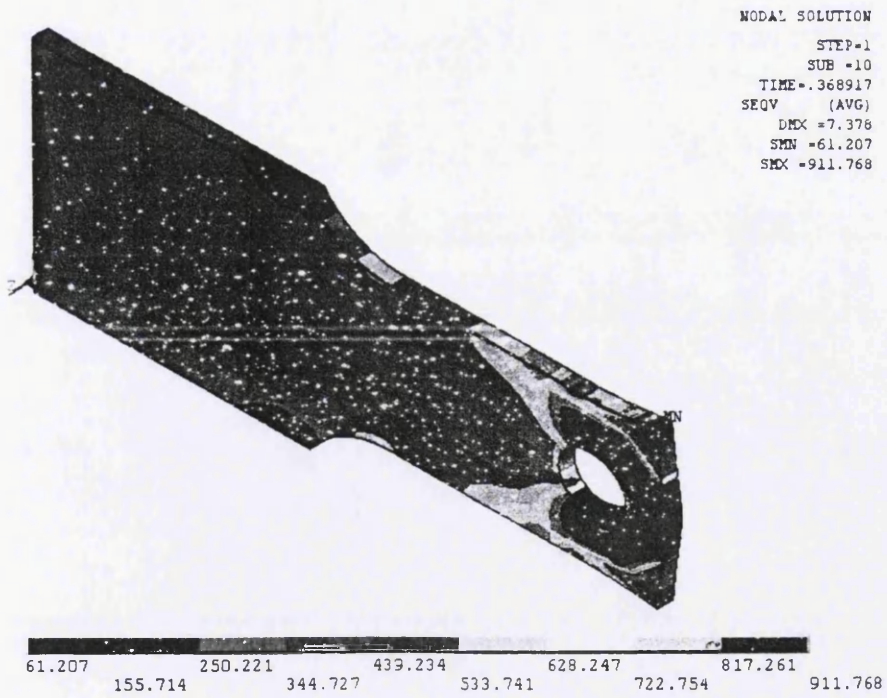


Figure 5.71 Stress contours of the S690 plate with $e_1/d_0=1.2$ at the ultimate stress

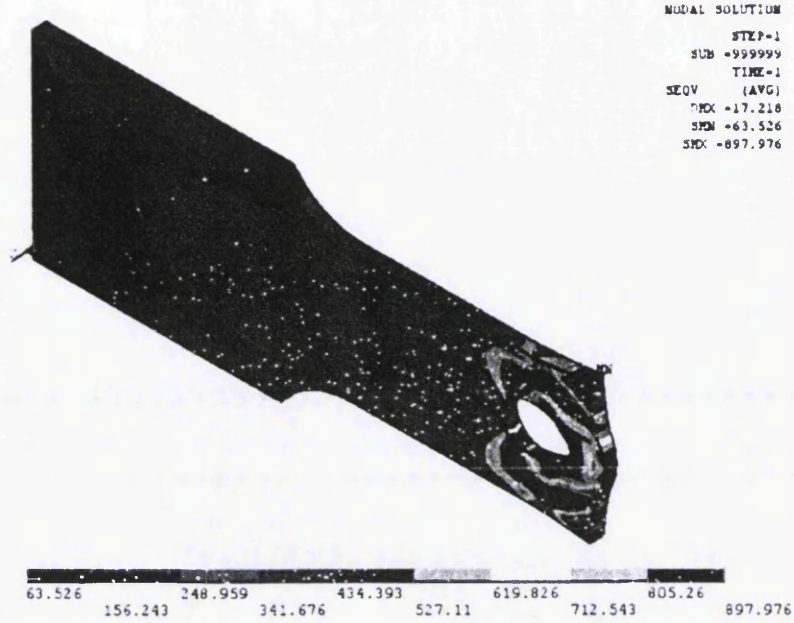


Figure 5.72 Stress contours of the S690 plate with $e_1/d_0=1.2$ at the rupture condition

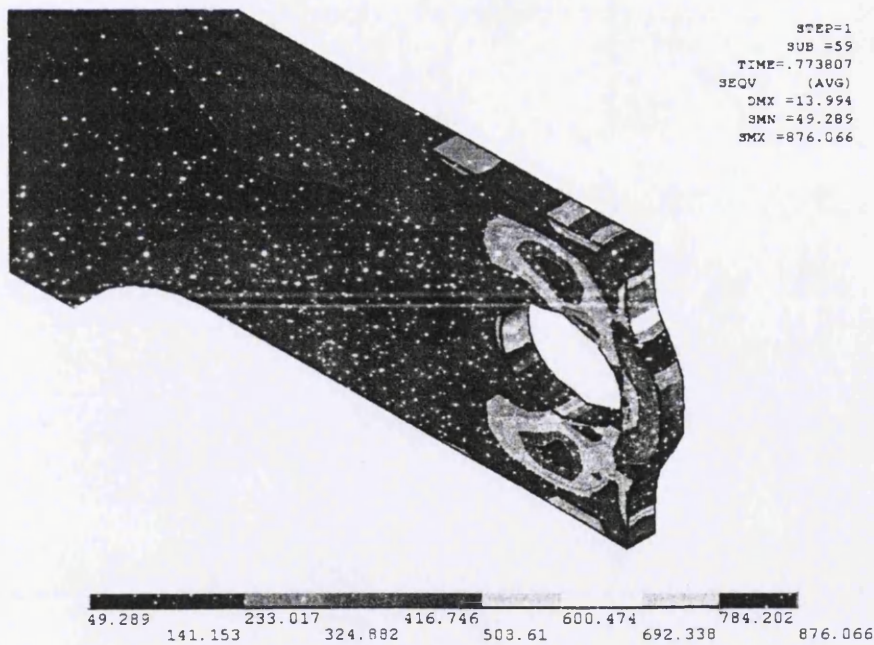


Figure 5.73 Stress contours of S690 plate with $e_1/d_0=1.0$ at the rupture condition

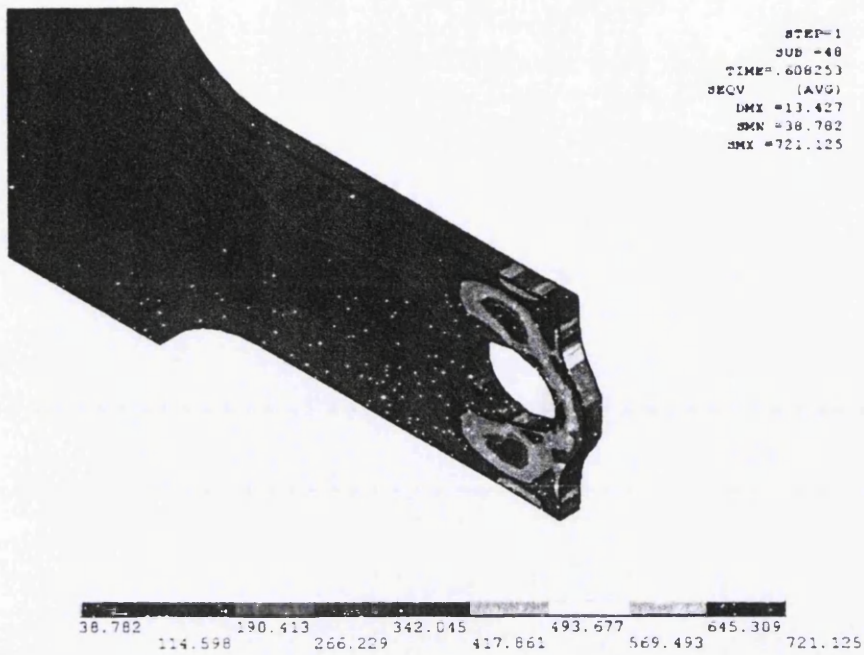


Figure 5.74 Stress contours of the SS2205 plate with $e_1/d_0=1.0$ at the rupture condition

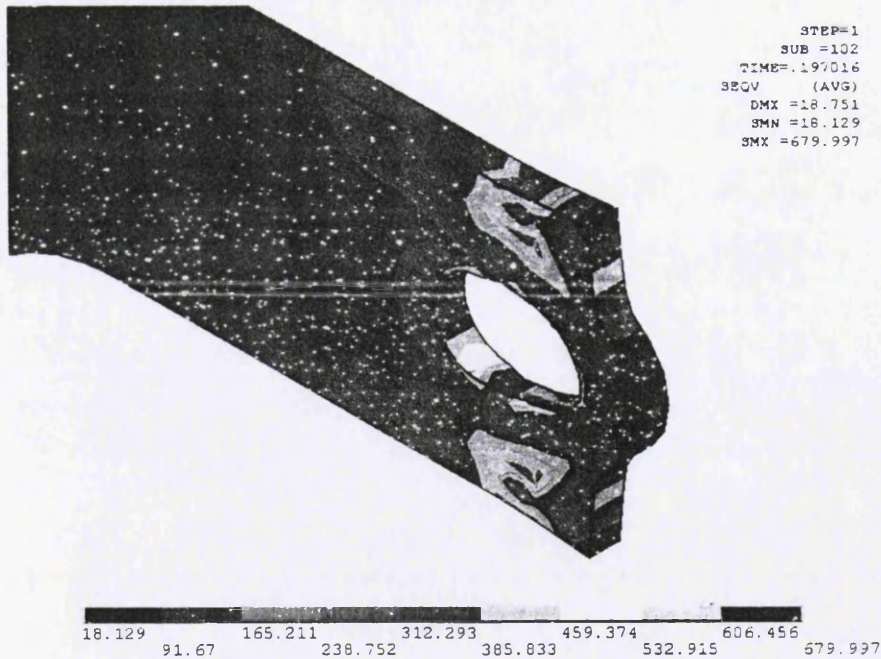


Figure 5.75 Stress contours of the SS2205 plate with $e_1/d_0=1.2$ at the rupture condition

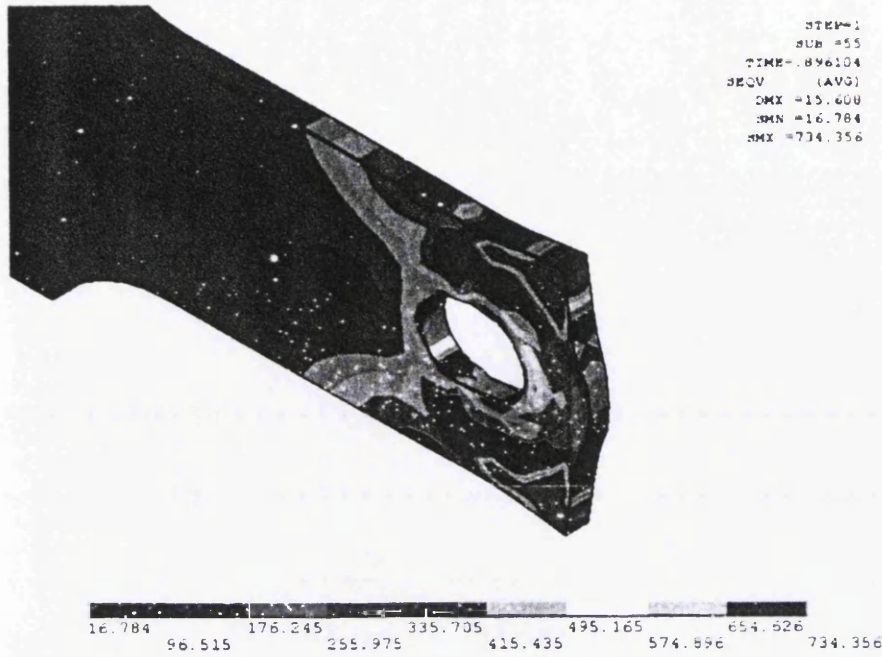


Figure 5.76 Stress contours of the SS2205 plate with $e_1/d_0=1.5$ at the rupture condition

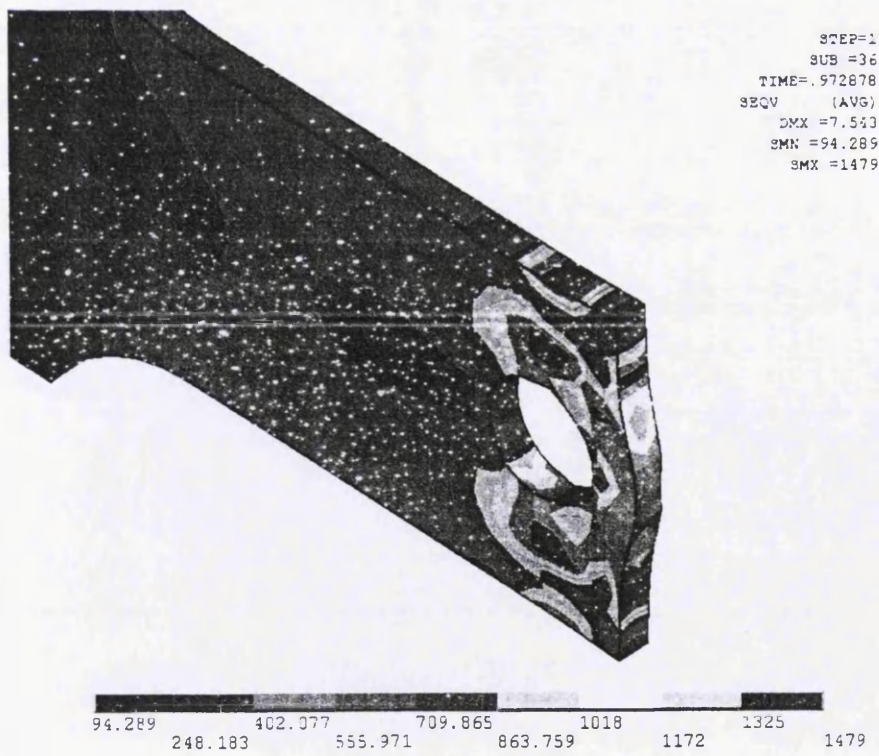


Figure 5.77 Stress contours of the S1350 plate with $e_1/d_0=1.0$ at the ultimate stress

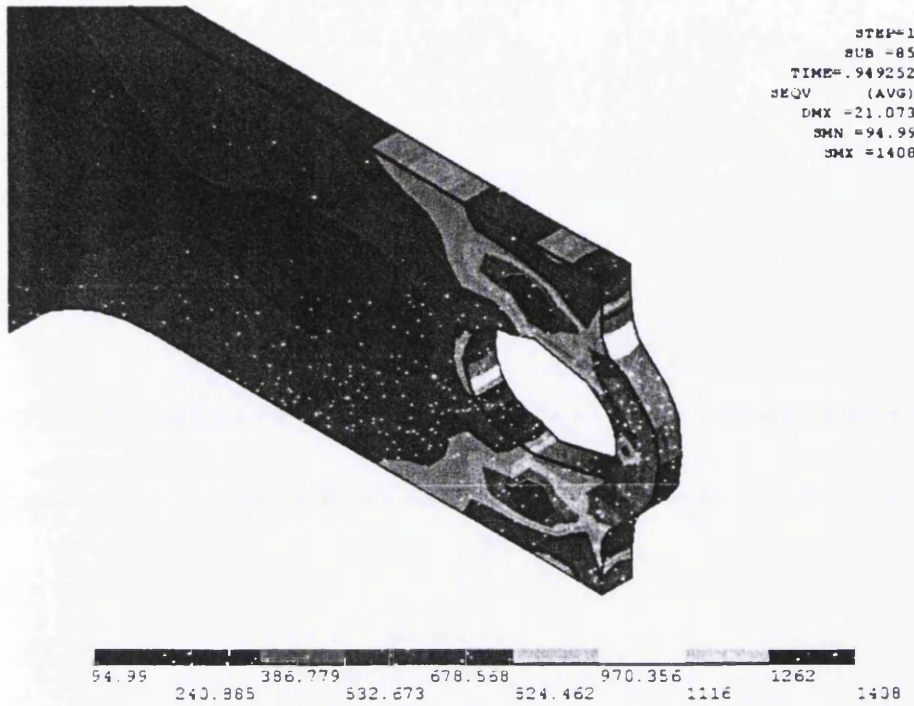


Figure 5.78 Stress contours of the S1350 plate with $e_1/d_0=1.0$ at the rupture condition

Figures 5.79 – 5.81 show the complete stress-deformation curves with the response of the connection due to the softening effect.

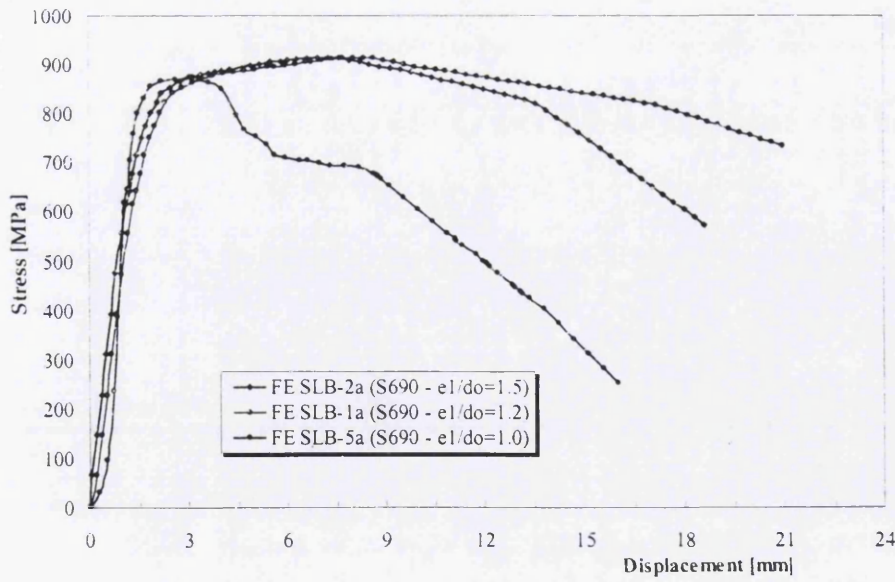


Figure 5.79 Complete stress-deformation curves of the S690 SLB connection

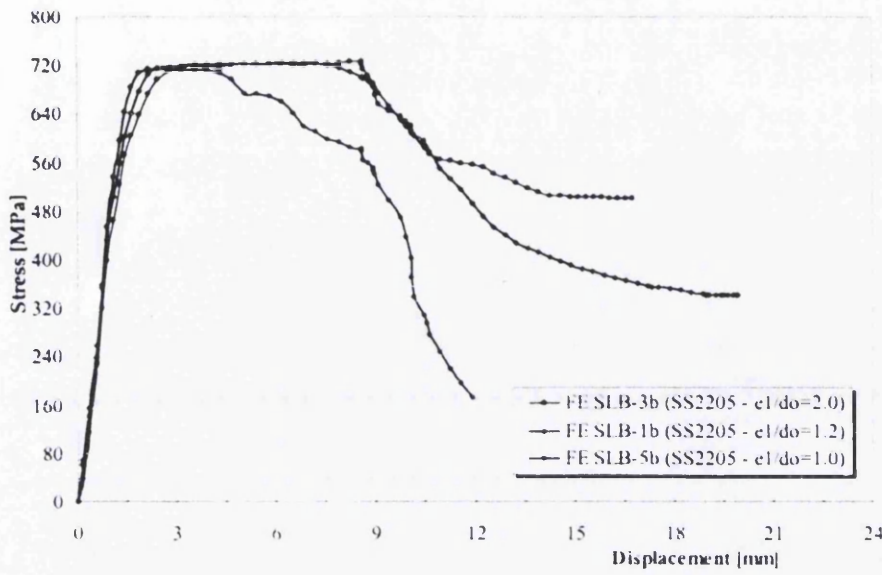


Figure 5.80 Complete stress-deformation curves of the SS2205 SLB connection

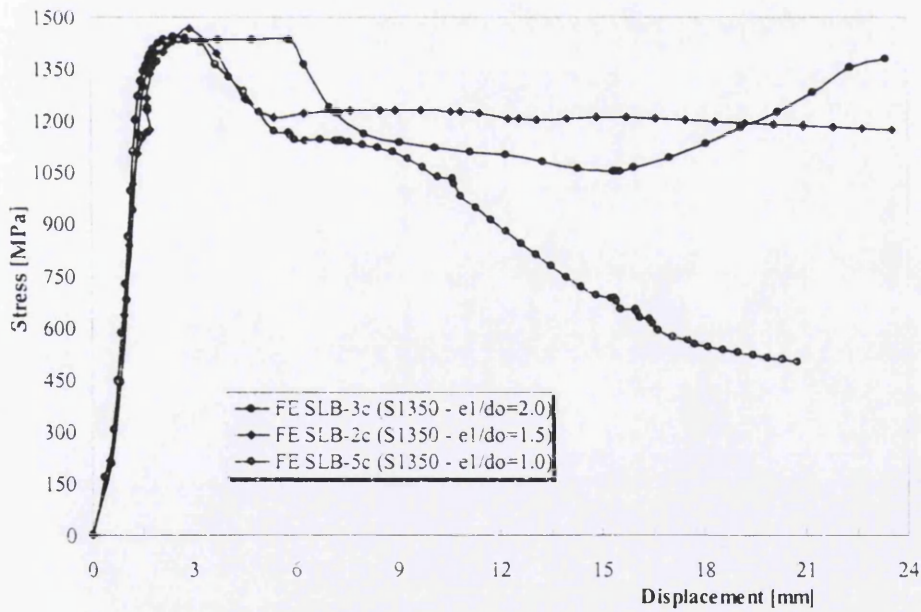


Figure 5.81 Complete stress-deformation curves of the S1350 SLB connection

Splice lap bolted connections based on FE modelling with double shear resistance are also analyzed with reference [11] and [14] to modern design codes. The comparison of the FEA results and EC3 design code are depicted in Tables 5.12 – 5.14. The design

bearing and net section resistance of the plate and bolt are considered with different considered parameters such as the end distance from the bolt centre to the edge and the net section of the plate.

The design bearing resistance of the bolts should be taken as:

$$F_{b,Rd} = \frac{k_1 \cdot \alpha_b \cdot f_u \cdot d \cdot t_p}{\gamma_{M2}} \quad (5.6)$$

where

- k_1 is the smallest of (2.5 ; 2.8 $e_2/d_0 - 1.7$; 1.4 $e_2/d_0 - 1.7$)
- α_b is the smallest of (1.0 ; $e_1/3d_0$; $p_1/3d_0 - 1/4$; f_{ub}/f_u)
- f_u is the specified ultimate strength
- f_{ub} is the specified ultimate strength of the bolt
- d is the nominal bolt diameter
- t_p is the thickness of plate
- γ_{M2} is the partial factor for net section resistance for steels, $\gamma_{M12} = \gamma_{M2} = 1.25$

For steel with grades greater than S460 and up to S700 the design resistance of a net section should be taken as:

$$N_{t,Rd} = \frac{0.9 A_{net} \cdot f_u}{\gamma_{M12}} \quad (5.7)$$

where

- A_{net} is the net area of the plate
- f_u is the specified ultimate strength
- γ_{M12} is the partial factor for net section resistance for steels, $\gamma_{M12} = \gamma_{M2} = 1.25$

Table 5.12

Ultimate load and failure mode of the S690 SLB model

| connection destination | plate (mm) | bolt grade | P_{ult} (FE) (KN) | P_{ult} (EC3) (KN) | Failure mode |
|-------------------------------|-------------------|-------------------|----------------------------------|-----------------------------------|-----------------------|
| SLB-1a | 10.0 | M27 – 10.9 | 264.7 | 192.6 | bearing |
| SLB-2a | 10.0 | M27 – 10.9 | 280.6 | 231.1 | bearing |
| SLB-3a | 10.0 | M27 – 10.9 | 360.3 | 288.9 | bearing & net section |
| SLB-4a | 10.0 | M27 – 10.9 | 480.4 | 395.3 | net section |
| SLB-5a | 10.0 | M27 – 10.9 | 521.8 | 395.3 | net section |
| SLB-6a | 8.0 | M27 – 10.9 | 206.5 | 154.1 | bearing |
| SLB-7a | 8.0 | M27 – 10.9 | 221.7 | 184.9 | bearing |
| SLB-8a | 8.0 | M27 – 10.9 | 286.4 | 231.1 | bearing & net section |
| SLB-9a | 8.0 | M27 – 10.9 | 384.3 | 316.2 | net section |
| SLB-10a | 8.0 | M27 – 10.9 | 417.4 | 316.2 | net section |

Table 5.13

Ultimate load and failure mode of the SS2205 SLB model

| connection destination | plate (mm) | bolt grade | P_{ult} (FE) (KN) | P_{ult} (EC3) (KN) | Failure mode |
|-------------------------------|-------------------|-------------------|----------------------------------|-----------------------------------|-----------------------|
| SLB-1b | 10.0 | M27 – 10.9 | 219.5 | 156.0 | bearing |
| SLB-2b | 10.0 | M27 – 10.9 | 247.7 | 187.2 | bearing |
| SLB-3b | 10.0 | M27 – 10.9 | 317.6 | 337.0 | bearing & net section |
| SLB-4b | 10.0 | M27 – 10.9 | 338.2 | 337.0 | net section |
| SLB-6b | 8.0 | M27 – 10.9 | 173.4 | 124.8 | bearing |
| SLB-7b | 8.0 | M27 – 10.9 | 196.9 | 149.8 | bearing |
| SLB-8b | 8.0 | M27 – 10.9 | 254.1 | 269.0 | bearing & net section |
| SLB-9b | 8.0 | M27 – 10.9 | 270.6 | 269.0 | net section |

Table 5.14

Ultimate load and failure mode of the S1350 SLB model

| connection destination | plate (mm) | bolt grade | P_{ult} (FE) (KN) | P_{ult} (EC3) (KN) | Failure mode |
|------------------------|------------|------------|---------------------|----------------------|--------------|
| SLB-1c | 10.0 | M27 – 12.9 | 431.9 | 225.0 | bearing |
| SLB-2c | 10.0 | M27 – 12.9 | 637.0 | 652.3 | bearing |
| SLB-4c | 10.0 | M27 – 12.9 | 690.0 | 652.3 | net section |
| SLB-6c | 8.0 | M27 – 12.9 | 336.8 | 180.0 | bearing |
| SLB-7c | 8.0 | M27 – 12.9 | 503.2 | 521.8 | bearing |
| SLB-9c | 8.0 | M27 – 12.9 | 552.0 | 521.8 | net section |

From the results in Tables 5.12 – 5.14, it can be seen that the designs are somewhat conservative despite the omission of factors of safety. The FE model of SLB connection with net section failure shows significant results close to EC3 resistance design, and also for connections with combined bearing and net section failure. At the ultimate load, the failure mode type 3) which is a complete failure of the plate occurred for almost all of the connection with $e_1/d_0 \geq 1.5$ and different steel grades except for the connection with S690 plate. For the connection with $e_1/d_0=1.0$, the bearing failure occurred for all the steel grade plate with the ultimate load much higher compared with EC3 resistance design. The minimum edge distance may be reduced to at least $e_1=1.0d_0$. For the connection with $e_1/d_0=1.2$, bearing failure occurred for all the steel grade plates with the ultimate load showing a reasonable value compared with EC3 resistance design. The finite element model was used to confirm the predictions by studying the bearing and net section failure of the bolt and plate.

5.5 Conclusions

Chapter 5 has focused on the development of the finite element model with high strength and stainless steel. This chapter has three parts: angle bolted connections with high strength steel, endplate connections with high strength steel and shear connection with high strength and stainless steel. The influence of different steel grades were presented on the connection behaviour as well as the softening effect on the shear connection. In addition to this, the moment rotation and load-deflection behaviour of the connections was presented. Furthermore, stress contours of each connection are given. From the study carried out, the following conclusions are drawn.

The overall results show that the application of the high strength angles gives a significant increasing moment capacity of 40%-95% for thinner angles whilst only 20%-50% for thicker angles except for the double web angle connection which only increased by 2-20%. For the improvement of the TSAW connection capacity, it is necessary to consider applying only higher strength top and seat angles, whilst the thin web angle can be kept as mild carbon steel. The TSA connection with high strength steel gives a significant improvement of the connection capacity, whilst it is not advisable to apply the high strength angle on the DWA connection.

Thicker high strength endplates gives a much higher by 10%-25% ultimate moment capacity, whilst the ultimate moment of thinner high strength endplates can be increased by up to 40%. Waiving of column web stiffeners is not advisable because their absence causes premature failure in the column flange. This consequently leads to a drastic drop in moment and rotation capacities. However, connections with column web stiffeners is advisable because their presence increases the moment capacity up to 25%. In the case of the thickness of the endplate almost being twice than the column flange, it is found that, no advantage will be gained to increase the moment capacity of connection for S275 grade steel due to excessive deflection of the column flange and web. However, a marginal increase in moment capacity can be achieved by increasing the grade of steel to S355 for the column section only.

The application of high strength and stainless steel for the shear bolted connection gives two approaches of resistance design calculation such as bearing resistance and net section resistance. Both design resistance from FEA show reasonable agreement with EC3, except for the connection with $e_1/d_0=1.0$ which is rather conservative. It is reasonable that minimum edge distance e_1 can be used with the value of $1.0d_0$ instead of $1.2d_0$ for all high strength steel grade including stainless steel grade SS2205 and very high strength steel grade S1350.

Chapter 6

Parametric Study

6.1 Introduction

This chapter discusses the results from the previous analyses. These are the results of finite element analyses of high strength and stainless steel bolted connections. Furthermore, the results of parametric studies will be discussed in order to understand the effects of each component acting on the whole structure.

6.2 The Parametric Study

In order to find out which factor is the most influential for the behaviour of the bolted connection, a series of combinations of the structural elements with different geometry had been analysed on the previous model. Results obtained are presented herein.

6.2.1 Effect of different steel grades of the angle and endplate

6.2.1.1 DWA connection

The two cases were modelled using 9.5mm and 12.5mm web angle thickness with different steel grade. The model produced the results shown in Table 6.1

Table 6.1
Initial stiffness and ultimate moment of 9.5 and 12.5mm angles

| model | grade | R_{ki} (KN.m/mRad) | M_u (KN.m) | failure mode |
|--------|-------|----------------------|--------------|----------------|
| DWA-1b | S460 | 2.88 | 25.6 | angle yielding |
| DWA-1c | S550 | 2.93 | 28.1 | angle yielding |
| DWA-1d | S690 | 2.70 | 32.7 | angle yielding |
| DWA-4b | S460 | 9.92 | 75.0 | angle yielding |
| DWA-4c | S550 | 9.92 | 80.0 | angle yielding |
| DWA-4d | S690 | 9.56 | 92.5 | angle yielding |

The effect of the different yield and ultimate stresses on the ultimate moment of each of the two cases can be more clearly seen in Figure 6.1.

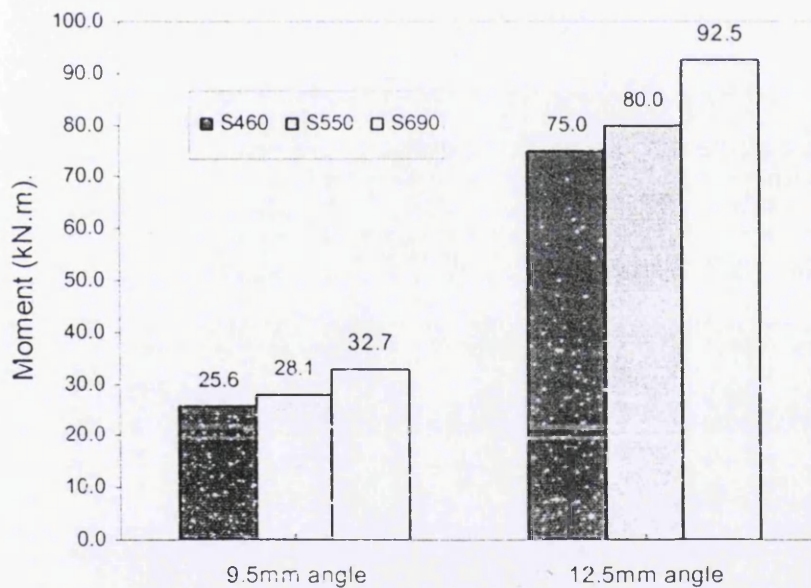


Figure 6.1 Chart showing ultimate moment for each case study

6.2.1.2 TSA connection

The two cases were modelled using 8.0mm and 12.5mm angle cleat thickness with different steel grade. The model produced the results shown in Table 6.2.

Table 6.2
Initial stiffness and ultimate moment of 9.5 and 12.5 mm angles

| model | grade | R_{ki} (KN.m/mRad) | M_u (KN.m) | failure mode |
|--------|-------|----------------------|--------------|----------------|
| TSA-3c | S550 | 5.34 | 43.7 | angle yielding |
| TSA-3b | S460 | 5.15 | 40.0 | angle yielding |
| TSA-1c | S550 | 23.96 | 120.0 | angle yielding |
| TSA-1b | S460 | 24.14 | 115.0 | angle yielding |

The effect of the different yield and ultimate stresses on the ultimate moment of each of the two cases can be more clearly seen in Figure 6.2

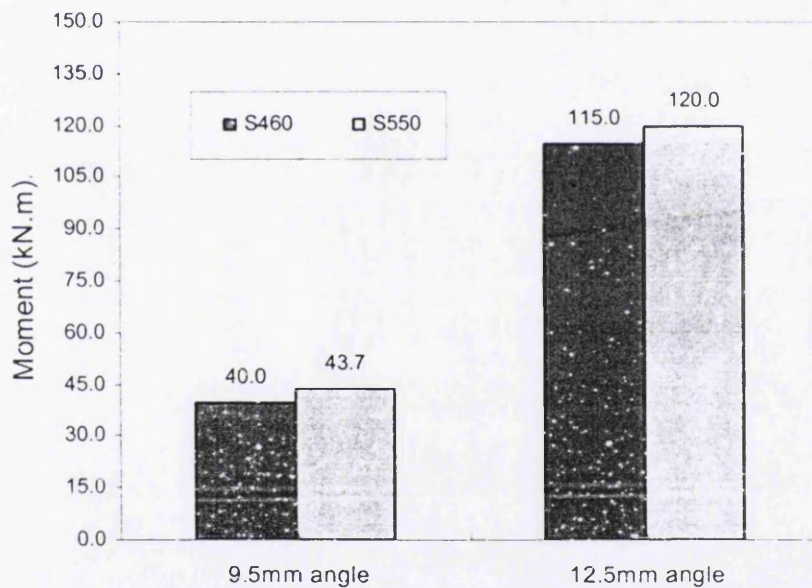


Figure 6.2 Chart showing ultimate moment for each case study

6.2.1.3 TSAW connection

The two cases were modelled using 8.0mm and 9.5mm angle cleat thickness with different steel grades. The model produced the results shown in Table 6.3.

Table 6.3
Initial stiffness and ultimate moment of 8.0 and 9.5 mm angles

| model | grade | R_{ki} (KN.m/mRad) | M_u (KN.m) | failure mode |
|---------|-------|----------------------|--------------|----------------|
| TSAW-1b | S460 | 16.33 | 50.8 | angle yielding |
| TSAW-1c | S690 | 14.96 | 75.8 | angle yielding |
| TSAW-2b | S460 | 16.41 | 52.1 | angle yielding |
| TSAW-2c | S690 | 15.54 | 76.2 | angle yielding |

The effect of the different yield and ultimate stresses on the ultimate moment of each of the two cases can be more clearly seen in Figure 6.3.

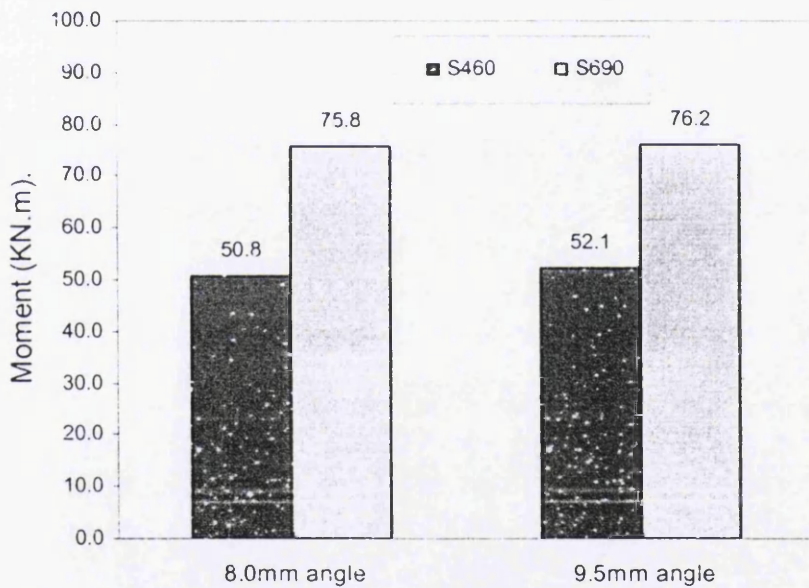


Figure 6.3 Chart showing ultimate moment for each case study

6.2.1.4 FEP connection

The two cases were modelled using 12.0mm and 15.0mm end plate thicknesses with different steel grades. The model produced the results shown in Table 6.4.

Table 6.4
Initial stiffness and ultimate moment of 12.0 and 15.0mm plates

| model | grade | R_{ki} (KN.m/mRad) | M_u (KN.m) | failure mode |
|---------|-------|----------------------|--------------|-----------------|
| FEP-1b | S550 | 11.35 | 103.8 | plate yielding |
| FEP-1d* | S690 | 11.90 | 120.0 | column yielding |
| FEP-1c | S550 | 11.93 | 118.8 | plate yielding |
| FEP-1f* | S690 | 12.38 | 127.0 | Bolt yielding |

The effect of the different yield and ultimate stresses on the ultimate moment of each of the two cases can be more clearly seen in Figure 6.4.

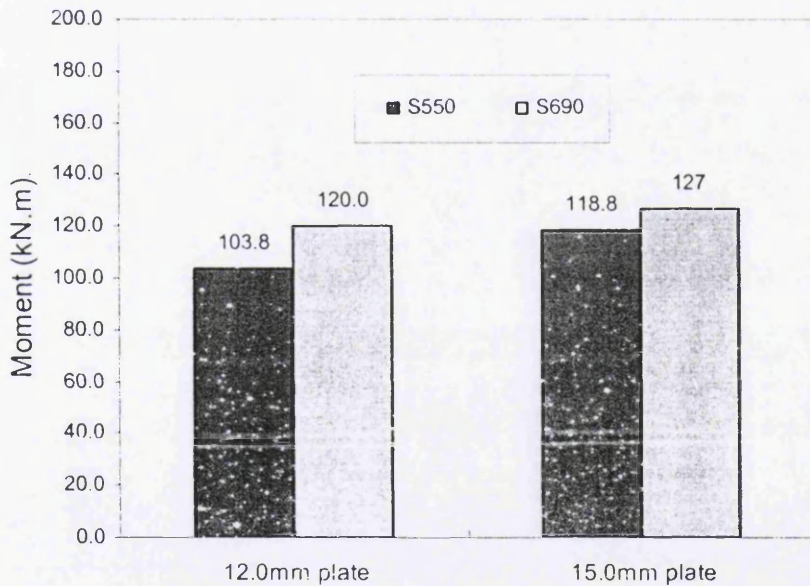


Figure 6.4 Chart showing ultimate moment for each case study

6.2.1.5 EPTB connection

The two cases were modelled using 10.0mm and 15.0mm endplate thicknesses with different steel grades. The model produced the results shown in Table 6.5.

Table 6.5
Initial stiffness and ultimate moment of 10.0 and 15.0mm plates

| model | grade | R_{ki} (KN.m/mRad) | M_u (KN.m) | failure mode |
|---------|-------|----------------------|--------------|----------------|
| EPHS-5b | S550 | 9.42 | 60.8 | plate yielding |
| EPHS-5c | S690 | 9.22 | 68.7 | plate yielding |
| EPHS-1b | S550 | 19.42 | 102.3 | plate yielding |
| EPHS-1c | S690 | 19.15 | 115.2 | bolt yielding |

The effect of the different yield and ultimate stresses on the ultimate moment of each of the two cases can be more clearly seen in Figure 6.5

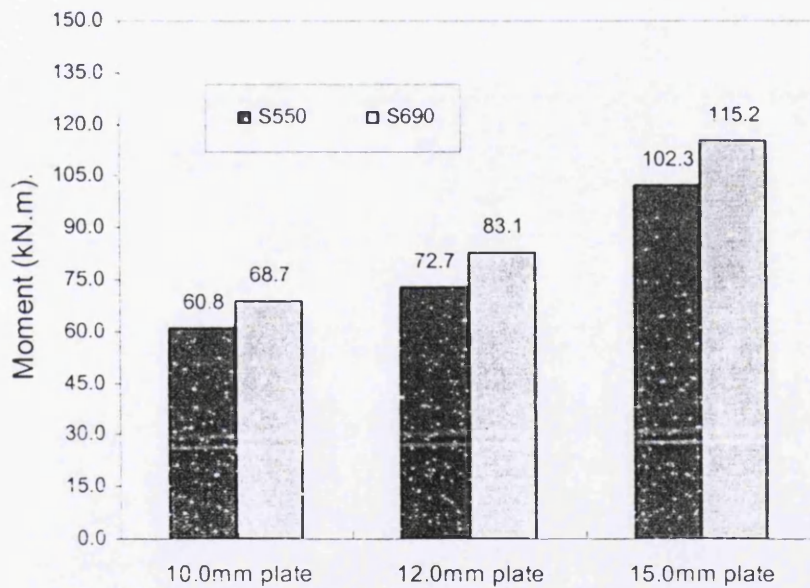


Figure 6.5 Chart showing ultimate moment for each case study

6.2.1.6 SCC connection

The two cases were modelled using 10.0mm and 20.0mm endplate thicknesses with different steel grade. The model produced the results shown in Table 6.6.

Table 6.6
Initial stiffness and ultimate moment of 10.0 and 20.0mm plates

| model | grade | R_{ki} (KN.m/mRad) | M_u (KN.m) | failure mode |
|--------|-------|----------------------|--------------|-----------------|
| SCC-1d | S460 | 67.53 | 220.2 | plate yielding |
| SCC-1b | S690 | 66.33 | 229.2 | column yielding |
| SCC-1e | S460 | 73.25 | 223.2 | plate yielding |
| SCC-1c | S690 | 72.80 | 233.5 | bolt yielding |

The effect of the different yield and ultimate stresses on the ultimate moment of each of the two cases can be more clearly seen in Figure 6.6.

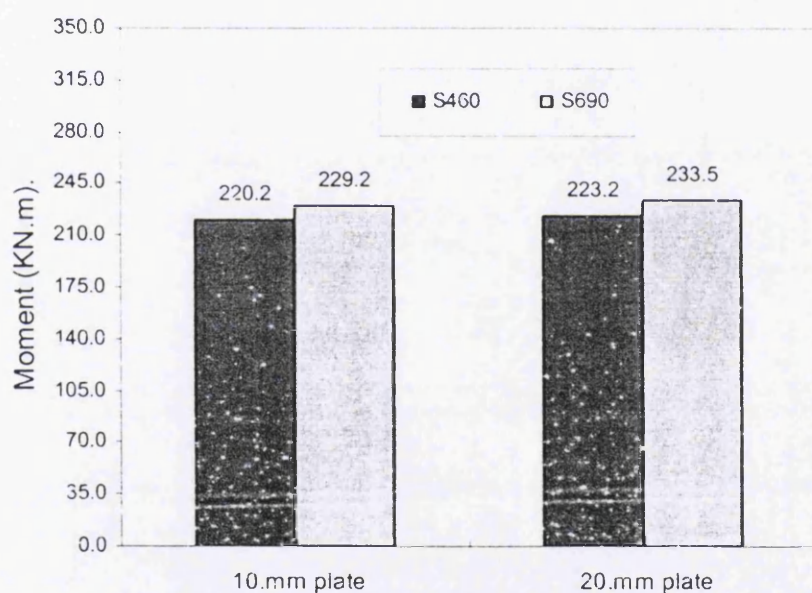


Figure 6.6 Chart showing ultimate moment for each case study

6.2.2 Effect of the different thicknesses of the angle and endplate

6.2.2.1 DWA connection

The two cases were modelled using S460 and S690 web angle with different angle thickness. The model produced the results shown in Table 6.7

Table 6.7

Initial stiffness and ultimate moment of S460 and S690 angles

| model | t_{wa} (mm) | R_{ki} (KN.m/mRad) | M_u (KN.m) | failure mode |
|--------|---------------|----------------------|--------------|----------------|
| DWA-1b | 9.5 | 2.88 | 25.6 | angle yielding |
| DWA-2b | 11.0 | 4.46 | 40.0 | angle yielding |
| DWA-4b | 12.5 | 9.92 | 75.0 | angle yielding |
| DWA-1c | 9.5 | 2.70 | 32.7 | angle yielding |
| DWA-2c | 11.0 | 4.56 | 43.7 | angle yielding |
| DWA-4c | 12.5 | 9.56 | 92.4 | angle yielding |

The effect of the different angle thicknesses on the ultimate moment of each of the two cases can be more clearly seen in Figure 6.7

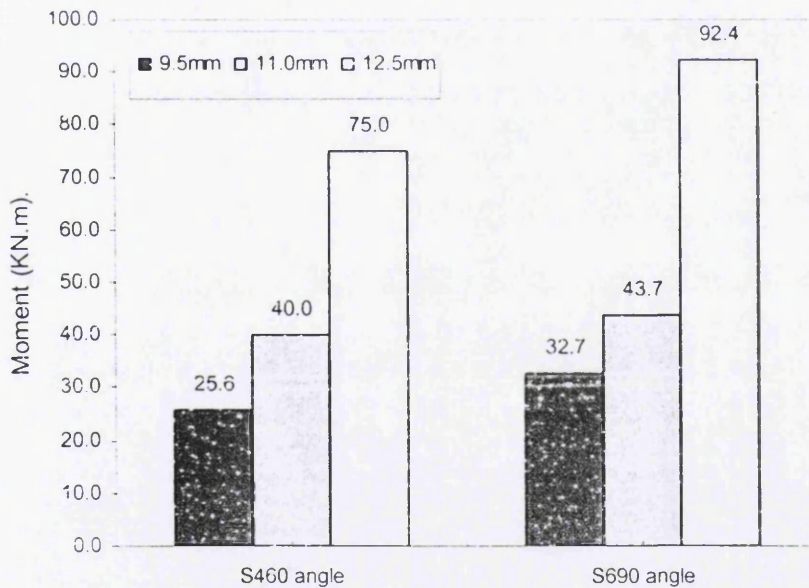


Figure 6.7 Chart showing ultimate moment for each case study

6.2.2.2 TSA connection

The two cases were modelled using 8.0mm and 12.5mm angle cleat thickness with different steel grades. The model produced the results shown in Table 6.8

Table 6.8
Initial stiffness and ultimate moment of S460 and S550 angles

| model | t_{wa} (mm) | R_{kl} (KN.m/mRad) | M_u (KN.m) | failure mode |
|--------|---------------|----------------------|--------------|----------------|
| TSA-4b | 8.0 | 3.84 | 28.8 | angle yielding |
| TSA-3b | 9.5 | 5.15 | 40.0 | angle yielding |
| TSA-1b | 12.5 | 7.33 | 60.0 | angle slip |
| TSA-4c | 8.0 | 4.02 | 33.1 | angle yielding |
| TSA-3c | 9.5 | 5.34 | 43.7 | angle yielding |
| TSA-1c | 12.5 | 7.96 | 67.0 | angle slip |

The effect of the different angle thicknesses on the ultimate moment of each of the two cases can be more clearly seen in Figure 6.8.

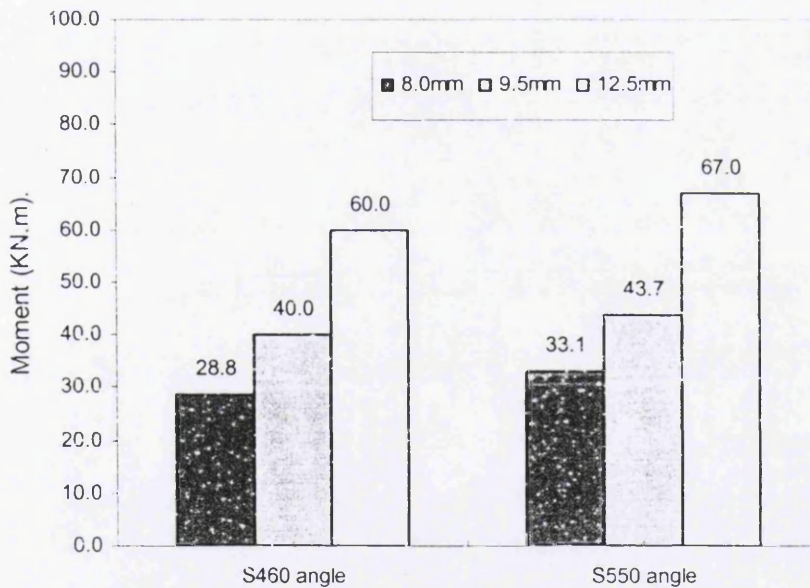


Figure 6.8 Chart showing ultimate moment for each case study

6.2.2.3 TSAW connection

The two cases were modelled using S460 and S690 angle cleat thickness with different angle thicknesses. The model produced the results shown in Table 6.9.

Table 6.9
Initial stiffness and ultimate moment of S460 and S690 angles

| Model | t_{sa} (mm) | R_{ki} (KN.m/mRad) | M_u (KN.m) | failure mode |
|---------|---------------|----------------------|--------------|----------------|
| TSAW-1b | 8.0 | 16.33 | 50.8 | angle yielding |
| TSAW-2b | 9.5 | 16.41 | 52.1 | angle yielding |
| TSAW-3b | 12.5 | 37.21 | 76.2 | angle slip |
| TSAW-1c | 8.0 | 14.96 | 75.8 | angle yielding |
| TSAW-2c | 9.5 | 15.54 | 76.1 | angle yielding |
| TSAW-3c | 12.5 | 36.18 | 110.4 | angle slip |

The effect of the different angle cleat thicknesses on the ultimate moment of each of the two cases can be more clearly seen in Figure 6.9.

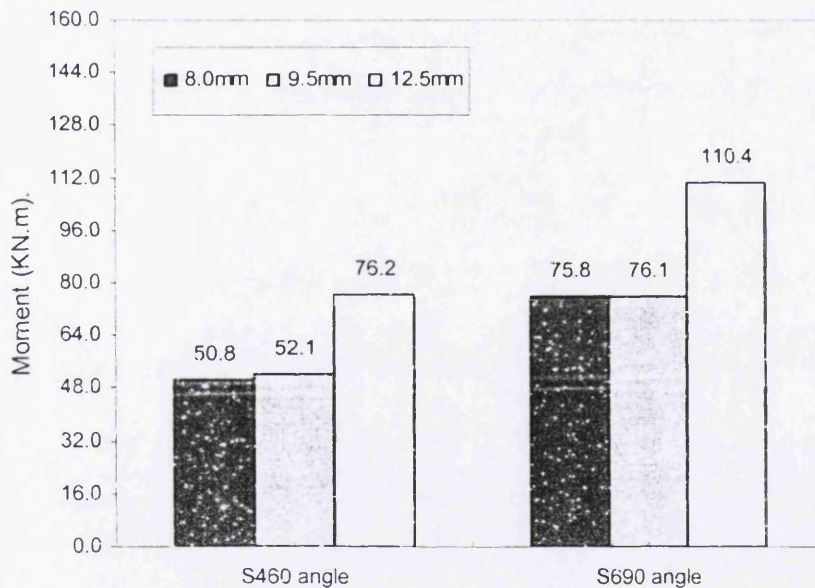


Figure 6.9 Chart showing ultimate moment for each case study

6.2.2.4 FEP connection

The two cases were modelled using S460 and S690 endplate with different endplate thicknesses. The model produced the results shown in Table 6.10.

Table 6.10

Initial stiffness and ultimate moment of S550 and S690 endplates

| Model | t_{ep} (mm) | R_{ki} (KN.m/mRad) | M_u (KN.m) | failure mode |
|---------|---------------|----------------------|--------------|-----------------|
| FEP-1b | 12.0 | 12.10 | 103.8 | plate yielding |
| FEP-1c | 15.0 | 12.93 | 118.8 | plate yielding |
| FEP-1c* | 18.0 | 18.50 | 133.6 | column yielding |
| FEP-1d* | 12.0 | 11.90 | 120.0 | plate yielding |
| FEP-1f* | 15.0 | 12.38 | 127.0 | plate yielding |
| FEP-1g* | 18.0 | 12.90 | 143.6 | column yielding |

The effect of the different endplate thicknesses on the ultimate moment of each of the two cases can be more clearly seen in Figure 6.10.

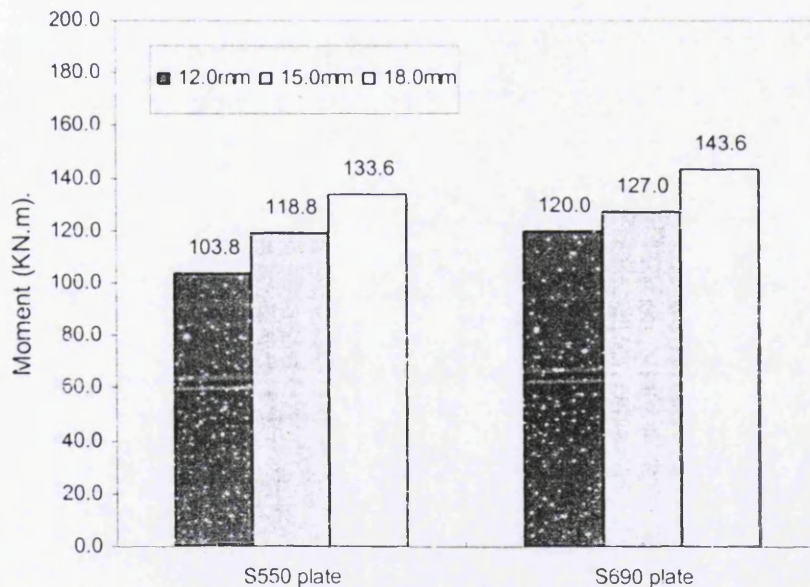


Figure 6.10 Chart showing ultimate moment for each case study

6.2.2.5 EPTB connection

The two cases were modelled using S550 and S690 endplate with different endplate thicknesses. The model produced the results shown in Table 6.11.

Table 6.11

Initial stiffness and ultimate moment of S550 and S690 plates

| model | t_{ep} (mm) | R_{ki} (KN.m/mRad) | M_u (KN.m) | failure mode |
|---------|---------------|----------------------|--------------|----------------|
| EPTB-5b | 10.0 | 9.42 | 60.8 | plate yielding |
| EPTB-5c | 15.0 | 19.42 | 102.3 | plate yielding |
| EPTB-1b | 10.0 | 9.22 | 68.7 | plate yielding |
| EPTB-1c | 15.0 | 19.15 | 115.2 | plate yielding |

The effect of the different plate thicknesses on the ultimate moment of each of the two cases can be more clearly seen in Figure 6.11.

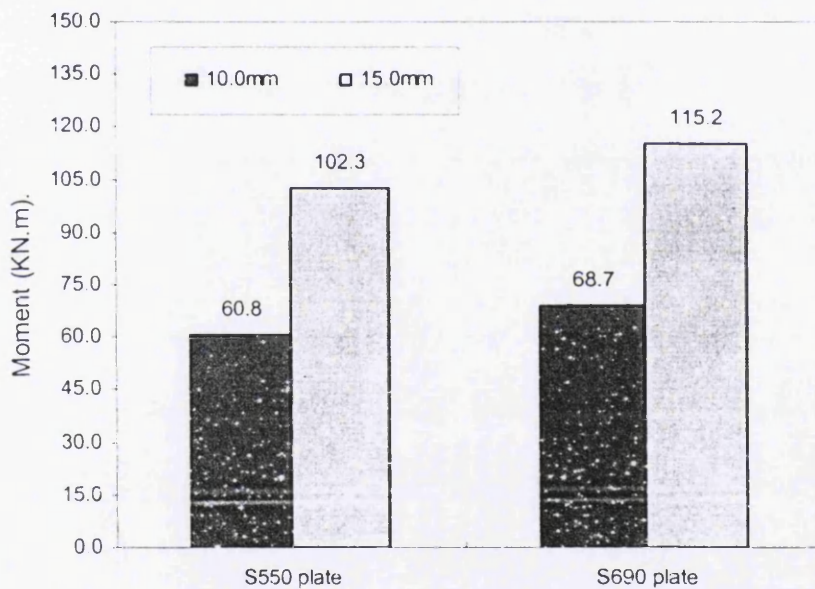


Figure 6.11 Chart showing ultimate moment for each case study

6.2.2.6 SCC connection

The two cases were modelled using S460 and S690 endplate with different end plate thicknesses. The model produced the results shown in Table 6.12.

Table 6.12
Initial stiffness and ultimate moment of S460 and S690 plates

| Model | t_{ep} (mm) | R_{ki} (KN.m/mRad) | M_u (KN.m) | failure mode |
|--------|---------------|----------------------|--------------|-----------------|
| SCC-1d | 10.0 | 67.53 | 220.2 | plate yielding |
| SCC-1b | 20.0 | 73.25 | 223.2 | plate yielding |
| SCC-1e | 10.0 | 66.33 | 229.1 | column yielding |
| SCC-1c | 20.0 | 72.80 | 233.5 | bolt yielding |

The effect of the different endplate thicknesses on the ultimate moment of each of the two cases can be more clearly seen in Figure 6.12.

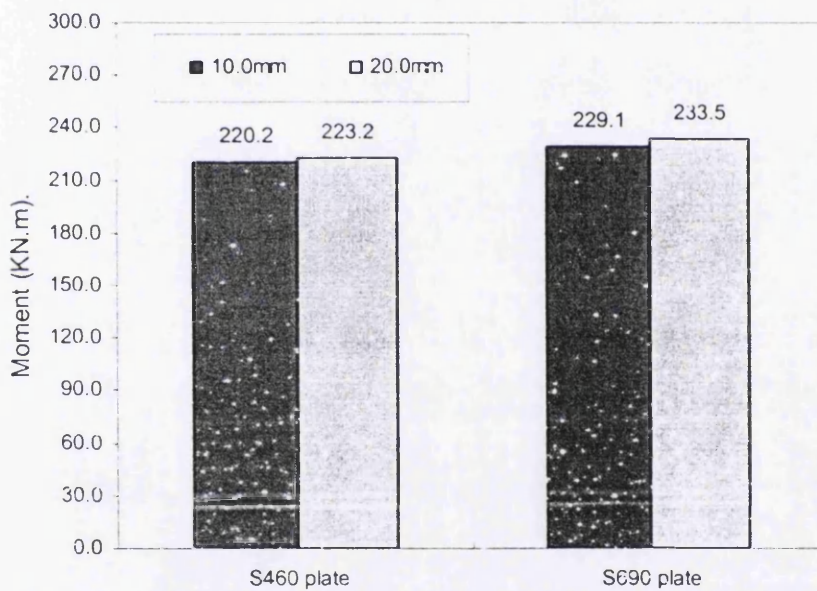


Figure 6.12 Chart showing ultimate moment for each case study

6.2.3 Effect of different sizes of beam

6.2.3.1 DWA connection

The two cases were modelled using W12x27 and W18x50 beams with different steel grades. The model produced the results shown in Table 6.13.

Table 6.13

Initial stiffness and ultimate moment of S460 and S690 angles

| model | beam size | R_{ki} (KN.m/mRad) | M_u (KN.m) | failure mode |
|--------|-----------|----------------------|--------------|----------------|
| DWA-1b | W12x27 | 4.46 | 40.0 | angle yielding |
| DWA-2b | W18x50 | 9.92 | 75.0 | angle yielding |
| DWA-1c | W12x27 | 4.56 | 43.7 | angle yielding |
| DWA-2c | W18x50 | 9.56 | 92.5 | angle yielding |

The effect of the beam sizes on the ultimate moment of each of the two cases can be more clearly seen in Figure 6.13.

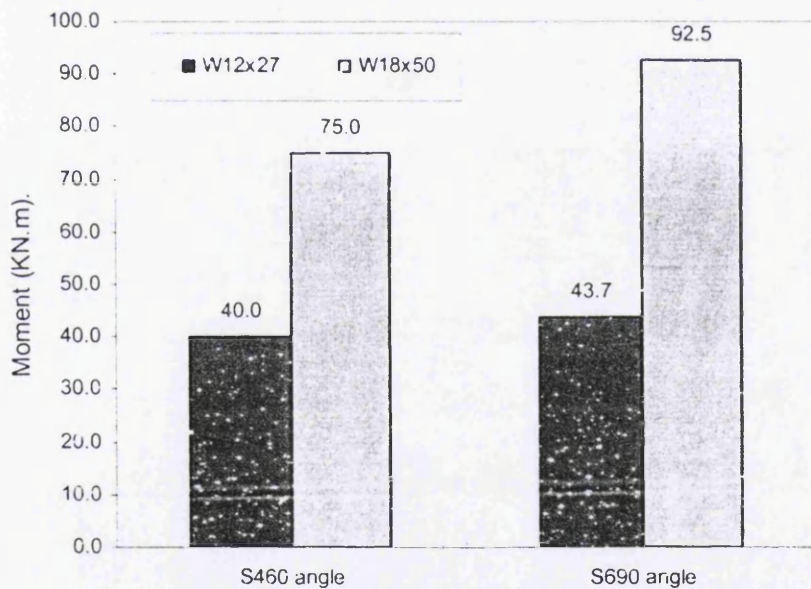


Figure 6.13 Chart showing ultimate moment for each case study

6.2.3.2 TSA connection

The two cases were modelled using 457x191x67UB and 305x165x40UB with different steel grades. The model produced the results shown in Table 6.14.

Table 6.14
Initial stiffness and ultimate moment of S460 and S550 angles

| model | beam size | R_{ki} (KN.m/mRad) | M_u (KN.m) | failure mode |
|--------|--------------|----------------------|--------------|----------------|
| TSA-1b | 305x165x40UB | 5.15 | 40.0 | angle yielding |
| TSA-2b | 457x191x67UB | 15.12 | 87.4 | angle yielding |
| TSA-1c | 305x165x40UB | 5.34 | 43.7 | angle yielding |
| TSA-2c | 457x191x67UB | 14.27 | 94.0 | angle yielding |

The effect of the different beam sizes on the ultimate moment of each of the two cases can be more clearly seen in Figure 6.14.

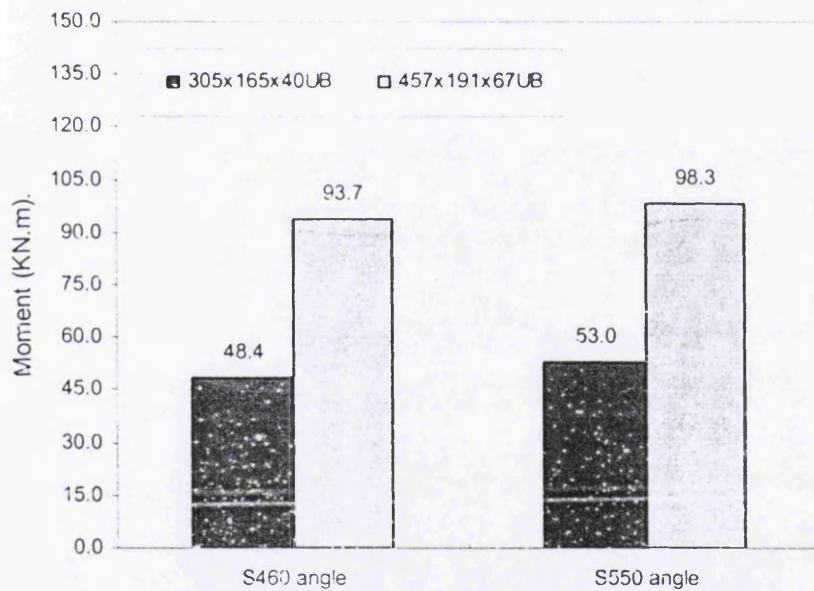


Figure 6.14 Chart showing ultimate moment for each case study

6.2.3.3 TSAW connection

The two cases were modelled using W8x21 and W14x38 beam with different steel grades. The model produced the results shown in Table 6.15.

Table 6.15
Initial stiffness and ultimate moment of S460 and S690 angles

| model | beam size | R_{ki} (KN.m/mRad) | M_u (KN.m) | Failure mode |
|---------|-----------|----------------------|--------------|----------------|
| TSAW-1b | W8x21 | 16.33 | 50.8 | angle yielding |
| TSAW-2b | W14x38 | 16.41 | 97.1 | angle yielding |
| TSAW-1c | W8x21 | 14.96 | 52.1 | angle yielding |
| TSAW-2c | W14x38 | 15.54 | 103.7 | angle yielding |

The effect of the different beam size on the ultimate moment of each of the two cases can be more clearly seen in Figure 6.15.

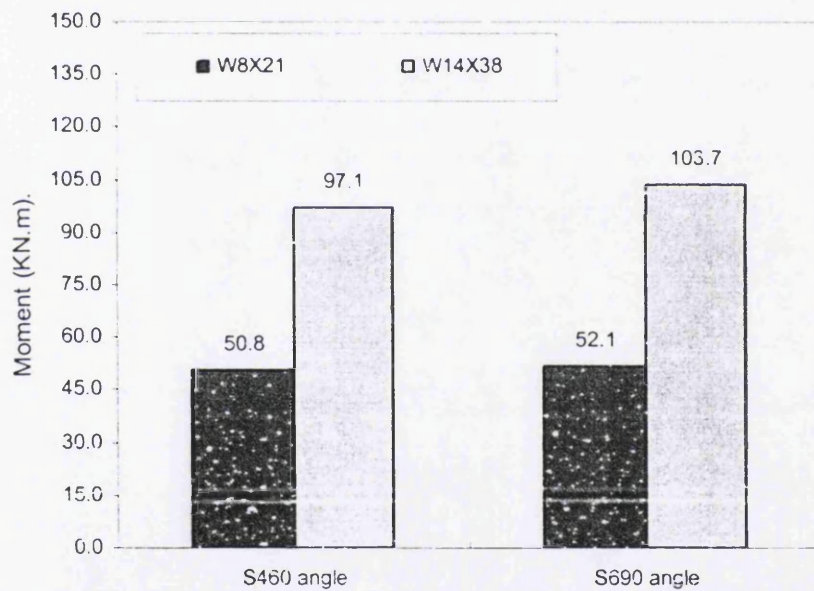


Figure 6.15 Chart showing ultimate moment for each case study

6.2.3.4 FEP connection

The two cases were modelled using IPE240, HE320A and 406x178x60UB beams with different steel grade. The model produced the results shown in Table 6.16.

Table 6.16
Initial stiffness and ultimate moment of S550 and S690 plates

| model | beam size | R_{ki} (KN.m/mRad) | M_u (KN.m) | failure mode |
|---------|------------|----------------------|--------------|----------------|
| FEP-1b | IPE240 | 11.93 | 118.8 | plate yielding |
| FEP1-3b | HE320A | 14.54 | 128.5 | plate yielding |
| FEP-1d* | 406x178x60 | 44.60 | 173.4 | plate yielding |
| FEP-1c | IPE240 | 12.38 | 127.0 | plate yielding |
| FEP1-3c | HE320A | 14.42 | 140.0 | bolt yielding |
| FEP-1f* | 406x178x60 | 43.58 | 178.2 | plate yielding |

The effect of the different yield and ultimate stresses on the ultimate moment of each of the two cases can be more clearly seen in Figure 6.16.

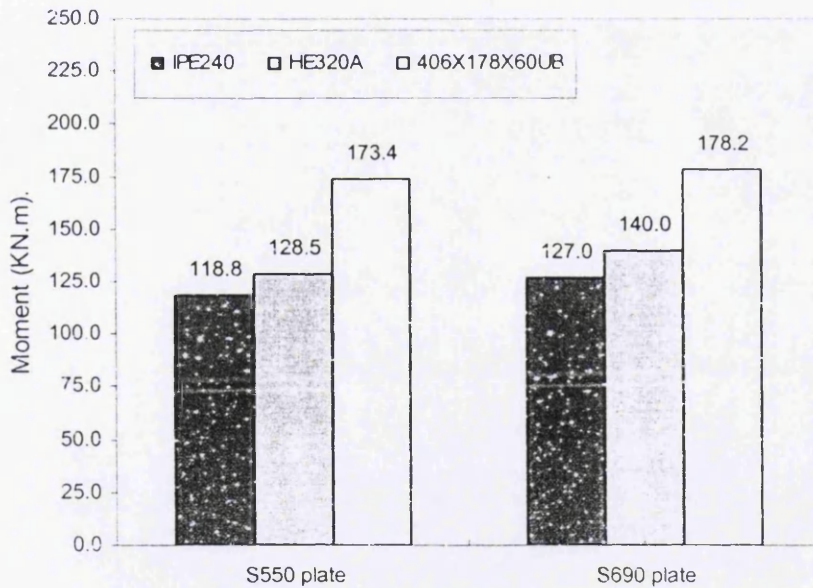


Figure 6.16 Chart showing ultimate moment for each case study

6.2.3.5 EPTB connection

The two cases were modelled using 200x100x9RHS and 150x150x9SHS beams with different steel grades. The model produced the results shown in Table 6.17.

Table 6.17

Initial stiffness and ultimate moment of S550 and S690 plates

| model | beam size | R_{ki} (KN.m/m.Rad) | M_u (KN.m) | failure mode |
|---------|-----------|-----------------------|--------------|----------------|
| EPTB-7b | 200x100x9 | 12.57 | 85.4 | plate yielding |
| EPTB-8b | 150x150x9 | 9.54 | 73.0 | plate yielding |
| EPTB-7c | 200x100x9 | 12.43 | 92.1 | plate yielding |
| EPTB-8c | 150x150x9 | 9.32 | 84.2 | plate yielding |

The effect of the different beam sizes on the ultimate moment of each of the two cases can be more clearly seen in Figure 6.17.

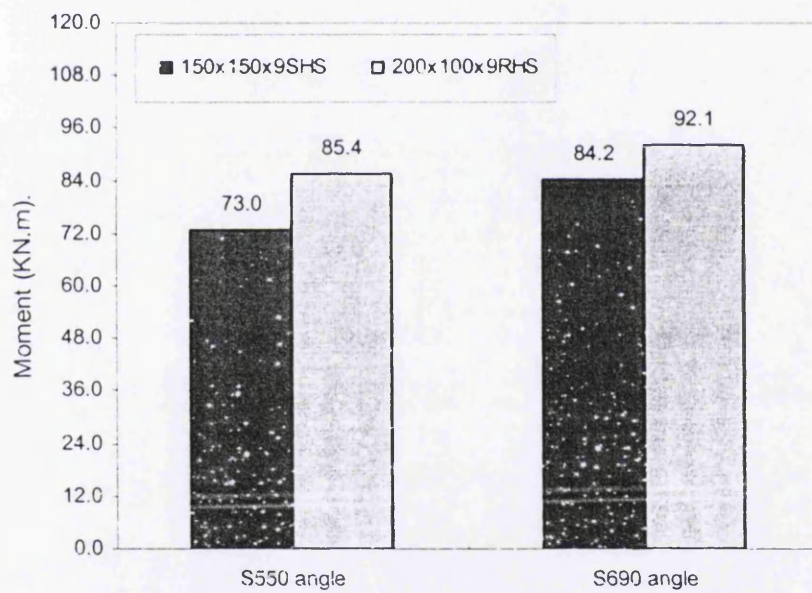


Figure 6.17 Chart showing ultimate moment for each case study

6.2.4 Effect of the stiffened column

6.2.4.1 TSAW connection

The two cases were modelled using stiffened and un-stiffened column with different steel grades. The model produced the results shown in Table 6.18.

Table 6.18

Initial stiffness and ultimate moment of S460 and S690 angles

| Model | column | R_{ki} (KN.m/mRad) | M_u (KN.m) | Failure mode |
|---------|--------------|----------------------|--------------|----------------|
| TSAW-1b | stiffened | 16.33 | 50.8 | angle yielding |
| TSAW-1c | un-stiffened | 15.51 | 49.5 | angle yielding |
| TSAW-2b | stiffened | 14.96 | 75.8 | angle yielding |
| TSAW-2c | un-stiffened | 14.26 | 74.3 | angle yielding |

The effect of the column stiffener on the ultimate moment of each of the two cases can be more clearly seen in Figure 6.18.

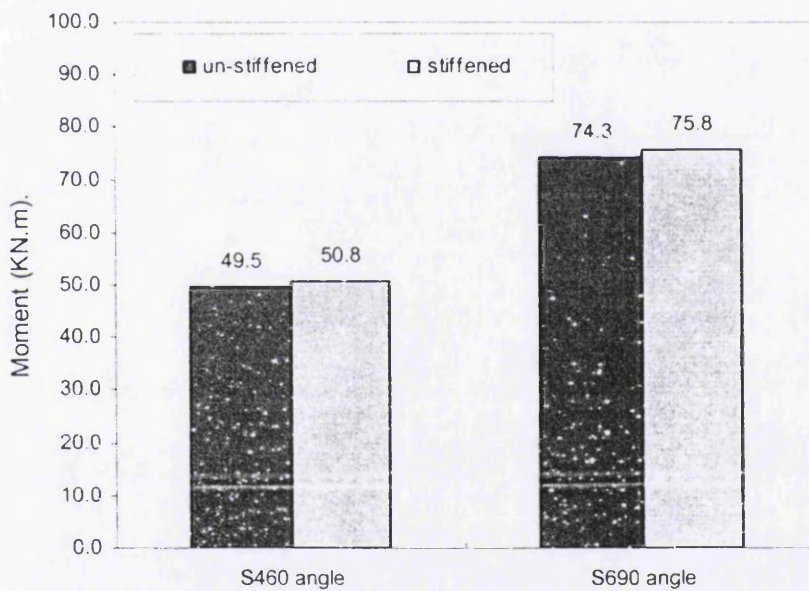


Figure 6.18 Chart showing ultimate moment for each case study

6.2.4.2 FEP connection

The two cases were modelled using stiffened and un-stiffened column with different steel grades. The model produced the results shown in Table 6.19.

Table 6.19

Initial stiffness and ultimate moment of S550 and S690 plates

| Model | column | R_{ki} (KN.m/mRad) | M_u (KN.m) | failure mode |
|---------|--------------|----------------------|--------------|-----------------|
| FEP-1c* | stiffened | 11.93 | 127.0 | plate yielding |
| FEP-1c | un-stiffened | 11.35 | 103.8 | column yielding |
| FEP-1f* | stiffened | 12.38 | 131.0 | plate yielding |
| FEP-1f | un-stiffened | 11.58 | 118.8 | column yielding |

The effect of the column stiffener on the ultimate moment of each of the two cases can be more clearly seen in Figure 6.19.

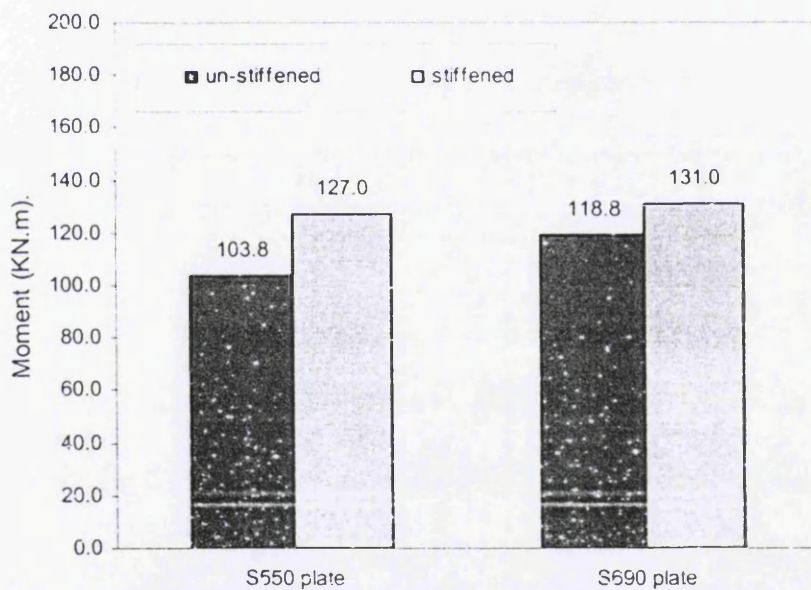


Figure 6.19 Chart showing ultimate moment for each case study

6.2.4.3 SCC connection

The two cases were modelled using stiffened and un-stiffened column with different steel grades. The model produced the results shown in Table 6.20.

Table 6.20

Initial stiffness and ultimate moment of S460 and S690 plates

| Model | column | R_{ki} (KN.m/mRad) | M_u (KN.m) | Failure mode |
|--------|--------------|----------------------|--------------|-----------------|
| SCC-2c | stiffened | 67.53 | 220.2 | plate yielding |
| SCC-1c | un-stiffened | 61.25 | 210.2 | column yielding |
| SCC-2b | stiffened | 73.71 | 288.0 | plate yielding |
| SCC-1b | un-stiffened | 66.33 | 229.0 | column yielding |

The effect of the column stiffener on the ultimate moment of each of the two cases can be more clearly seen in Figure 6.20.

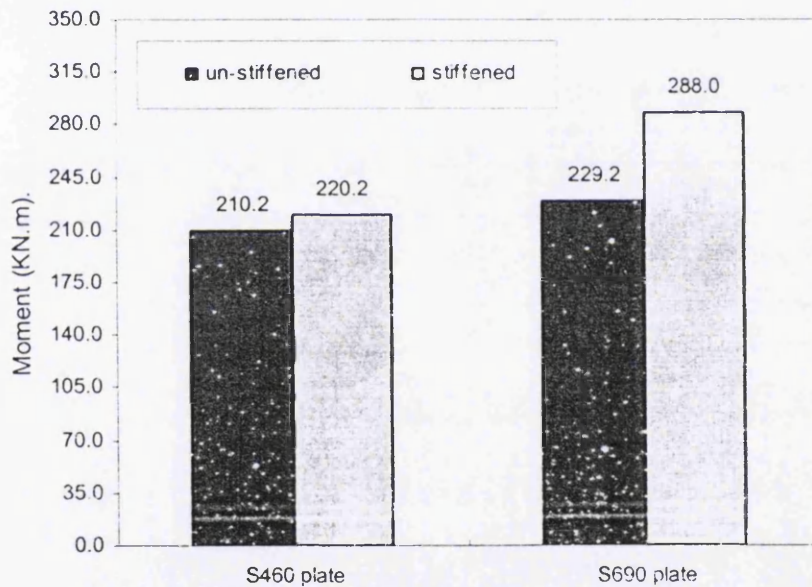


Figure 6.20 Chart showing ultimate moment for each case study

6.2.5 Effect of different steel grades of spliced plate

6.2.5.1 SLB connection (mode-1)

The two cases were modelled using 10.0mm spliced plate thickness and edge distance of 36mm and 45mm with different steel grades. The model produced the results shown in Table 6.21.

Table 6.21

Maximum resistance and rupture load for $e_1/d_o=1.2$ and 1.5

| model | grade | P_{max} (KN) | P_{rp} (KN) | failure mode |
|--------|-------|----------------|---------------|--------------|
| SLB-1a | S690 | 280.8 | 204.9 | bearing |
| SLB-1b | 2205 | 248.1 | 225.2 | bearing |
| SLB-1c | S1350 | 435.2 | 370.4 | bearing |
| SLB-2a | S690 | 360.3 | 252.3 | bearing |
| SLB-2b | 2205 | 317.7 | 243.5 | bearing |
| SLB-2c | S1350 | 637.5 | 601.8 | bearing |

The effect of the different yield and ultimate stresses on the maximum resistance of each of the two cases can be more clearly seen in Figure 6.21.

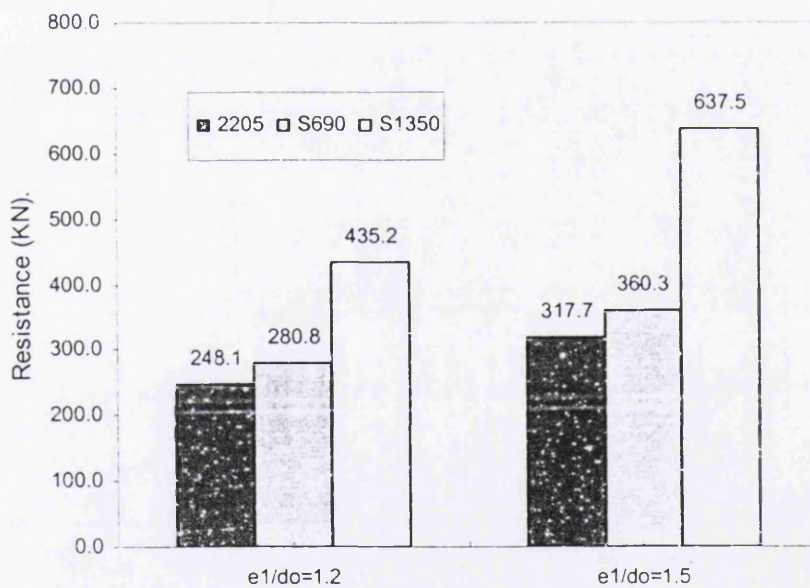


Figure 6.21 Chart showing maximum resistance for each case study

6.2.5.2 SLB connection (mode-2)

The two cases were modelled using 10.0mm spliced plate thickness and edge distances of 36mm and 45mm with different steel grades. The model produced the results shown in Table 6.22.

Table 6.22
Maximum resistance and rupture load for $e_1/d_o=2.0$ and 2.5

| model | grade | P_{max} (KN) | P_{rp} (KN) | failure mode |
|--------|-------|----------------|---------------|--------------|
| SLB-3a | S690 | 480.4 | 435.5 | net section |
| SLB-3b | 2205 | 317.6 | 291.5 | net section |
| SLB-3c | S1350 | 690.0 | 627.0 | net section |
| SLB-4a | S690 | 521.7 | 459.4 | net section |
| SLB-4b | 2205 | 344.9 | 275.3 | net section |
| SLB-4c | S1350 | 740.3 | 635.0 | net section |

The effect of the different yield and ultimate stresses on the maximum resistance two cases can be more clearly seen in Figure 6.22.

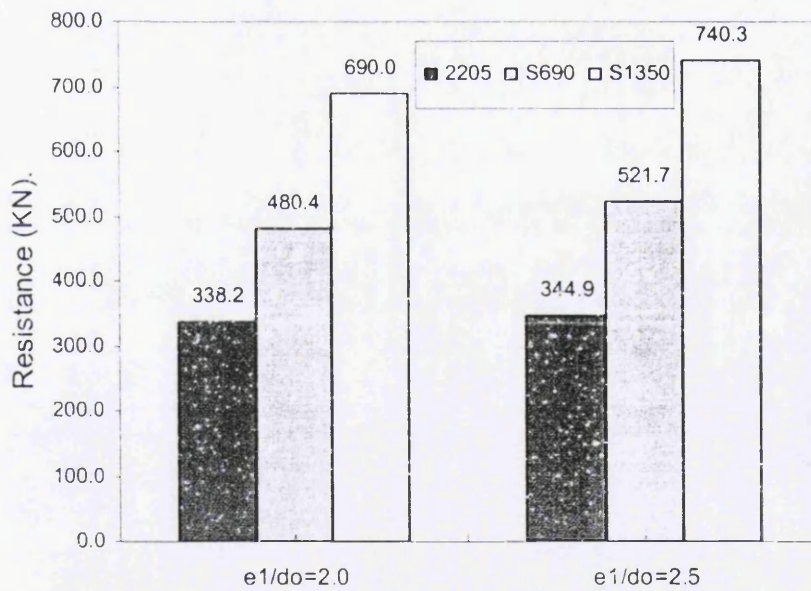


Figure 6.22 Chart showing maximum resistance for each case study

6.2.6 Effect of different thicknesses of the spliced plate

6.2.6.1 SLB connection (mode-3)

The three cases were modelled using edge distances of 36mm and steel grades 2205, S690 and S1350 plate with different plate thicknesses. The model produced the results shown in Table 6.23.

Table 6.23

Maximum resistance and rupture load for 2205, S690 and S1350 plates

| model | t_p (mm) | P_{max} (KN) | P_{rp} (KN) | failure mode |
|--------|------------|----------------|---------------|--------------|
| SLB-6b | 8.0 | 196.9 | 182.0 | bearing |
| SLB-1b | 10.0 | 248.1 | 225.2 | bearing |
| SLB-6a | 8.0 | 221.7 | 175.3 | bearing |
| SLB-1a | 10.0 | 280.8 | 204.9 | bearing |
| SLB-6c | 8.0 | 340.2 | 325.0 | bearing |
| SLB-1c | 10.0 | 435.2 | 370.4 | bearing |

The effect of different thicknesses of the spliced plates on the maximum resistance of each of the three cases can be more clearly seen in Figure 6.23.

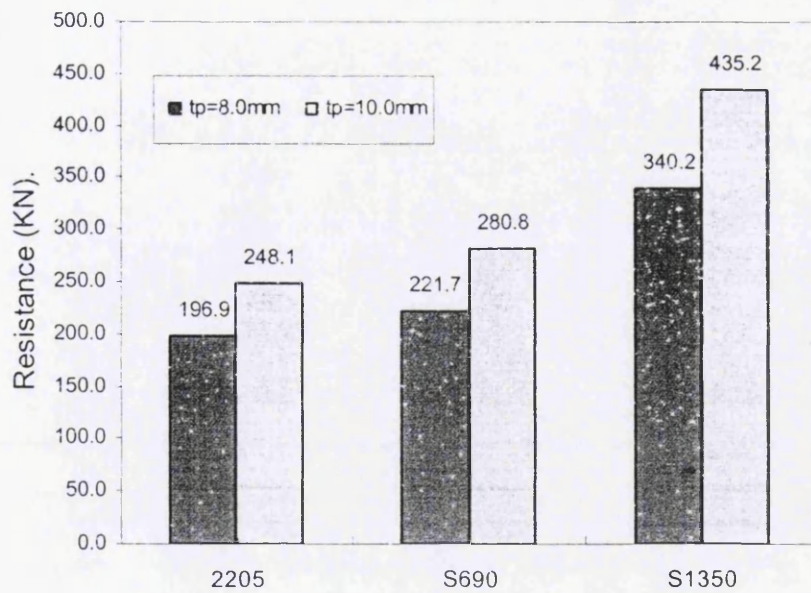


Figure 6.23 Chart showing maximum resistance for each case study

6.2.6.2 SLB connection (mode-4)

The three cases were modelled using edge an distance of 60mm and stainless steel grade 2205 plate with different plate thicknesses. The model produced the results shown in Table 6.24.

Table 6.24

Maximum resistance and rupture load for 2205, S690 and S1350 plates

| model | t_p (mm) | P_{max} (KN) | P_{rp} (KN) | failure mode |
|--------|------------|----------------|---------------|--------------|
| SLB-8b | 8.0 | 270.6 | 240.3 | net section |
| SLB-3b | 10.0 | 338.2 | 291.5 | net section |
| SLB-8a | 8.0 | 384.3 | 364.5 | net section |
| SLB-3a | 10.0 | 480.4 | 435.5 | net section |
| SLB-8c | 8.0 | 525.3 | 429.6 | net section |
| SLB-3c | 10.0 | 655.2 | 627.0 | net section |

The effect of different thickness of the spliced plates on the maximum resistance of each of the three cases can be more clearly seen in Figure 6.24.

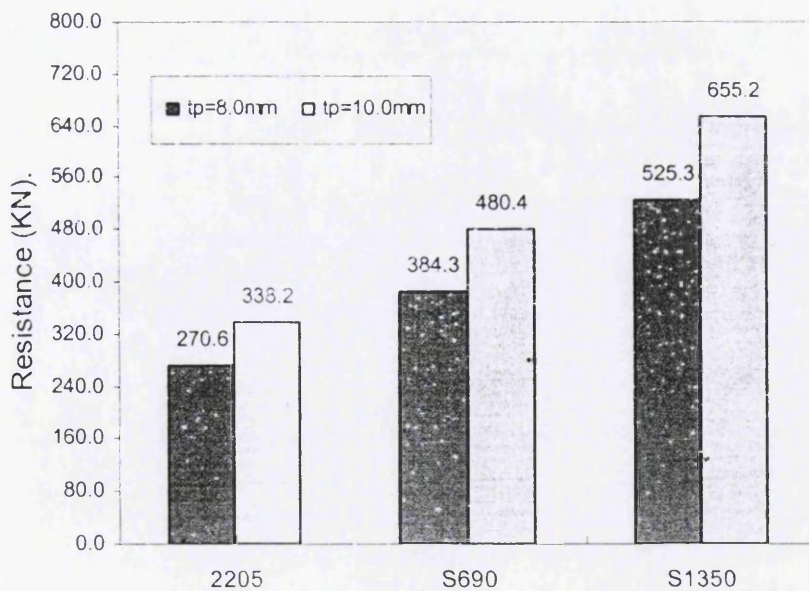


Figure 6.24 Chart showing maximum resistance for each case study

6.2.7 Effect of different edge distances of the bolt

6.2.7.1 SLB connection (mode-5)

The two cases were modelled using spliced plate thickness of 8mm and 10mm with steel grade 2205 and different edge distance to centre of bolt. The model produced the results shown in Table 6.25.

Table 6.25

Maximum resistance and rupture load with $t_p=8.0$ and 10mm

| model | e_1/d_o | P_{max} (KN) | P_{rp} (KN) | failure mode |
|---------|-----------|----------------|---------------|--------------|
| SLB-10b | 1.0 | 173.4 | 156.3 | bearing |
| SLB-6b | 1.2 | 196.9 | 169.8 | bearing |
| SLB-8b | 2.0 | 270.6 | 245.6 | net section |
| SLB-5b | 1.0 | 219.5 | 197.4 | bearing |
| SLB-1b | 1.2 | 248.1 | 225.4 | bearing |
| SLB-3b | 2.0 | 338.2 | 291.5 | net section |

The effect of the varying edge distances of the bolt on the maximum resistance of each of the two cases can be more clearly seen in Figure 6.25.

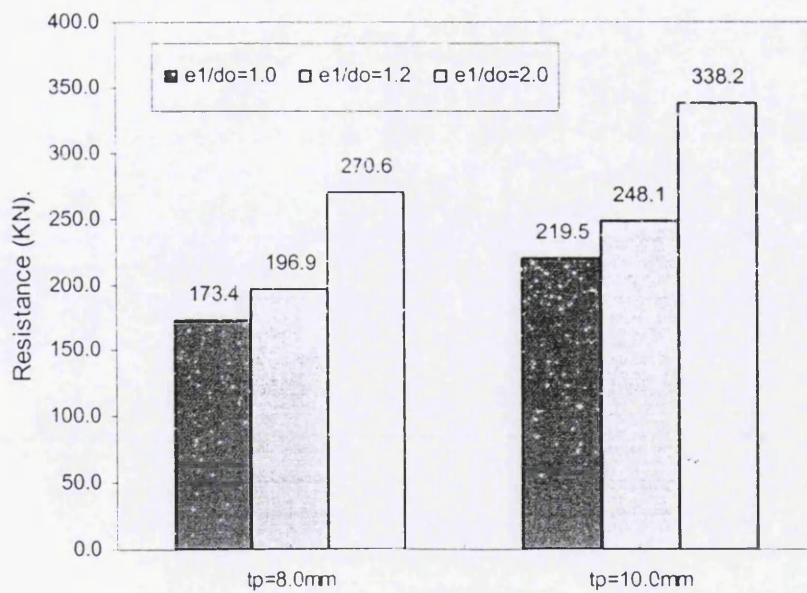


Figure 6.25 Chart showing maximum resistance for each case study

6.2.7.2 SLB connection (mode-6)

The two cases were modelled using spliced plate thicknesses of 8mm and 10mm with steel grade S690 and different edge distances to centre of bolt. The model produced the results shown in Table 6.26.

Table 6.26
Maximum resistance and rupture load with $t_p=8.0$ and 10mm

| model | e_1/d_o | P_{max} (KN) | P_{rp} (KN) | failure mode |
|---------|-----------|----------------|---------------|--------------|
| SLB-10a | 1.0 | 206.5 | 165.3 | bearing |
| SLB-6a | 1.2 | 221.7 | 175.3 | bearing |
| SLB-8a | 2.0 | 384.3 | 364.5 | net section |
| SLB-5a | 1.0 | 264.7 | 222.0 | bearing |
| SLB-1a | 1.2 | 280.8 | 204.9 | bearing |
| SLB-3a | 2.0 | 480.4 | 435.6 | net section |

The effect of the different edge distances to centre of the bolt on the maximum resistance of each of the two cases can be more clearly seen in Figure 6.26.

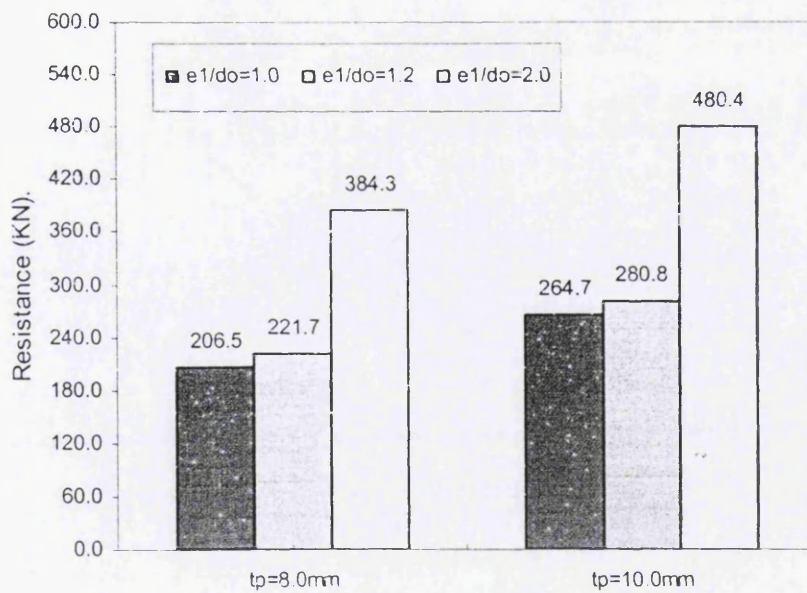


Figure 6.26 Chart showing maximum resistance for each case study

6.2.7.3 SLB connection (mode-7)

The two cases were modelled using spliced plate thicknesses of 8mm and 10mm with steel grade S1350 and different edge distances to centre of bolt. The model produced the results shown in Table 6.27.

Table 6.27

Maximum resistance and rupture load with $t_p=8.0$ and 10mm

| model | e_1/d_o | P_{max} (KN) | P_{rp} (KN) | failure mode |
|---------|-----------|----------------|---------------|--------------|
| SLB-10c | 1.0 | 337.0 | 277.0 | bearing |
| SLB-6c | 1.2 | 340.2 | 276.5 | bearing |
| SLB-8c | 2.0 | 525.7 | 358.7 | net section |
| SLB-5c | 1.0 | 432.0 | 370.0 | bearing |
| SLB-1c | 1.2 | 435.2 | 362.2 | bearing |
| SLB-3c | 2.0 | 690.0 | 635.0 | net section |

The effect of varying edge distances of the bolt on the maximum resistance of each of the two cases can be more clearly seen in Figure 6.27.

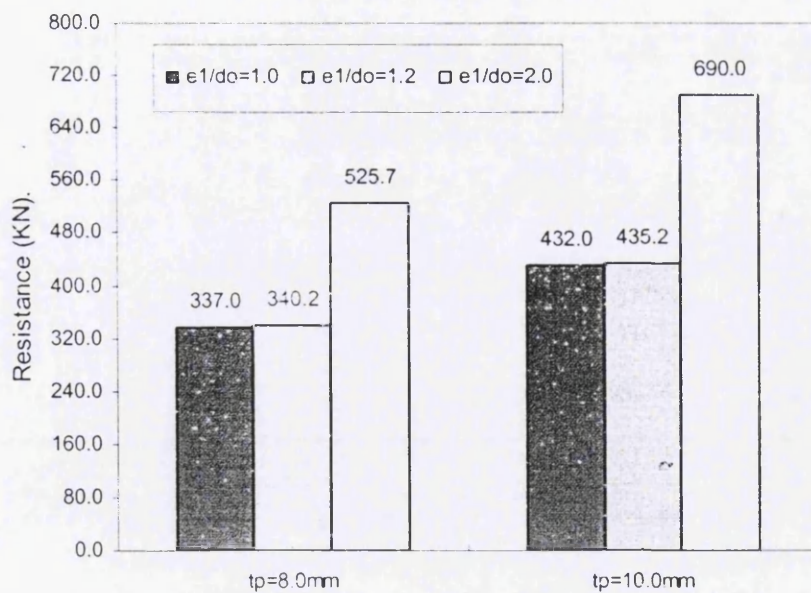


Figure 6.27 Chart showing maximum resistance for each case study

6.3 Discussion from the Parametric Study

Based on the parametric study, it can be seen that the different steel grades, plate thicknesses, beam sizes, and e_1/d_0 ratio have significant influence on the resistance of the connections. Three different material properties of steel grade S460, S550 and S690 are being applied on the PR connection to investigate the associated changes in the ultimate moment and rotational capacity. The effect of beam size on the connection capacity is also investigated by applying different levels of beam depth. Three different sets of steel grade S2205, S690 and S1350 are being applied on the SLB connection to investigate the associated changes in the ultimate load and load resistance at fracture of the joint. The effect of stiffer material on the maximum resistance is investigated by applying different levels of angle and plate thickness. The effect of edge distance on the SLB connection resistance is also investigated by applying different levels of e_1/d_0 ratio.

The ultimate moment of the angle bolted connection for different steel grade is plotted in the Figures 6.1 - 6.3. It can be observed that with the increase in the ultimate strength, there is a significant increase in the ultimate moment whilst the initial stiffness is no significant change. The ultimate moment of the S690 and S550 angles increases by $(f_{u3}/f_{u1})^{0.83}$ and $(f_{u2}/f_{u1})^{0.85}$ respectively, when compared with S460 angles. The ultimate moment of the end plate connection for different steel grade is plotted in the Figure 6.4 - 6.5. It can be seen that with the increase in the ultimate strength, there is a significant increase in the ultimate moment whilst the initial stiffness is no significant change. The ultimate moment of the S690 thin end-plates increases by $(f_{u3}/f_{u2})^{0.80}$ times when compared with S550 ones, whilst the ultimate moment of S690 thicker end plates increases by $(f_{u3}/f_{u2})^{0.45}$ times when compared with S550 ones. The ultimate moment of the SCC connection is plotted in Figure 6.6. The ultimate moment of the S690 end plates increases by $(f_{u3}/f_{u1})^{0.20}$ times when compared with S460 ones.

Since the stiffer angles of the angle bolted connection are likely to increase the ultimate moment and initial stiffness significantly as plotted in the Figures 6.7 – 6.9. The ultimate moment of the 11.0mm and 12.5mm thick web angles increases by $(t_{wa2}/t_{wa1})^{1.98}$ and $(t_{wa3}/t_{wa1})^{1.95}$ times when compared with 9.5mm thick ones. The ultimate moment and

initial stiffness of the 9.5mm and 12.5mm thick seat angles increases by $(t_{sa2}/t_{sa1})^{1.93}$ and $(t_{sa4}/t_{sa1})^{1.58}$ times when compared with 8.0mm thick ones. When the web angle is applied on the TSAW connection, there is no significance changes on the ultimate moment and initial stiffness as the increase is only by $(t_{sa3}/t_{sa2})^{0.50}$ times.

The ultimate moment of the endplate connection for different endplate thickness is plotted in the Figures 6.10 – 6.12. It can be observed that with the increase in the angle thickness, there is a significant increase in the ultimate moment. The ultimate moment of the 15.0mm and 18.0mm thick flush endplates increases by $(t_{ep2}/t_{ep1})^{1.68}$ and $(t_{ep3}/t_{ep1})^{1.61}$ times, respectively, when compared with 12.0mm thick ones. The ultimate moment of the 15.0mm thick endplates of EPTB connection increases by $(t_{ep2}/t_{ep1})^{1.30}$ times when compared with 10mm thick ones. When the concrete slab is applied on the SCC connection, there is no significance changes on the ultimate moment and initial stiffness as the increase is only by $(t_{sa3}/t_{sa2})^{0.10}$ or approximately 1.1 times.

The ultimate moment of the PR connection for different beam depth is plotted in the Figures 6.13 - 6.18. As expected, the ultimate strength increases, there is a significant increase in the ultimate moment and initial stiffness. The ultimate moment of the deeper beam increases by $(h_2/h_1)^{1.92}$ times when compared with the shallow beam. The presence of the column web stiffener on the end plates connection gives significance change on the ultimate moment, whilst there is no significance change on the angle bolted connection as shown in Figure 6.18 - 6.20.

The ultimate resistance and rupture resistance of the SLB connection increases significantly when the ultimate strength and e_1/d_0 ratio increase as plotted in the Figures 6.21 - 6.27. The ultimate resistance of S690 and S1350 spliced plates under bearing failure increases by $(f_{u2.3}/f_{u1})^{0.28}$ and $(f_{u2.3}/f_{u1})^{0.66}$ times, respectively, compared with SS2205 ones, whilst the rupture resistance of S690 and S1350 plates increases by $(f_{u2.3}/f_{u1})^{-0.25}$ and $(f_{u2.3}/f_{u1})^{0.50}$ times, respectively. The ultimate and rupture resistance of S690 and S1350 spliced plates under net section failure increases by $(f_{u2.3}/f_{u1})^{0.92}$ times compared with SS2205 ones. The ultimate and rupture resistance of SLB connection with $e_1/d_0 < 1.5$ and $e_1/d_0 \geq 1.5$ increases by $(e_{1.1}/e_{1.2})^{0.35}$ and $(e_{1.1}/e_{1.2})^{0.25}$ times, respectively.

6.4 Static Frame Analyses

The model uses the BEAM23 and COMBIN39 elements for the static frame analyses. For this stage both the beam-to-column and the base rotational stiffness were changed to check how the mid span beam and sway deflection are effected; by conducting a total of 126 analyses for both cases, of which results are given in tables that are reported in each section. The single story frame model shown in Figure 6.28 has been loaded with two point loads F (KN) at one third span on each beam and one horizontal point loads at floor level of $1/5$ of the vertical force.

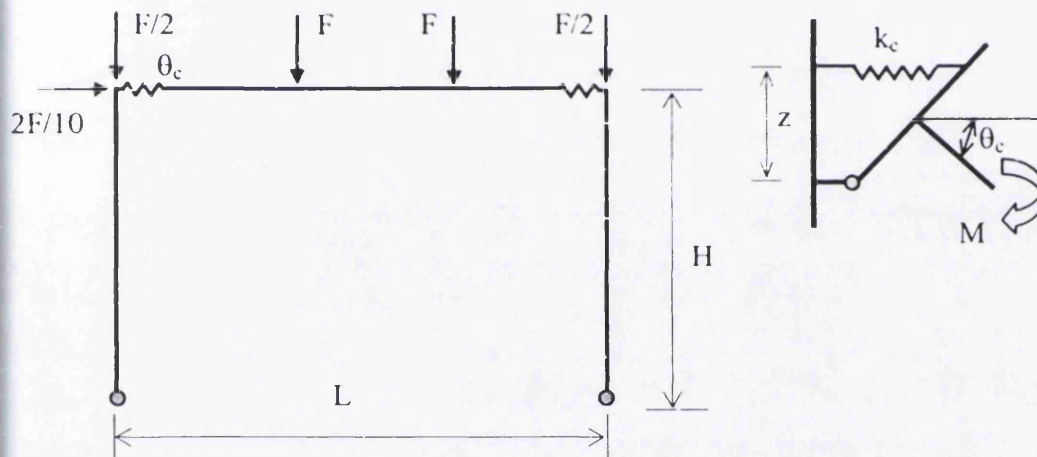


Figure 6.28 Single storey frame model

6.4.1 Non-Sway Static Analyses

For the non-sway analyses the frame model has been restrained from moving horizontally as shown below. Three sets of analyses were carried out, the first one considered this frame with an angle connection, the second set of analyses with endplate connection, and the third set of analyses was carried out with slab; the influence of this last on the static performance of a frame with different joint stiffness is investigated.

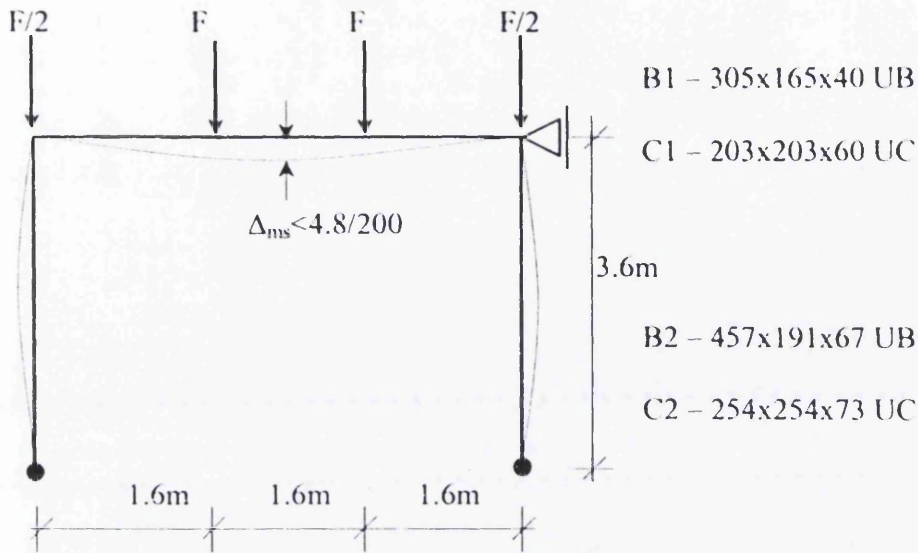


Figure 6.29 Non-sway model

Two types of non-sway frame are modeled, which the first model was built using 305x165x40UB main beam (B1) and 203x203x60UC column (C1) and the second model was built using 457x191x67 UB main beam (B2) and 254x254x73UC column (C2). The results give values of the deflection at mid-span of the main beams (Δ_{ms}), at the first and second set of the analyses with the applied point load of 100KN and 200KN are reported in Tables 6.28 and 6.29, respectively. The maximum-recorded value of first model is 14.13mm and the minimum is 6.22mm, which shows that with the combined increase in stiffness of the base and beam-to-column joint with a 25% decrease in beam deflection. The maximum-recorded value of second model is 11.27mm and the minimum is 5.58mm, which shows that with the combined increase in stiffness of the base and beam-to-column joint with a 17.5% decrease in beam deflection. Within the range of values selected for the joint stiffness, these that most influence the deflection of the main beams were within the middle of the range spanning between 3.21 to 97.53 KN.m/mRad for the first model and 9.56 to 48.23 KN.m/mRad for the second model.

Table 6.28

Maximum vertical deflection of the main beams for the non-sway frame (1)

| BC \ CB | R _{ki} | DWA | TSA1 | TSA2 | TSAW | FEP1 | FEP2 | SCC |
|-----------------|-----------------|-------|-------|-------|-------|-------|-------|-------|
| R _{ki} | -- | 3.21 | 5.60 | 9.60 | 14.96 | 21.00 | 28.50 | 97.53 |
| Pinned | 0 | 14.13 | 13.37 | 12.68 | 12.20 | 11.90 | 11.68 | 6.73 |
| Semi-rigid | 64.0 | 14.06 | 13.22 | 12.59 | 12.02 | 11.76 | 11.58 | 6.67 |
| Fixed | ∞ | 13.99 | 13.12 | 12.29 | 11.69 | 11.31 | 11.03 | 6.22 |

Table 6.29

Maximum vertical deflection of the main beams for the non-sway frame (2)

| BC \ CB | R _{ki} | DWA | TSA1 | TSA2 | TSAW1 | TSAW2 | FEP1 | SCC |
|-----------------|-----------------|-------|-------|-------|-------|-------|-------|--------|
| R _{ki} | -- | 9.56 | 14.27 | 15.21 | 30.82 | 37.21 | 47.15 | 125.87 |
| Pinned | 0 | 11.27 | 10.84 | 10.77 | 10.09 | 9.93 | 9.84 | 5.85 |
| Semi-rigid | 64.0 | 11.20 | 10.75 | 10.70 | 9.95 | 9.82 | 9.71 | 5.79 |
| Fixed | ∞ | 11.14 | 10.63 | 10.55 | 9.72 | 9.53 | 9.32 | 5.58 |

The values reported above are plotted in Figure 6.30, where the beam-to-column (BC) stiffness is plotted against the maximum vertical deflection of the main beams. Each different line on the chart shown the results for different column base (CB) connection stiffnesses.

Looking at the stress in the top end columns, one can see that if both joints stiffness are increased, a gradual increase in bending moment obtained. The maximum value recorded is 139.0 KN.m and the minimum is 108.0 KN.m, with a total difference of 22%. The graphical representation of the bending moment distribution, from ANSYS, within the non-sway frame with low and high stiffness is shown in Figure 6.31.

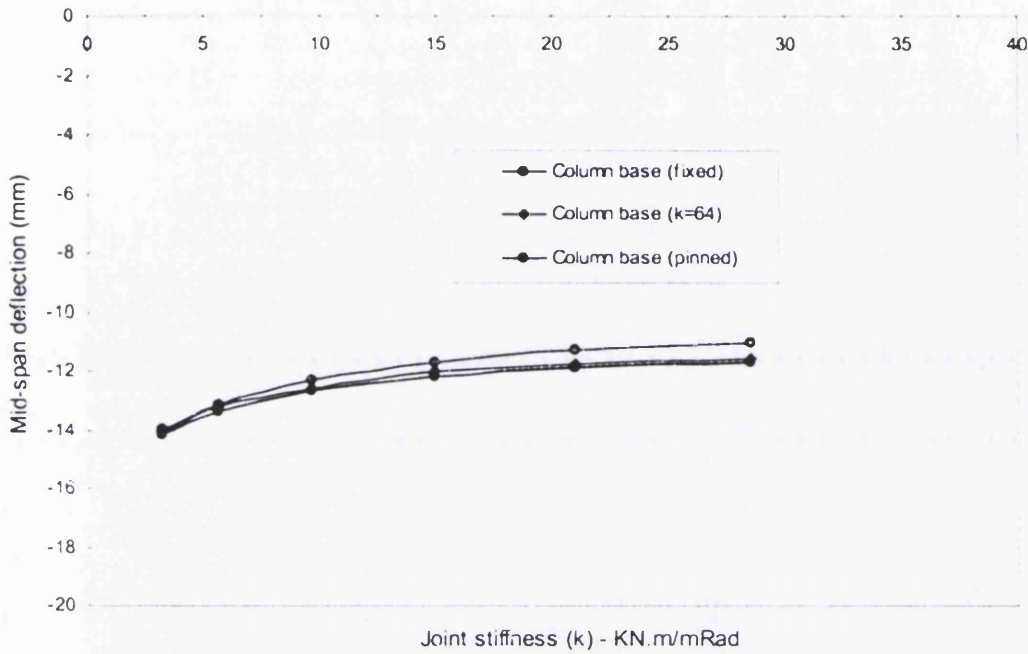


Figure 6.30 Maximum vertical deflection of the main beams for the non-sway frame

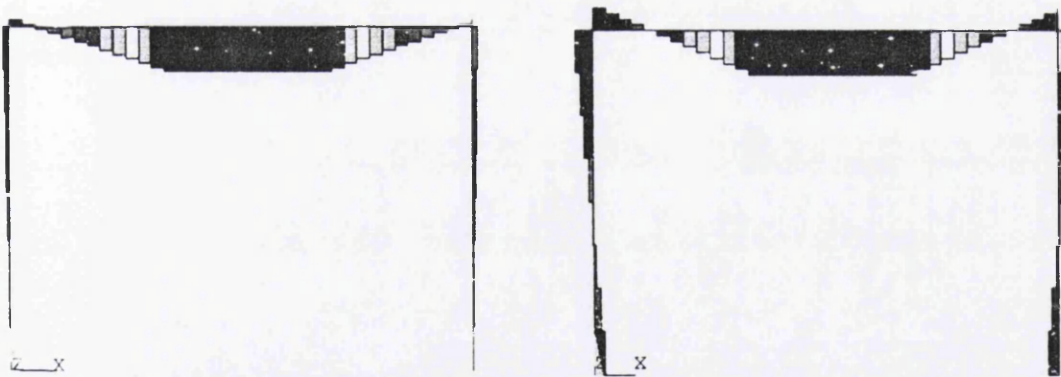


Figure 6.31 Bending moment distribution of the non-sway model for: (a) fully pinned base and beam-to-column joint (b) fully fixed base and beam-to-column joint

The column base stiffness rigidity is an important parameter in the performance of the frame and suggestion is that it has to be considered in the design process. If we compare the two sets of analyses we immediately see the difference of response of the two different frames subjected to the same loading and constraints. The addition of the

concrete slab considerably increases the strength of the frame and this has a direct impact on the local deflections and internal stresses of the frame, decreasing them both.

6.4.2 Sway Static Analyses

The same model used from the previous section is used here for the sway analyses, with the only difference that the horizontal constraint at the column ends, Figure 6.31, the loads applied on the frame are the same too. Three sets of analyses were performed, first on the steel frame only with angle connections, and on the steel frame with end plate connection, and then on the same one frame with concrete floor. Both vertical and horizontal deflections of the frame have been recorded. The vertical corresponding to the maximum beam deflection and horizontal to the maximum lateral displacement at the top of the columns, where the load is applied.

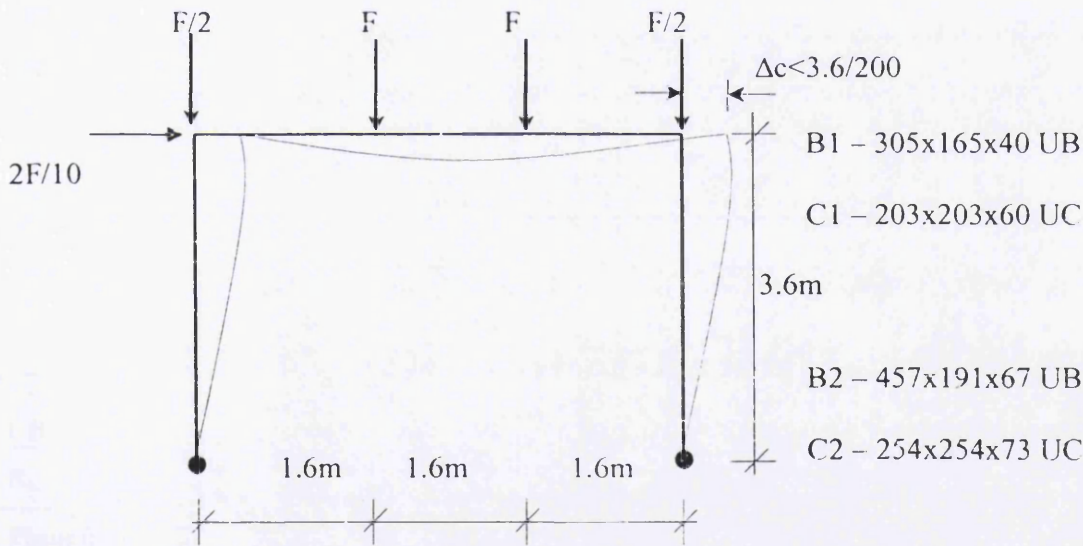


Figure 6.32 Sway model

Two types of sway frame are modeled, which the first model was built using 305x165x40UB main beam (B1) and 203x203x60UC column (C1) and the second model was built using 457x191x67 UB main beam (B2) and 254x254x73UC column (C2). The result values of the horizontal deflection at top of the columns (Δ_c), of the first and

second set of the analyses with the applied point load of 125KN and 250KN are reported in Tables 6.30 and 6.31, respectively. All of the curves show the same pattern, exponentially decreasing as the base rigidity, which overall it has a considerable influence reducing by six times the lateral displacement, from 61mm to 9.9mm.

Table 6.30

Horizontal deflection at the top of the column for the sway frame (1)

| CB \ BC | R _{ki} | DWA | TSA1 | TSA2 | TSAW | FEP1 | FEP2 | SCC |
|-----------------|-----------------|-------|-------|-------|-------|-------|-------|-------|
| R _{ki} | -- | 3.21 | 5.60 | 9.60 | 14.96 | 21.00 | 28.50 | 97.53 |
| Pinned | 0 | 76.11 | 54.59 | 42.54 | 36.49 | 33.44 | 31.76 | 17.10 |
| Semi-rigid | 2.0 | 38.05 | 27.28 | 21.26 | 18.15 | 16.78 | 15.88 | 8.54 |
| Semi-rigid | 4.0 | 19.79 | 13.91 | 10.84 | 10.51 | 9.48 | 9.34 | 5.60 |
| Semi-rigid | 32.0 | 16.10 | 12.79 | 9.56 | 9.01 | 8.56 | 8.44 | 5.03 |
| Fixed | ∞ | 12.38 | 10.59 | 9.35 | 8.88 | 8.61 | 8.44 | 4.90 |

Table 6.31

Horizontal deflection at the top of the column for the sway frame (2)

| CB \ BC | R _{ki} | DWA | TSA1 | TSA2 | TSAW1 | TSAW2 | FEP | SCC |
|-----------------|-----------------|-------|-------|-------|-------|-------|-------|--------|
| R _{ki} | -- | 9.56 | 14.27 | 15.21 | 30.82 | 37.21 | 47.15 | 125.87 |
| Pinned | 0 | 54.48 | 43.30 | 41.89 | 31.11 | 29.31 | 28.66 | 20.14 |
| Semi-rigid | 2.0 | 26.54 | 21.54 | 20.91 | 15.84 | 14.81 | 14.28 | 9.69 |
| Semi-rigid | 4.0 | 12.91 | 11.08 | 10.29 | 8.15 | 7.86 | 7.40 | 5.19 |
| Semi-rigid | 32.0 | 11.54 | 10.03 | 9.46 | 7.44 | 7.19 | 7.03 | 4.94 |
| Fixed | ∞ | 9.48 | 8.48 | 8.33 | 7.21 | 7.08 | 6.99 | 4.14 |

The results tabulated above are graphed below, Figures 6.33 and 6.34 which also shows how the sway of the frame varies with column base rigidity. The scale of the graph has been reduced to highlight the variation of response of the frame in the reasonable range of values. The maximum value is 60.89mm and the minimum is 3.32mm for the first model, whilst the maximum value is 43.58mm and the minimum is 3.31mm for the second model. All of the curves show the same patterns, exponentially decreasing as the base rigidity is increased, which overall it has a considerable influence reducing by five times the lateral displacement, from 43.58mm to 7.58mm.

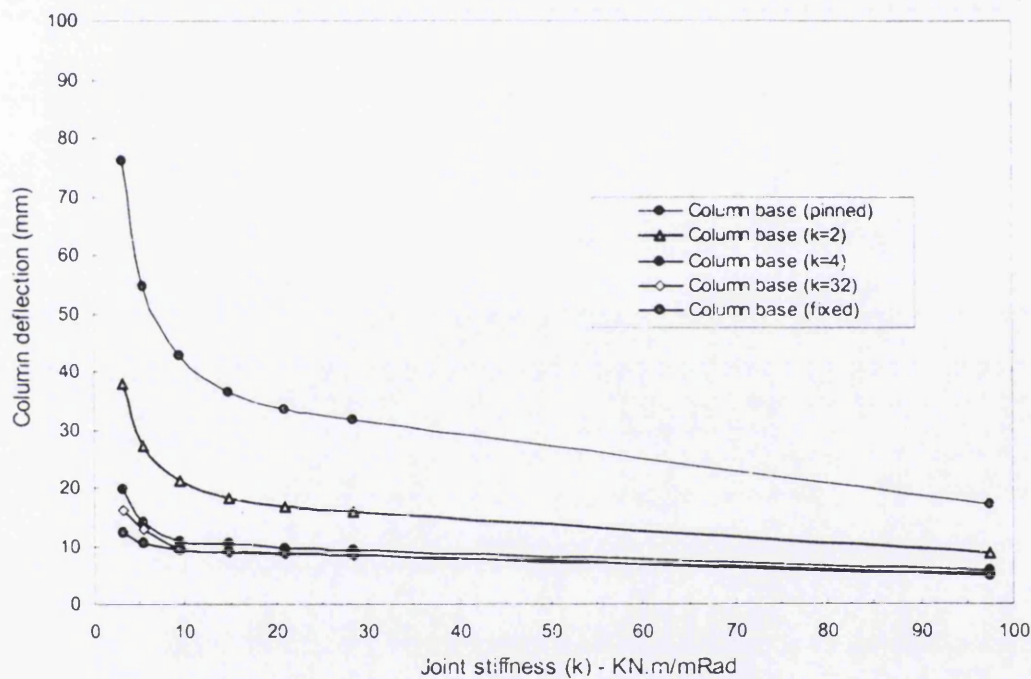


Figure 6.33 Horizontal deflection at the top of the column for the sway frame (1)

Looking at the stress in the top end columns, one can see that if both joints stiffness are increased, a gradual increase in bending moment obtained. The maximum value recorded is 129.0 KN.m and the minimum is 114.0 KN.m, with a total difference of 11%. The graphical representation of the bending moment distribution, from ANSYS, within the frame with low and high stiffness is shown in Figure 6.35.

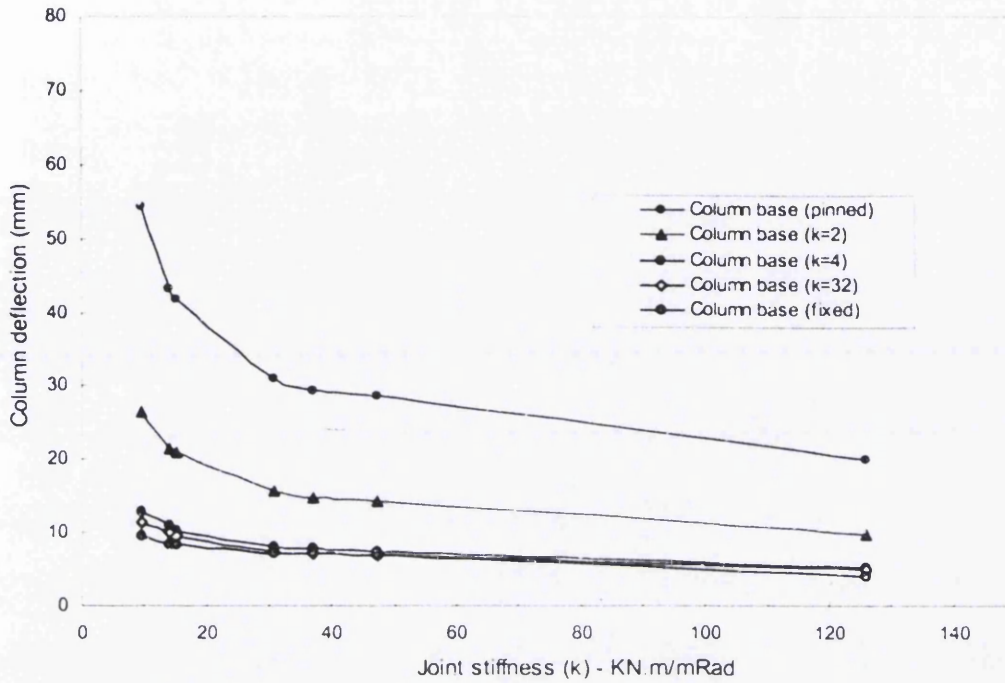


Figure 6.34 Horizontal deflection at the top of the column for the sway frame (2)

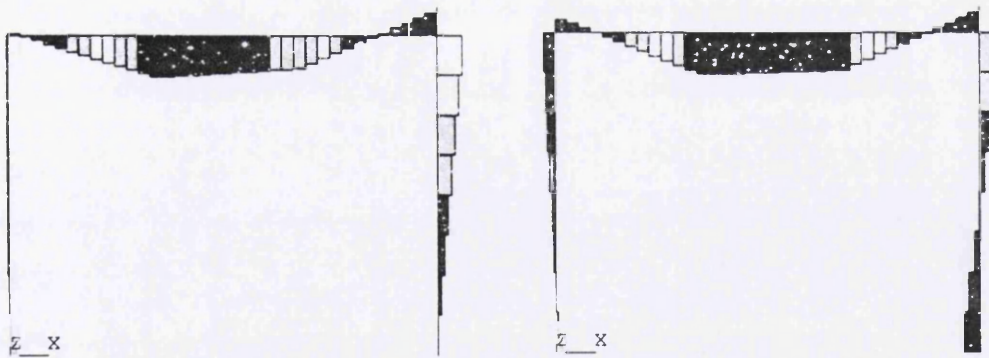


Figure 6.35 Bending moment distribution of the sway model for: (a) fully pinned base and beam-to-column joint (b) fully fixed base and beam-to-column joint

6.5 Summary and Conclusion

Chapter 6 has focused on the parametrical study of the bolted connections with high strength and stainless steel by the finite element analyses. The chapter has three main parts: angle bolted connections with high strength steel, endplate connections with high strength steel and spliced shear connections with high strength and stainless steel. The influence of different steel grades on the connection behaviour as well as the softening effect on the spliced shear connection have been studied. In addition, the comparison of ultimate moment and load resistance of the connections in each part to these was presented. Furthermore, the change of the connection capacity of each connection from each part was given. From the study carried out, the following conclusions are drawn:

The results show that the application of higher strength steel, stiffer angles and deeper beams for the angle bolted connection gives significant increase in moment capacity and initial stiffness except for TSAW which little change of initial stiffness due to web angles restraint. In the presence of the higher and stiffer plates and deeper beams, the endplate connection gave a significant increasing of moment capacity and initial stiffness except for FEP and SCC when the ultimate moment and initial stiffness increased slightly. The presence of a column web stiffener on endplate connection gives significant changes on the ultimate moment, whilst there is no significant change on the angle bolted connection.

The application of high strength and stainless steel for the shear bolted connection could be calculated by two approaches of resistance design such as bearing resistance and net section resistance. As expected, the ultimate resistance and rupture resistance of the SLB connection have been increased significantly when the ultimate strength and e_1/d_0 ratio increase. The ultimate and rupture resistance of the connection under net section failure shows a linearity relationship with the change of the ultimate strength, whilst the ultimate and rupture resistance of the connection under bearing failure shows a non-linear relationship with the change of the ultimate strength. The effect of the edge distance of bolt hole shows a consistency of the change in the resistance for both under bearing and net section failure.

When a PR connection is applied to the portal frame, there is a significant influence of the stiffness rigidity of beam-column and column base connection with different responses. The presence of the concrete slab on the SCC connection gives better resistance in the vertical deflection of the main beams for the non-sway frame, whilst the bare steel joint shows not much improvement. Increased beam-column and column base connection stiffness on the sway frame could have the most considerable influence on reducing the lateral displacement by at least five times. The presence of high strength angles and endplates will reduce the connection weight with higher capacity.

Chapter 7

Design Equations

7.1 Introduction

Extensive research has been conducted to study the ultimate moment and load behaviour of high strength and stainless steel bolted connections. The analytical studies of the flexural strength of partially restrained connection and axial strength of shear bolted connection have been completed. The analyses and design of bolted connections can be accomplished by using the computational modelling and empirical methods. There are several methods that can achieve the computational modelling including the finite element modelling that was introduced in Chapter 3 and developed in Chapter 5. The parametric study is presented in Chapter 6. The finite element modelling method will be evaluated by introducing the empirical method that will be developed in this chapter according to EC3.

Although validated computational model and procedures may be used to find the moment-rotation relationship of a connection in lieu of physical testing, it is time consuming and inconvenient to use this approach in design practice since one analyses may take a few hours to finish using even the fastest PC. Therefore, it is desirable to derive design equations to represent the moment-rotation relationship for a specific connection, such as a partially restrained connection. Several researchers have conducted research in developing such moment-rotation mathematical models. For example,

Abolmaali [81] has attempted to derive a moment-rotation function for flush endplate connections using a three-parameter power model. In this chapter, the development of a mathematical model to describe the moment-rotation behaviour of partially restrained connections is presented.

7.2 Analytical Model for Moment-rotation Relationship

The stiffness of any PR connection is dependant upon its moment-rotation characteristic. Many attempts have been made to establish curve-fitting techniques that can be used to provide suitable models for PR connections. Abolmaali et.al [81] have developed moment-rotation model equations for flush end-plate connections. It was shown that the Three-Parameter Power model predicted the $M-\theta$ curve accurately. The Three-Parameter Power model was originally proposed by Richard and Abbott [97] and Chen and Kishi [98] to predict the moment-rotation ($M-\theta$) characteristics of PR connections. There are three independent parameters that define this model equation, which are: initial stiffness, R_{ki} , ultimate moment, M_u , and rigidity parameter, n . This equation is described by:

$$M = \frac{R_{ki}\theta}{\left[1 + (\theta/\theta_0)^n\right]^{\frac{1}{n}}} \quad (7.1)$$

where:

M_u = ultimate moment capacity

n = rigidity parameter

R_{ki} = initial connection stiffness

θ_0 = reference plastic rotation defined by:

$$\theta_0 = M_u / R_{ki} \quad (7.2)$$

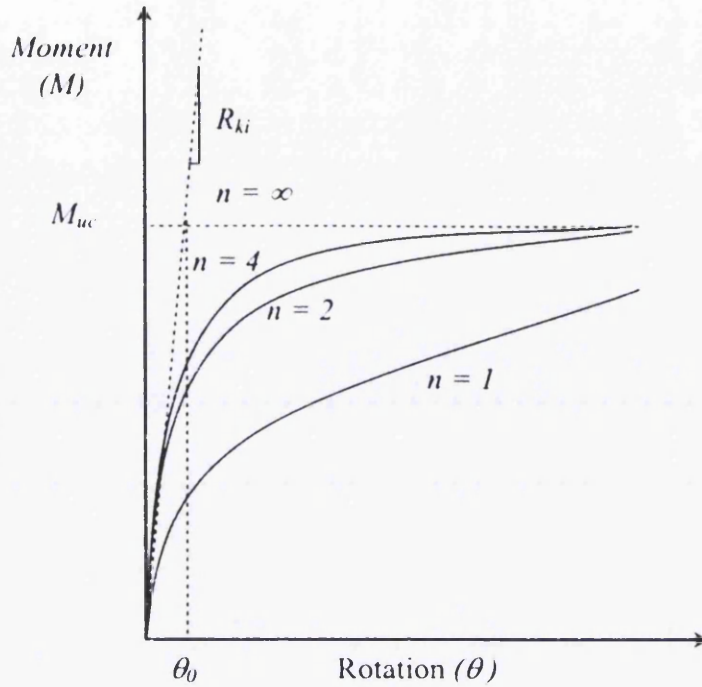


Figure 7.1 Three-Parameter Power model.

Figure 7.1 shows the schematic of the Three-Parameter Power model with different values of rigidity parameter, n , which defines a more flexible model as n increases. The $M-\theta$ data obtained from these analyses were curve fitted to Equations 7.3 and 7.4 by minimizing their error-square to obtain model parameters M_u , n , and θ_0 . Consequently, regression equations were developed for the aforementioned parameters of each equation in terms of geometric variables for a connection.

The three parameter is expanded into a proposed equation to accommodate the change in the curve shape due to the non-linear behaviour of different steel grades of each member in the connection. The rigidity parameter n will be expanded into parameter q , with the dependent variables are considered, the prediction equations is defined as:

$$M = \frac{R_{ki}\theta}{\left[1 + (\theta/\theta_0)^n\right]^{1/q}} \quad (7.3)$$

where

M_u = ultimate moment capacity

n = rigidity parameter

q = rigidity parameter with influence of steel grades

R_{ki} = initial connection stiffness

θ_0 = reference plastic rotation defined by:

$$\theta_0 = M_u / R_{ki} \quad (7.4)$$

In this study, several test cases were selected using the FEM connection model developed in Chapters 5 and 6. The $M-\theta$ data points obtained from the analyses were curve fitted to obtain model parameters. Consequently, regression equations were developed for the aforementioned parameters of each equation in terms of geometric variables of the connection region. In the development of the prediction equations, the independent variables (connection geometric variables) are defined as:

g = the gauge distance

d_b = the nominal bolt diameter

P_f = the bolt pitch

t_w = the beam web thickness

h_b = the beam depth

b_p = the width of end-plate

t_{cp} = the thickness of end-plate

t_{wa} = the thickness of web angle

t_{sa} = the thickness of top and seat angle

t_{st} = the thickness of column stiffener

F_{ya} = material yield stress of angle cleat

F_{yp} = material yield stress of end plate

F_{yb} = material yield stress of beam

F_{yc} = material yield stress of column steel

E_o = Young's modulus

Unit of independent variables: mm and MPa

For the DWA connection, the top and seat angles are not present, therefore $t_{sa} = 0$, whilst for the TSA connection, the web angles are not present, therefore $t_{wa} = 0$. The end plates could be zero on the angle bolted connection as $t_{cp} = 0$. Similarly, the angles could be zero for the end plate connections, therefore $t_{wa} = 0$ and $t_{sa} = 0$.

Using these results and the multiple regression technique, a prediction equation was developed for each independent parameter using the following general form:

$$R_{ki} = \prod_{j=1}^m A a_j^{w_j}; \quad M_u = \prod_{j=1}^m B a_j^{x_j}; \quad n = \prod_{j=1}^m C a_j^{y_j}; \quad q = \prod_{j=1}^m D a_j^{z_j} \quad (7.5)$$

where A, B, C and D are unknown coefficients, a_j is the j th independent parameter, w_j , x_j , y_j , and z_j are the exponents to be determined through regression, and m is the number of independent parameters considered. Taking logarithms of both sides of the formulae in Equation 7.5, linear forms of these formulae are obtained as:

$$\ln R_{ki} = \ln A + \sum_{j=1}^m w_j \ln a_j \quad (7.6)$$

$$\ln M_u = \ln B + \sum_{j=1}^m x_j \ln a_j \quad (7.7)$$

$$\ln n = \ln C + \sum_{j=1}^m y_j \ln a_j \quad (7.8)$$

$$\ln q = \ln D + \sum_{j=1}^m z_j \ln a_j \quad (7.9)$$

Multiple regression using spreadsheet software is applied to each formula in Equations 7.6 – 7.9 to determine the coefficients A, B, C, D, w_j , x_j , y_j , and z_j . From regression analyses, Equations 7.10 – 7.13 represent independent parameters of the design equation for ultimate moment, reference plastic rotation and rigidity parameter. Sensitivity and error band analyses were conducted to validate the behavior of each

equation to the variation of independent variables and the error associated with each equation, respectively.

The design equations for the four dependant parameters of the double web angle connection are obtained as:

$$R_{ki} = 1.10 Pf^{0.77} h^{2.40} t_{wa}^{2.17} E_{0,a}^{1.25} E_{0,c}^{-1.25} \text{ (N.mm/rad)} \quad (7.10)$$

$$M_u = 0.004 d_b^{0.61} h_b^{2.10} t_{wa}^{2.13} F_{ya}^{2.17} \text{ (N.mm)} \quad (7.11)$$

$$n = 0.02 d_b^{-0.24} F_{ya}^{0.78} \quad (7.12)$$

$$q = 0.02 d_b^{-0.23} F_{ya}^{0.78} F_{yc}^{0.01} \quad (7.13)$$

The design equations for the four dependant parameters of the top and seat angle connection are obtained as:

$$R_{ki} = 695.79 g^{-2.21} Pf^{0.77} h_b^{2.29} t_{wa}^{1.16} E_{0,a}^{1.15} E_{0,c}^{-1.15} \text{ (N.mm/rad)} \quad (7.14)$$

$$M_u = 0.00025 d_b^{0.76} g^{-0.69} Pf^{0.76} h_b^{2.14} t_{sa}^{1.79} F_{ya}^{0.93} (t_{sa}/t_{wa})^{0.67} \text{ (N.mm)} \quad (7.15)$$

$$n = 0.07 d_b^{-0.24} t_{sa}^{0.001} (t_{sa}/t_w)^{0.90} F_{ya}^{0.58} \quad (7.16)$$

$$q = 0.07 d_b^{-0.24} t_{sa}^{0.001} (t_{sa}/t_w)^{0.90} F_{ya}^{0.58} F_{yb}^{0.01} \quad (7.17)$$

Similarly, the design equations for the four dependant parameters of the top and seat angle with double web angle connection are obtained as:

$$R_{ki} = 5068.70 d_b^{0.74} g^{-0.42} Pf^{1.23} h_b^{1.19} t_{sa}^{1.06} t_{wa}^{0.23} \text{ (N.mm/rad)} \quad (7.18)$$

$$M_u = 491.52 d_b^{0.77} g^{-0.49} Pf^{0.15} h_b^{1.09} t_{sa}^{1.06} F_{ya}^{0.39} \text{ (N.mm)} \quad (7.19)$$

$$n = 0.10 h_b^{-0.26} t_{sa}^{0.21} F_{ya}^{0.49} \quad (7.20)$$

$$q = 0.09 h_b^{-0.26} t_{sa}^{0.21} F_{ya}^{0.49} F_{yb}^{0.01} \quad (7.21)$$

The design equations for the four dependant parameters of the flush end plate connection are obtained as:

$$R_{ki} = 176.13 g^{0.77} P_f^{1.89} d_b^{0.34} t_{ep}^{1.52} \text{ (N.mm/rad)} \quad (7.22)$$

$$M_u = 38.26 d_b^{0.66} t_{cf}^{0.82} h_b^{0.48} t_{ep}^{1.08} t_{st}^{0.03} F_{yp}^{0.46} \text{ (N.mm)} \quad (7.23)$$

$$n = 95.14 d_b^{-0.25} P_f^{0.89} h_b^{-0.82} t_{ep}^{0.04} t_{cf}^{-0.77} F_{yp}^{-0.24} \quad (7.24)$$

$$q = 125.05 d_b^{-0.25} P_f^{0.89} h_b^{-0.82} t_{ep}^{0.04} t_{cf}^{-0.78} F_{yc}^{-0.28} \quad (7.25)$$

Similarly, the design equations for the four dependant parameters of the end plate with hollow section beam connection are obtained as:

$$R_{ki} = 162.02 g^{0.77} P_f^{1.28} d_b^{0.34} t_{ep}^{1.71} \text{ (N.mm/rad)} \quad (7.26)$$

$$M_u = 3.57 d_b^{0.76} t_{cf}^{0.82} h_b^{0.37} t_{ep}^{1.25} F_{ya}^{0.85} \text{ (N.mm)} \quad (7.27)$$

$$n = 21.22 d_b^{-0.25} P_f^{0.64} h_b^{-0.82} t_{ep}^{0.28} t_{cf}^{-0.77} F_{yp}^{0.25} F_{yc}^{-0.24} \quad (7.28)$$

$$q = 23.01 d_b^{-0.25} P_f^{0.64} h_b^{-0.82} t_{ep}^{0.27} t_{cf}^{-0.78} F_{yp}^{0.29} F_{yc}^{-0.28} \quad (7.29)$$

The design equations for the four dependant parameters of the semi continuous composite connection are obtained as:

$$R_{ki} = 2230.54 g^{0.77} P_f^{1.28} d_b^{0.54} t_{ep}^{0.25} t_{st}^{0.02} \text{ (N.mm/rad)} \quad (7.30)$$

$$M_u = 5731.77 g^{0.26} P_f^{0.30} d_b^{0.76} t_{ep}^{0.12} F_{yp}^{0.32} t_{st}^{0.03} \text{ (N.mm)} \quad (7.31)$$

$$n = 165.64 d_b^{-0.25} P_f^{0.89} h_b^{-0.82} t_{st}^{0.11} F_{yp}^{0.25} F_{yc}^{-0.24} \quad (7.32)$$

$$q = 167.72 d_b^{-0.25} P_f^{0.89} h_b^{-0.82} t_{st}^{0.10} F_{yp}^{0.26} F_{yc}^{-0.24} \quad (7.33)$$

Tables 7.1 – 7.3 below have given the parameters for power model obtained through curve fitting for each PR connection.

Table 7.1

Different parameters for power model obtained through curve fitting (1)

| Connection destination | R_{ki} (KN.m/mRad) | M_{uc} (kN.m) | Rigidity parameter (n) | Rigidity parameter (q) | Correlation coefficient (r) |
|------------------------|-------------------------|--------------------|-------------------------------|-------------------------------|------------------------------------|
| DWA-1b | 3.20 | 25.63 | 1.35 | 1.36 | 0.9995 |
| DWA-1c | 3.15 | 28.12 | 1.52 | 1.53 | 0.9994 |
| DWA-1d | 3.10 | 32.75 | 1.69 | 1.70 | 0.9992 |
| DWA-2b | 8.45 | 60.00 | 1.35 | 1.36 | 0.9993 |
| DWA-2c | 8.32 | 64.75 | 1.52 | 1.53 | 0.9992 |
| DWA-2d | 8.01 | 75.00 | 1.69 | 1.70 | 0.9991 |
| DWA-3b | 4.40 | 35.00 | 1.35 | 1.36 | 0.9992 |
| DWA-3c | 4.35 | 38.12 | 1.52 | 1.53 | 0.9991 |
| DWA-3d | 4.20 | 42.40 | 1.69 | 1.70 | 0.9992 |
| DWA-4b | 10.15 | 75.00 | 1.35 | 1.36 | 0.9941 |
| DWA-4c | 9.80 | 80.00 | 1.52 | 1.53 | 0.9885 |
| DWA-4d | 9.60 | 93.00 | 1.69 | 1.70 | 0.9990 |
| TSA1-4d | 3.81 | 37.75 | 1.75 | 1.78 | 0.9989 |
| TSA1-3d | 4.65 | 51.38 | 1.75 | 1.78 | 0.9979 |
| TSA1-2d | 5.81 | 61.25 | 1.75 | 1.78 | 0.9989 |
| TSA1-1d | 6.61 | 66.90 | 2.10 | 2.12 | 0.9991 |
| TSA2-4d | 9.61 | 88.25 | 1.58 | 1.60 | 0.9989 |
| TSA2-3d | 16.50 | 104.00 | 1.58 | 1.60 | 0.9991 |
| TSA2-2d | 17.41 | 123.25 | 1.85 | 1.86 | 0.9989 |
| TSA2-1d | 17.46 | 130.00 | 2.24 | 2.25 | 0.9991 |

Table 7.2

Different parameters for power model obtained through curve fitting (2)

| Connection destination | R_{ki} (KN.m/mRad) | M_{uc} (KN.m) | Rigidity parameter (n) | Rigidity parameter (q) | Correlation coefficient (r) |
|------------------------|-------------------------|--------------------|---------------------------|---------------------------|--------------------------------|
| TSAW-1b | 30.33 | 51.50 | 0.81 | 0.82 | 0.9989 |
| TSAW-1c | 29.56 | 76.50 | 0.95 | 0.96 | 0.9991 |
| TSAW-2b | 36.41 | 58.50 | 0.84 | 0.85 | 0.9989 |
| TSAW-2c | 32.56 | 78.50 | 0.94 | 0.95 | 0.9991 |
| TSAW-3b | 59.30 | 82.60 | 0.70 | 0.72 | 0.9989 |
| TSAW-3c | 43.23 | 85.00 | 0.78 | 0.79 | 0.9991 |
| TSAW-3b* | 46.20 | 95.00 | 1.30 | 1.32 | 0.9989 |
| TSAW-3c* | 39.50 | 110.00 | 1.10 | 1.13 | 0.9989 |
| TSAW-3b** | 30.41 | 55.00 | 0.94 | 0.95 | 0.9991 |
| TSAW-3c** | 29.58 | 76.50 | 0.95 | 0.96 | 0.9989 |
| TSAW-3c*) | 38.33 | 120.00 | 1.26 | 1.28 | 0.9991 |
| EPTB-5b | 9.85 | 60.78 | 1.43 | 1.45 | 0.9989 |
| EPTB-3b | 16.59 | 87.60 | 1.43 | 1.45 | 0.9991 |
| EPTB-1b | 19.71 | 102.3 | 1.60 | 1.62 | 0.9989 |
| EPTB-7c | 8.07 | 57.20 | 1.50 | 1.53 | 0.9991 |
| EPTB-5c | 9.78 | 68.75 | 1.50 | 1.53 | 0.9989 |
| EPTB-3c | 11.70 | 80.85 | 1.62 | 1.64 | 0.9991 |
| EPTB-6b | 6.48 | 55.2 | 1.48 | 1.50 | 0.9989 |
| EPTB-4b | 10.16 | 72.75 | 1.48 | 1.50 | 0.9991 |
| EPTB-2b | 12.90 | 93.25 | 1.65 | 1.67 | 0.9989 |
| EPTB-8c | 5.79 | 52.00 | 1.50 | 1.52 | 0.9991 |
| EPTB-6c | 7.04 | 62.50 | 1.50 | 1.52 | 0.9989 |
| EPTB-4c | 7.60 | 73.00 | 1.82 | 1.83 | 0.9989 |

Table 7.3

Different parameters for power model obtained through curve fitting (3)

| Connection destination | R_{ki} (KNm/mRad) | M_{uc} (KN.m) | Rigidity parameter (n) | Rigidity parameter (q) | Correlation coefficient (r) |
|------------------------|------------------------|--------------------|-------------------------------|-------------------------------|------------------------------------|
| FEP-1c | 12.10 | 103.80 | 1.56 | 1.59 | 0.9995 |
| FEP-1g* | 18.50 | 133.62 | 1.60 | 1.62 | 0.9994 |
| FEP-1d* | 12.73 | 118.80 | 1.74 | 1.76 | 0.9992 |
| FEP-2a | 11.50 | 97.00 | 1.38 | 1.41 | 0.9993 |
| FEP-2b | 12.60 | 100.00 | 1.38 | 1.41 | 0.9992 |
| FEP-2c | 14.30 | 104.50 | 1.38 | 1.41 | 0.9991 |
| FEP-2d | 16.20 | 106.80 | 1.38 | 1.41 | 0.9992 |
| FEP-3a | 14.30 | 132.60 | 1.12 | 1.25 | 0.9991 |
| FEP-3b | 21.00 | 205.70 | 1.24 | 1.42 | 0.9992 |
| FEP-3a* | 14.88 | 139.70 | 1.18 | 1.28 | 0.9941 |
| FEP-3b* | 22.80 | 227.50 | 1.20 | 1.32 | 0.9885 |
| SCC-1b | 72.90 | 229.20 | 0.90 | 0.93 | 0.9989 |
| SCC-1c | 86.91 | 133.40 | 0.78 | 0.80 | 0.9983 |
| SCC-2b | 76.43 | 288.10 | 1.25 | 1.27 | 0.9979 |
| SCC-2c | 78.39 | 295.50 | 1.25 | 1.27 | 0.9969 |
| SCC-2d | 83.22 | 304.10 | 1.25 | 1.27 | 0.9971 |
| SCC-2e | 88.05 | 313.70 | 1.25 | 1.27 | 0.9982 |

Figures 7.2 – 7.5 show comparisons between typical FEM $M-\theta$ results and the predicted proposed $M-\theta$ model values for each connection obtained from Tables 7.1 – 7.3. It can be seen from these figures that the predicted curves give very close correlation with FEA results.

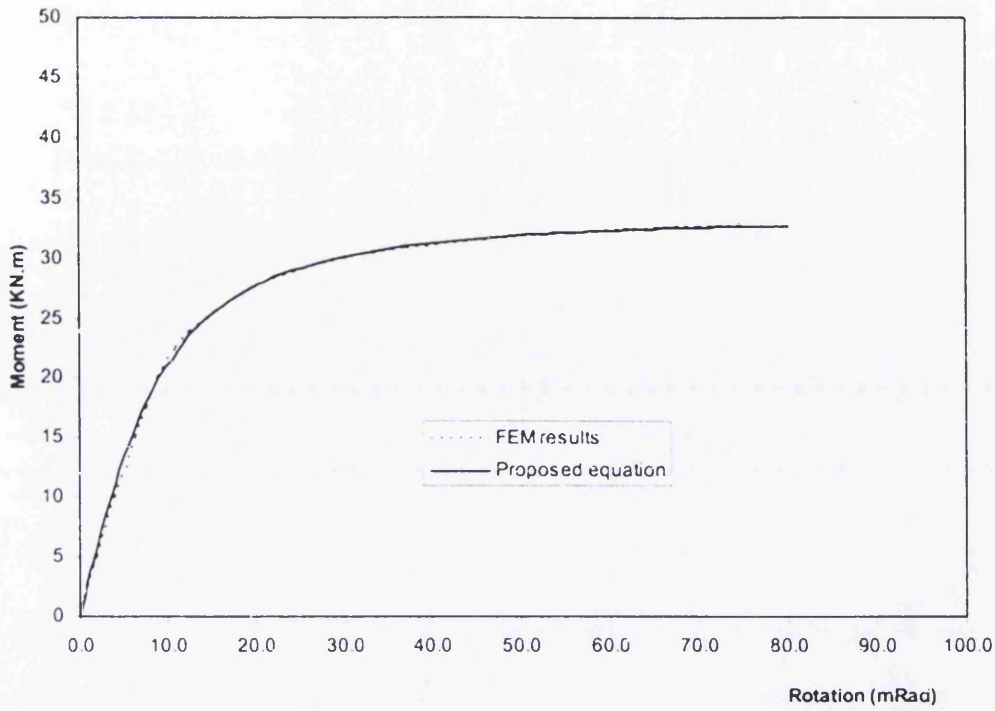


Figure 7.2 Comparison of FEM results with proposed equation; DWA1d model

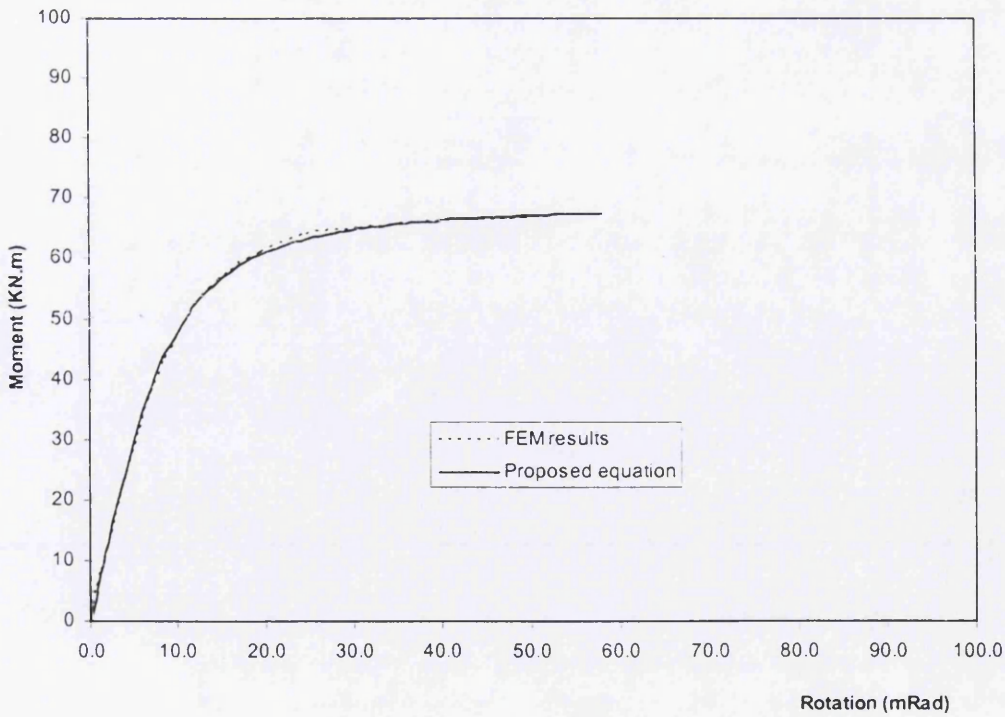


Figure 7.3 Comparison of FEM results with proposed equation; TSA-1d model

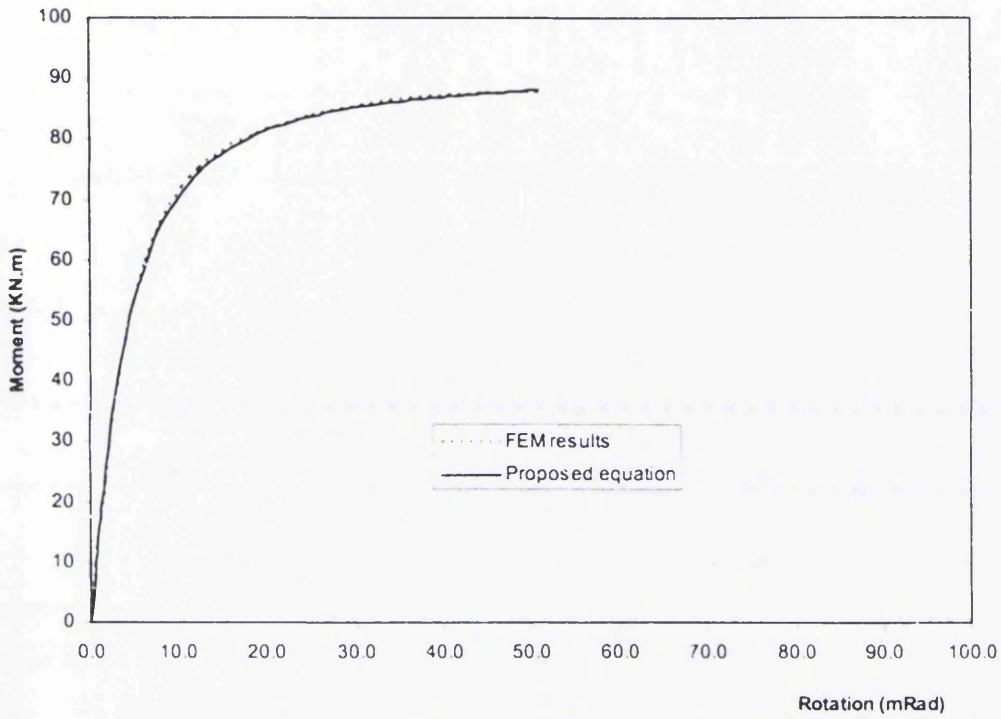


Figure 7.5 Comparison of FEM results with proposed equation; EPTB-3b model

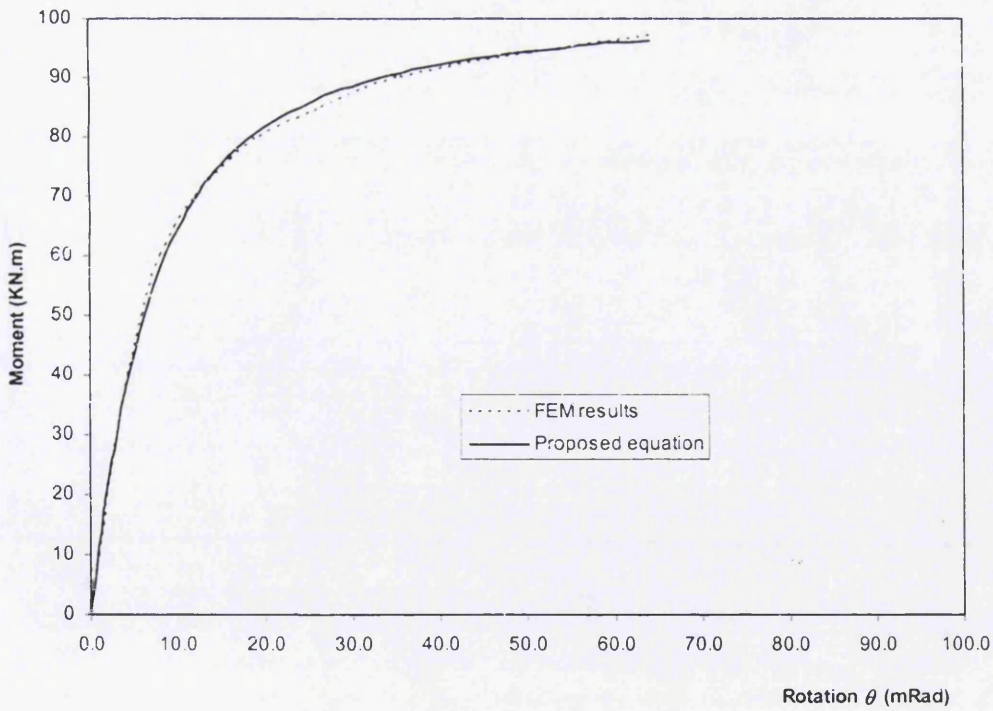


Figure 7.6 Comparison of FEM results with proposed equation; FEP-2a model

7.3 Ductility Analyses

The ductility characteristics of a joint reflect the length of the yield plateau of the $M-\theta$ response. This property can be quantified by means of a joint ductility index at maximum load $\eta_{j, \max \text{ load}}$ that relates the rotation capacity of the joint, $\theta_{Mj, \max}$ to the rotation value corresponding to the joint plastic resistance, $\theta_{Mj, R}$ [99]:

$$\eta_{j, \max \text{ load}} = \frac{\theta_{Mj, \max}}{\theta_{Mj, R}} \quad (7.34)$$

Tables 7.4 and 7.5 evaluate the joint ductility index η_j for several specimens. Numerically, the rotation capacity was defined at the rotation level for which failure of one or more components occurred.

Table 7.4
Joint ductility index of angle bolted connections

| Connection ID | Steel grade | $\theta_{Mj, \max}$ (mRad) | $\theta_{Mj, R}$ (mRad) | $\eta_{j, \max \text{ load}}$ |
|---------------|-------------|----------------------------|-------------------------|-------------------------------|
| DWA-1d | S690 | 12.0 | 76.0 | 6.33 |
| DWA-2d | S690 | 9.0 | 89.0 | 9.89 |
| DWA-3d | S690 | 8.0 | 75.0 | 9.38 |
| DWA-4d | S690 | 11.0 | 85.0 | 7.72 |
| TSA1-2c | S550 | 10.0 | 55.0 | 5.50 |
| TSA1-2d | S690 | 10.0 | 65.0 | 6.50 |
| TSA2-2c | S550 | 8.5 | 51.0 | 6.00 |
| TSA3-2d | S690 | 8.5 | 59.5 | 7.00 |
| TSAW-1c | S690 | 4.5 | 70.0 | 15.56 |
| TSAW-2c | S690 | 5.0 | 80.0 | 16.00 |
| TSAW-3c | S690 | 4.8 | 46.5 | 9.69 |
| TSAW-3c* | S690 | 4.2 | 38.0 | 9.04 |
| TSAW-3c*) | S690 | 4.5 | 36.0 | 8.00 |

Table 7.5
Joint ductility index of endplate connections

| Connection ID | Steel grade | $\theta_{Mj,max}$ (mRad) | $\theta_{Mj,R}$ (Rad) | $\eta_{j,max load}$ |
|---------------|-------------|--------------------------|-----------------------|---------------------|
| FEP-1e* | S550 | 12.0 | 68.0 | 5.67 |
| FEP-1f* | S690 | 12.5 | 55.0 | 4.40 |
| FEP-1g* | S550 | 8.5 | 64.0 | 7.53 |
| FEP-2c | S690 | 8.1 | 57.0 | 7.04 |
| FEP-2d | S690 | 7.1 | 54.0 | 7.60 |
| FEP-3a | S690 | 13.0 | 37.0 | 2.85 |
| FEP-3b | S690 | 12.0 | 33.0 | 2.75 |
| FEP-3a* | S690 | 11.0 | 46.0 | 4.18 |
| FEP-3b* | S690 | 10.0 | 41.2 | 4.12 |
| EPTB-1b | S550 | 9.5 | 38.0 | 4.00 |
| EPTB-5b | S550 | 11.0 | 52.0 | 4.73 |
| EPTB-3c | S690 | 9.0 | 51.0 | 5.67 |
| EPTB-7c | S690 | 10.0 | 51.5 | 5.10 |
| EPTB-2b | S550 | 8.5 | 48.0 | 5.64 |
| EPTB-6b | S550 | 11.0 | 70.0 | 6.36 |
| EPTB-4c | S690 | 11.0 | 69.0 | 6.27 |
| EPTB-8c | S690 | 12.0 | 69.0 | 5.75 |
| SCC1-10mm | S690 | 5.1 | 49.0 | 9.61 |
| SCC1-12mm | S690 | 5.0 | 48.5 | 9.70 |
| SCC1-15mm | S690 | 4.9 | 48.0 | 9.80 |
| SCC1-20mm | S690 | 4.8 | 48.0 | 10.00 |
| SCC2-10mm | S690 | 3.6 | 44.0 | 12.22 |
| SCC2-12mm | S690 | 3.5 | 44.5 | 12.70 |
| SCC2-15mm | S690 | 3.4 | 45.0 | 13.23 |
| SCC2-20mm | S690 | 3.3 | 45.5 | 13.79 |

Some preliminary conclusions can be drawn from the analyses of the values in Tables 7.4 and 7.5:

1. Within the same FE analyses series, the ductility indices are similar for each type of connection configurations; this means that the yield stress did not play an important role in the joint deformation behaviour.
2. For FEP connections with M24 bolts, the endplate configuration yields a lower ductility index as well as a lower rotation capacity.
3. M27 bolts 8.8 ensure a more ductile behaviour when compared to M24 bolts 12.9 (see results for specimens FEP-3a* and FEP-3a).

The requirements for available ductility and rotation capacity should be set together. For mild steel, it is generally accepted that a minimum of 35–40 mRad ensures “sufficient rotation capacity”. Wilkinson et al. suggested that a moment connection in steel moment resisting frames in a seismic area must develop a minimum plastic rotation of 30 mRad [100]. The analyses of the data collected in Tables 7.5 and 7.6 shows that all specimens with angles and end-plates satisfy both criteria.

The requirements for ductility ensure that brittle failures are avoided, i.e. inelastic deformations are sufficiently large. Girão Coelho et al. [99] proposed a minimum of 4.0 for the joint ductility index η_j for mild steel grades. If this value is taken as a reference for HSS as well, then only specimens FEP-3a and FEP-3b do not meet this criterion. Naturally, the verification of such criteria for HSS needs further investigation with different connection configurations.

7.4 Proposed Equations for Resistance Design

There are two approaches of resistance design calculation such as bearing resistance and net section resistance. There are several parameter that should be considered such as the end distance from the bolt centre to the edge and the net section of the plate. The design bearing resistance of the bolt should be taken as :

$$F_{b,Rd} = \frac{k_1 \cdot \alpha_b \cdot f_u \cdot d \cdot t_p}{\gamma_{M2}} \quad (7.35)$$

where

- k_1 is the smallest of (2.5 ; 2.8 $e_2/d_0 - 1.7$; 1.4 $e_2/d_0 - 1.7$)
- α_b is the smallest of (1.0 ; $e_1/2d_0$; $p_1/3d_0 - 1/4$; f_{ub}/f_u)
- f_u is the specified ultimate strength
- f_{ub} is the specified ultimate strength of the bolt
- d is the nominal bolt diameter
- t_p is the thickness of plate
- γ_{M2} is the partial factor for net section resistance for steels, $\gamma_{M2} = \gamma_{M2} = 1.15$

After the derivation of the constitutive design equations for the bearing resistance of high strength lap connection, the validation of the results obtained from the design equations to the results obtained from the modelling is shown below.

Table 7.6

**The comparison results between modelling and the design equations
(modelling results obtained from Chapters 4 and 5)**

| Configuration | Ultimate Load (KN) | | Design / Modelling |
|-------------------------------|--------------------|--------|-----------------------|
| | Modelling | Design | |
| $e_1/d_0 = 1.0$, 2205 plate | 219.5 | 217.1 | 0.99 |
| $e_1/d_0 = 1.2$, 2205 plate | 248.1 | 260.6 | 1.11 |
| $e_1/d_0 = 1.0$, S690 plate | 264.7 | 268.5 | 1.05 |
| $e_1/d_0 = 1.2$, S690 plate | 280.8 | 322.2 | 1.15 |
| $e_1/d_0 = 1.0$, S1350 plate | 432.0 | 406.5 | 0.94 |
| $e_1/d_0 = 1.2$, S1350 plate | 435.2 | 487.7 | 1.12 |
| Average | | | 1.04 |
| Standard deviation | | | 0.10 |

The design resistance of a net section is considered with net section area and edge distance (e_1) and should be taken as:

$$N_{t,Rd} = \frac{0.9 \cdot \alpha_1 \cdot A_{net} \cdot f_u}{\gamma_{M12}} \quad (7.36)$$

where

A_{net} is the net area of the plate

f_u is the specified ultimate strength

γ_{M12} is the partial factor for net section resistance for steels, $\gamma_{M12} = \gamma_{M2} = 1.20$

α_1 is the edge distance factor $(e_1/1.5d_0)^{0.5}$

After the derivation of the constitutive design equations for net section resistance of high strength lap connection, the validation of the results obtained from the design equations to the results obtained from the modelling is shown below.

Table 7.7

**The comparison results between modelling and the design equations
(modelling results obtained from Chapters 4 and 5)**

| Configuration | Ultimate Load (KN) | | Design / Modelling |
|-------------------------------|--------------------|--------|-----------------------|
| | Modelling | Design | |
| $e_1/d_0 = 1.5$, 2205 plate | 317.7 | 296.8 | 0.93 |
| $e_1/d_0 = 2.0$, 2205 plate | 338.2 | 306.6 | 0.91 |
| $e_1/d_0 = 2.5$, 2205 plate | 344.9 | 342.8 | 0.99 |
| $e_1/d_0 = 1.5$, S690 plate | 360.3 | 411.8 | 1.14 |
| $e_1/d_0 = 2.0$, S690 plate | 480.4 | 475.4 | 0.99 |
| $e_1/d_0 = 2.5$, S690 plate | 521.7 | 531.6 | 1.02 |
| $e_1/d_0 = 1.5$, S1350 plate | 637.5 | 623.3 | 0.98 |
| $e_1/d_0 = 2.0$, S1350 plate | 690.0 | 719.7 | 1.04 |
| $e_1/d_0 = 2.5$, S1350 plate | 740.3 | 804.6 | 1.09 |
| Average | | | 1.01 |
| Standard deviation | | | 0.07 |

7.5 Summary and Conclusion

Chapter 7 has presented the development of formulations for predicting the moment-rotation curves of the PR connection and the design equations for the resistance of the shear bolted connection. The proposed expressions that can predict the moment capacity and resistance of high strength bolted connection and have been compared with expressions proposed by other investigators for high strength steel. Moreover, the proposed design equations were compared with all results obtained from the analytical works presented in this research. From the study carried out, the following conclusions were drawn:

A power model expression was proposed to predict the ultimate moment and initial stiffness of the high strength PR connection. The expression is a function of the corresponding strength of plates and angles. The average predicted correlation coefficients (r) of the angle bolted connection were in the range of 0.9989 and 0.9995. The average predicted correlation coefficients (r) of the end plate connection were in the range of 0.9885 and 0.9995. Average predicted correlation coefficients (r) of the SCC connection were in the range of 0.9871 and 0.9989. The small standard deviations indicate that the predicted values are close to the values obtained from the modelling work. On the other hand, a reasonably good prediction was obtained for high strength PR connection. The proposed expressions presented better predictions than the expressions proposed by previous researchers for high strength steel.

A simple expression was proposed to predict the bearing and net section resistance. The expression is a function of the corresponding strength of the plate and bolt. The proposed expression presented a significant prediction for load resistance of high strength lap connection. The average predicted/modelling ratios were 1.04 and 1.01 respectively. In addition, the standard deviations were 0.10 and 0.07 respectively. The small standard deviations indicate that the predicted values are close to the values obtained from the experimental work. On the other hand, a reasonably good prediction was obtained for high strength lap connection. The proposed expressions presented better predictions than the expressions proposed by previous researchers .

Design equations have been developed according to the EC3 regulations and codes. The validation of the design equations was conducted by using FEM result. Results in this investigation, were presented in Chapter 5, and the parametrical study is presented in Chapter 6. A very close agreement has been achieved between the results on the ultimate loads obtained from the proposed expression and the results obtained from the experimental works and numerical modelling. In addition to this, small standard deviation values were obtained. The proposed design equations adequately predicted the ultimate loads of the high strength bolted connection, having different section properties and different configuration.

Chapter 8

Conclusions and Recommendations

8.1 Introduction

Finite element analysis and laboratory work could be combined efficiently as shown in this research. Both can demonstrate the behaviour of steel bolted connection structures in different ways. With the use of both methods a better understanding can be given to any steel structures. Nevertheless, laboratory work is costly and time consuming. Therefore, finite element analysis is the good alternative method, which can both predict the real behaviour of bolted connection structures and simulate the failure modes of it, simply and efficiently, compared to the laboratory work. This is based on the model needs extensive validation.

The previous chapters have reported the behaviour of bolted connections from computing work and its validation. With the experimental results obtained from literature the research was carried out to verify the finite element modelling. By using the ANSYS programme, two modelling techniques were proposed for the different failure modes. A close agreement was obtained between the experimental work and the finite element modelling. Stresses, failure modes, rupture patterns as well as the load-deflection and moment-rotation behaviour were closely matched. Therefore, a complete parametric study on finite element analysis was carried out to study the influence by different parameters. Finally, the design equations were developed according to EC3 regulations and codes. The obtained results from the computing work of this research with other researchers' work and the parametric study work have resulted in the development of design equations.

8.2 Conclusions

From the research results it is concluded that, the finite element modelling is well constructed and proved to be very adequate in producing results that are in good agreement with the experimental results. The fine FE model is a result of the excellent level of detailing produced to accurately match the actual geometry of all the structural components as given by the experimental setup. Accurate modelling of the material properties of steel grades has also been used. The attention given to the level and location of mesh refinement is adequate and contributed to the good agreement of the results obtained. Special attention is given to the description of the boundary conditions to simulate the modelling configuration.

Research into connection modelling using the finite element method has been performed to improve the understanding of detailed stresses, strain and failure mode. A series of models with high strength and stainless steel material were constructed to find the most accurate and efficient numerical models. The high strength bolted connections were analysed and the following conclusions can be drawn.

- 1) Solid elements are suitable for simple connection problems, but shell elements are more efficient for the more complicated structures such as beam to column connections. The additional flexibility allows either the angle or plate bending to be modeled accurately.
- 2) The initial stiffness determined from the FE model agrees with previous experimental results. The effect of angle thicknesses gives small change of the initial stiffness, whilst the thicker one has more clear effect on the slippage of angle bolted connection.
- 3) The plastic strain and stress patterns of high strength angle are very similar, in general. The model can predict the increased moment and rotational capacity accurately.
- 4) The connection capacity of high strength thicker angles of TSA is slightly more than that of DWA connection except for the connection with bigger beam depth and very high strength angle.

- 5) High strength angles have a large area of maximum yield stress distribution, whereas the beam and column are kept to mild carbon steel. The stiffer high strength steel applied to the TSAW connection gives very limited ductility and hardly any deformation in bending.
- 6) The moment rotation curve of connections developed with corner strength enhancement in the angle bolted of FEM model shows results which correlate with each other with only marginal increase of 3% to 5%
- 7) The moment rotation curve of connections developed with circular hole and hexagonal hole in the PR connection of FEM model shows results are correlates with each other with only marginal difference of 3% to 5%. But circular hole modelling avoids the stress concentration.
- 8) The effect of plate thicknesses gives significant change of the initial stiffness, whilst the thin higher strength endplate will be more pronounced on the moment capacity of connection. The high strength endplate gives significant proportion of maximum stress distribution, whereas the beam and column are kept to mild carbon steel.
- 9) The results obtained from the FEA for the moment-rotation curves of different specimens of endplate connection are within the range of 3% to 5% compared to the experimental results.
- 10) Waiving of column web stiffeners is not advisable because their absence causes premature failure in the column web. This leads to consequently a drastic drop in moment and rotation capacities. However, connection with column web stiffeners is advisable because their presence increases moment capacity up to 15%.
- 11) It can be observed that, if thickness of endplate is bigger than the thickness of column flange, the moment capacity of the connection will not be increased in clearly to excessive deformation of column flange and web.
- 12) For the case of bare steel joint FEP, compressive and tensile stresses were almost similar. The joint's moment rotational responses of FEM analysis follows the same trend of experimental investigation which are almost identical in both the positive and negative moment regions because of symmetry of the connection.
- 13) Thick high strength endplate connections provide additional rotational stiffness and moment capacity but the rotation capacity may be compromised by bolt failure.

This type of failure mode is not acceptable for semi-rigid frame design because a large rotation capacity is required to allow moment redistribution.

- 14) Thin low strength endplates provide enough deformation capacity to allow semi-rigid connection design but yielding of the endplate may produce excessive deflection. Also the thin endplate increases the prying forces with an associated increasing in bolt loads. Higher strength endplate may delay the end plate yielding and excessive deflection.
- 15) The stiffer high strength endplate applied to the FEP and SCC connection gives the very limited ductility and hardly any deformation in bending. The increase of bolt diameter with low grade gives significant increase in deformation, as this bolt have higher ductility.
- 16) The column is suggested to be kept to mild carbon steel, whilst the S355 grade column with the minimum thickness as that of the high strength endplates should be considered. The grade 8.8 bolt with minimum diameter M22 should be used.
- 17) The moment capacity prediction following EC3 has been shown to be reasonable. The nature of the failure mode was predicted reliably for the connections studied. It is however clear that more complicated arrangements of stiffeners and bolts may be come less accurate. Provided this is no brittle failure they are acceptable.
- 18) The plastic strain and stress patterns of high strength endplate connection are very similar, in general. The model presented gives excellent results for increasing the moment and rotational capacity significantly.
- 19) Proposed design equation for the PR connections is defined as:

$$M = \frac{R_{kl}\theta}{[1+(\theta/\theta_0)^n]^{\frac{1}{q}}}$$

- 20) Ductility index values of all of the PR connections are satisfied except those of FEP3a and FEP3b. Ductility index is defined as:

$$\eta_{j,max.load} = \frac{\theta_{Mj,max}}{\theta_{Mj,R}}$$

- 21) The application of high strength and stainless steel for the shear bolted connection could be calculated by two approaches of bearing resistance and net section resistance.

- 22) As expected, the ultimate resistance and rupture resistance of the shear bolted connection increases significantly when the ultimate strength and e_1/d_0 ratio increase. The ultimate and rupture resistance of the connection under net section failure shows a linear relationship with the change of the ultimate strength, whilst those of the connection under bearing failure shows a non-linear relationship.
- 23) The effect of the edge distance of bolt hole shows a consistency of the change in the resistance for both bearing and net section failure. Design resistance from FEA is reasonable, except for the value of α_b and γ_{M2} is conservative. It is advisable for minimum edge distance e_1 needs to be used with the value of $1.0 d_0$ instead of $1.2 d_0$ for all high strength steel grade.
- 24) Proposed design equations for the SLB connections are defined as:

$$F_{b,Rd} = \frac{k_1 \cdot \alpha_b \cdot f_u \cdot d \cdot t_p}{\gamma_{M2}} ; \text{ for bearing resistance}$$

$$N_{t,Rd} = \frac{0.9 \cdot \alpha_1 \cdot A_{net} \cdot f_u}{\gamma_{M2}} ; \text{ for net-section resistance}$$

8.3 Recommendations for Further Work

The finite element analysis developed in this research could be continually developed. Further research could be conducted to investigate the behaviour of high strength and stainless steel bolted connection.

1. If the computing time and resource is not limited, it is recommended to include the contact forces between the bolt shanks and the bolt holes and between high strength plates to show the effects of those phenomena.
2. Because this research has only been conducted to show the effects of thickness of angle and plates, steel grades and bolt configuration, it is recommended to include the effects of gauge distance and number of bolts for future study.
3. The application of stainless steel on the PR connections should be investigated further both using experimental testing and finite element modelling approach.

4. Effect of strain softening should be taken into account to investigate rupture behaviour characteristic of the PR connection in the steel frame performance. The ductile manner should be considered further to for the behaviour of the high strength beam-column connection.
5. Improvement of the current design code such as British Standard or EC3 rules would be useful. This should include further tests where, for instance, the end distance over hole diameter e_1/d_0 is also reduced from 1.0 to 0.9.

References

Appendix

References

- [1] Burgan B., Guidance on the use of Stainless Steel in construction, The Steel Construction Institute, Ascot, U.K. Paper presented on the occasion of the Symposium Structural Applications of Stainless Steel in Building and Architecture on 24th February 2000 in Brussels organised by Euro Inox, Brussels.
- [2] Bjorhovde R., Development and use of high performance steel, *Journal of Constructional Steel Research* 60 (2004) 393–400.
- [3] Weynand K., Jaspart J.P., and Steenhuis M., Economy studies of steel building frames with semi-rigid joints, *Journal of Constructional Steel Research*, 1998, 46:1-3, Paper No. 63.
- [4] Di Sarno L., Elnashai A.S., and Nethercot D.A., Seismic performance assessment of stainless steel frames, *Journal of Constructional Steel Research* 59 (2003) 1289–1319.
- [5] ENV 1993-1-3 (2001). Eurocode 3: Design of steel structures, Part 1.3: general rules, supplementary rules for cold formed thin gauge members and sheetings, European Committee for Standardisation (CEN).
- [6] EN 1993-1-4 (2006). Eurocode 3: Design of steel structures, Part 1.4: general rules, supplementary rules for stainless steel, European Committee for Standardisation (CEN).
- [7] Sivakumaran K.S. and Yuan B., Slenderness Limits and Ductility of High Strength Steel Sections, *Journal of Constructional Steel Research* Volume 46, Issues 1-3, April-June 1998, Pages 149-151.
- [8] Green P.S., Sause R., and Ricles J.M., Strength and ductility of HPS flexural members, *Journal of Constructional Steel Research* 2002, 58: 907–941.
- [9] Hancock G. J. and Rogers C. A., Design of cold-formed steel structures of high strength steel, *Journal of Constructional Steel Research*, Volume 46, Issues 1-3, April-June 1998, Pages 167-168.

- [10] Moze P., Beg D. and Lopatic J., Bolted Connections Made of High Strength Steel S690", ECCS_ TC10-05-587, Paris, October 2005.
- [11] ASTM, Standard Terminology Relating to Methods of Mechanical Testing, ASTM Designation E6, 1998; 03.01, 17-27.
- [12] EN 1993-1-12 (2007). Eurocode 3: Design of steel structures, Part 1.12: Additional rules for the extension of EN 1993 up to steel grades S 700, European Committee for Standardisation (CEN).
- [13] Zhao X.L, Section capacity of very high strength (VHS) circular tubes under compression, Journal of Thin-Walled Structures, Volume 37, Issue 3, July 2000, Pages 223-240
- [14] Burgan B. A., Baddoo N. R. and Gilsean K. A., Structural design of stainless steel members — comparison between Eurocode 3, Part 1.4 and test results, Journal of Constructional Steel Research Volume 54, Issue 1 , April 2000, Pages 51-73
- [15] EN 1993-1-8 (2005), Eurocode 3: Design of Steel Structures Part 1.8: Joints, European Committee for Standardisation (CEN).
- [16] Rasmussen K.J.R. et.al, Numerical modelling of stainless steel plates in compression, Journal of Constructional Steel Research Volume 59, Issue 11 , November 2003, Pages 1345-1362
- [17] Rasmussen K.J.R., Full-range stress–strain curves for stainless steel alloys, Journal of Constructional Steel Research, Volume 59, Issue 1, January 2003, Pages 47-61
- [18] Zhou Y., Yang Wang Y., Mallick P.K. and Xia Y., Strain softening constitutive equation for tungsten heavy alloy under tensile impact, Materials Letters 58, Issues 22-23, 2725-2729.
- [19] Tangaramvong S., and Tin-Loi F., Simultaneous ultimate load and deformation analysis of strain softening frames under combined stresses, Engineering Structures 30 (2008) 664–674

- [20] Mistakidis E. S., Thomopoulos K. T. and Tzaferopoulos M.Ap., Effective methods for the analysis of steel structures with strain-softening behaviour, *Journal of Constructional Steel Research*. 1997, Vol. 44, Nos. 1-2: 3-21.
- [21] Almusallam T. H., and Richard R. M., Steel frame analysis with flexible joints exhibiting a strain-softening behavior, *Computers & Structures*, 1993, 46 (1): 55-65
- [22] Tangaramvong S. and Tin-Loi F., Limit analysis of strain softening steel frames under pure bending, *Engineering Structures* 63 (2007) 1151–1159
- [23] Kuroda M., Uenishi A., Yoshida H., and Igarashi A., Ductility of interstitial-free steel under high strain rate tension: Experiments and macroscopic modeling with a physically-based consideration, *International Journal of Solids and Structures* 43 (2006) 4465–4483
- [24] Chausov M.G., and Pylypenko A.P., Laws of deformation processes and fracture of plastic steel from the point of view of dynamic overloading, *Mechanika* 2005, ISSN 1392 – 1207, Nr.4(54)
- [25] Kim H.J., and Yura J.A., The effect of ultimate-to-yield ratio on the bearing strength of bolted connections. *Journal of Constructional Steel Research* 1999;49(3):255–69.
- [26] Aalberg A. and Larsen P.K., The effect of steel strength and ductility on bearing failure of bolted connections, In: Lamas A, Simoes da Silva L, editors. *Proceedings of the 3rd European conference on steel structures, Eurosteel 2002*.
- [27] Aalberg A. and Larsen PK. Bearing strength of bolted connections in high strength steel. In: *Proceedings of Nordic Steel Construction Conference*. 2001.
- [28] de Freitas S.T., de Vries P. and Bijlaard F.S.K., Experimental research on single bolt connections for high strength steel S690, *Proceeding of Congresso de Construção Metálica e Mista*, páges II-679 - II-688, Lisboa-Portugal, 2005.
- [29] Rogers C.A. and Hancock G.J., Bolted connection tests of thin G550 and G300 sheet steels, *Journal of Structural Engineering*, July 1998, Volume 124, Issue 7, pp. 798-808

- [30] Moze P., Beg D., and Lopatic J., Net cross-section design resistance and local ductility of elements made of high strength steel, *Journal of Constructional Steel Research* 2007, 63: 1431–1441
- [31] Puthli R. and Fleischer O., Investigations on bolted connections for high strength steel members, *Journal of Constructional Steel Research* 2001, 57(1): 313-26.
- [32] Wolfram M., *Literature Survey on Semi Rigid Connections*. Virginia Polytechnic Institute and State University, 1996.
- [33] Liew, J.Y.R, Chen W.F., and White D.W., Limit States Design of Semi-Rigid Frames Using Advanced Analysis: Part 2: Analysis and Design, *Journal of Construction and Steel Research*. 1993, 26, 29-57.
- [34] Azizinamini A. and Radziminski JB., Static and Cyclic Performance of Semi-rigid Steel Beam to Column Connections, *Journal Structural Engineering, ASCE*, 1989, 115:2, 2979-99.
- [35] Davison J.B., Kirby P.A., and Nethercot D.A., Rotational stiffness characteristics of steel beam-to-column connections, *Journal of Constructional Steel Research* 1987; 8:17–54.
- [36] Xiao Y., Choo B.S. and Nethercot D.A., “Composite Connections in Steel and Concrete. Part 1–Experimental Behaviour of Composite Beam-column Connections”, *Journal of Constructional Steel Research*, 31(1), 3-30, 1994.
- [37] Wheeler A.T, Clarke M.J and Hancock G.J., *Bending Tests of Bolted End Plate Connections in Cold Formed Rectangular Hollow Sections*, Research Report No. R736, Department of Civil Engineering, The University of Sydney, January 1997
- [38] Willibald, S., Packer, J.A. and Puthli, R.S., Bolted connections for RHS tension members. CIDECT Report 8D/8E-10/01, 2001, University of Toronto, Canada.
- [39] Broderick BM, and Thomson AW. Cyclic testing of flush end-plate semi-rigid steel connections. In: *Proceedings of the STESSA, 2000: Behaviour of steel structures in seismic areas*. 2000. p. 135–40.

- [40] Bose B., Design resistance of unstiffened column web subject to transverse compression in beam to-column joints, *Journal Constructional Steel Research* 1998; 45(1):1-15.
- [41] Simões Da Silva L. et.al, Experimental behaviour of end-plate beam-to-column joints under bending and axial force, Database reporting and discussion results of ECCS Technical Committee 10 "Connections" TWG 10.2 meeting in Ljubljana, April 2001.
- [42] Girão Coelho A.M. and Bijlaard, F.S.K., Experimental behaviour of high strength steel end-plate connections, *Journal of Constructional Steel Research*, 2007, 63: 1228-1240
- [43] Kukreti, A. R., Murray, T. M., and Abolmaali, A, End-Plate Connection Moment-Rotation Relationship, *Journal of Constructional Steel Research*, 1987, 8: 137-157
- [44] Hasan, R., Kishi, N., Chen, W. F., and Komuro, M., Evaluation of rigidity of extended end-plate connections, *Journal of Structural Engineering, ASCE*, 1997, 123: 1595-1602.
- [45] Goto, Y., and Miyashita, S., Classification system for rigid and semirigid connections, *Journal of Structural Engineering, ASCE*, 1998, 124: 750-757.
- [46] Foley, C. M., and Vinnakota, S., "Toward design office moment-rotation curves for end-plate beam-to-column connections," *Journal of Constructional Steel Research*, 1995,35: 217-253.
- [47] Coric, B., and Markovic, Z., Non-linear analysis of steel structures with semi-rigid connections, *Structural Engineers World Congress, San Francisco, 1998*, Paper No. T196-6.
- [48] Yu, C. H., Liew, J. Y. R., and Shanmugam, Y. H. N. Collapse behaviour of sway frames with end-plate connections," *Journal of Constructional Steel Research*, 1998, 48: 169-188.

- [49] Elghazouli, A. Y., Seismic design of steel frames with partial strength connections," Sixth SECED Conference on Seismic Design Practice, 1998, Oxford, UK,
- [50] Rodrigues, F. C., Saldanha, A. C., and Pfeil, M. S., Non-linear analysis of steel plane frames with semi-rigid connections, *Journal of Constructional Steel Research*, 1998, 46, Paper No. 145.
- [51] Fu, Z., Kenichi, O., Takanashi, K., and Xiaoguang, L., Seismic behavior of steel frames with semi-rigid connections and braces, *Journal of Constructional Steel Research*, 1998, 46, Paper No. 217.
- [52] Leon, R. T., Analysis and design problems for PR composite frames subjected to seismic loads," *Engineering Structures*, 1998, 20, 364-371.
- [53] Brown ND, Hughes AF, and Anderson D., Prediction of the initial stiffness of ductile end-plate steel connections. *Proceeding Institutional of Civil Engineering: Structural Buildings*, 2001, 146:17-29.
- [54] Krishnamurthy, N., Correlation between 2- and 3-dimensional finite element analysis of steel bolted end-plate connections," *Computers & Structures*, 1976, 6, 381-389.
- [55] Bursi, O. S., and Jaspart, J. P., Benchmarks for finite-element modelling of bolted steel connections, *Journal of Constructional Steel Research*, 1997, 43(1), 17-42.
- [56] Bursi, O. S., and Jaspart, J. P., Calibration of a Finite element model for isolated bolted end-plate steel connections, *Journal of Constructional Steel Research*, 1997, 42, 225-262
- [57] Bursi, O. S., and Leonelli, L., A finite element model for the rotational behaviour of end plate steel connections, *Proceedings of the SSRC Annual Technical Session, Structural Stability Research Council, Bethlehem, PA*, 1994, 163-175.
- [58] Richard, R. M., and Abbott, B. J., Versatile elastic-plastic stress-strain formula, *Journal of the Engineering Mechanics Division, ASCE*, 1975, 101, 511-515.

- [59] Sherbourne, A. N., and Bahaari, M. R., "Finite element prediction of end plate bolted connection behaviour. I: Parametric Study," *Journal of Structural Engineering*, 1997, ASCE, 123, 157-164.
- [60] Gebbeken, N., Rothert, H., and Binder, B., On the numerical analysis of endplate connections, *Journal of Constructional Steel Research*, 1994, 30, 177-196.
- [61] Rothert, H., Gebbeken, N., and Binder, B. "Non-linear three-dimensional finite element contact analysis of bolted connections in steel frames," *International Journal for Numerical Methods in Engineering*, 1992, 34, 303-318.
- [62] Bahaari, M. R., and Sherbourne, A. N., Finite element prediction of end plate bolted connection behavior. II: Analytic Formulation," *Journal of Structural Engineering*, ASCE, 1997, 123, 165-175.
- [63] Sherbourne, A. N., and Bahaari, M. R., 3D simulation of end-plate bolted connections," 1994, *Journal of Structural Engineering*, ASCE, 120, 3122-3136.
- [64] Choi, C.K. and Chung, G.T., Refined three-dimensional finite element model for end-plate connection, *Journal of Structural Engineering*, 1996, Vol. 122, No. 11, pp. 1307-1316.
- [65] Bose B, Sarkar S, and Bahrami M, Finite element analysis of unstiffened extended end plate connections, *Structural Engineering Review*, 1991, 3, 211-224.
- [66] Troup, S. Xiao, R. Y., and Moy, S. S. J., Numerical modelling of bolted steel connections, *Journal of Constructional Steel Research*, 1998, 46, Paper No. 362.
- [67] Leon, R. T., and Swanson, J. A. (1998), "Bolted Connections in Moment Resisting Frames," *Structural Engineers World Congress*, San Francisco, Paper No. T158-6.
- [68] Fanning P, Tucker M, Broderick BM. Non-linear finite element analysis of semi-rigid bolted endplate connections. In: *Proceedings of the Fifth International Conference on Computational Structures Technology*. 2000. p. 397-403.

- [69] Bursi, O. S., and Jaspart, J. P., Basic issues in the finite element simulation of extended end plate connections, 1998, *Computers & Structures*, 69, 361-382.
- [70] Sherbourne, A. N., and Bahaari, M. R., 3D Simulation of Bolted Connections to Unstiffened Columns--I. T-stub Connections, *Journal of Constructional Steel Research*, 1996, 40, 169-187.
- [71] Yang J.-G., Murray T.M., and Plaut R.H., Three-dimensional finite element analysis of double angle connections under tension and shear, *Journal of Constructional Steel Research*, 2000, Volume 54(2), pp. 227-244.
- [72] Danesh F, Pirmoz A., and Saedi Daryan A., Effect of shear force on the initial stiffness of top and seat angle connections with double web angles, *Journal of Constructional Steel Research*, 2007, 63 (9): 1208-1218.
- [73] Citipitouglu A.M., Haj-Ali R.M. and White D.W., Refined 3D finite element modeling of partially restrained connections including slip, *Journal of Constructional Steel Research*, 2002, 58, 995-1013.
- [74] Shi Y.J., Chan S.L. and Wong Y.L., Modelling for moment-rotation characteristics for end-plate connections. *ASCE J Struct Engng*, ASCE 1996;122(6):1300-6.
- [75] Taufik S. and Xiao R.Y., 3D finite element predictions of angle bolted connection with high strength steel, *Proceeding of the Fourth International Conference on Advance in Steel Structures*, Shanghai – China, Z.Y.Shen, G.Q.LI and S.L.Chan, (Eds), Elsevier, Volume II, paper no. ISP-26, 1775-1782, 2005
- [76] Taufik S. and Xiao R.Y., Simplified finite element modelling of beam-column bolted connection with shell element, *Proceedings of the Eighth International Conference on Computational Structures Technology*, B.H.V. Topping, G. Montero and R. Montenegro, (Eds), Civil-Comp Press, Stirlingshire, UK, paper no. CST-118, 2006
- [77] Taufik S. and Xiao R.Y., 3D finite element modelling of flush end plate connection with high strength steel, *Proceedings of the Eighth International Conference on Computational Structures Technology*, B.H.V. Topping, G.

Montero and R. Montenegro, (Eds), Civil-Comp Press, Stirlingshire, UK, paper no.CST-119, 2006.

- [78] Taufik S. and Xiao R.Y., Finite element modelling of end plate connection with hollow section beam, Proceedings of the 6th International Conference on Steel and Aluminium Structures, Oxford, UK, July 2007.
- [79] Taufik S. and Xiao R.Y., Numerical modelling of semi-continuous composite connection with high strength steel, Proceedings of The Eleventh International Conference on Civil, Structural and Environmental Engineering Computing, B.H.V. Topping, G. Montero and R. Montenegro, (Eds), Civil-Comp Press, Stirlingshire, UK, paper no. 153, 2007
- [80] Xiao R.Y. and Taufik S., Finite element modelling of partially restrained connection with cold-formed high strength steel section, Proceeding of the Fifth International Conference on Advance in Steel Structures, Singapore, JY Richard Liew and YS Choo, Editor(s), Research Publishing Services, Volume III, paper no. 111, December 2007
- [81] Abolmaali A., Matthysa J.H., Farooqib M., and Choic Y., 'Development of moment-rotation model equations for flush end-plate connections', Journal of Constructional Steel Research 61 (2005) 1595-1612
- [82] Faella, C., Piluso, V., and Rizzano, G., Structural Steel Semirigid Connections: Theory, Design and Software. CRC Press, Boca Raton, FL. 2000
- [83] ANSYS, ANSYS Documentations, Manual Set and Theory Reference Manual. ANSYS Inc.
- [84] Robert D. Cook, 'Finite Element Modelling for Stress Analysis', John Wiley & Sons, INC. 1995. ISBN: 0-471-10774-3.
- [85] Tirupathi R. Chandrupatla and Ashok D. Belegundu, 'Introduction to Finite Elements in Engineering', Third Edition, 2002, Prentice-Hall, Inc. ISBN: 0130615919.
- [86] Daryl L. Logan, 'A First Course in the Finite Element Method', Wadsworth Group, A Division of Thomson Learning, Inc. 2002. ISBN: 0534385176.

- [87] Robert D. Cook, David S. Malkus and Michael E. Plesha, 'Concepts and Application of Finite Element Analysis', Third Edition, John Wiley & Sons, Inc. 1989. ISBN: 0-471-8788-7.
- [88] 'State of the Art Report on Finite Element Analysis of Reinforced Concrete', ASCE, New York, 1982, 553 pp, ISBN: 0-87262-307-6.
- [89] Ottosen N.S. and Ristinmaa M. The Mechanics of Constitutive Modelling. Oxford: Elsevier Ltd, 2005.
- [90] Lemaitre J. and Chaboche J.-L. Mechanics of solid materials. Cambridge: Cambridge University Press, 1990.
- [91] Stein E., de Borst R. and Hughes T.J.R. (2004) Encyclopedia of Computational Mechanics Vol 2: Solids and Structures. Chichester: John Wiley and Sons
- [92] Simo, J. C. and Taylor, R. L., 'Consistent Tangent Operators for Rate-Independent Elastoplasticity', Computer Methods in Applied Mechanics and Engineering, Vol. 48, 1985, pp.101-118.
- [93] Krieg, R. D., and Krieg, D. B., 'Accuracies of Numerical Solution Methods for the Elastic-Perfectly Plastic Model', Journal of pressure vessel technology, Vol. 99, No, 4, Series J, Transactions of the ASME, November 1977, pp. 510-515.
- [94] Karren K.W., Corner properties of cold-formed steel shapes, Journal of the Structural Division, ASCE, 1967, Vol. 93 (ST1), pp. 401-432.
- [95] ENV 1993-1-3, Eurocode 3: Design of steel structures, Part 1.3: general rules, supplementary rules for cold formed thin gauge members and sheetings, CEN, 1996.
- [96] Gardner L., and Nethercot D.A., Numerical modelling of stainless steel structural components—a consistent approach, Journal of Structural Engineering ASCE, 2004, Vol.130 No. 10, pp. 1586-1601.
- [97] Richard RM, Abbott BJ. Versatile elastic-plastic stress-strain formula. Journal of the Engineering Mechanics Division, ASCE 1975; 101 (EM4): 511-5.

- [98] Chen W.F. and Kishi N., Moment-rotation relation of top and seat angle connections, CE-STR-87-4, In: Proceedings of the international colloquium on bolted and special connections. 1989.
- [99] Girão Coelho A.M., Simões da Silva L. and Bijlaard F.S.K., Ductility analysis of bolted extended end-plate beam-to-column connections in the framework of the component method. *Steel Computer Structure*, 2006;6(1):33-53.
- [100] Wilkinson S., Hurdman G. and Crowther A., A moment resisting connection for earthquake resistant structures. *Journal of Constructional Steel Research* 2006;62:295-302.

Appendix A

Table A.1 Stress-strain values of S460 angles

Stress-strain values of S460 flat

| No. | Strain | Stress (MPa) |
|-----|--------|--------------|
| 1 | 0.0000 | 0.0 |
| 2 | 0.0018 | 380.0 |
| 3 | 0.0028 | 440.0 |
| 4 | 0.0034 | 460.0 |
| 5 | 0.0040 | 470.0 |
| 6 | 0.0048 | 484.0 |
| 7 | 0.0075 | 500.0 |
| 8 | 0.0120 | 515.0 |
| 9 | 0.0200 | 529.0 |
| 10 | 0.0250 | 535.0 |
| 11 | 0.0300 | 540.0 |
| 12 | 0.0400 | 550.0 |
| 13 | 0.0500 | 560.0 |
| 14 | 0.0600 | 565.0 |
| 15 | 0.0700 | 570.0 |
| 16 | 0.0800 | 575.0 |
| 17 | 0.0900 | 577.0 |
| 18 | 0.1000 | 578.0 |
| 19 | 0.1200 | 583.0 |
| 20 | 0.1550 | 584.0 |

Stress-strain values of S460 corner

| No. | Strain | Stress (MPa) |
|-----|--------|--------------|
| 1 | 0.0000 | 0.0 |
| 2 | 0.0018 | 380.0 |
| 3 | 0.0025 | 450.0 |
| 4 | 0.0032 | 475.0 |
| 5 | 0.0036 | 486.0 |
| 6 | 0.0041 | 500.0 |
| 7 | 0.0051 | 524.0 |
| 8 | 0.0100 | 550.0 |
| 9 | 0.0200 | 565.0 |
| 10 | 0.0250 | 570.0 |
| 11 | 0.0300 | 575.0 |
| 12 | 0.0400 | 582.0 |
| 13 | 0.0500 | 589.0 |
| 14 | 0.0600 | 595.0 |
| 15 | 0.0700 | 600.0 |
| 16 | 0.0800 | 605.0 |
| 17 | 0.0900 | 611.0 |
| 18 | 0.1000 | 615.0 |
| 19 | 0.1200 | 621.0 |
| 20 | 0.1500 | 624.0 |

Appendix A

Table A.2 Stress-strain values of S550 angles

Stress-strain values of S550 flat

Stress-strain values of S550 corner

| No. | Strain | Stress (MPa) |
|-----|--------|--------------|
| 1 | 0.0000 | 0.0 |
| 2 | 0.0024 | 500.0 |
| 3 | 0.0030 | 550.0 |
| 4 | 0.0040 | 564.0 |
| 5 | 0.0047 | 570.0 |
| 6 | 0.0063 | 580.0 |
| 7 | 0.0090 | 588.0 |
| 8 | 0.0100 | 592.0 |
| 9 | 0.0200 | 610.0 |
| 10 | 0.0250 | 615.0 |
| 11 | 0.0300 | 620.0 |
| 12 | 0.0400 | 625.0 |
| 13 | 0.0500 | 630.0 |
| 14 | 0.0600 | 635.0 |
| 15 | 0.0700 | 640.0 |
| 16 | 0.0800 | 645.0 |
| 17 | 0.0900 | 646.0 |
| 18 | 0.0950 | 648.0 |
| 19 | 0.1000 | 649.0 |
| 20 | 0.1150 | 650.0 |

| No. | Strain | Stress (MPa) |
|-----|--------|--------------|
| 1 | 0.0000 | 0.0 |
| 2 | 0.0024 | 500.0 |
| 3 | 0.0030 | 555.0 |
| 4 | 0.0034 | 570.0 |
| 5 | 0.0038 | 590.0 |
| 6 | 0.0051 | 610.0 |
| 7 | 0.0080 | 625.0 |
| 8 | 0.0100 | 630.0 |
| 9 | 0.0200 | 648.0 |
| 10 | 0.0250 | 652.0 |
| 11 | 0.0300 | 656.0 |
| 12 | 0.0400 | 663.0 |
| 13 | 0.0500 | 670.0 |
| 14 | 0.0600 | 675.0 |
| 15 | 0.0700 | 680.0 |
| 16 | 0.0800 | 685.0 |
| 17 | 0.0900 | 687.0 |
| 18 | 0.0950 | 688.0 |
| 19 | 0.1050 | 689.0 |
| 20 | 0.1100 | 690.0 |

Appendix A

Table A.3 Stress-strain values of S690 angles

Stress-strain values of S690 flat

Stress-strain values of S690 corner

| No. | Strain | Stress (MPa) |
|-----|--------|--------------|
| 1 | 0.0000 | 0.0 |
| 2 | 0.0030 | 600.0 |
| 3 | 0.0032 | 645.0 |
| 4 | 0.0040 | 680.0 |
| 5 | 0.0045 | 690.0 |
| 6 | 0.0052 | 705.0 |
| 7 | 0.0065 | 720.0 |
| 8 | 0.0120 | 736.0 |
| 9 | 0.0160 | 746.0 |
| 10 | 0.0200 | 752.0 |
| 11 | 0.0250 | 762.0 |
| 12 | 0.0300 | 770.0 |
| 13 | 0.0350 | 778.0 |
| 14 | 0.0400 | 784.0 |
| 15 | 0.0450 | 788.0 |
| 16 | 0.0500 | 791.0 |
| 17 | 0.0550 | 795.0 |
| 18 | 0.0600 | 798.0 |
| 19 | 0.0650 | 805.0 |

| No. | Strain | Stress (MPa) |
|-----|--------|--------------|
| 1 | 0.0000 | 0.0 |
| 2 | 0.0030 | 600.0 |
| 3 | 0.0033 | 645.0 |
| 4 | 0.0040 | 685.0 |
| 5 | 0.0043 | 695.0 |
| 6 | 0.0050 | 712.0 |
| 7 | 0.0067 | 740.0 |
| 8 | 0.0110 | 755.0 |
| 9 | 0.0150 | 765.0 |
| 10 | 0.0200 | 775.0 |
| 11 | 0.0250 | 783.0 |
| 12 | 0.0300 | 789.0 |
| 13 | 0.0350 | 793.0 |
| 14 | 0.0400 | 797.0 |
| 15 | 0.0450 | 801.0 |
| 16 | 0.0490 | 803.0 |
| 17 | 0.0550 | 809.0 |
| 18 | 0.0600 | 810.0 |
| 19 | 0.0660 | 814.0 |

Appendix A

Table A.4 Stress-strain values of S550 endplates and S690 plates

Stress-strain values of S550 endplate

| No. | Strain | Stress (MPa) |
|-----|--------|--------------|
| 1 | 0.0000 | 0.0 |
| 2 | 0.0024 | 500.0 |
| 3 | 0.0030 | 550.0 |
| 4 | 0.0040 | 564.0 |
| 5 | 0.0047 | 570.0 |
| 6 | 0.0063 | 580.0 |
| 7 | 0.0090 | 588.0 |
| 8 | 0.0100 | 592.0 |
| 9 | 0.0200 | 610.0 |
| 10 | 0.0250 | 615.0 |
| 11 | 0.0300 | 620.0 |
| 12 | 0.0400 | 625.0 |
| 13 | 0.0500 | 630.0 |
| 14 | 0.0600 | 635.0 |
| 15 | 0.0700 | 640.0 |
| 16 | 0.0800 | 645.0 |
| 17 | 0.0900 | 646.0 |
| 18 | 0.0950 | 648.0 |
| 19 | 0.1000 | 649.0 |
| 20 | 0.1150 | 650.0 |

Stress-strain values of S690 plates

| No. | Strain | Stress (MPa) |
|-----|--------|--------------|
| 1 | 0.0000 | 0.0 |
| 2 | 0.0005 | 207.1 |
| 3 | 0.0015 | 378.7 |
| 4 | 0.0025 | 506.1 |
| 5 | 0.0045 | 671.2 |
| 6 | 0.0065 | 762.7 |
| 7 | 0.0085 | 813.8 |
| 8 | 0.0105 | 842.7 |
| 9 | 0.0155 | 873.2 |
| 10 | 0.0255 | 890.1 |
| 11 | 0.0355 | 900.5 |
| 12 | 0.0500 | 914.0 |
| 13 | 0.0650 | 915.0 |
| 14 | 0.0750 | 910.0 |
| 15 | 0.0900 | 890.0 |
| 16 | 0.1000 | 860.0 |
| 17 | 0.1100 | 830.0 |
| 18 | 0.1200 | 790.0 |
| 19 | 0.1300 | 750.0 |
| 20 | 0.1400 | 680.0 |

Appendix A

Table A.5 Stress-strain values of S1350 and SS2205 spliced plates

Stress-strain values of S1350 plate

| No. | Strain | Stress (MPa) |
|-----|--------|--------------|
| 1 | 0.0000 | 0.0 |
| 2 | 0.0030 | 600.0 |
| 3 | 0.0050 | 985.2 |
| 4 | 0.0070 | 1207.5 |
| 5 | 0.0090 | 1335.9 |
| 6 | 0.0110 | 1410.0 |
| 7 | 0.0130 | 1452.9 |
| 8 | 0.0150 | 1477.8 |
| 9 | 0.0170 | 1492.2 |
| 10 | 0.0190 | 1500.6 |
| 11 | 0.0210 | 1505.5 |
| 12 | 0.0280 | 1511.8 |
| 13 | 0.0330 | 1513.1 |
| 14 | 0.0380 | 1513.8 |
| 15 | 0.0430 | 1514.4 |
| 16 | 0.0480 | 1513.0 |
| 17 | 0.0530 | 1450.0 |
| 18 | 0.0580 | 1350.0 |
| 19 | 0.0630 | 1200.0 |
| 20 | 0.0680 | 1100.0 |

Stress-strain values of SS2205 plate

| No. | Strain | Stress (MPa) |
|-----|--------|--------------|
| 1 | 0.0000 | 0.0 |
| 2 | 0.0010 | 200.0 |
| 3 | 0.0020 | 295.0 |
| 4 | 0.0030 | 375.0 |
| 5 | 0.0050 | 450.0 |
| 6 | 0.0100 | 530.0 |
| 7 | 0.0200 | 585.0 |
| 8 | 0.0400 | 640.0 |
| 9 | 0.0700 | 690.0 |
| 10 | 0.0900 | 715.0 |
| 11 | 0.1200 | 740.0 |
| 12 | 0.1500 | 752.0 |
| 13 | 0.1800 | 763.0 |
| 14 | 0.2200 | 762.0 |
| 15 | 0.2500 | 760.0 |
| 16 | 0.2800 | 750.0 |
| 17 | 0.3200 | 728.0 |
| 18 | 0.3300 | 718.0 |
| 19 | 0.3400 | 700.0 |
| 20 | 0.3500 | 670.0 |

Appendix B

Moment-rotation calculation of DWA connection.

| | |
|-----------------------|--|
| $\delta_{v,1}$ (mm) | horizontal deformation of the connection at the top flange of the beam |
| $\delta_{v,2}$ (mm) | horizontal deformation of the connection at the bottom flange of the beam |
| δ_{β} (mm) | relative total horizontal deformation of the connection measured from the top to the bottom flange of the beam |
| h (mm) | depth of the beam |
| θ (rad) | connection rotation ($\theta = \text{atan}(\delta_{\beta}/h)$) |
| d (mm) | length of the beam |
| F (KN) | point load at the end of the beam |
| M (KN.m) | moment at the column flange face ($M = 2 * F * d$) |

Table B.1 – Moment – rotation calculation of DWA-1b connection

| δ_{v1} (mm) | δ_{v2} (mm) | δ_g (mm) | δ_g/h | θ (rad) | θ (mRad) | M (KN.m) | P (KN) |
|--------------------|--------------------|-----------------|--------------|----------------|-----------------|------------|----------|
| 0.000 | 0.000 | 0.000 | 0.0000 | 0.0000 | 0.000 | 0.000 | 0.000 |
| 0.102 | -0.026 | 0.127 | 0.0004 | 0.0004 | 0.434 | 1.250 | 1.000 |
| 0.205 | -0.062 | 0.266 | 0.001 | 0.001 | 0.909 | 2.500 | 2.000 |
| 0.309 | -0.099 | 0.408 | 0.001 | 0.001 | 1.392 | 3.750 | 3.000 |
| 0.417 | -0.137 | 0.555 | 0.002 | 0.002 | 1.892 | 5.000 | 4.000 |
| 0.529 | -0.176 | 0.705 | 0.002 | 0.002 | 2.403 | 6.250 | 5.000 |
| 0.646 | -0.216 | 0.862 | 0.003 | 0.003 | 2.940 | 7.500 | 6.000 |
| 0.765 | -0.257 | 1.021 | 0.003 | 0.003 | 3.482 | 8.750 | 7.000 |
| 0.885 | -0.297 | 1.183 | 0.004 | 0.004 | 4.033 | 10.000 | 8.000 |
| 1.008 | -0.339 | 1.347 | 0.005 | 0.005 | 4.594 | 11.250 | 9.000 |
| 1.139 | -0.382 | 1.521 | 0.005 | 0.005 | 5.186 | 12.500 | 10.000 |
| 1.279 | -0.426 | 1.704 | 0.006 | 0.006 | 5.813 | 13.750 | 11.000 |
| 1.469 | -0.486 | 1.955 | 0.007 | 0.007 | 6.668 | 15.000 | 12.000 |
| 1.751 | -0.575 | 2.327 | 0.008 | 0.008 | 7.935 | 16.250 | 13.000 |
| 2.137 | -0.687 | 2.824 | 0.010 | 0.010 | 9.631 | 17.500 | 14.000 |
| 2.660 | -0.834 | 3.494 | 0.012 | 0.012 | 11.915 | 18.750 | 15.000 |
| 3.418 | -1.040 | 4.459 | 0.015 | 0.015 | 15.206 | 20.000 | 16.000 |
| 4.514 | -1.330 | 5.844 | 0.020 | 0.020 | 19.929 | 21.250 | 17.000 |
| 6.330 | -1.795 | 8.125 | 0.028 | 0.028 | 27.704 | 22.500 | 18.000 |
| 8.145 | -2.261 | 10.406 | 0.035 | 0.035 | 35.476 | 23.250 | 18.600 |
| 10.324 | -2.790 | 13.114 | 0.045 | 0.045 | 44.699 | 23.750 | 19.000 |
| 11.902 | -3.320 | 15.223 | 0.052 | 0.052 | 51.873 | 24.125 | 19.300 |
| 13.024 | -3.979 | 17.003 | 0.058 | 0.058 | 57.926 | 24.375 | 19.500 |
| 14.955 | -4.638 | 19.592 | 0.067 | 0.067 | 66.723 | 24.750 | 19.800 |
| 17.028 | -4.457 | 21.485 | 0.073 | 0.073 | 73.146 | 25.000 | 20.000 |
| 19.510 | -4.276 | 23.786 | 0.081 | 0.081 | 80.949 | 25.250 | 20.200 |
| 20.893 | -5.662 | 26.555 | 0.091 | 0.090 | 90.323 | 25.625 | 20.500 |

Table B.2 – Moment – rotation calculation of DWA-1c connection

| δ_{u1} (mm) | δ_{u2} (mm) | δ_p (mm) | δ_p/h | θ (rad) | θ (mRad) | M (KN.m) | P (KN) |
|--------------------|--------------------|-----------------|--------------|----------------|-----------------|------------|----------|
| 0.000 | 0.000 | 0.000 | 0.000 | 0.000 | 0.000 | 0.000 | 0.000 |
| 0.144 | -0.044 | 0.188 | 0.001 | 0.001 | 0.641 | 1.875 | 1.500 |
| 0.295 | -0.099 | 0.394 | 0.001 | 0.001 | 1.344 | 3.750 | 3.000 |
| 0.451 | -0.157 | 0.608 | 0.002 | 0.002 | 2.072 | 5.625 | 4.500 |
| 0.619 | -0.216 | 0.835 | 0.003 | 0.003 | 2.847 | 7.500 | 6.000 |
| 0.790 | -0.278 | 1.067 | 0.004 | 0.004 | 3.641 | 9.375 | 7.500 |
| 0.964 | -0.340 | 1.304 | 0.004 | 0.004 | 4.448 | 11.250 | 9.000 |
| 1.144 | -0.405 | 1.549 | 0.005 | 0.005 | 5.284 | 13.125 | 10.500 |
| 1.338 | -0.471 | 1.809 | 0.006 | 0.006 | 6.171 | 15.000 | 12.000 |
| 1.596 | -0.558 | 2.153 | 0.007 | 0.007 | 7.344 | 16.875 | 13.500 |
| 2.014 | -0.695 | 2.709 | 0.009 | 0.009 | 9.241 | 18.750 | 15.000 |
| 2.638 | -0.881 | 3.519 | 0.012 | 0.012 | 12.002 | 20.625 | 16.500 |
| 3.628 | -1.159 | 4.786 | 0.016 | 0.016 | 16.323 | 22.500 | 18.000 |
| 5.219 | -1.589 | 6.807 | 0.023 | 0.023 | 23.213 | 24.375 | 19.500 |
| 6.810 | -2.019 | 8.828 | 0.030 | 0.030 | 30.101 | 25.500 | 20.400 |
| 8.539 | -2.443 | 10.982 | 0.037 | 0.037 | 37.440 | 26.250 | 21.000 |
| 10.363 | -3.340 | 13.703 | 0.047 | 0.047 | 46.703 | 26.875 | 21.500 |
| 11.866 | -4.238 | 16.104 | 0.055 | 0.055 | 54.869 | 27.250 | 21.800 |
| 13.826 | -3.984 | 17.810 | 0.061 | 0.061 | 60.670 | 27.500 | 22.000 |
| 16.466 | -3.731 | 20.197 | 0.069 | 0.069 | 68.774 | 27.750 | 22.200 |
| 18.526 | -4.940 | 23.466 | 0.080 | 0.080 | 79.866 | 28.125 | 22.500 |

Table B.3 – Moment – rotation calculation of DWA-1d connection

| δ_{u1} (mm) | δ_{u2} (mm) | δ_n (mm) | δ_p/h | θ (rad) | θ (mRad) | M (KN.m) | P (KN) |
|--------------------|--------------------|-----------------|--------------|----------------|-----------------|------------|----------|
| 0.000 | 0.000 | 0.000 | 0.000 | 0.000 | 0.000 | 0.000 | 0.000 |
| 0.209 | -0.063 | 0.272 | 0.001 | 0.001 | 0.927 | 2.500 | 2.000 |
| 0.425 | -0.140 | 0.565 | 0.002 | 0.002 | 1.927 | 5.000 | 4.000 |
| 0.659 | -0.220 | 0.879 | 0.003 | 0.003 | 2.998 | 7.500 | 6.000 |
| 0.902 | -0.302 | 1.204 | 0.004 | 0.004 | 4.106 | 10.000 | 8.000 |
| 1.152 | -0.386 | 1.538 | 0.005 | 0.005 | 5.245 | 12.500 | 10.000 |
| 1.407 | -0.471 | 1.878 | 0.006 | 0.006 | 6.405 | 15.000 | 12.000 |
| 1.672 | -0.558 | 2.230 | 0.008 | 0.008 | 7.604 | 17.500 | 14.000 |
| 1.966 | -0.651 | 2.617 | 0.009 | 0.009 | 8.926 | 20.000 | 16.000 |
| 2.420 | -0.794 | 3.214 | 0.011 | 0.011 | 10.960 | 22.500 | 18.000 |
| 3.171 | -1.020 | 4.191 | 0.014 | 0.014 | 14.293 | 25.000 | 20.000 |
| 4.409 | -1.366 | 5.774 | 0.020 | 0.020 | 19.692 | 27.500 | 22.000 |
| 5.365 | -1.711 | 7.076 | 0.024 | 0.024 | 24.127 | 28.750 | 23.000 |
| 6.760 | -1.999 | 8.759 | 0.030 | 0.030 | 29.863 | 30.000 | 24.000 |
| 8.555 | -2.286 | 10.841 | 0.037 | 0.037 | 36.957 | 30.750 | 24.600 |
| 10.377 | -2.395 | 12.772 | 0.044 | 0.044 | 43.532 | 31.250 | 25.000 |
| 11.598 | -2.504 | 14.102 | 0.048 | 0.048 | 48.059 | 31.625 | 25.300 |
| 12.238 | -3.194 | 15.431 | 0.053 | 0.053 | 52.581 | 31.875 | 25.500 |
| 13.277 | -3.883 | 17.160 | 0.059 | 0.058 | 58.461 | 32.125 | 25.700 |
| 15.058 | -4.085 | 19.144 | 0.065 | 0.065 | 65.200 | 32.500 | 26.000 |
| 16.239 | -4.288 | 20.527 | 0.070 | 0.070 | 69.897 | 32.625 | 26.100 |
| 17.411 | -4.710 | 22.121 | 0.075 | 0.075 | 75.304 | 32.750 | 26.200 |

Table B.4 – Moment – rotation calculation of DWA-3b connection

| δ_{D1} (mm) | δ_{D2} (mm) | δ_B (mm) | δ_B/h | θ (rad) | θ (mRad) | M (KN.m) | P (KN) |
|--------------------|--------------------|-----------------|--------------|----------------|-----------------|------------|----------|
| 0.000 | 0.000 | 0.000 | 0.000 | 0.000 | 0.000 | 0.000 | 0.000 |
| 0.152 | -0.050 | 0.202 | 0.001 | 0.001 | 0.689 | 2.500 | 2.000 |
| 0.311 | -0.113 | 0.424 | 0.001 | 0.001 | 1.447 | 5.000 | 4.000 |
| 0.483 | -0.178 | 0.661 | 0.002 | 0.002 | 2.255 | 7.500 | 6.000 |
| 0.664 | -0.245 | 0.909 | 0.003 | 0.003 | 3.100 | 10.000 | 8.000 |
| 0.848 | -0.313 | 1.161 | 0.004 | 0.004 | 3.960 | 12.500 | 10.000 |
| 1.039 | -0.384 | 1.423 | 0.005 | 0.005 | 4.852 | 15.000 | 12.000 |
| 1.244 | -0.458 | 1.702 | 0.006 | 0.006 | 5.804 | 17.500 | 14.000 |
| 1.522 | -0.554 | 2.076 | 0.007 | 0.007 | 7.082 | 20.000 | 16.000 |
| 1.983 | -0.703 | 2.686 | 0.009 | 0.009 | 9.161 | 22.500 | 18.000 |
| 2.639 | -0.902 | 3.541 | 0.012 | 0.012 | 12.077 | 25.000 | 20.000 |
| 3.759 | -1.225 | 4.984 | 0.017 | 0.017 | 16.998 | 27.500 | 22.000 |
| 4.591 | -1.455 | 6.047 | 0.021 | 0.021 | 20.620 | 28.750 | 23.000 |
| 5.822 | -1.788 | 7.610 | 0.026 | 0.026 | 25.950 | 30.000 | 24.000 |
| 7.971 | -2.365 | 10.336 | 0.035 | 0.035 | 35.238 | 31.250 | 25.000 |
| 9.520 | -2.942 | 12.462 | 0.043 | 0.042 | 42.478 | 32.000 | 25.600 |
| 11.575 | -3.330 | 14.905 | 0.051 | 0.051 | 50.793 | 32.500 | 26.000 |
| 14.057 | -4.012 | 18.069 | 0.062 | 0.062 | 61.550 | 33.125 | 26.500 |
| 16.612 | -4.692 | 21.304 | 0.073 | 0.073 | 72.532 | 33.750 | 27.000 |
| 19.725 | -5.526 | 25.251 | 0.086 | 0.086 | 85.910 | 34.375 | 27.500 |
| 22.828 | -6.380 | 29.208 | 0.100 | 0.099 | 99.292 | 35.000 | 28.000 |

Table B.5 – Moment – rotation calculation of DWA-3c connection

| δ_{u1} (mm) | δ_{u2} (mm) | δ_0 (mm) | δ_0/h | θ (rad) | θ (mRad) | M (KN.m) | P (KN) |
|--------------------|--------------------|-----------------|--------------|----------------|-----------------|------------|----------|
| 0.000 | 0.000 | 0.000 | 0.000 | 0.000 | 0.000 | 0.000 | 0.000 |
| 0.142 | -0.050 | 0.192 | 0.001 | 0.001 | 0.654 | 2.500 | 2.000 |
| 0.293 | -0.112 | 0.405 | 0.001 | 0.001 | 1.382 | 5.000 | 4.000 |
| 0.456 | -0.177 | 0.634 | 0.002 | 0.002 | 2.162 | 7.500 | 6.000 |
| 0.627 | -0.244 | 0.871 | 0.003 | 0.003 | 2.970 | 10.000 | 8.000 |
| 0.800 | -0.313 | 1.113 | 0.004 | 0.004 | 3.794 | 12.500 | 10.000 |
| 0.975 | -0.383 | 1.358 | 0.005 | 0.005 | 4.632 | 15.000 | 12.000 |
| 1.157 | -0.457 | 1.614 | 0.006 | 0.006 | 5.504 | 17.500 | 14.000 |
| 1.358 | -0.536 | 1.894 | 0.006 | 0.006 | 6.458 | 20.000 | 16.000 |
| 1.621 | -0.634 | 2.254 | 0.008 | 0.008 | 7.688 | 22.500 | 18.000 |
| 2.037 | -0.779 | 2.816 | 0.010 | 0.010 | 9.605 | 25.000 | 20.000 |
| 2.632 | -0.975 | 3.607 | 0.012 | 0.012 | 12.302 | 27.500 | 22.000 |
| 3.539 | -1.262 | 4.801 | 0.016 | 0.016 | 16.374 | 30.000 | 24.000 |
| 5.007 | -1.714 | 6.721 | 0.023 | 0.023 | 22.919 | 32.500 | 26.000 |
| 6.475 | -2.066 | 8.541 | 0.029 | 0.029 | 29.122 | 34.000 | 27.200 |
| 7.852 | -2.536 | 10.388 | 0.035 | 0.035 | 35.416 | 35.000 | 28.000 |
| 9.230 | -3.006 | 12.236 | 0.042 | 0.042 | 41.708 | 35.750 | 28.600 |
| 11.285 | -2.935 | 14.220 | 0.048 | 0.048 | 48.461 | 36.250 | 29.000 |
| 12.840 | -2.863 | 15.704 | 0.054 | 0.054 | 53.509 | 36.625 | 29.300 |
| 13.729 | -3.694 | 17.422 | 0.059 | 0.059 | 59.351 | 36.875 | 29.500 |
| 14.617 | -4.524 | 19.141 | 0.065 | 0.065 | 65.189 | 37.125 | 29.700 |
| 16.255 | -4.966 | 21.221 | 0.072 | 0.072 | 72.252 | 37.500 | 30.000 |
| 17.894 | -5.408 | 23.302 | 0.079 | 0.079 | 79.308 | 37.875 | 30.300 |
| 19.533 | -5.850 | 25.383 | 0.087 | 0.086 | 86.357 | 38.000 | 30.400 |
| 18.235 | -8.840 | 27.075 | 0.092 | 0.092 | 92.080 | 38.125 | 30.500 |

Table B.6 – Moment – rotation calculation of DWA-3d connection

| δ_{v1} (mm) | δ_{v2} (mm) | δ_n (mm) | δ_p/h | θ (rad) | θ (mRad) | M (KN.m) | P (KN) |
|--------------------|--------------------|-----------------|--------------|----------------|-----------------|------------|----------|
| 0.000 | 0.000 | 0.000 | 0.000 | 0.000 | 0.000 | 0.000 | 0.000 |
| 0.145 | -0.051 | 0.195 | 0.001 | 0.001 | 0.666 | 2.500 | 2.000 |
| 0.299 | -0.114 | 0.413 | 0.001 | 0.001 | 1.407 | 5.000 | 4.000 |
| 0.465 | -0.180 | 0.646 | 0.002 | 0.002 | 2.202 | 7.500 | 6.000 |
| 0.639 | -0.248 | 0.887 | 0.003 | 0.003 | 3.025 | 10.000 | 8.000 |
| 0.815 | -0.318 | 1.133 | 0.004 | 0.004 | 3.865 | 12.500 | 10.000 |
| 0.993 | -0.389 | 1.383 | 0.005 | 0.005 | 4.715 | 15.000 | 12.000 |
| 1.173 | -0.462 | 1.635 | 0.006 | 0.006 | 5.576 | 17.500 | 14.000 |
| 1.355 | -0.537 | 1.892 | 0.006 | 0.006 | 6.453 | 20.000 | 16.000 |
| 1.544 | -0.613 | 2.157 | 0.007 | 0.007 | 7.358 | 22.500 | 18.000 |
| 1.751 | -0.694 | 2.445 | 0.008 | 0.008 | 8.339 | 25.000 | 20.000 |
| 2.010 | -0.796 | 2.806 | 0.010 | 0.010 | 9.570 | 27.500 | 22.000 |
| 2.383 | -0.943 | 3.326 | 0.011 | 0.011 | 11.343 | 30.000 | 24.000 |
| 2.918 | -1.150 | 4.068 | 0.014 | 0.014 | 13.872 | 32.500 | 26.000 |
| 3.694 | -1.453 | 5.146 | 0.018 | 0.018 | 17.550 | 35.000 | 28.000 |
| 4.951 | -2.000 | 6.960 | 0.024 | 0.024 | 23.734 | 37.500 | 30.000 |
| 5.928 | -2.747 | 8.674 | 0.030 | 0.030 | 29.576 | 39.000 | 31.200 |
| 7.301 | -3.351 | 10.652 | 0.036 | 0.036 | 36.314 | 40.000 | 32.000 |
| 7.964 | -4.702 | 12.667 | 0.043 | 0.043 | 43.174 | 40.500 | 32.400 |
| 9.641 | -4.602 | 14.244 | 0.049 | 0.049 | 48.542 | 40.750 | 32.600 |
| 11.318 | -4.502 | 15.821 | 0.054 | 0.054 | 53.907 | 41.125 | 32.900 |
| 12.377 | -5.451 | 17.827 | 0.061 | 0.061 | 60.727 | 41.250 | 33.000 |
| 13.435 | -6.399 | 19.833 | 0.068 | 0.068 | 67.542 | 41.375 | 33.100 |
| 15.102 | -7.012 | 22.115 | 0.075 | 0.075 | 75.283 | 41.625 | 33.300 |
| 16.770 | -7.626 | 24.396 | 0.083 | 0.083 | 83.015 | 41.750 | 33.400 |
| 17.828 | -8.574 | 26.403 | 0.090 | 0.090 | 89.807 | 42.000 | 33.600 |

Appendix C

Moment-rotation calculation of TSA connection.

| | |
|---------------------|--|
| $\delta_{v,1}$ (mm) | horizontal deformation of the connection at the top flange of the beam |
| $\delta_{v,2}$ (mm) | horizontal deformation of the connection at the bottom flange of the beam |
| δ_{pl} (mm) | relative total horizontal deformation of the connection measured from the top to the bottom flange of the beam |
| h (mm) | depth of the beam |
| θ (rad) | connection rotation ($\theta = \text{atan}(\delta_{pl}/h)$) |
| d (mm) | length of the beam |
| F (KN) | point load at the end of the beam |
| M (KN.m) | moment at the column flange face ($M = 2 * F.d$) |

Table C.1 – Moment – rotation calculation of TSA2-4b connection

| δ_{u1} (mm) | δ_{u2} (mm) | δ_B (mm) | δ_p/h | θ (rad) | θ (mRad) | M (KN.m) | P (KN) |
|--------------------|--------------------|-----------------|--------------|----------------|-----------------|------------|----------|
| 0.000 | 0.000 | 0.000 | 0.0000 | 0.0000 | 0.000 | 0.000 | 0.000 |
| 0.131 | -0.009 | 0.140 | 0.0005 | 0.0005 | 0.479 | 5.000 | 4.000 |
| 0.278 | -0.023 | 0.301 | 0.001 | 0.001 | 1.026 | 10.000 | 8.000 |
| 0.431 | -0.037 | 0.468 | 0.002 | 0.002 | 1.596 | 15.000 | 12.000 |
| 0.603 | -0.050 | 0.653 | 0.002 | 0.002 | 2.228 | 20.000 | 16.000 |
| 0.794 | -0.063 | 0.858 | 0.003 | 0.003 | 2.925 | 25.000 | 20.000 |
| 1.006 | -0.077 | 1.083 | 0.004 | 0.004 | 3.694 | 30.000 | 24.000 |
| 1.254 | -0.090 | 1.344 | 0.005 | 0.005 | 4.585 | 35.000 | 28.000 |
| 1.550 | -0.102 | 1.652 | 0.006 | 0.006 | 5.635 | 40.000 | 32.000 |
| 1.923 | -0.114 | 2.037 | 0.007 | 0.007 | 6.948 | 45.000 | 36.000 |
| 2.421 | -0.127 | 2.547 | 0.009 | 0.009 | 8.688 | 50.000 | 40.000 |
| 3.182 | -0.139 | 3.321 | 0.011 | 0.011 | 11.326 | 55.000 | 44.000 |
| 4.406 | -0.153 | 4.559 | 0.016 | 0.016 | 15.548 | 60.000 | 48.000 |
| 6.643 | -0.169 | 6.812 | 0.023 | 0.023 | 23.231 | 65.000 | 52.000 |
| 8.259 | -0.179 | 8.438 | 0.029 | 0.029 | 28.771 | 67.250 | 53.800 |
| 10.569 | -0.191 | 10.760 | 0.037 | 0.037 | 36.681 | 69.500 | 55.600 |
| 11.879 | -0.202 | 12.081 | 0.041 | 0.041 | 41.181 | 70.500 | 56.400 |
| 13.873 | -0.208 | 14.080 | 0.048 | 0.048 | 47.986 | 71.750 | 57.400 |
| 15.867 | -0.213 | 16.079 | 0.055 | 0.055 | 54.787 | 72.500 | 58.000 |
| 17.713 | -0.227 | 17.940 | 0.061 | 0.061 | 61.111 | 73.650 | 58.920 |
| 20.554 | -0.246 | 20.800 | 0.071 | 0.071 | 70.822 | 74.500 | 59.600 |

Table C.2 – Moment – rotation calculation of TSA2-4c connection

| δ_{u1} (mm) | δ_{u2} (mm) | δ_p (mm) | δ_p/h | θ (rad) | θ (mRad) | M (KN.m) | P (KN) |
|--------------------|--------------------|-----------------|--------------|----------------|-----------------|------------|----------|
| 0.000 | 0.000 | 0.000 | 0.0000 | 0.0000 | 0.000 | 0.000 | 0.000 |
| 0.133 | -0.009 | 0.142 | 0.0005 | 0.0005 | 0.484 | 5.000 | 4.000 |
| 0.281 | -0.023 | 0.304 | 0.001 | 0.001 | 1.037 | 10.000 | 8.000 |
| 0.435 | -0.037 | 0.472 | 0.002 | 0.002 | 1.610 | 15.000 | 12.000 |
| 0.607 | -0.051 | 0.658 | 0.002 | 0.002 | 2.244 | 20.000 | 16.000 |
| 0.791 | -0.064 | 0.855 | 0.003 | 0.003 | 2.917 | 25.000 | 20.000 |
| 0.985 | -0.077 | 1.062 | 0.004 | 0.004 | 3.623 | 30.000 | 24.000 |
| 1.196 | -0.091 | 1.287 | 0.004 | 0.004 | 4.388 | 35.000 | 28.000 |
| 1.430 | -0.104 | 1.534 | 0.005 | 0.005 | 5.230 | 40.000 | 32.000 |
| 1.700 | -0.117 | 1.817 | 0.006 | 0.006 | 6.196 | 45.000 | 36.000 |
| 2.030 | -0.130 | 2.160 | 0.007 | 0.007 | 7.368 | 50.000 | 40.000 |
| 2.496 | -0.143 | 2.639 | 0.009 | 0.009 | 9.000 | 55.000 | 44.000 |
| 3.203 | -0.156 | 3.359 | 0.011 | 0.011 | 11.455 | 60.000 | 48.000 |
| 4.294 | -0.170 | 4.464 | 0.015 | 0.015 | 15.225 | 65.000 | 52.000 |
| 6.222 | -0.187 | 6.409 | 0.022 | 0.022 | 21.856 | 70.000 | 56.000 |
| 7.746 | -0.195 | 7.941 | 0.027 | 0.027 | 27.077 | 72.250 | 57.800 |
| 9.734 | -0.204 | 9.938 | 0.034 | 0.034 | 33.882 | 74.500 | 59.600 |
| 12.543 | -0.216 | 12.759 | 0.044 | 0.043 | 43.487 | 76.750 | 61.400 |
| 15.775 | -0.229 | 16.004 | 0.055 | 0.055 | 54.531 | 79.000 | 63.200 |
| 18.004 | -0.237 | 18.240 | 0.062 | 0.062 | 62.131 | 80.000 | 64.000 |
| 20.431 | -0.246 | 20.677 | 0.071 | 0.070 | 70.405 | 81.000 | 64.800 |

Table C.3 – Moment – rotation calculation of TSA2-3d connection

| δ_{v1} (mm) | δ_{v2} (mm) | δ_B (mm) | δ_B/h | θ (rad) | θ (mRad) | M (KN.m) | P (KN) |
|--------------------|--------------------|-----------------|--------------|----------------|-----------------|------------|----------|
| 0.000 | 0.000 | 0.000 | 0.0000 | 0.0000 | 0.000 | 0.000 | 0.000 |
| 0.135 | -0.009 | 0.144 | 0.0005 | 0.0005 | 0.493 | 5.000 | 4.000 |
| 0.286 | -0.023 | 0.309 | 0.001 | 0.001 | 1.054 | 10.000 | 8.000 |
| 0.443 | -0.037 | 0.480 | 0.002 | 0.002 | 1.638 | 15.000 | 12.000 |
| 0.618 | -0.051 | 0.668 | 0.002 | 0.002 | 2.280 | 20.000 | 16.000 |
| 0.804 | -0.064 | 0.868 | 0.003 | 0.003 | 2.961 | 25.000 | 20.000 |
| 0.996 | -0.078 | 1.074 | 0.004 | 0.004 | 3.664 | 30.000 | 24.000 |
| 1.199 | -0.092 | 1.291 | 0.004 | 0.004 | 4.402 | 35.000 | 28.000 |
| 1.415 | -0.105 | 1.520 | 0.005 | 0.005 | 5.186 | 40.000 | 32.000 |
| 1.647 | -0.119 | 1.766 | 0.006 | 0.006 | 6.022 | 45.000 | 36.000 |
| 1.906 | -0.132 | 2.038 | 0.007 | 0.007 | 6.951 | 50.000 | 40.000 |
| 2.213 | -0.146 | 2.360 | 0.008 | 0.008 | 8.048 | 55.000 | 44.000 |
| 2.615 | -0.160 | 2.775 | 0.009 | 0.009 | 9.466 | 60.000 | 48.000 |
| 3.159 | -0.174 | 3.333 | 0.011 | 0.011 | 11.367 | 65.000 | 52.000 |
| 4.018 | -0.189 | 4.207 | 0.014 | 0.014 | 14.347 | 70.000 | 56.000 |
| 5.450 | -0.207 | 5.657 | 0.019 | 0.019 | 19.291 | 75.000 | 60.000 |
| 6.482 | -0.225 | 6.707 | 0.023 | 0.023 | 22.871 | 77.500 | 62.000 |
| 7.805 | -0.225 | 8.030 | 0.027 | 0.027 | 27.381 | 80.000 | 64.000 |
| 8.973 | -0.225 | 9.198 | 0.031 | 0.031 | 31.360 | 81.500 | 65.200 |
| 10.127 | -0.236 | 10.363 | 0.035 | 0.035 | 35.330 | 82.500 | 66.000 |
| 11.221 | -0.240 | 11.461 | 0.039 | 0.039 | 39.069 | 83.500 | 66.800 |
| 12.224 | -0.245 | 12.469 | 0.043 | 0.043 | 42.502 | 84.500 | 67.600 |
| 13.439 | -0.250 | 13.689 | 0.047 | 0.047 | 46.653 | 85.500 | 68.400 |
| 14.877 | -0.254 | 15.131 | 0.052 | 0.052 | 51.561 | 86.500 | 69.200 |
| 16.606 | -0.259 | 16.865 | 0.058 | 0.057 | 57.457 | 87.500 | 70.000 |
| 18.334 | -0.264 | 18.599 | 0.063 | 0.063 | 63.348 | 88.500 | 70.800 |
| 20.063 | -0.269 | 20.332 | 0.069 | 0.069 | 69.236 | 89.000 | 71.200 |

Appendix D

Moment-rotation calculation of TSAW connection.

| | |
|-----------------------|--|
| δ_{U_1} (mm) | horizontal deformation of the connection at the top flange of the beam |
| δ_{U_2} (mm) | horizontal deformation of the connection at the bottom flange of the beam |
| δ_{β} (mm) | relative total horizontal deformation of the connection measured from the top to the bottom flange of the beam |
| h (mm) | depth of the beam |
| θ (rad) | connection rotation ($\theta = \text{atan}(\delta_{\beta}/h)$) |
| d (mm) | length of the beam |
| F (KN) | point load at the end of the beam |
| M (KN.m) | moment at the column flange face ($M = 2 * F.d$) |

Table D.1 – Moment – rotation calculation of TSAW2-2b connection

| δ_{vj} (mm) | δ_{wv} (mm) | δ_p (mm) | δ_p/h | θ (rad) | θ (mRad) | M (KN.m) | P (KN) |
|--------------------|--------------------|-----------------|--------------|----------------|-----------------|------------|----------|
| 0.000 | 0.000 | 0.000 | 0.0000 | 0.0000 | 0.000 | 0.000 | 0.000 |
| 0.084 | 0.007 | 0.091 | 0.0003 | 0.0003 | 0.255 | 7.500 | 6.000 |
| 0.149 | 0.014 | 0.162 | 0.0004 | 0.0004 | 0.453 | 13.125 | 10.500 |
| 0.239 | 0.022 | 0.261 | 0.001 | 0.001 | 0.729 | 20.625 | 16.500 |
| 0.345 | 0.031 | 0.375 | 0.001 | 0.001 | 1.049 | 28.125 | 22.500 |
| 0.489 | 0.040 | 0.528 | 0.001 | 0.001 | 1.476 | 35.625 | 28.500 |
| 0.695 | 0.049 | 0.744 | 0.002 | 0.002 | 2.079 | 43.125 | 34.500 |
| 1.017 | 0.059 | 1.076 | 0.003 | 0.003 | 3.005 | 50.625 | 40.500 |
| 1.288 | 0.065 | 1.353 | 0.004 | 0.004 | 3.779 | 54.375 | 43.500 |
| 1.724 | 0.072 | 1.796 | 0.005 | 0.005 | 5.017 | 58.125 | 46.500 |
| 2.384 | 0.080 | 2.463 | 0.007 | 0.007 | 6.881 | 61.875 | 49.500 |
| 2.843 | 0.087 | 2.931 | 0.008 | 0.008 | 8.186 | 63.750 | 51.000 |
| 3.490 | 0.089 | 3.579 | 0.010 | 0.010 | 9.996 | 65.625 | 52.500 |
| 4.103 | 0.094 | 4.197 | 0.012 | 0.012 | 11.722 | 67.500 | 54.000 |
| 5.067 | 0.101 | 5.168 | 0.014 | 0.014 | 14.433 | 69.375 | 55.500 |
| 6.208 | 0.109 | 6.317 | 0.018 | 0.018 | 17.644 | 71.250 | 57.000 |
| 7.640 | 0.122 | 7.762 | 0.022 | 0.022 | 21.678 | 73.125 | 58.500 |
| 9.571 | 0.134 | 9.705 | 0.027 | 0.027 | 27.101 | 75.000 | 60.000 |
| 12.020 | 0.152 | 12.171 | 0.034 | 0.034 | 33.984 | 76.875 | 61.500 |
| 14.453 | 0.168 | 14.622 | 0.041 | 0.041 | 40.820 | 78.750 | 63.000 |
| 17.040 | 0.186 | 17.225 | 0.048 | 0.048 | 48.079 | 80.625 | 64.500 |
| 19.733 | 0.204 | 19.936 | 0.056 | 0.056 | 55.631 | 82.500 | 66.000 |

Table D.2 – Moment – rotation calculation of TSAW-2c connection

| δ_{v1} (mm) | δ_{v2} (mm) | δ_p (mm) | δ_p/h | θ (rad) | θ (mRad) | M (KN.m) | P (KN) |
|--------------------|--------------------|-----------------|--------------|----------------|-----------------|------------|----------|
| 0.000 | 0.000 | 0.000 | 0.0000 | 0.0000 | 0.000 | 0.000 | 0.000 |
| 0.125 | 0.010 | 0.135 | 0.0004 | 0.0004 | 0.378 | 7.500 | 6.000 |
| 0.254 | 0.021 | 0.275 | 0.001 | 0.001 | 0.769 | 15.000 | 12.000 |
| 0.387 | 0.032 | 0.420 | 0.001 | 0.001 | 1.172 | 22.500 | 18.000 |
| 0.534 | 0.044 | 0.577 | 0.002 | 0.002 | 1.612 | 30.000 | 24.000 |
| 0.734 | 0.056 | 0.791 | 0.002 | 0.002 | 2.209 | 37.500 | 30.000 |
| 1.036 | 0.070 | 1.107 | 0.003 | 0.003 | 3.091 | 45.000 | 36.000 |
| 1.484 | 0.085 | 1.569 | 0.004 | 0.004 | 4.384 | 52.500 | 42.000 |
| 1.782 | 0.093 | 1.875 | 0.005 | 0.005 | 5.238 | 56.250 | 45.000 |
| 2.187 | 0.101 | 2.289 | 0.006 | 0.006 | 6.393 | 60.000 | 48.000 |
| 2.461 | 0.105 | 2.567 | 0.007 | 0.007 | 7.169 | 61.875 | 49.500 |
| 2.829 | 0.110 | 2.938 | 0.008 | 0.008 | 8.208 | 63.750 | 51.000 |
| 3.269 | 0.115 | 3.384 | 0.009 | 0.009 | 9.451 | 65.625 | 52.500 |
| 3.787 | 0.231 | 4.018 | 0.011 | 0.011 | 11.224 | 67.500 | 54.000 |
| 4.443 | 0.237 | 4.679 | 0.013 | 0.013 | 13.070 | 69.375 | 55.500 |
| 5.214 | 0.242 | 5.456 | 0.015 | 0.015 | 15.239 | 71.250 | 57.000 |
| 6.260 | 0.252 | 6.512 | 0.018 | 0.018 | 18.188 | 73.125 | 58.500 |
| 7.456 | 0.262 | 7.718 | 0.022 | 0.022 | 21.555 | 75.000 | 60.000 |
| 8.962 | 0.274 | 9.236 | 0.026 | 0.026 | 25.793 | 76.875 | 61.500 |
| 10.821 | 0.290 | 11.111 | 0.031 | 0.031 | 31.026 | 78.750 | 63.000 |
| 12.738 | 0.241 | 12.979 | 0.036 | 0.036 | 36.237 | 80.625 | 64.500 |
| 15.776 | 0.320 | 16.095 | 0.045 | 0.045 | 44.928 | 82.500 | 66.000 |
| 18.836 | 0.390 | 19.225 | 0.054 | 0.054 | 53.650 | 84.375 | 67.500 |
| 21.836 | 0.439 | 22.274 | 0.062 | 0.062 | 62.138 | 85.625 | 68.500 |

Table D.3 – Moment – rotation calculation of TSAW-3b connection

| δ_{v1} (mm) | δ_{v2} (mm) | δ_B (mm) | δ_B/h | θ (rad) | θ (mRad) | M (KN.m) | P (KN) |
|--------------------|--------------------|-----------------|--------------|----------------|-----------------|------------|----------|
| 0.000 | 0.000 | 0.000 | 0.0000 | 0.0000 | 0.000 | 0.000 | 0.000 |
| 0.088 | 0.009 | 0.097 | 0.0003 | 0.0003 | 0.271 | 10.160 | 8.000 |
| 0.178 | 0.020 | 0.198 | 0.001 | 0.001 | 0.553 | 20.320 | 16.000 |
| 0.274 | 0.031 | 0.304 | 0.001 | 0.001 | 0.850 | 30.480 | 24.000 |
| 0.394 | 0.042 | 0.436 | 0.001 | 0.001 | 1.218 | 40.640 | 32.000 |
| 0.564 | 0.054 | 0.618 | 0.002 | 0.002 | 1.725 | 50.800 | 40.000 |
| 0.791 | 0.067 | 0.858 | 0.002 | 0.002 | 2.396 | 60.960 | 48.000 |
| 1.147 | 0.083 | 1.230 | 0.003 | 0.003 | 3.437 | 71.120 | 56.000 |
| 1.928 | 0.109 | 2.037 | 0.006 | 0.006 | 5.689 | 81.280 | 64.000 |
| 2.271 | 0.119 | 2.390 | 0.007 | 0.007 | 6.675 | 83.820 | 66.000 |
| 2.715 | 0.204 | 2.919 | 0.008 | 0.008 | 8.153 | 86.360 | 68.000 |
| 3.348 | 0.343 | 3.691 | 0.010 | 0.010 | 10.310 | 88.900 | 70.000 |
| 4.237 | 0.575 | 4.813 | 0.013 | 0.013 | 13.442 | 91.440 | 72.000 |
| 5.779 | 1.130 | 6.909 | 0.019 | 0.019 | 19.297 | 93.980 | 74.000 |
| 7.452 | 1.232 | 8.684 | 0.024 | 0.024 | 24.251 | 95.250 | 75.000 |
| 9.352 | 1.339 | 10.691 | 0.030 | 0.030 | 29.853 | 96.520 | 76.000 |
| 11.252 | 1.446 | 12.698 | 0.035 | 0.035 | 35.453 | 96.520 | 76.000 |

Table D.4 – Moment – rotation calculation of TSAW-3c connection

| δ_{v1} (mm) | δ_{v2} (mm) | δ_g (mm) | δ_g/h | θ (rad) | θ (mRad) | M (KN.m) | P (KN) |
|--------------------|--------------------|-----------------|--------------|----------------|-----------------|------------|----------|
| 0.000 | 0.000 | 0.000 | 0.0000 | 0.0000 | 0.000 | 0.000 | 0.000 |
| 0.121 | 0.009 | 0.131 | 0.0004 | 0.0004 | 0.365 | 10.000 | 8.000 |
| 0.246 | 0.021 | 0.267 | 0.001 | 0.001 | 0.745 | 20.000 | 16.000 |
| 0.382 | 0.032 | 0.413 | 0.001 | 0.001 | 1.155 | 30.000 | 24.000 |
| 0.524 | 0.043 | 0.567 | 0.002 | 0.002 | 1.583 | 40.000 | 32.000 |
| 0.712 | 0.054 | 0.766 | 0.002 | 0.002 | 2.138 | 50.000 | 40.000 |
| 0.975 | 0.066 | 1.041 | 0.003 | 0.003 | 2.908 | 60.000 | 48.000 |
| 1.329 | 0.078 | 1.407 | 0.004 | 0.004 | 3.929 | 70.000 | 56.000 |
| 1.858 | 0.089 | 1.947 | 0.005 | 0.005 | 5.438 | 80.000 | 64.000 |
| 2.202 | 0.095 | 2.297 | 0.006 | 0.006 | 6.416 | 84.500 | 67.600 |
| 2.702 | 0.102 | 2.804 | 0.008 | 0.008 | 7.834 | 89.000 | 71.200 |
| 3.057 | 0.306 | 3.363 | 0.009 | 0.009 | 9.394 | 91.500 | 73.200 |
| 3.142 | 0.812 | 3.953 | 0.011 | 0.011 | 11.043 | 94.000 | 75.200 |
| 3.813 | 0.981 | 4.794 | 0.013 | 0.013 | 13.391 | 96.500 | 77.200 |
| 4.412 | 1.133 | 5.545 | 0.015 | 0.015 | 15.487 | 99.000 | 79.200 |
| 5.054 | 1.340 | 6.394 | 0.018 | 0.018 | 17.860 | 101.500 | 81.200 |
| 5.860 | 1.548 | 7.408 | 0.021 | 0.021 | 20.689 | 104.000 | 83.200 |
| 6.558 | 1.756 | 8.314 | 0.023 | 0.023 | 23.219 | 106.500 | 85.200 |
| 7.598 | 1.964 | 9.562 | 0.027 | 0.027 | 26.703 | 109.000 | 87.200 |
| 8.704 | 2.025 | 10.729 | 0.030 | 0.030 | 29.961 | 110.875 | 88.700 |
| 9.910 | 2.286 | 12.196 | 0.034 | 0.034 | 34.055 | 112.500 | 90.000 |
| 11.116 | 2.547 | 13.663 | 0.038 | 0.038 | 38.147 | 114.125 | 91.300 |

Appendix E

Moment-rotation calculation of EPTB connection.

| | |
|-----------------------|--|
| $\delta_{v,1}$ (mm) | horizontal deformation of the connection at the top flange of the beam |
| $\delta_{v,2}$ (mm) | horizontal deformation of the connection at the bottom flange of the beam |
| δ_{β} (mm) | relative total horizontal deformation of the connection measured from the top to the bottom flange of the beam |
| h (mm) | depth of the beam |
| θ (rad) | connection rotation ($\theta = \arctan(\delta_{\beta}/h)$) |
| d (mm) | length of the beam |
| F (KN) | point load at the end of the beam |
| M (KN.m) | moment at the column flange face ($M = 2 * F.d$) |

Table E.1 – Moment – rotation calculation of EPHS-1b connection

| δ_{v1} (mm) | δ_{v2} (mm) | δ_p (mm) | δ_p/h | θ (rad) | θ (mRad) | M (KN.m) | P (KN) |
|--------------------|--------------------|-----------------|--------------|----------------|-----------------|------------|----------|
| 0.000 | 0.000 | 0.000 | 0.0000 | 0.0000 | 0.000 | 0.000 | 0.000 |
| 0.040 | -0.017 | 0.057 | 0.0003 | 0.0003 | 0.283 | 5.500 | 2.750 |
| 0.060 | -0.025 | 0.085 | 0.0004 | 0.0004 | 0.423 | 8.105 | 4.053 |
| 0.081 | -0.032 | 0.114 | 0.001 | 0.001 | 0.568 | 10.711 | 5.355 |
| 0.105 | -0.040 | 0.145 | 0.001 | 0.001 | 0.723 | 13.316 | 6.658 |
| 0.128 | -0.048 | 0.176 | 0.001 | 0.001 | 0.880 | 15.921 | 7.960 |
| 0.164 | -0.059 | 0.223 | 0.001 | 0.001 | 1.116 | 19.829 | 9.915 |
| 0.216 | -0.076 | 0.292 | 0.001 | 0.001 | 1.458 | 25.329 | 12.665 |
| 0.270 | -0.092 | 0.362 | 0.002 | 0.002 | 1.810 | 30.829 | 15.415 |
| 0.327 | -0.109 | 0.436 | 0.002 | 0.002 | 2.180 | 36.329 | 18.165 |
| 0.389 | -0.126 | 0.515 | 0.003 | 0.003 | 2.575 | 41.829 | 20.915 |
| 0.459 | -0.143 | 0.602 | 0.003 | 0.003 | 3.008 | 47.329 | 23.665 |
| 0.539 | -0.160 | 0.698 | 0.003 | 0.003 | 3.492 | 52.829 | 26.415 |
| 0.633 | -0.177 | 0.811 | 0.004 | 0.004 | 4.053 | 58.328 | 29.164 |
| 0.745 | -0.195 | 0.940 | 0.005 | 0.005 | 4.702 | 63.828 | 31.914 |
| 0.808 | -0.204 | 1.012 | 0.005 | 0.005 | 5.059 | 66.435 | 33.217 |
| 0.878 | -0.213 | 1.090 | 0.005 | 0.005 | 5.452 | 69.042 | 34.521 |
| 0.957 | -0.222 | 1.179 | 0.006 | 0.006 | 5.896 | 71.643 | 35.822 |
| 1.048 | -0.231 | 1.279 | 0.006 | 0.006 | 6.396 | 74.250 | 37.125 |
| 1.152 | -0.241 | 1.393 | 0.007 | 0.007 | 6.967 | 76.857 | 38.429 |
| 1.277 | -0.251 | 1.528 | 0.008 | 0.008 | 7.640 | 79.459 | 39.729 |
| 1.424 | -0.262 | 1.687 | 0.008 | 0.008 | 8.432 | 82.066 | 41.033 |
| 1.611 | -0.274 | 1.885 | 0.009 | 0.009 | 9.424 | 84.673 | 42.336 |
| 1.830 | -0.287 | 2.117 | 0.011 | 0.011 | 10.583 | 87.274 | 43.637 |
| 2.135 | -0.302 | 2.437 | 0.012 | 0.012 | 12.185 | 89.881 | 44.941 |
| 2.539 | -0.319 | 2.859 | 0.014 | 0.014 | 14.293 | 92.488 | 46.244 |
| 2.944 | -0.336 | 3.280 | 0.016 | 0.016 | 16.401 | 95.095 | 47.548 |
| 3.535 | -0.353 | 3.888 | 0.019 | 0.019 | 19.439 | 97.702 | 48.851 |
| 3.999 | -0.371 | 4.369 | 0.022 | 0.022 | 21.843 | 99.000 | 49.500 |
| 4.576 | -0.388 | 4.963 | 0.025 | 0.025 | 24.811 | 100.100 | 50.050 |
| 5.070 | -0.405 | 5.475 | 0.027 | 0.027 | 27.366 | 101.200 | 50.600 |
| 5.656 | -0.422 | 6.078 | 0.030 | 0.030 | 30.381 | 101.750 | 50.875 |
| 6.206 | -0.439 | 6.645 | 0.033 | 0.033 | 33.211 | 102.300 | 51.150 |
| 7.090 | -0.422 | 7.512 | 0.038 | 0.038 | 37.541 | 102.300 | 51.150 |

Table E.2 – Moment – rotation calculation of EPHS-3c connection

| δ_{y1} (mm) | δ_{y2} (mm) | δ_g (mm) | δ_g/h | θ (rad) | θ (mRad) | M (KN.m) | P (KN) |
|--------------------|--------------------|-----------------|--------------|----------------|-----------------|------------|----------|
| 0.000 | 0.000 | 0.000 | 0.0000 | 0.0000 | 0.000 | 0.000 | 0.000 |
| 0.068 | -0.029 | 0.097 | 0.0005 | 0.0005 | 0.483 | 5.500 | 5.000 |
| 0.148 | -0.057 | 0.204 | 0.001 | 0.001 | 1.021 | 11.000 | 10.000 |
| 0.233 | -0.085 | 0.318 | 0.002 | 0.002 | 1.589 | 16.500 | 15.000 |
| 0.322 | -0.114 | 0.435 | 0.002 | 0.002 | 2.177 | 22.000 | 20.000 |
| 0.416 | -0.142 | 0.558 | 0.003 | 0.003 | 2.792 | 27.500 | 25.000 |
| 0.518 | -0.172 | 0.690 | 0.003 | 0.003 | 3.449 | 33.000 | 30.000 |
| 0.633 | -0.201 | 0.834 | 0.004 | 0.004 | 4.170 | 38.500 | 35.000 |
| 0.767 | -0.232 | 0.999 | 0.005 | 0.005 | 4.994 | 44.000 | 40.000 |
| 0.933 | -0.263 | 1.195 | 0.006 | 0.006 | 5.977 | 49.500 | 45.000 |
| 1.154 | -0.296 | 1.450 | 0.007 | 0.007 | 7.252 | 55.000 | 50.000 |
| 1.288 | -0.313 | 1.601 | 0.008 | 0.008 | 8.003 | 57.607 | 52.370 |
| 1.449 | -0.331 | 1.779 | 0.009 | 0.009 | 8.897 | 60.209 | 54.735 |
| 1.642 | -0.349 | 1.992 | 0.010 | 0.010 | 9.958 | 62.816 | 57.105 |
| 1.903 | -0.370 | 2.273 | 0.011 | 0.011 | 11.365 | 65.423 | 59.475 |
| 2.253 | -0.392 | 2.645 | 0.013 | 0.013 | 13.223 | 68.024 | 61.840 |
| 2.729 | -0.416 | 3.145 | 0.016 | 0.016 | 15.723 | 70.631 | 64.210 |
| 3.448 | -0.441 | 3.889 | 0.019 | 0.019 | 19.443 | 73.238 | 66.580 |
| 4.528 | -0.477 | 5.005 | 0.025 | 0.025 | 25.019 | 75.840 | 68.945 |
| 6.667 | -0.529 | 7.196 | 0.036 | 0.036 | 35.966 | 78.447 | 71.315 |
| 9.737 | -0.599 | 10.336 | 0.052 | 0.052 | 51.633 | 80.850 | 73.500 |

Table E.3 – Moment – rotation calculation of EPHS-5c connection

| δ_{u1} (mm) | δ_{u2} (mm) | δ_B (mm) | δ_p/h | θ (rad) | θ (mRad) | M (KN.m) | P (KN) |
|--------------------|--------------------|-----------------|--------------|----------------|-----------------|------------|----------|
| 0.000 | 0.000 | 0.000 | 0.000 | 0.000 | 0.000 | 0.000 | 0.000 |
| 0.084 | -0.035 | 0.119 | 0.001 | 0.001 | 0.596 | 5.500 | 5.000 |
| 0.129 | -0.051 | 0.180 | 0.001 | 0.001 | 0.902 | 8.105 | 7.369 |
| 0.178 | -0.068 | 0.246 | 0.001 | 0.001 | 1.230 | 10.711 | 9.737 |
| 0.228 | -0.084 | 0.312 | 0.002 | 0.002 | 1.560 | 13.316 | 12.106 |
| 0.278 | -0.101 | 0.379 | 0.002 | 0.002 | 1.894 | 15.921 | 14.474 |
| 0.357 | -0.126 | 0.483 | 0.002 | 0.002 | 2.415 | 19.829 | 18.027 |
| 0.440 | -0.152 | 0.591 | 0.003 | 0.003 | 2.957 | 23.737 | 21.579 |
| 0.568 | -0.188 | 0.756 | 0.004 | 0.004 | 3.781 | 29.237 | 26.579 |
| 0.717 | -0.225 | 0.942 | 0.005 | 0.005 | 4.710 | 34.737 | 31.579 |
| 0.902 | -0.264 | 1.166 | 0.006 | 0.006 | 5.830 | 40.237 | 36.579 |
| 1.147 | -0.305 | 1.451 | 0.007 | 0.007 | 7.256 | 45.737 | 41.579 |
| 1.295 | -0.325 | 1.620 | 0.008 | 0.008 | 8.099 | 48.342 | 43.948 |
| 1.488 | -0.347 | 1.836 | 0.009 | 0.009 | 9.179 | 50.948 | 46.316 |
| 1.735 | -0.371 | 2.107 | 0.011 | 0.011 | 10.533 | 53.552 | 48.684 |
| 2.057 | -0.398 | 2.455 | 0.012 | 0.012 | 12.272 | 56.161 | 51.055 |
| 2.503 | -0.425 | 2.928 | 0.015 | 0.015 | 14.637 | 58.762 | 53.420 |
| 3.161 | -0.454 | 3.615 | 0.018 | 0.018 | 18.074 | 61.369 | 55.790 |
| 4.251 | -0.492 | 4.742 | 0.024 | 0.024 | 23.707 | 63.976 | 58.160 |
| 6.203 | -0.543 | 6.746 | 0.034 | 0.034 | 33.717 | 66.578 | 60.525 |
| 8.155 | -0.595 | 8.750 | 0.044 | 0.044 | 43.720 | 68.200 | 62.000 |
| 9.829 | -0.629 | 10.458 | 0.052 | 0.052 | 52.242 | 68.750 | 62.500 |

Appendix F

Moment-rotation calculation of FEP connection.

| | |
|-----------------------|--|
| δ_{v1} (mm) | horizontal deformation of the connection at the top flange of the beam |
| δ_{v2} (mm) | horizontal deformation of the connection at the bottom flange of the beam |
| δ_{β} (mm) | relative total horizontal deformation of the connection measured from the top to the bottom flange of the beam |
| h (mm) | depth of the beam |
| θ (rad) | connection rotation ($\theta = \text{atan}(\delta_{\beta}/h)$) |
| d (mm) | length of the beam |
| F (KN) | point load at the end of the beam |
| M (KN.m) | moment at the column flange face ($M = 2 * F.d$) |

Table F.1 – Moment – rotation calculation of FEP-3a connection

| δ_{v1} (mm) | δ_{v2} (mm) | δ_p (mm) | δ_p/h | θ (rad) | θ (mRad) | M (KN.m) | P (KN) |
|--------------------|--------------------|-----------------|--------------|----------------|-----------------|------------|----------|
| 0.000 | 0.000 | 0.000 | 0.0000 | 0.0000 | 0.000 | 0.000 | 0.000 |
| 0.117 | -0.016 | 0.133 | 0.0004 | 0.0004 | 0.452 | 6.500 | 2.500 |
| 0.270 | -0.034 | 0.304 | 0.001 | 0.001 | 1.034 | 13.000 | 5.000 |
| 0.437 | -0.053 | 0.490 | 0.002 | 0.002 | 1.667 | 19.500 | 7.500 |
| 0.609 | -0.071 | 0.681 | 0.002 | 0.002 | 2.315 | 26.000 | 10.000 |
| 0.793 | -0.089 | 0.882 | 0.003 | 0.003 | 3.001 | 32.500 | 12.500 |
| 0.985 | -0.107 | 1.092 | 0.004 | 0.004 | 3.714 | 39.000 | 15.000 |
| 1.189 | -0.125 | 1.314 | 0.004 | 0.004 | 4.469 | 45.500 | 17.500 |
| 1.412 | -0.143 | 1.556 | 0.005 | 0.005 | 5.292 | 52.000 | 20.000 |
| 1.658 | -0.163 | 1.821 | 0.006 | 0.006 | 6.194 | 58.500 | 22.500 |
| 1.940 | -0.184 | 2.124 | 0.007 | 0.007 | 7.223 | 65.000 | 25.000 |
| 2.283 | -0.205 | 2.489 | 0.008 | 0.008 | 8.464 | 71.500 | 27.500 |
| 2.682 | -0.228 | 2.910 | 0.010 | 0.010 | 9.898 | 78.000 | 30.000 |
| 3.177 | -0.253 | 3.430 | 0.012 | 0.012 | 11.665 | 84.500 | 32.500 |
| 3.821 | -0.284 | 4.105 | 0.014 | 0.014 | 13.961 | 91.000 | 35.000 |
| 4.645 | -0.327 | 4.972 | 0.017 | 0.017 | 16.909 | 97.500 | 37.500 |
| 5.474 | -0.390 | 5.864 | 0.020 | 0.020 | 19.944 | 104.000 | 40.000 |
| 6.384 | -0.429 | 6.813 | 0.023 | 0.023 | 23.169 | 110.500 | 42.500 |
| 7.189 | -0.481 | 7.670 | 0.026 | 0.026 | 26.081 | 117.000 | 45.000 |
| 8.205 | -0.550 | 8.755 | 0.030 | 0.030 | 29.770 | 123.500 | 47.500 |
| 9.022 | -0.609 | 9.631 | 0.033 | 0.033 | 32.747 | 126.750 | 48.750 |
| 9.800 | -0.613 | 10.413 | 0.035 | 0.035 | 35.403 | 130.000 | 50.000 |
| 10.350 | -0.619 | 10.969 | 0.037 | 0.037 | 37.292 | 131.560 | 50.600 |
| 10.795 | -0.629 | 11.424 | 0.039 | 0.039 | 38.837 | 132.600 | 51.000 |
| 10.982 | -0.639 | 11.621 | 0.040 | 0.040 | 39.507 | 131.950 | 50.750 |
| 11.240 | -0.639 | 11.879 | 0.040 | 0.040 | 40.382 | 131.300 | 50.500 |
| 11.590 | -0.639 | 12.229 | 0.042 | 0.042 | 41.571 | 130.000 | 50.000 |
| 12.385 | -0.649 | 13.034 | 0.044 | 0.044 | 44.304 | 126.750 | 48.750 |
| 13.180 | -0.659 | 13.839 | 0.047 | 0.047 | 47.036 | 123.500 | 47.500 |

Table F.2 – Moment – rotation calculation of FEP-3b connection

| $\delta_{v,z}$ (mm) | $\delta_{v,z}$ (mm) | δ_{θ} (mm) | δ_{θ}/h | θ (rad) | θ (mRad) | M (KN.m) | P (KN) |
|---------------------|---------------------|------------------------|---------------------|----------------|-----------------|------------|----------|
| 0.000 | 0.000 | 0.000 | 0.0000 | 0.0000 | 0.000 | 0.000 | 0.000 |
| 0.117 | -0.016 | 0.133 | 0.0004 | 0.0004 | 0.452 | 9.750 | 3.750 |
| 0.270 | -0.034 | 0.304 | 0.001 | 0.001 | 1.034 | 19.500 | 7.500 |
| 0.437 | -0.053 | 0.490 | 0.002 | 0.002 | 1.667 | 29.250 | 11.250 |
| 0.609 | -0.071 | 0.681 | 0.002 | 0.002 | 2.315 | 39.000 | 15.000 |
| 0.793 | -0.089 | 0.882 | 0.003 | 0.003 | 3.001 | 48.750 | 18.750 |
| 0.985 | -0.107 | 1.092 | 0.004 | 0.004 | 3.714 | 58.500 | 22.500 |
| 1.189 | -0.125 | 1.314 | 0.004 | 0.004 | 4.469 | 68.250 | 26.250 |
| 1.412 | -0.143 | 1.556 | 0.005 | 0.005 | 5.292 | 78.000 | 30.000 |
| 1.658 | -0.163 | 1.821 | 0.006 | 0.006 | 6.194 | 87.750 | 33.750 |
| 1.940 | -0.184 | 2.124 | 0.007 | 0.007 | 7.223 | 97.500 | 37.500 |
| 2.283 | -0.205 | 2.489 | 0.008 | 0.008 | 8.464 | 107.250 | 41.250 |
| 2.682 | -0.228 | 2.910 | 0.010 | 0.010 | 9.898 | 120.900 | 46.500 |
| 3.177 | -0.253 | 3.430 | 0.012 | 0.012 | 11.665 | 136.500 | 52.500 |
| 3.821 | -0.284 | 4.105 | 0.014 | 0.014 | 13.961 | 150.150 | 57.750 |
| 4.645 | -0.327 | 4.972 | 0.017 | 0.017 | 16.909 | 165.750 | 63.750 |
| 5.374 | -0.390 | 5.764 | 0.020 | 0.020 | 19.604 | 175.500 | 67.500 |
| 6.384 | -0.429 | 6.813 | 0.023 | 0.023 | 23.169 | 187.200 | 72.000 |
| 7.189 | -0.481 | 7.670 | 0.026 | 0.026 | 26.081 | 195.000 | 75.000 |
| 8.205 | -0.550 | 8.755 | 0.030 | 0.030 | 29.770 | 202.800 | 78.000 |
| 9.022 | -0.619 | 9.641 | 0.033 | 0.033 | 32.781 | 205.725 | 79.125 |
| 9.521 | -0.619 | 10.140 | 0.034 | 0.034 | 34.476 | 202.215 | 77.775 |
| 9.721 | -0.619 | 10.340 | 0.035 | 0.035 | 35.156 | 199.875 | 76.875 |
| 10.050 | -0.619 | 10.669 | 0.036 | 0.036 | 36.273 | 196.950 | 75.750 |
| 10.295 | -0.629 | 10.924 | 0.037 | 0.037 | 37.139 | 193.050 | 74.250 |
| 10.482 | -0.639 | 11.121 | 0.038 | 0.038 | 37.809 | 190.125 | 73.125 |
| 10.740 | -0.639 | 11.379 | 0.039 | 0.039 | 38.684 | 186.225 | 71.625 |
| 11.090 | -0.639 | 11.729 | 0.040 | 0.040 | 39.873 | 183.300 | 70.500 |
| 11.735 | -0.649 | 12.384 | 0.042 | 0.042 | 42.097 | 181.350 | 69.750 |
| 12.590 | -0.659 | 13.249 | 0.045 | 0.045 | 45.033 | 179.400 | 69.000 |

Appendix G

Moment-rotation calculation of SCC connection.

| | |
|---------------------|--|
| $\delta_{t,1}$ (mm) | horizontal deformation of the connection at the top flange of the beam |
| $\delta_{t,2}$ (mm) | horizontal deformation of the connection at the bottom flange of the beam |
| δ_y (mm) | relative total horizontal deformation of the connection measured from the top to the bottom flange of the beam |
| h (mm) | depth of the beam |
| θ (rad) | connection rotation ($\theta = \text{atan}(\delta_y/h)$) |
| l (mm) | length of the beam |
| F (KN) | point load at the end of the beam |
| M (KN.m) | moment at the column flange face ($M = 2 * F.l$) |

Table G.1 – Moment – rotation calculation of SCC-1b connection

| δ_{v1} (mm) | δ_{v2} (mm) | δ_B (mm) | δ_B/h | θ (rad) | θ (mRad) | M (KN.m) | P (KN) |
|--------------------|--------------------|-----------------|--------------|----------------|-----------------|------------|----------|
| 0.000 | 0.000 | 0.000 | 0.0000 | 0.0000 | 0.000 | 0.000 | 0.000 |
| 0.085 | -0.046 | 0.131 | 0.0004 | 0.0004 | 0.443 | 29.400 | 10.000 |
| 0.206 | -0.096 | 0.302 | 0.001 | 0.001 | 1.025 | 58.800 | 20.000 |
| 0.370 | -0.151 | 0.522 | 0.002 | 0.002 | 1.771 | 88.200 | 30.000 |
| 0.652 | -0.222 | 0.874 | 0.003 | 0.003 | 2.967 | 117.600 | 40.000 |
| 1.189 | -0.395 | 1.584 | 0.005 | 0.005 | 5.378 | 147.000 | 50.000 |
| 2.105 | -1.039 | 3.144 | 0.011 | 0.011 | 10.675 | 176.400 | 60.000 |
| 3.212 | -1.682 | 4.895 | 0.017 | 0.017 | 16.619 | 194.040 | 66.000 |
| 4.128 | -2.428 | 6.556 | 0.022 | 0.022 | 22.258 | 204.330 | 69.500 |
| 6.051 | -3.418 | 9.468 | 0.032 | 0.032 | 32.139 | 217.560 | 74.000 |
| 8.273 | -4.070 | 12.343 | 0.042 | 0.042 | 41.888 | 223.440 | 76.000 |
| 9.684 | -5.404 | 15.088 | 0.051 | 0.051 | 51.186 | 229.320 | 78.000 |

Table G.2 – Moment – rotation calculation of SCC-1c connection

| δ_{v1} (mm) | δ_{v2} (mm) | δ_3 (mm) | δ_B/h | θ (rad) | θ (mRad) | M (KN.m) | P (KN) |
|--------------------|--------------------|-----------------|--------------|----------------|-----------------|------------|----------|
| 0.000 | 0.000 | 0.000 | 0.0000 | 0.0000 | 0.000 | 0.000 | 0.000 |
| 0.044 | -0.033 | 0.078 | 0.0003 | 0.0003 | 0.264 | 22.050 | 10.000 |
| 0.092 | -0.068 | 0.160 | 0.001 | 0.001 | 0.543 | 44.100 | 20.000 |
| 0.150 | -0.103 | 0.253 | 0.001 | 0.001 | 0.860 | 66.150 | 30.000 |
| 0.259 | -0.146 | 0.405 | 0.001 | 0.001 | 1.374 | 88.200 | 40.000 |
| 0.378 | -0.190 | 0.568 | 0.002 | 0.002 | 1.929 | 110.250 | 50.000 |
| 0.656 | -0.229 | 0.885 | 0.003 | 0.003 | 3.006 | 132.300 | 60.000 |
| 0.996 | -0.368 | 1.364 | 0.005 | 0.005 | 4.631 | 154.350 | 70.000 |
| 1.336 | -0.692 | 2.028 | 0.007 | 0.007 | 6.885 | 176.400 | 80.000 |
| 1.676 | -1.015 | 2.691 | 0.009 | 0.009 | 9.138 | 187.425 | 85.000 |
| 2.016 | -1.339 | 3.355 | 0.011 | 0.011 | 11.392 | 194.040 | 88.000 |
| 2.917 | -1.650 | 4.567 | 0.016 | 0.016 | 15.507 | 198.450 | 90.000 |
| 3.982 | -1.961 | 5.943 | 0.020 | 0.020 | 20.179 | 202.860 | 92.000 |
| 5.147 | -2.593 | 7.740 | 0.026 | 0.026 | 26.276 | 207.270 | 94.000 |

Publications

The author has six jointed international conference publications.

The conference publications:

Taufik S. and Xiao R.Y., "3D Finite Element Predictions of Angle Bolted Connection with High Strength Steel", Proceeding of the Fourth International Conference on Advance in Steel Structures, Shanghai – China, Z.Y.Shen, G.Q.LI and S.L.Chan, (Eds), Elsevier, Volume II, paper no. ISP-26, 1775-1782, 2005

Taufik S. and Xiao R.Y., "Simplified Finite Element Modelling of Beam-column Bolted Connection with Shell Element", Proceedings of the Eighth International Conference on Computational Structures Technology, B.H.V. Topping, G. Montero and R. Montenegro, (Eds), Civil-Comp Press, Stirlingshire, UK, paper no. CST-118, 2006

Taufik S. and Xiao R.Y., "3D Finite Element Modelling of Flush End Plate Connection With High Strength Steel", Proceedings of the Eighth International Conference on Computational Structures Technology, B.H.V. Topping, G. Montero and R. Montenegro, (Eds), Civil-Comp Press, Stirlingshire, UK, paper no.CST-119, 2006.

Taufik S. and Xiao R.Y., "Finite Element Modelling of End Plate Connection with Hollow Section Beam", Proceedings of the 6th International Conference on Steel and Aluminium Structures, Oxford, UK, July 2007.

Xiao R.Y. and Taufik S., "Numerical Modelling of Semi-continuous Composite Connection with High Strength Steel", Proceedings of The Eleventh International Conference on Civil, Structural and Environmental Engineering Computing, B.H.V. Topping (Editor), Civil-Comp Press, Stirlingshire, UK, paper no. 153, 2007

Xiao R.Y. and Taufik S., "Finite Element Modelling of Partially Restrained Connection with Cold-formed High Strength Steel Section", Proceeding of the Fifth International Conference on Advance in Steel Structures, Singapore, JY Richard Liew and YS Choo, Editor(s), Research Publishing Services, Volume III, paper no. 111, December 2007